

# Identified particle production in Pb-Pb and pp collisions at LHC energies

by

**Subhash Singha**

Enrollment Number: PHYS07200904008

National Institute of Science Education and Research

Bhubaneswar - 751005, India

A Thesis Submitted to the  
Board of Studies in Physical Sciences  
In partial fulfillment of requirements  
for the degree of  
DOCTOR OF PHILOSOPHY  
of  
HOMI BHABHA NATIONAL INSTITUTE



September, 2014

# Homi Bhabha National Institute

## Recommendations of the The Viva Voce Committee

As members of the Viva Voce Committee, we certify that we have read the dissertation prepared by Mr Subhash Singha, HBNI Enrolment No PHYS07200904008 titled "Identified Particle Production in Pb-Pb and pp collisions at LHC energies" and recommend that it may be accepted as fulfilling the thesis requirement for the award of Degree of Doctor of Philosophy.

Prof Ajit Srivastava (Chairman)

*Ajit Srivastava 4-9-14*

Dr. Bedangadas Mohanty (Guide / Convener)

*Bedangadas Mohanty 4/9/2014*

Prof. Bhartendu K Singh (External – Member)

*Bhartendu K Singh*

Dr Subhankar Bedanta (Member)

*S Bedanta*

Dr Prolay Mal (Member)

*P Mal 4/9/2014*

Dr Sanjay Swain (Member)

*Sanjay Kumar Swain*

Final approval and acceptance of this thesis is contingent upon the candidate's submission of the final copies of the thesis to HBNI.

I/We hereby certify that I/we have read this thesis prepared under my/our direction and recommend that it may be accepted as fulfilling the thesis requirement.

Place: NISER, Bhubaneswar

Date: 4/9/2014

Signature

Co-guide (if applicable)

*Bedangadas Mohanty*  
Signature 4/9/2014  
Guide

*Dedicated*  
*To*  
*My Parents and Teachers*

## Statement by Author

This dissertation has been submitted in partial fulfillment of requirements for an advanced degree at Homi Bhabha National Institute (HBNI) and is deposited in the Library to be made available to borrowers under rules of the HBNI. Brief quotations from this dissertation are allowable without special permission, provided that accurate acknowledgement of source is made. Requests for permission for extended quotation from or reproduction of this manuscript in whole or in part may be granted by the Competent Authority of HBNI when in his or her judgment the proposed use of the material is in the interests of scholarship. In all other instances, however, permission must be obtained from the author.



Subhash Singha

## Declaration

I, Subhash Singha, hereby declare that the investigation presented in the thesis has been carried out by me. The work is original and has not been submitted earlier as a whole or in part for a degree/diploma at this or any other Institution/University.



Subhash Singha

# Acknowledgement

First and foremost I would like to express my sincere gratitude to my supervisor Prof. Bedangadas Mohanty for giving me the opportunity to work on such fascinating subject. It was never possible for me to continue without his precious guidance and support. I would like to express my sincere thanks for his dedicated supervision and tired-less help during this period. I am greatly benefited by his wide knowledge and logical way of thinking. I would like to thank Prof. Mohanty for providing me the opportunities to present my work in prestigious conferences and to visit international labs.

I am thankful to all my teachers during the pre-doctoral course work at VECC and introducing me to the basics of heavy ion physics. It was a great opportunity to interact with Dr. Jane e Alam, Dr. Saurav Sarkar, Dr. D. N. Basu, Dr. Asis Kumar Chowdhury, Dr. Gopal Mukherjee and Dr. V. S. Pandit during the pre-doctoral course.

I would like to thank all the members of Experimental High Energy Physics and Application Group at VECC. I would like to thank Dr. Tapan Nayak, Dr. Subhashis Chattopadhyay, Dr. Rama Singaraju, Dr. Anand Dubey and Dr. Sushant Pal of VECC for their help and suggestions during this period. I would like to thank Mr. Shuaib Ahmed Khan, Mr. Jogender Saini and Dr. Satyajit Jena for their help during the PMD installation and data taking at CERN. I would like to thank Mr. Vikas Singhal and acknowledge the services provided by the grid computing facility at VECC-Kolkata, for facilitating to perform a part of the computation used in this thesis.

I would like to express my thanks to Dr. T. Chandrashekhar (Director , NISER), Dr. D. K. Srivastava (Director, VECC) and Dr. Y. P. Viyogi for helping me during my

transfer to NISER from VECC. I would like to thank Dr. Sudhakar Panda (Director, IOP), Dr. D. P. Mahapatra and Dr. P. K. Sahu for providing a sitting place at IOP. I would like to thank all the members of my doctoral committee in VECC and NISER. I would like to take the opportunity to thank all the members of physics group at VECC, NISER, IOP and all members of PMD collaboration.

I would like express my thanks to Dr. Ajay Kumar Dash, Dr. Sidharth Kumar Prasad, Dr. Sadhana Dash and Dr. Ranbir Singh for their immense help at the very beginning of Ph.D career. I would like to thank Dr. Md Nasim for his constant support and encouragement like a best friend and philosopher. I would like to thank Mr. Riham Haque for his help and support. I would like thank Dr. Sudipan De and Dr. Nihar Ranjan Sahoo for their help and physics discussions during my stay at VECC. I will never forget the sleepless nights and stimulating physics discussions and all the fun in last five years with Ajay bhai, Sidharth bhai, Ranbir bhai, Nasim, Riham, Sudipan and Nihar bhai. I would like to thank Dr. Lokesh Kumar, Dr. Saikat Biswas, Dr. Sandeep Chatterjee, Mr. Kishora Nayak, Mr. Vipul Bairathi, Mr. Shreekanth Tripathy, Mr. Rama Chandra Baral, Mr. Shikshit Gupta, Mr. Mukesh Sharma and Mrs. Sabita Das many useful discussions, specially the weekly group meeting helped me a lot. Its my pleasure to thank all my fellow friends at VECC, NISER and IOP for their support and encouragement. I enjoyed your company in last five years.

I would like to thank Dr. Paolo Giubellino (Spokesperson, ALICE) for his help in various matters in spite of his busy schedule. I would like to thank Dr. Jurgen Schukraft and Dr. Helmut Oeschler for giving many helpful suggestions in my analysis. I would like to thank Dr. Alberto Pulvirenti for introducing me into the resonance analysis framework in ALICE. I would like to thank the physics analysis group conveners in ALICE, specially Dr. Angela Badala, Dr. Christina Markert,

Dr. Boris Hippolyte, Dr. Luciano Ramello, Dr. Michele Floris, Dr. Lee Barnby and Dr. Roberto Preghnella for their help. Their valuable suggestions and constructive criticism helped me in understanding the analysis in great detail. I would like to thank ALICE software team and Dr. Latchezar Betev for helping me in computation matters and providing the resources for computation. I would like to thank the LEGO train operator team in ALICE for their help in computation. I would like to thank Dr. Anders Knospe, Dr. Francesca Bellini and Dr. Martin Vala for their help in resonance analysis. I would like to express my thanks to Dr. Angela Badala for inviting me to INFN, Catania and introducing me to the interesting analysis of jet-hadron correlation. Numerous physics discussions with her helped me a lot during the analysis.

I am indebted to all my teachers from my school days to university. I was very lucky to have Prof. Samiran Chattopadhyay, Prof. Basudeb Ghoshal, Prof. Atish Dipankar Jana, Prof. Chirantan Neogi and Prof. Yatra Mohan Jana as my teachers during my college and university days. I always wonder about their depth in knowledge and wisdom. They are the inspiration in considering physics as a career. I would like to thank Dr. Manas Mukhopadhyay for inspiring me towards research. I would like to thank my family members, friends and colleagues for their constant support and encouragement during the whole period. Above all it would be never possible for me to continue without constant support, encouragement and blessings from my parents. My apologies, if I missed someone who deserved to be in this list.



Subhash Singha



# SYNOPSIS

The main goal of ultra relativistic heavy-ion collisions is to investigate the strongly interacting matter, called the Quark Gluon Plasma (QGP), expected to produce in such collisions. The Large Hadron Collider (LHC) at CERN provides an unique opportunity to study such strongly interacting matter at extreme energy densities.

The short lived resonances are very useful tool in high energy collisions to study the dynamics and properties of a strongly interacting medium. In particular, the  $K^{*0}(892)$  meson is important because its lifetime (4 fm/c) is comparable to the time scale of the hot and dense matter produced. Owing to short lifetime, the characteristic properties such as mass, width, yield and transverse momentum spectra of  $K^{*0}$  is very sensitive to the dynamics and in-medium effects. Basically the decay products of  $K^{*0}$ , the pions and kaons, may undergo in-medium effects. The decay products of high momentum resonances have a larger probability to escape the system and thereby detected, while that of low momentum resonances can be re-scattered by other hadrons present in the medium. Thus, we can not reconstruct back the resonance and the signal is lost. On the other hand, the pions and kaons in the medium can re-generate  $K^{*0}$  via pseudo-elastic interactions ( $K\pi \rightarrow K^{*0} \rightarrow K\pi$ ) during the phase between the chemical freeze-out (when inelastic collision ceases) and the kinetic freeze out (when elastic collision ceases). This re-generation process could compensate for the  $K^{*0}$  yield, lost in re-scattering, if the system formed has a long expansion time. It was observed that the pion-pion interaction cross section is five times larger than the kaon-pion interaction cross section. The pion-pion interaction cross-section is responsible for the re-scattering, while the kaon-pion cross-section for the re-generation processes. Thus, the interplay of the two processes, re-scattering and re-generation, will decide the final resonance yield and a resonance to non-resonance particle ratio can be used to understand these processes. Since the  $K^{*0}$  and  $K^-$  have different masses and spins, but they have identical quark content, the  $K^{*0}/K^-$  ratio can be used as a tool to understand the re-scattering and re-generation processes in the hadronic phase. The production of  $K^{*0}$  has been measured in STAR experiment at RHIC, which shows the dominance of re-scattering effect over the re-generation mech-

anism. In this thesis, we will present the results of  $K^{*0}$  production via its hadronic decay channel ( $K^{*0} \rightarrow \pi^- K^+$  and  $\bar{K}^{*0} \rightarrow \pi^+ K^-$ ) at mid rapidity ( $-0.5 < y < 0.5$ ) in Pb+Pb collisions at  $\sqrt{s_{NN}} = 2.76$  TeV and in minimum bias p+p collisions at  $\sqrt{s} = 2.76$  TeV. We will present the mass, width, yield and transverse momentum spectra of  $K^{*0}$  meson. This will enable us to understand the in-medium effects and freeze-out conditions at unprecedented higher energies attained at the LHC. The mean transverse momentum ( $\langle p_T \rangle$ ) of  $K^{*0}$  will be obtained and compared with other hadrons and lower energy measurements to investigate particle production mechanism at LHC energies. The particle ratio  $K^{*0}/K^-$  will be obtained in different collision centralities in Pb+Pb collisions and minimum bias p+p collisions. It will also be compared with lower energy measurements at SPS and RHIC. Such results will shed light on the evolution of the hadronic medium formed at higher energies and one can estimate the lower limit of the lifetime of the hadronic interacting phase. Also, the  $K^{*0}/K^-$  ratio will be compared to  $\phi/K^-$  ratio, which is expected to be less affected by the hadronic interactions since the lifetime of  $\phi$  is about 10 times longer than that of  $K^{*0}$ .

The nuclear modification factor  $R_{CP}$  (ratio of yields of  $K^{*0}$  in central to those in peripheral collisions and appropriately normalized by the number of binary collisions) or  $R_{AA}$  (scaled to p+p collisions) are the variables to study the effect of the medium on  $K^{*0}$  production in heavy ion collisions. These variables are very sensitive to the size and the density of the system formed in such collisions. The  $R_{CP}$  is expected to be less than unity if there is a creation of strongly interacting matter. In addition, it can show baryon-meson splitting at intermediate  $p_T$  region where quark recombination model is expected to be followed. If the heavy-ion collision is a simple super position of p+p collision, one would expect the value of  $R_{AA}$  to be unity. Any value of  $R_{AA}$  less than unity at high transverse momentum ( $p_T > 6$  GeV/c) signifies the energy loss of the high  $p_T$  partons inside the hot and dense medium formed. In this thesis we will obtain the  $R_{CP}$  and  $R_{AA}$  of  $K^{*0}$  to understand the partons energy loss in the hot and dense medium formed in high energy collisions. It will be compared with other particles to understand the baryon-meson effect at intermediate  $p_T$ .

The in-medium effects can also be studied through other observables like elliptic

flow coefficient  $v_2$ . The  $v_2$  of  $K^{*0}$  at low  $p_T$  could be modified due to the effect of hadronic re-scattering. In this thesis, we will present the measurement of  $v_2$  of  $K^{*0}$  in non-central Pb+Pb collisions at  $\sqrt{s_{NN}} = 2.76$  TeV. The  $v_2$  will be compared with that of other particles.

The high momentum heavy resonances can be used to look for the in-medium effects through the study of correlation with respect to a jet or a leading particle. The resonance-jet correlation in the same side and away side can distinguish between in-medium and in-vacuum fragmentation by assuming that the same side resonance properties and production remain unaffected due to surface bias, whereas the away side of the resonances are likely interacting with the hot and dense partonic medium. The enhanced cross-section of jets at LHC energies make such study more promising and interesting. In this thesis, we will present the study of  $K^{*0}$ -jet correlation in p+p collisions at  $\sqrt{s} = 7$  TeV. We will study the mass, width and yield of  $K^{*0}$  with respect to the leading particle. This analysis will be a baseline for the future study in Pb+Pb collisions.

The second part of the thesis deals with the production mechanism of another identified particle, the photons. A Photon Multiplicity Detector (PMD) was build and installed at the LHC to provide the photon multiplicity and pseudo-rapidity distribution at forward rapidity ( $2.3 < \eta < 3.9$ ). The photon measurement provides a complimentary information to that of charged pions as majority of photons are the decay of neutral pions. Such a measurement extends our knowledge of particle production to forward rapidities where one enters into a regime of small Bjorken  $x$ , in which gluon saturation is expected to occur. In this thesis, we have developed a technique of unfolding for PMD which is used for correcting the detector acceptance and efficiency. We will present the multiplicity and pseudo-rapidity distribution of photons at  $2.3 < \eta < 3.9$  in p+p collisions at  $\sqrt{s} = 900$  GeV. To understand the particle production mechanism in different rapidity regions, we will compare our photon results at forward rapidity to that of charged particles at mid-rapidity. We will also compare the results with the expectation from various models like PYTHIA and PHOJET. These results will also be used to study the limiting fragmentation

behaviour at LHC energies.

Finally we will discuss through a phenomenological study of the production of identified baryons (specifically protons and anti-protons) in proton-proton collisions at high energy. The study of anti-proton to proton ratio ( $\bar{p}/p$ ) provides a valuable information to the production mechanism of baryons. In this thesis, we will present the results of  $\bar{p}/p$  ratio in p+p collisions at various beam energies (23 GeV to 7 TeV) using different models PYTHIA, PHOJET and HIJING- $B\bar{B}$ . We will compare our results of  $\bar{p}/p$  ratio from various models with the available experimental data to understand the mechanism of baryon production and baryon stopping at mid-rapidity in p+p collisions.

## Publications

### List of publication related to Thesis:

1.  **$K^*(892)^0$  and  $\phi(1020)$  production in Pb-Pb collisions at  $\sqrt{s_{NN}} = 2.76$  TeV\***  
ALICE Collaboration (B. Abelev *et al.*), e-Print: arXiv:1404.0495v1 [nucl-ex],  
(Submitted to Phys. Rev. C)
2. **Production of  $K^*(892)^0$  and  $\phi(1020)$  in pp collisions at  $\sqrt{s} = 7$  TeV \***  
ALICE Collaboration (B. Abelev *et al.*), Eur. Phys. J. C72 (2012) 2183, e-  
Print: arXiv:1208.5717 [nucl-ex]
3. **Strange hadron and resonance production in Pb-Pb collisions at  $\sqrt{s_{NN}} = 2.76$  TeV with ALICE experiment at LHC\***  
Subhash Singha (for ALICE Collaboration), Nuclear Physics A904-905 (2013)  
539c-542c e-Print: arXiv:1211.0187 [nucl-ex]
4. **Hadronic resonance production with ALICE experiment at LHC\***  
Subhash Singha (for ALICE Collaboration), Proceedings of science (CPOD  
2013) 055 e-Print: arXiv:1306.0673 [nucl-ex]
5. **Inclusive photon production at forward rapidities for proton-proton collisions at  $\sqrt{s} = 0.9, 2.76$  and 7 TeV\***  
Under ALICE Collaboration review. (Target journal Eur. Phys. J C)

### List of DAE Proceedings in India:

1. **Energy dependence of anti-proton/proton ratio in p+p collisions\***  
Subhash Singha, P.K. Netrakanti, Lokesh Kumar and B. Mohanty, DAE sym-  
posium 2010,  
<http://www.sympnp.org/proceedings/55/F17.pdf>

2. **Unfolding method for obtaining the photon multiplicity distribution at forward pseudo-rapidity in high energy p+p collisions\***  
S.K.Prasad, Subhash Singha, B. Mohanty and S. Chattopadhyay, DAE symposium 2010,  
<http://www.sympnp.org/proceedings/55/G37.pdf>
3.  **$K^{*0}$  resonance production in Pb-Pb collisions at  $\sqrt{s_{NN}} = 2.76$  TeV\***  
Subhash Singha (for ALICE collaboration), DAE symposium 2012,  
<http://www.sympnp.org/proceedings/56/F9.pdf>
4. **Expectation of photon multiplicity in p-p collisions at LHC energies\***  
Subhash Singha, S. De, B. Mohanty and T.K. Nayak, DAE symposium 2012,  
<http://www.sympnp.org/proceedings/56/F45.pdf>

### List of Non-ALICE Publications :

1. **Energy dependence of  $\bar{p}/p$  ratio in p+p collisions\***  
Subhash Singha, P.K. Netrakanti, L. Kumar and B. Mohanty, Phys. Rev. C82 (2010) 044902 e-Print: arXiv:1009.5437 [nucl-ex]
2. **Studying re-scattering effect in heavy ion collision through  $K^*$  production\***  
Subhash Singha, B. Mohanty and Z. W. Lin (Submitted to Phys. Rev. C)

### List of Publication as a part of ALICE Collaboration:

1. **Mid-rapidity anti-baryon to baryon ratio in pp collisions  $\sqrt{s} = 0.9, 2.76$  and 7 TeV measured by ALICE**  
ALICE Collaboration (E. Abbas *et al.*), Eur. Phys. J. C73 (2013) 2496, e-Print: arXiv:1308.6726 [nucl-ex]
2. **Charge correlation using the balance function in Pb-Pb collisions at  $\sqrt{s_{NN}} = 2.76$  TeV**

ALICE Collaboration (B. Abelev *et al.*), Phys. Lett. B723 (2013) 267-279, e-Print: arXiv:1308.6726 [nucl-ex]

3. **Measurement of the inclusive differential jet cross section in pp collisions at  $\sqrt{s} = 2.76$  TeV**

ALICE Collaboration (B. Abelev *et al.*), Phys. Lett. B722 (2013) 262-272, e-Print: arXiv:1301.3475 [nucl-ex]

4. **Long-range angular correlations on the near and away side in p-Pb collisions at  $\sqrt{s_{NN}} = 5.02$  TeV**

ALICE Collaboration (B. Abelev *et al.*), Phys. Lett. B719 (2013) 29-41, e-Print: arXiv:1212.2001 [nucl-ex]

5. **Transverse momentum distribution and nuclear modification factor of charged particles in p-Pb collisions at  $\sqrt{s_{NN}} = 5.02$  TeV**

ALICE Collaboration (B. Abelev *et al.*), Phys. Rev. Lett. 110 (2013) 082302, e-Print: arXiv:1210.4520 [nucl-ex]

6. **Pseudorapidity density of charged particles in p-Pb collisions at  $\sqrt{s_{NN}} = 5.02$  TeV**

ALICE Collaboration (B. Abelev *et al.*), Phys. Rev. Lett. 110 (2013) 032301, e-Print: arXiv:1210.3615 [nucl-ex]

7. **Coherent  $J/\Psi$  photoproduction in ultra-peripheral Pb-Pb collisions at  $\sqrt{s_{NN}} = 2.76$  TeV**

ALICE Collaboration (B. Abelev *et al.*), Phys. Lett. B718 (2013) 1273-1283, e-Print: arXiv:1209.3715 [nucl-ex]

8. **Measurement of inelastic, single- and double-diffraction cross sections in proton-proton collisions at the LHC with ALICE**

ALICE Collaboration (B. Abelev *et al.*), Eur. Phys. J. C73 (2013) 2456, e-Print: arXiv:1208.4968 [nucl-ex]

9. **Centrality Dependence of Charged Particle Production at Large Transverse Momentum in Pb–Pb Collisions at  $\sqrt{s_{NN}} = 2.76$  TeV**  
ALICE Collaboration (B. Abelev *et al.*), Phys. Lett. B720 (2013) 52-62, e-Print: arXiv:1208.2711 [nucl-ex]
10. **Pion, Kaon, and Proton Production in Central Pb-Pb Collisions at  $\sqrt{s_{NN}} = 2.76$  TeV**  
ALICE Collaboration (B. Abelev *et al.*), Phys. Rev. Lett. 109 (2012) 252301, e-Print: arXiv:1208.1974 [nucl-ex]
11. **Ds+ meson production at central rapidity in proton–proton collisions at  $\sqrt{s} = 7$  TeV**  
ALICE Collaboration (B. Abelev *et al.*), Phys. Lett. B718 (2012) 279-294, e-Print: arXiv:1208.1908 [nucl-ex]
12. **Measurement of electrons from beauty hadron decays in pp collisions at  $\sqrt{s}=7$  TeV**  
ALICE Collaboration (B. Abelev *et al.*), Phys. Lett. B721 (2013) 13-23, e-Print: arXiv:1208.1902 [nucl-ex]
13. **Net-Charge Fluctuations in Pb-Pb collisions at  $\sqrt{s_{NN}} = 2.76$  TeV**  
ALICE Collaboration (B. Abelev *et al.*), Phys. Rev. Lett. 110 (2013) 152301, e-Print: arXiv:1207. 6068 [nucl-ex]
14. **Charge separation relative to the reaction plane in Pb-Pb collisions at  $\sqrt{s_{NN}} = 2.76$  TeV**  
ALICE Collaboration (B. Abelev *et al.*). Published in Phys. Rev. Lett. 110 (2013) 012301 e-Print: arXiv:1207. 0900 [nucl-ex]
15.  **$K_s^0 - K_s^0$  correlations in pp collisions at  $\sqrt{s} = 7$  TeV from the LHC ALICE experiment**

ALICE Collaboration (B. Abelev *et al.*), Phys. Lett. B717 (2012) 151-161,  
e-Print: arXiv:1206.2056 [nucl-ex]

16. **Production of muons from heavy flavour decays at forward rapidity in pp and Pb-Pb collisions at  $\sqrt{s_{NN}} = 2.76$  TeV**

ALICE Collaboration (B. Abelev *et al.*), Phys. Rev. Lett. 109 (2012) 112301,  
e-Print: arXiv:1205.6443 [nucl-ex]

17. **Measurement of prompt  $J/\Psi$  and beauty hadron production cross sections at mid-rapidity in pp collisions at  $\sqrt{s} = 7$  TeV**

ALICE Collaboration (B. Abelev *et al.*), JHEP 1211 (2012) 065, e-Print: arXiv:1205.5880[nucl-ex]

18. **Anisotropic flow of charged hadrons, pions and (anti-)protons measured at high transverse momentum in Pb-Pb collisions at  $\sqrt{s_{NN}} = 2.76$  TeV**

ALICE Collaboration (B. Abelev *et al.*), Phys. Lett. B 719 (2013) 18-28,  
e-Print: arXiv:1205.5761 [nucl-ex]

19. **Neutral pion and eta meson production in proton-proton collisions at  $\sqrt{s}=0.9$  TeV and  $s=7$  TeV**

ALICE Collaboration (B. Abelev *et al.*), Phys. Lett. B717 (2012) 162-172,  
e-Print: arXiv:1205.5724 [nucl-ex]

20. **Measurement of electrons from semileptonic heavy-flavour hadron decays in pp collisions at  $\sqrt{s} = 7$  TeV**

ALICE Collaboration (B. Abelev *et al.*), Phys.Rev. D86 (2012) 112007, e-Print: arXiv:1205.5423 [nucl-ex]

21. **Measurement of charm production at central rapidity in proton-proton collisions at  $\sqrt{s}=2.76$  TeV**

- ALICE Collaboration (B. Abelev *et al.*), JHEP 1207 (2012) 191, e-Print: arXiv:1205.4007 [nucl-ex]
22. **Transverse sphericity of primary charged particles in minimum bias proton-proton collisions at  $\sqrt{s}=0.9, 2.76$  and 7 TeV**  
ALICE Collaboration (B. Abelev *et al.*), Eur. Phys. J. C72 (2012) 2124, e-Print: arXiv:1205.3963 [nucl-ex]
23. **Multi-strange baryon production in pp collisions at  $\sqrt{s} = 7$  TeV with ALICE**  
ALICE Collaboration (B. Abelev *et al.*), Phys. Lett. B712 (2012) 309-318, e-Print: arXiv:1204.0282 [nucl-ex]
24. **Inclusive J/ $\Psi$  production in pp collisions at  $\sqrt{s} = 2.76$  TeV**  
ALICE Collaboration (B. Abelev *et al.*), Phys. Lett. B718 (2012) 295-306, e-Print: arXiv:1203.3641[nucl-ex]
25. **Measurement of the Cross Section for Electromagnetic Dissociation with Neutron Emission in Pb-Pb Collisions at  $\sqrt{s_{NN}} = 2.76$  TeV**  
ALICE Collaboration (B. Abelev *et al.*), Phys. Rev. Lett. 109 (2012) 252302, e-Print: arXiv:1203.2436 [nucl-ex]
26. **Suppression of high transverse momentum D mesons in central Pb-Pb collisions at  $\sqrt{s_{NN}}=2.76$  TeV**  
ALICE Collaboration (B. Abelev *et al.*), JHEP 1209 (2012) 1, e-Print: arXiv:1203.2160 [nucl-ex]
27. **J/ $\Psi$  Production as a Function of Charged Particle Multiplicity in pp collisions at  $\sqrt{s} = 7$  TeV**  
ALICE Collaboration (B. Abelev *et al.*), Phys. Lett. B712 (2012) 165-175, e-Print: arXiv:1202.2816[nucl-ex]

28. **J/ $\Psi$  suppression at forward rapidity in Pb-Pb collisions at  $\sqrt{s_{NN}}=2.76$  TeV**  
 ALICE Collaboration (B. Abelev *et al.*), Phys. Rev. Lett. 109 (2012) 072301,  
 e-Print: arXiv:1202.1383 [nucl-ex]
29. **Heavy flavour decay muon production at forward rapidity in proton proton collisions at  $\sqrt{s} = 7$  TeV**  
 ALICE Collaboration (B. Abelev *et al.*), Phys. Lett. B708 (2012) 265-275,  
 e-Print: arXiv:1201.3791 [nucl-ex]
30. **Measurement of Event Background Fluctuations for Charged Particle Jet Reconstruction in Pb-Pb collisions at  $\sqrt{s_{NN}} = 2.76$  TeV**  
 ALICE Collaboration (B. Abelev *et al.*), JHEP 1203 (2012) 053, e-Print: arXiv:1207.  
 [nucl-ex]
31. **Light vector meson production in pp collisions at  $\sqrt{s} = 7$  TeV**  
 ALICE Collaboration (B. Abelev *et al.*), Phys. Lett. B710 (2012) 557-568,  
 e-Print: arXiv:1112.2222[nucl-ex]
32. **Underlying Event measurements in pp collisions at  $\sqrt{s}=0.9$  and 7 TeV with the ALICE experiment at the LHC**  
 ALICE Collaboration (B. Abelev *et al.*), JHEP 1207 (2012) 116, e-Print: arXiv:1112.2082  
 [nucl-ex]
33. **Measurement of charm production at central rapidity in proton-proton collisions at  $\sqrt{s} = 7$  TeV**  
 ALICE Collaboration (B. Abelev *et al.*), Published in JHEP 1201 (2012) 128  
 e-Print: arXiv:1111.1553 [nucl-ex]
34. **J/ $\Psi$  polarization in pp collisions at  $\sqrt{s}=7$  TeV**  
 ALICE Collaboration (B. Abelev *et al.*), Phys. Rev. Lett. 108 (2012) 082001,  
 e-Print: arXiv:1111.1630 [nucl-ex]

35. **Particle-yield modification in jet-like azimuthal di-hadron correlations in Pb-Pb collisions at  $\sqrt{s_{NN}} = 2.76$  TeV**  
 ALICE Collaboration (B. Abelev *et al.*), Phys. Rev. Lett. 108 (2012) 092301,  
 e-Print: arXiv:1110.0121 [nucl-ex]
36. **Harmonic decomposition of two-particle angular correlations in Pb-Pb collisions at  $\sqrt{s_{NN}}=2.76$  TeV**  
 ALICE Collaboration (B. Abelev *et al.*), Phys. Lett. B708 (2012) 249-264,  
 e-Print: arXiv:1109.2501 [nucl-ex]
37. **Higher harmonic anisotropic flow measurements of charged particles in Pb-Pb collisions at  $\sqrt{s_{NN}}=2.76$  TeV**  
 ALICE Collaboration (B. Abelev *et al.*), Phys. Rev. Lett. 107 (2011) 032301,  
 e-Print: arXiv:1105.3865 [nucl-ex]
38. **Rapidity and transverse momentum dependence of inclusive J/psi production in pp collisions at  $\sqrt{s} = 7$  TeV**  
 ALICE Collaboration (B. Abelev *et al.*), Phys. Lett. B704 (2011) 442-455,  
 e-Print: arXiv:1105.0380 [nucl-ex]
39. **D meson elliptic flow in non-central Pb-Pb collisions at  $\sqrt{s_{NN}} = 2.76$  TeV**  
 ALICE Collaboration (B. Abelev *et al.*), Phys. Rev. Lett. 111 (2013) 102301,  
 e-Print: arXiv:1305.2707 [nucl-ex]
40. **Long range angular correlations of  $\phi$ , K and p in p-Pb collisions at  $\sqrt{s_{NN}} = 5.02$  TeV**  
 ALICE Collaboration (B. Abelev *et al.*), Phys. Lett. B726 (2013) 164-177,  
 e-Print: arXiv:1307.3237 [nucl-ex]
41. **Centrality dependence of pseudorapidity density distribution for charged particles in Pb-Pb collisions  $\sqrt{s_{NN}} = 2.76$  TeV**

ALICE Collaboration (B. Abelev *et al.*), Phys. Lett. B726 (2013) 610-622,  
e-Print: arXiv:1304.0347 [nucl-ex]

42. **Multiplicity dependence of two-particle azimuthal correlations in pp collisions at the LHC**

ALICE Collaboration (B. Abelev *et al.*), DOI: 10.1007/JHEP09 (2013) 049

43. **Performance of ALICE V0 system in pp**

ALICE Collaboration (B. Abelev *et al.*), DOI: 10.1088/1748-0221/8/10/P10016

44. **Centrality determination of Pb-Pb collisions at  $\sqrt{s_{NN}} = 2.76$  TeV in the ALICE experiment**

ALICE Collaboration (B. Abelev *et al.*), Phys. Rev. C 88 (2013) 044910

45. **J/ $\Psi$  Elliptic flow in Pb-Pb collisions at  $\sqrt{s_{NN}} = 2.76$  TeV**

ALICE Collaboration (B. Abelev *et al.*). Published in DOI: 10.1103/Phys. Rev. Lett. 111.162301

46. **Multiplicity dependence of average transverse momentum in pp, p-Pb and Pb-Pb collisions at the LHC**

ALICE Collaboration (B. Abelev *et al.*), DOI: 10.1016/j.physletb.2013.10.054

47. **Charmonium and e+e- pair photo production at mid-rapidity in ultra-peripheral Pb-Pb collisions at  $\sqrt{s_{NN}} = 2.76$  TeV**

ALICE Collaboration (B. Abelev *et al.*), Eur. Phys. J. C (2013) 73:2617

48. **K<sup>0S</sup> and Lambda production in Pb-Pb collision at  $\sqrt{s_{NN}} = 2.76$  TeV**

ALICE Collaboration (B. Abelev *et al.*), Phys. Rev. Lett. 111, 222301 (2013).

49. **Multiplicity dependence of  $\pi^\pm$ ,  $K^\pm$ ,  $K_0^S$ , p( $\bar{p}$ ) and  $\Lambda$  ( $\bar{\Lambda}$ ) in p-Pb collisions  $\sqrt{s_{NN}} = 5.02$  TeV**

ALICE Collaboration (B. Abelev *et al.*), Physics Letters B 728 (2014) 2538.

50. **Multi-strange baryon production at mid-rapidity in Pb-Pb collisions at  $\sqrt{s_{NN}} = 2.76$  TeV**  
ALICE Collaboration (B. Abelev *et al.*), Physics Letters B 728 (2014) 216227.
51. **Energy dependence of the Transverse Momentum Distributions of Charged Particles in pp Collisions with ALICE**  
ALICE Collaboration (B. Abelev *et al.*), Eur. Phys. J. C (2013) 73:2662.
52. **Directed flow of charged particles at mid-rapidity relative to the spectator plane in Pb-Pb collisions at  $\sqrt{s_{NN}} = 2.76$  TeV**  
ALICE Collaboration (B. Abelev *et al.*), Phys. Rev. Lett. 111, 232302 (2013).
53. **Two and Three-Pion Quantum Statistics Correlation in Pb-Pb Collisions at  $\sqrt{s_{NN}} = 2.76$  TeV at the LHC**  
ALICE Collaboration (B. Abelev *et al.*), Phys. Rev. C 89 (2), 024911 (2014).
54. **J/ $\Psi$  production and nuclear effects in p-Pb collisions at  $\sqrt{s_{NN}} = 5.02$  TeV**  
ALICE Collaboration (B. Abelev *et al.*), JHEP02(2014)073
55. **Measurement of charged suppression in Pb-Pb collisions at  $\sqrt{s_{NN}} = 2.76$  TeV**  
ALICE Collaboration (B. Abelev *et al.*), JHEP03(2014)013.

**List of analysis notes submitted to ALICE Collaboration website:**

1.  **$K^*0$  resonance production in Pb-Pb collisions at  $\sqrt{s_{NN}} = 2.76$  TeV\***  
<https://aliceinfo.cern.ch/Notes/node/82>  
<https://aliceinfo.cern.ch/Notes/node/160>

<https://aliceinfo.cern.ch/Notes/node/184>

2.  $K^{*0}$  resonance production in pp collisions at  $\sqrt{s} = 2.76$  TeV\*

<https://aliceinfo.cern.ch/Notes/node/219>

3. Inclusive photon production at forward rapidities for pp collisions at  $\sqrt{s} = 0.9, 2.76$  and 7 TeV in ALICE at the LHC\*

<https://aliceinfo.cern.ch/Notes/node/149>

### **INFN Internal Note:**

1. Report on  $K(892)^*$ -hadron correlation analysis in pp collisions at  $\sqrt{s} = 7$  TeV\*

Subhash Singha and Angela Badala, (Submitted to INFN, Sezione di Catania)

(\*) indicate papers on which this thesis is based.

Signature of Student: 

Date: 04/09/2014

# Contents

<b>1</b>	<b>Introduction</b>	<b>1</b>
1.1	Standard Model . . . . .	1
1.2	Quantum Chromodynamics (QCD) . . . . .	3
1.3	QCD phase diagram . . . . .	4
1.4	Heavy Ion Collision . . . . .	5
1.5	Experimental facilities for heavy ion collisions . . . . .	7
1.6	Quark Gluon Plasma (QGP) . . . . .	7
1.6.1	Hadron yield and spectra . . . . .	8
1.6.2	Jet quenching . . . . .	9
1.6.3	Nuclear modification factor ( $R_{AA}$ ) . . . . .	10
1.6.4	$J/\Psi$ suppression . . . . .	13
1.6.5	Strangeness enhancement . . . . .	14
1.6.6	Elliptic flow . . . . .	15
1.7	pp collisions . . . . .	17
1.8	Event generators . . . . .	20
1.8.1	PYTHIA . . . . .	21
1.8.2	PHOJET . . . . .	22
1.8.3	HIJING . . . . .	23
1.8.4	HIJING B- $\bar{B}$ . . . . .	24
1.8.5	AMPT . . . . .	24
1.9	Thesis Motivation . . . . .	25
1.9.1	Resonance production in Pb-Pb and pp collisions at LHC energies	25

1.9.2	Inclusive photon production in pp collisions at LHC energies . . . . .	28
1.9.3	Energy dependence of anti-proton to proton ratio . . . . .	30
1.10	Organization of the thesis . . . . .	31
<b>2</b>	<b>The Experimental Setup</b>	<b>39</b>
2.1	Large Hadron Collider at CERN . . . . .	39
2.2	ALICE at the LHC . . . . .	41
2.3	Central Barrel Detectors . . . . .	45
2.3.1	Inner Tracking System (ITS) . . . . .	45
2.3.2	Time Projection Chamber (TPC) . . . . .	46
2.3.3	Transition Radiation Detector (TRD) . . . . .	50
2.3.4	Time of Flight (TOF) . . . . .	51
2.3.5	High Momentum Particle Identification (HMPID) . . . . .	52
2.3.6	PHOton Spectrometer (PHOS) . . . . .	52
2.3.7	Electro Magnetic Calorimeter (EMCAL) . . . . .	52
2.3.8	ALICE Cosmic Ray Detector (ACORDE) . . . . .	53
2.3.9	Muon Spectrometer . . . . .	53
2.4	Forward detectors . . . . .	54
2.4.1	Zero Degree Calorimeter (ZDC) . . . . .	54
2.4.2	Forward Multiplicity Detector (FMD) . . . . .	54
2.4.3	Photon Multiplicity Detector (PMD) . . . . .	55
2.4.4	VZERO (V0) . . . . .	55
2.4.5	TZERO (T0) . . . . .	56
2.5	Online and Trigger . . . . .	56
2.5.1	CTP . . . . .	56
2.5.2	HLT . . . . .	57
2.5.3	DAQ . . . . .	57
2.6	Offline and computing . . . . .	58
2.6.1	Data processing . . . . .	58
2.6.2	ALICE Grid . . . . .	59
2.6.3	AliRoot simulation framework . . . . .	60

2.7	Details of PMD . . . . .	63
2.7.1	Working principle of PMD . . . . .	64
2.7.2	Construction of PMD . . . . .	65
2.7.3	Front End Electronics and readout . . . . .	67
<b>3</b>	<b><math>K^{*0}</math> Resonance Production in Pb–Pb and pp collisions</b>	<b>74</b>
3.1	Introduction . . . . .	74
3.2	Data Set . . . . .	75
3.3	Event Selection . . . . .	76
3.4	Track Selection . . . . .	78
3.5	PID Selection . . . . .	79
3.6	Signal reconstruction . . . . .	80
3.6.1	Event mixing method . . . . .	82
3.6.2	Like sign method . . . . .	83
3.6.3	Residual background . . . . .	84
3.7	Mass and Width . . . . .	85
3.8	Yield extraction . . . . .	88
3.9	Efficiency and branching ratio correction . . . . .	89
3.10	Results . . . . .	91
3.10.1	Mass and Width . . . . .	91
3.10.2	Transverse momentum distribution . . . . .	93
3.10.3	$K^{*0}$ -meson yield per unit rapidity . . . . .	97
3.10.4	$K^{*0}$ -meson $\langle p_T \rangle$ . . . . .	100
3.10.5	Particle ratio: . . . . .	103
3.10.6	Study of spectral shapes . . . . .	107
3.10.7	Nuclear modification factor ( $R_{CP}$ and $R_{AA}$ ) . . . . .	111
3.11	Systematic uncertainties . . . . .	113
3.11.1	Uncertainty from signal extraction background . . . . .	114
3.11.2	Uncertainty from yield extraction method . . . . .	114
3.11.3	Uncertainty in particle identification . . . . .	115
3.11.4	Uncertainty from track cut variations . . . . .	115

3.11.5	Uncertainty from material budget . . . . .	115
3.11.6	Total systematic uncertainty . . . . .	115
3.11.7	Systematic uncertainties in mass and width . . . . .	118
3.12	Summary . . . . .	119
3.13	Appendix . . . . .	124
3.13.1	$K^{*0}$ signals in different centrality bins . . . . .	124
<b>4</b>	<b>Studying re-scattering in heavy-ion collisions through <math>K^{*0}</math> production using AMPT</b>	<b>137</b>
4.1	Introduction . . . . .	137
4.2	The AMPT model . . . . .	138
4.3	Results . . . . .	139
4.3.1	Invariant mass distribution . . . . .	140
4.3.2	Observables for re-scattering . . . . .	141
4.3.3	Estimation of hadronic phase time . . . . .	143
4.4	Summary . . . . .	146
<b>5</b>	<b>Elliptic flow <math>K^{*0}</math> meson in Pb-Pb collisions at <math>\sqrt{s_{NN}} = 2.76</math> TeV</b>	<b>149</b>
5.1	Introduction . . . . .	149
5.2	Analysis Method . . . . .	150
5.2.1	Estimation of event plane . . . . .	150
5.2.2	Event plane resolution correction . . . . .	151
5.2.3	Event plane flattening . . . . .	152
5.2.4	$v_2$ vs. invariant mass method . . . . .	152
5.3	Event selection . . . . .	153
5.4	Track selection . . . . .	153
5.5	PID selection . . . . .	154
5.6	Analysis . . . . .	155
5.7	Results . . . . .	157
5.8	Summary . . . . .	158
5.9	Appendix . . . . .	160

<b>6</b>	<b><math>K^{*0}</math>-hadron correlation in pp collisions at <math>\sqrt{s} = 7</math> TeV</b>	<b>164</b>
6.1	Introduction . . . . .	164
6.2	Analysis Details . . . . .	165
6.2.1	Event selection . . . . .	165
6.2.2	Track selection . . . . .	165
6.2.3	Leading particle selection . . . . .	166
6.2.4	PID selection . . . . .	167
6.2.5	Analysis technique . . . . .	169
6.2.6	Signal extraction: . . . . .	170
6.3	Results . . . . .	170
6.4	Summary . . . . .	177
<b>7</b>	<b>Inclusive Photon Production in pp collisions at <math>\sqrt{s} = 0.9</math> TeV</b>	<b>179</b>
7.1	Introduction . . . . .	179
7.2	Detector subsystem used for this analysis . . . . .	180
7.3	Simulation framework . . . . .	181
7.3.1	Pedestal . . . . .	182
7.3.2	Hot/Noisy cell removal . . . . .	183
7.3.3	Clustering . . . . .	184
7.3.4	Photon-hadron discrimination . . . . .	185
7.4	Event Selection . . . . .	188
7.4.1	Corrections for trigger and vertex reconstruction efficiency . . . . .	189
7.5	Material budget study . . . . .	190
7.5.1	Material distribution in front of the PMD . . . . .	190
7.5.2	Effect of upstream material: Deflection of the original photon track . . . . .	193
7.5.3	Study of split clusters . . . . .	195
7.5.4	Study of occupancy . . . . .	196
7.6	Acceptance of PMD . . . . .	198
7.7	Analysis details . . . . .	198
7.8	Uncorrected photon multiplicity ( $N_{\gamma-like}$ ) . . . . .	198

7.9	Method of unfolding . . . . .	200
7.9.1	$\chi^2$ minimization method . . . . .	200
7.9.2	Bayesian method . . . . .	202
7.9.3	Optimization of unfolding . . . . .	203
7.10	Results . . . . .	206
7.10.1	Corrected Photon multiplicity . . . . .	206
7.10.2	Comparison with models . . . . .	206
7.11	Negative binomial distributions (NBD) Fitting . . . . .	208
7.12	KNO scaling . . . . .	209
7.13	Energy dependence of photon multiplicity . . . . .	210
7.14	Pseudo-rapidity distributions of photons . . . . .	212
7.15	Comparison between photon and charged particle production . . . . .	213
7.16	Limiting fragmentation behavior . . . . .	215
7.16.1	Systematic Uncertainties . . . . .	216
7.16.2	Estimation of systematic errors due to upstream materials in front of PMD . . . . .	219
7.17	Summary . . . . .	220
7.18	Appendix . . . . .	222
<b>8</b>	<b>Energy dependence of anti-proton to proton ratio in pp collisions</b>	<b>228</b>
8.1	Introduction . . . . .	228
8.2	Baryon production mechanism in models . . . . .	229
8.3	Results . . . . .	230
8.4	Summary . . . . .	236
<b>9</b>	<b>Summary</b>	<b>240</b>

# List of Figures

1.1	(Color online) The schematic representation of standard model. Figure has been taken from [5]. . . . .	2
1.2	(Color online) Schematic representation of QCD phase diagram. Figure has been taken from [16]. . . . .	4
1.3	(Color online) Schematic picture of a heavy ion collision. Figure has been taken from [19]. . . . .	5
1.4	(Color online) Schematic representation of space time evolution in a heavy ion collision. . . . .	6
1.5	(Color online) $T_{kin}$ vs. $\beta_T$ extracted by a simultaneous fit to the pion, kaon and proton spectra (measured in ALICE [21] and STAR [22] experiment) to a Blast Wave function [25]. . . . .	8
1.6	(Color online) Fit of the hadron yields measured in ALICE [21] with statistical hadronization model [18]. The $K^{*0}$ is not included in fit. . . . .	9
1.7	(Color online) Schematic representation jet quenching in heavy ion collisions. . . . .	10
1.8	(Color online) Dijet azimuthal correlation at $\sqrt{s_{NN}} = 200$ GeV in pp, d-Au and Au-Au collisions measured in STAR experiment [27]. . . . .	11
1.9	(Color online) Dijet asymmetry observed in Pb-Pb collisions at $\sqrt{s_{NN}} = 2.76$ TeV in ATLAS experiment [28]. . . . .	11
1.10	(Color online) Nuclear modification factor in Pb-Pb at $\sqrt{s_{NN}} = 2.76$ TeV [29] and p-Pb [32] collisions at $\sqrt{s_{NN}} = 5.02$ TeV. The results on the left panel are compared with the measurements at RHIC [30, 31]. . . . .	12

1.11 (Color online) Nuclear modification factor $R_{AA}$ of $J/\Psi$ for Pb-Pb collisions measured in ALICE at $\sqrt{s_{NN}} = 2.76$ TeV [34]. The results are compared with the measurement from RHIC [35]. . . . .	14
1.12 (Color online) Strangeness enhancement for multi-strange hadrons measured in SPS [38], RHIC [39] and LHC [37] energies. . . . .	15
1.13 (Color online) Schematic representation of elliptic flow in a non-central heavy ion collision. . . . .	16
1.14 (Color online) Comparison of $v_2$ of identified hadrons measured in ALICE [44], STAR [45] and PHENIX experiments [46]. . . . .	16
1.15 (Color online) Left panel: $v_2$ of identified hadron for Pb-Pb collisions measured in ALICE [44]. Right panel: number of quark scaling for the identified hadrons measured in ALICE. . . . .	17
1.16 Rapidity distribution of ND, SD and DD processes from PYTHIA event generator. This figure has been taken from [48]. . . . .	18
1.17 (Color online) Pseudorapidity distribution of charged particles as a function of $\eta - y_{beam}$ for pp(p $\bar{p}$ ) collisions. This Figure has been taken from [55]. . . . .	20
1.18 (Color online) A schematic diagram of a pp collision in PYTHIA. Figure has been taken from [48]. . . . .	22
1.19 (Color online) Schematic representation of re-scattering and re-generation in heavy ion collision taking an example of $K^{*0}$ resonance. . . . .	26
1.20 (Color online) Qualitative plot showing the effect of re-scattering and re-generation only processes on $K^{*0}/K^-$ ratio in heavy ion collision with respect to pp collision. . . . .	27
1.21 (Color online) Photon pseudorapidity distribution in Au-Au collisions at $\sqrt{s} = 200$ GeV measured in STAR experiment [79]. . . . .	29
1.22 (Color online) Scaling of photon pseudorapidity distribution in Au-Au collisions at $\sqrt{s} = 62.4$ GeV in STAR experiment [78]. . . . .	30

1.23	(Color online) Left panel: Charged hadron multiplicity in pp collisions at $\sqrt{s} = 0.9$ TeV measured in ALICE [53]. Right panel: measurement of pseudorapidity distribution of charged hadrons in ALICE [53], UA5 [81] and CMS [82]. . . . .	31
2.1	(Color online) Otantants of LHC. . . . .	40
2.2	(Color online) CERN accelerator complex at the LHC. . . . .	41
2.3	(Color online) Schematic diagram of the ALICE detector. . . . .	42
2.4	(Color online) The Co-ordinate system of ALICE detector. . . . .	43
2.5	(Color online) Momentum ranges in which different detectors are able to identify different particles. . . . .	43
2.6	Layout of ITS detector [10]. . . . .	45
2.7	Layout ot TPC [10]. . . . .	47
2.8	(Color online) Working principle of TPC [21]. . . . .	48
2.9	(Color online) Event display of the tracks reconstructed inside TPC in Pb-Pb collisions at $\sqrt{s_{NN}} = 2.76$ TeV during 2010. . . . .	48
2.10	(Color online) The measurement of energy loss $dE/dx$ vs momentum using TPC in Pb-Pb collisions at $\sqrt{s_{NN}} = 2.76$ TeV [7]. . . . .	49
2.11	(Color online) Working principle of TRD [10]. . . . .	50
2.12	(Color online) The lay out of Muon spectrometer [24]. . . . .	53
2.13	The lay out of FMD in GEANT3. . . . .	55
2.14	VZERO-A and VZERO-C. . . . .	56
2.15	(Color online) Data Processing Framework in ALIROOT. . . . .	60
2.16	(Color online) Working principle of PMD [27, 28]. . . . .	64
2.17	Schematic picture of a unit module in PMD. (1) Top PCB, (2) 32-pin connectors, (3) edge frame, (4) honeycomb cells and (5) bottom PCB [27, 28]. . . . .	65
2.18	Cell of PMD [28]. . . . .	66
2.19	(Color online) Left panel: Picture of PMD (looking towards the IP) in data taking configuration. Right panel: PMD in parking position during 2012 technical shut down. . . . .	67

2.20	(Color online) Front end electronics of PMD [31]. . . . .	68
3.1	(Color online) The Z- position of vertex in Pb–Pb at $\sqrt{s_{NN}} = 2.76$ TeV and pp collisions at $\sqrt{s} = 2.76$ TeV. . . . .	76
3.2	(Color online) Centrality selection using the amplitude of VZERO detector in Pb-Pb collisions at $\sqrt{s_{NN}} = 2.76$ TeV [10]. . . . .	77
3.3	(Color online) dE/dx measured in the TPC as a function of momentum for different particle species in Pb–Pb collision at $\sqrt{s_{NN}} = 2.76$ TeV. The solid black curves represent the modified Bethe-Bloch parameterization [14, 15]. . . . .	80
3.4	(Color online) Unlike charged same event $\pi K$ invariant mass distribution in 0-20% centrality in Pb–Pb collisions at $\sqrt{s_{NN}} = 2.76$ TeV. The arrow indicates the PDG value of the mass ( $0.896 \text{ GeV}/c^2$ ) of $K^{*0}$ . . . . .	81
3.5	(Color online) Unlike charged same event $\pi K$ invariant mass distribution in minimum bias pp collisions at $\sqrt{s} = 2.76$ TeV. The arrow indicates the PDG value of the mass ( $0.896 \text{ GeV}/c^2$ ) of $K^{*0}$ . . . . .	81
3.6	Distribution of centrality percentile (left panel) and event plane angle (right panel) in Pb–Pb collision at $\sqrt{s_{NN}} = 2.76$ TeV. . . . .	83
3.7	(Color online) Left panel: $\pi K$ invariant mass distribution constructed using unlike charge pairs from the same event, unlike charged pair from mixed (different) events and taking like charge pairs from the same event in 0-20% central Pb–Pb collisions at $\sqrt{s_{NN}} = 2.76$ TeV. Right panel: $\pi K$ invariant mass distribution after the subtraction of normalized unlike charged mixed event distribution and like charged distribution from unlike charged same event distribution. . . . .	84
3.8	(Color online) Top panel: same event and mixed event $\pi K$ invariant mass distribution over the range $0.8 < p_T < 1.2 \text{ GeV}/c$ and $2.5 < p_T < 3.0 \text{ GeV}/c$ for Pb–Pb collisions in 0-20 % centrality at $\sqrt{s_{NN}} = 2.76$ TeV. Bottom panel: mixed event background subtracted $\pi K$ pair invariant mass distributions, which is fitted with a p-wave relativistic Breit Wigner function. The uncertainties are statistical only. . . . .	87

3.9	(Color online) Left panel: same event and mixed event $\pi K$ invariant mass distribution over the range $0.3 < p_T < 0.6$ GeV/c for pp collisions at $\sqrt{s} = 2.76$ TeV. Right panel: mixed event background subtracted $\pi K$ pair invariant mass distributions, which is fitted with a p-wave relativistic Breit Wigner function. The uncertainties are statistical only.	88
3.10	(Color online) Efficiency $\times$ Acceptance of $K^{*0}$ meson as a function of $p_T$ in Pb–Pb (left panel) at $\sqrt{s_{NN}} = 2.76$ TeV and pp collisions at $\sqrt{s} = 2.76$ TeV (right panel).	90
3.11	(Color online) $K^{*0}$ mass as a function of $p_T$ for Pb–Pb collisions at $\sqrt{s_{NN}} = 2.76$ TeV in four different collision centralities. The blue dotted line represents the PDG value 896.0 MeV/c <sup>2</sup> for the mass of $K^{*0}$ .	91
3.12	(Color online) $K^{*0}$ invariant mass distribution width as a function of $p_T$ for Pb–Pb collisions at $\sqrt{s_{NN}} = 2.76$ TeV in four different collision centralities. The blue dotted line represents the PDG value 48 MeV/c <sup>2</sup> for the invariant mass width of $K^{*0}$ .	92
3.13	(Color online) $K^{*0}$ mass and width as a function of $p_T$ for Pb–Pb collisions in 0-20% collision centrality at $\sqrt{s_{NN}} = 2.76$ TeV. The mass and width is compared with the results in pp collisions $\sqrt{s} = 2.76$ TeV and MC HIJNG (0-20%) simulations. The blue dotted line indicates the PDG value.	93
3.14	(Color online) Transverse momentum spectra of $K^{*0}$ in various centralities in Pb–Pb collisions at $\sqrt{s_{NN}} = 2.76$ TeV. The bars denotes the statistical uncertainties, while the boxes are the systematic uncertainties. The dashed line is the fitted Boltzmann Gibbs Blast-Wave function.	95
3.15	(Color online) Z-position of the vertex distribution in data and MC in pp collisions at $\sqrt{s} = 2.76$ TeV.	96

3.16 (Color online) Transverse momentum spectra of $K^{*0}$ in minimum bias pp collisions at $\sqrt{s} = 2.76$ TeV. The bars denote the statistical uncertainties, while the boxes are the systematic uncertainties. The dashed line is the fit with a Tsallis function. . . . .	98
3.17 (Color online) $dN/dy$ of $K^{*0}$ meson as a function of number of participants in Pb–Pb collisions at $\sqrt{s_{NN}} = 2.76$ TeV and pp collisions at $\sqrt{s} = 7$ TeV [32]. The results are compared with the measurements from STAR experiment [4, 5]. . . . .	99
3.18 (Color online) $\langle p_T \rangle$ of $K^{*0}$ meson as a function of number of participants in Pb–Pb collisions at $\sqrt{s_{NN}} = 2.76$ TeV and pp collisions at $\sqrt{s} = 2.76$ and 7 TeV [32]. The results are compared with measurements from STAR experiment [4, 5]. . . . .	101
3.19 (Color online) Comparison of $\langle p_T \rangle$ of $K^{*0}$ meson with $\pi$ , K and p in Pb–Pb collisions at $\sqrt{s_{NN}} = 2.76$ TeV [21]. . . . .	102
3.20 (Color online) $\langle p_T \rangle$ as a function of particle mass in pp collisions [34, 4, 32]. . . . .	102
3.21 (Color online) $K^{*0}/K^-$ as a function of beam energy in pp collisions. The solid red symbols are the measurements in ALICE, the solid black squares are the measurements in SPS [19] and the blue star denotes the measurements in STAR [4, 5]. open boxes denote the systematic uncertainties and the bars denote the statistical uncertainties. . . . .	104
3.22 (Color online) $K^{*0}/K^-$ as a function of beam energy in A+A and pp collisions [4, 32]. The solid red symbols are the measurements in ALICE, the solid black squares are the measurements in SPS [19] and the blue star denotes the measurements in STAR [4, 5]. open boxes denote the systematic uncertainties and the bars denote the statistical uncertainties. . . . .	105

3.23	(Color online) $K^{*0}/K^-$ ratio as a function of $(dN_{ch}/d\eta)^{1/3}$ . The results are compared with the measurements in pp collisions at $\sqrt{s} = 2.76$ TeV and 7 TeV [32] in ALICE. Also the results are compared with the lower energy measurements at STAR experiment [4, 5]. The open boxes denote the systematic uncertainties and the bars denote the statistical uncertainties. . . . .	106
3.24	(Color online) $K^{*0}/K^-$ and $\phi/K^-$ ratio as a function of mean number of participating nucleons. The results are compared with the measurements in pp collisions at $\sqrt{s} = 2.76$ TeV and 7 TeV [32]. the open boxes denote the systematic uncertainties and the bars denote the statistical uncertainties. . . . .	107
3.25	(Color online) $K^{*0}/K^-$ ratio as a function of mean number of participating nucleons. The results are compared with the measurements in pp collisions at $\sqrt{s} = 2.76$ TeV and 7 TeV [32]. the open boxes denote the systematic uncertainties and the bars denote the statistical uncertainties. . . . .	108
3.26	(Color online) $\phi/K^{*0}$ ratio as a function of $(dN_{ch}/d\eta)^{1/3}$ . The results are compared with the measurements in pp collisions at $\sqrt{s} = 2.76$ TeV and 7 TeV [32] in ALICE. Also the results are compared with the lower energy measurements at STAR experiment [4, 5]. The open boxes denote the systematic uncertainties and the bars denote the statistical uncertainties. . . . .	108
3.27	(Color online) Comparison of spectral shape of $K^{*0}$ and $\phi$ with respect to Boltzmann Gibbs Blast-Wave predictions. The open boxes denote the systematic uncertainties and the bars denote the statistical uncertainties. . . . .	110
3.28	(Color online) Nuclear modification factor $R_{CP}$ of $K^{*0}$ as a function of $p_T$ . The results are compared with that of $\Lambda$ baryon, $K_S^0$ and $\phi$ meson [43]. . . . .	112

3.29 (Color online) Nuclear modification factor $R_{AA}$ of $K^{*0}$ as a function of $p_T$ . It is compared with the results of charged hadrons [36] and $\phi$ meson [43]. The error bars on the charged hadrons are the systematic uncertainties only. For $K^{*0}$ and $\phi$ , the open boxes denote the systematic uncertainties and the bars denote the statistical uncertainties. . .	113
3.30 (Color online) Fractional systematic errors (in %) in the $p_T$ spectra of $K^{*0}$ in Pb–Pb collisions at $\sqrt{s_{NN}} = 2.76$ TeV. Different sources of errors are denoted by different lines of different colors. . . . .	117
3.31 (Color online) Fractional systematic errors (in %) in the $p_T$ spectra of $K^{*0}$ in pp collisions at $\sqrt{s} = 2.76$ TeV. Different sources of errors are denoted by different lines of different colors. . . . .	117
3.32 (Color online) Fractional systematic uncertainties (in %) in mass of $K^{*0}$ .	119
3.33 (Color online) $K^{*0}$ signals in various momentum bins within the rapidity interval $-0.5 < y < 0.5$ in Pb–Pb collisions in 0-20 % centrality at $\sqrt{s_{NN}} = 2.76$ TeV. . . . .	124
3.34 (Color online) $K^{*0}$ signals in various momentum bins within the rapidity interval $-0.5 < y < 0.5$ in Pb–Pb collisions in 20-40 % centrality at $\sqrt{s_{NN}} = 2.76$ TeV. . . . .	125
3.35 (Color online) $K^{*0}$ signals in various momentum bins within the rapidity interval $-0.5 < y < 0.5$ in Pb–Pb collisions in 40-60 % centrality at $\sqrt{s_{NN}} = 2.76$ TeV. . . . .	126
3.36 (Color online) $K^{*0}$ signals in various momentum bins within the rapidity interval $-0.5 < y < 0.5$ in Pb–Pb collisions in 60-80 % centrality at $\sqrt{s_{NN}} = 2.76$ TeV. . . . .	127
3.37 (Color online) $K^{*0}$ signals in various momentum bins within the rapidity interval $-0.5 < y < 0.5$ in minimum bias pp collisions at $\sqrt{s} = 2.76$ TeV. . . . .	128
3.38 (Color online) Signal by background and significance of $K^{*0}$ meson as a function of $p_T$ within the rapidity interval $-0.5 < y < 0.5$ in Pb–Pb collisions at $\sqrt{s_{NN}} = 2.76$ TeV. . . . .	129

4.1	(Color online) Schematic diagram of the default AMPT model. Figure has been taken from [1] . . . . .	139
4.2	(Color online) Number of $K^*$ as a function of hadronic cascade time in default AMPT model for Au+Au collisions at $\sqrt{s_{NN}} = 200$ GeV. Red solid triangles corresponds to total $K^*$ present at any given $\tau_{HC}$ . Blue open circle corresponds to total $K^*$ produced and black cross corresponds to total $K^*$ decayed. . . . .	140
4.3	(Color online) $K\pi$ invariant mass distribution in 0-80% minimum bias Au+Au collisions for different termination time of hadron cascade using the default AMPT model. Different lines corresponds to different termination time of hadron cascade. . . . .	141
4.4	$dN/dy$ and $\langle p_T \rangle$ of reconstructed $K^*$ as a function of hadronic cascade time for 0-80% minimum bias Au+Au collisions at $\sqrt{s_{NN}} = 200$ GeV. . . . .	142
4.5	$K^*/K^-$ as a function collision centrality for 0-80% minimum bias Au+Au collisions in AMPT model at $\sqrt{s_{NN}} = 200$ GeV. Results are shown for different hadron cascade time. . . . .	142
4.6	(Color online) $K^{*0}/K^-$ as a function of $(dN_{ch}/d\eta)^{1/3}$ from experimental data in heavy-ion [5, 6, 7] and p+p collisions [19, 7, 9]. . . . .	143
4.7	(Color online) $K^*/K^-$ ratio for p+p collisions [19, 7, 9] at various center mass energies. The data are fitted to a straight line. . . . .	144
4.8	(Color online) Estimate of the lower limit of time difference between the chemical and kinetic freeze out for various systems and beam energies using $K^*/K^-$ ratio. . . . .	145
5.1	Z-position of vertex distribution in 0-80% minimum bias Pb-Pb collisions at $\sqrt{s_{NN}} = 2.76$ TeV. . . . .	153

5.2	(Color online) Left panel: Unlike charged $\pi$ K invariant mass in same event and mixed event after normalization for 0-80% minimum bias Pb-Pb collisions at $\sqrt{s_{NN}} = 2.76$ TeV. Right panel: Unlike charged $\pi$ K invariant mass after combinatorial background subtraction. The data fitted with a Breit Wigner function (solid red line) and a residual background function (dotted magenta line). The uncertainties shown are statistical only. . . . .	156
5.3	(Color online) TPC event plane distribution in 0-80% minimum bias Pb-Pb collisions at $\sqrt{s_{NN}} = 2.76$ TeV within $0.5 <  \eta  < 0.8$ . The distribution is fitted with equation 5.13 . . . . .	157
5.4	(Color online) $v_2^{sig.+bkg.}$ as a function of $M_{\pi K}$ for 0-80% minimum bias Pb-Pb collisions at $\sqrt{s_{NN}} = 2.76$ TeV. The data is fitted with a function given in equation 5.9. The uncertainties shown are statistical only. . .	158
5.5	(Color online) Preliminary results of $v_2$ of $K^{*0}$ as a function of $p_T$ for 0-80% minimum bias Pb-Pb collisions at $\sqrt{s_{NN}} = 2.76$ TeV. The results are compared with the $v_2$ of $K^{*0}$ measured in STAR experiment. The uncertainties shown are statistical only. . . . .	159
5.6	(Color online) $K^{*0}$ signals after mixed event background subtraction in 0-80% minimum bias Pb-Pb collisions at $\sqrt{s_{NN}} = 2.76$ TeV. . . . .	160
5.7	(Color online) $v_2^{sig.+bkg.}$ as a function of $M_{\pi K}$ for 0-80% minimum bias Pb-Pb collisions at $\sqrt{s_{NN}} = 2.76$ TeV. . . . .	161
6.1	(Color online) The Z- position of vertex in pp collisions at $\sqrt{s} = 7$ TeV.	166
6.2	The azimuthal-angle distribution of TPC only tracks in pp collisions at $\sqrt{s} = 7$ TeV. . . . .	168
6.3	Multiplicity distribution of charged particles in TPC for pp collisions at $\sqrt{s} = 7$ TeV. . . . .	169
6.4	(Color online) $K\pi$ invariant mass distribution in same event (solid black circle) and mixed event (open red circle) after normalization for pp collisions at $\sqrt{s} = 7$ TeV. . . . .	171

6.5	(Color online) $K\pi$ invariant mass distribution in same event (solid black circle) and mixed event(open red circle) after normalization for pp collisions at $\sqrt{s} = 7$ TeV. . . . .	172
6.6	(Color online) $K\pi$ invariant mass distribution after the mixed event background subtraction. The signal is fitted with a Breit Wigner function (solid red line) plus a linear polynomial (dotted magenta line) in invariant mass. . . . .	173
6.7	(Color online) $K\pi$ invariant mass distribution after the mixed event background subtraction. The signal is fitted with a Breit Wigner function (solid red line) plus a linear polynomial (dotted magenta line) in invariant mass. . . . .	174
6.8	(Color online) $K^{*0}$ mass as a function of azimuthal angle ( $\Delta\phi$ ) with respect to the leading particle. The solid black line is the PDG value. . . . .	175
6.9	(Color online) $K^{*0}$ width as a function of azimuthal angle ( $\Delta\phi$ ) with respect to the leading particle. The solid black line is the PDG value. . . . .	176
6.10	(Color online) $K^{*0}$ yield as a function of azimuthal angle ( $\Delta\phi$ ) with respect to the leading particle. The solid red line is the double gaussian function with fixed mean. . . . .	176
7.1	Photon reconstruction chain in PMD . . . . .	181
7.2	(Color online) Variation of mean (left panel) and RMS (right panel) of pedestal in a module. The results obtained in test beam experiment [11] with prototype PMD module at the CERN-PS. . . . .	183
7.3	(Color online) The number of hits distribution in each channel in a module of PMD for pp collisions at $\sqrt{s} = 0.9$ TeV. Left panel: before the data clean up. Right panel: after data clean up. . . . .	184
7.4	(Color online) The number of hits distribution in each channel in a module of PMD for pp collisions at $\sqrt{s} = 0.9$ TeV. . . . .	185
7.5	(Color online) An isolated cell in PMD. The red region indicates the cell having non-zero energy deposition, the grey region having no energy deposition. . . . .	185

7.6	(Color online) Isolated cell ADC distribution in PMD for pp collisions at $\sqrt{s} = 0.9$ TeV. . . . .	186
7.7	(Color online) Efficiency (top panel) and purity (bottom panel) of photons in PMD as a function of photon-hadron discrimination thresholds for pp collisions at $\sqrt{s} = 0.9$ TeV. . . . .	187
7.8	(Color online) Z-vertex distribution in cm for pp collisions at $\sqrt{s} = 0.9$ TeV. The dotted lines indicate the Z-vertex used in this analysis. . .	188
7.9	(Color online) An Aliroot simulation plot of the FMD and V0 services in front of the PMD. . . . .	191
7.10	(Color online) An Aliroot simulation plot of ITS and its services in front of the PMD. . . . .	191
7.11	$\eta - \phi$ lego plot showing the amount material (in radiation length) in front of the PMD for six cases: (a) PMD itself, (b) only the beam pipe, (c) only VZERO, (d) only FMD, (e) only ITS, and (f) all detectors and services as implemented in Aliroot in front of PMD. . . . .	192
7.12	Deflection of photon tracks in pp collisions at $\sqrt{s} = 0.9$ TeV. Upper panel: the case with no discrimination threshold; the middle and lower panel: with two different discrimination thresholds. Solid line is for the case of PMD with all detectors and dotted line is for the case only PMD in the simulation. . . . .	194
7.13	(Color online) Fraction of area of the solid curve outside the window of the dotted curve for no threshold (open circles), and two different thresholds (open plus and open triangles) for pp collisions at $\sqrt{s} = 0.9$ TeV . . . . .	195
7.14	(Color online) Number of split clusters in % plotted versus $\eta$ for no threshold (open circles) and two different threshold settings for pp collisions at $\sqrt{s} = 0.9$ TeV. . . . .	196
7.15	(Color online) Occupancy as a function of pseudo-rapidity for pp collisions at $\sqrt{s} = 0.9$ TeV. The results are compared with PHOJET and PHOJET with 10% additional material simulations. . . . .	197

7.16 (Color online) The XY scatter plot of hits on the preshower plane of PMD for pp collisions at $\sqrt{s} = 0.9$ TeV. . . . .	197
7.17 (Color online) Acceptance of PMD versus $\eta$ for pp collisions at $\sqrt{s} = 0.9$ TeV. . . . .	198
7.18 (Color online) Analysis flow chart for obtaining photon multiplicity distribution using data from PMD. . . . .	199
7.19 (Color online) $N_{\gamma-like}$ distributions for two different photon hadron discrimination thresholds for pp collisions at $\sqrt{s} = 0.9$ TeV. . . . .	199
7.20 (Color online) Response matrix for pp collisions at $\sqrt{s} = 0.9$ TeV using PHOJET event generator. The x-axis is the true photon multiplicity and the y-axis is the measured photon multiplicity within $2.3 < \eta < 3.9$ . . . . .	203
7.21 (Color online) Test of unfolding using a PHOJET simulation with different $\beta$ values for pp collisions $\sqrt{s} = 0.9$ TeV. . . . .	204
7.22 (Color online) Test of unfolding method in simulated data using PHOJET event generator: True multiplicity distributions, the $\gamma$ -like distributions and the unfolded distributions for pp collisions at $\sqrt{s} = 0.9$ TeV. The lower panel shows the ratio of unfolded to true distribution. . . . .	205
7.23 (Color online) Unfolded multiplicity distributions using two different discrimination thresholds for pp collisions at $\sqrt{s} = 0.9$ TeV. . . . .	206
7.24 (Color online) Multiplicity distribution of photons for pp collisions at 0.9 TeV within $2.3 < \eta < 3.9$ . The red crosses are data points with statistical errors and the shaded regions represent the systematic errors. The black solid dotted are the expectations from PHOJET, the blue dotted lines are from PYTHIA Perugia 0, the green dashed lines are from PYTHIA Perugia 2011 and the dot-dashed magenta line from PYTHIA ATLAS-CSC. The bottom panel shows the ratio between data and MC. . . . .	207

7.25 (Color online) Photon multiplicity distributions are fitted with both single NBD (top panel) and double NBD (bottom panel) function for pp collisions at $\sqrt{s} = 0.9$ TeV. . . . .	208
7.26 (Color online) Top panel: photon multiplicity distribution in terms of KNO variable within $2.3 < \eta < 3.9$ for pp collisions at $\sqrt{s} = 0.9, 2.76$ and 7 TeV. Bottom panel: ratio of multiplicity distribution at 2.76 and 7 TeV to that in 0.9 TeV. . . . .	210
7.27 (Color online) Energy dependence of the average photon multiplicity in pp ( $p\bar{p}$ ) collisions. The blue circles are UA5 data and the red stars are PMD data within $2.3 < \eta < 3.9$ . . . . .	211
7.28 (Color online) Test of unfolding method in simulated data using PHOJET event generator: True pseudo-rapidity distributions, the $\gamma$ -like distributions and the unfolded distributions for pp collisions at 0.9 TeV.	212
7.29 (Color online) Pseudo-rapidity distribution of photons for pp collisions at $\sqrt{s} = 0.9$ TeV. Statistical errors are smaller than the size of the symbols and systematic errors are represented by the shaded regions. The black dotted lines are the expectation from PHOJET, the blue dotted lines are from PYTHIA Perugia 0 and the green dashed lines are from PYTHIA Perugia 2011 and the magenta dot-dashed line from PYTHIA ATLAS-CSC. . . . .	213
7.30 Pseudo-rapidity distributions of photons and charged particles at $\sqrt{s} = 0.9$ GeV in monte carlo. The circles represent photons and the squares represent charged particles. Left panel : PHOJET right panel: PYTHIA . . . . .	214

7.31	(Color online) Left panel: Pseudo-rapidity distribution of photons and charged particles for pp collisions at $\sqrt{s} = 0.9$ TeV. The blue squares and green open crosses represent ALICE and UA5 data for charged particles, respectively. Open blue squares represent the latest charged particle results. The solid red circles represent the ALICE data for photons. Right panel : The photon results (solid red points) are calculated using the UA5 cross-section. . . . .	214
7.32	(Color online) Limiting fragmentation for pp collisions at 0.9, 2.76 and 7 TeV. The solid points represent the data and the lines represent the expectations from the PHOJET event generator. . . . .	216
7.33	(Color online) Different sources of systematic errors: unfolded multiplicity distributions using two different discrimination thresholds, different event generators and different methods of unfolding for pp collisions at $\sqrt{s} = 0.9$ TeV. . . . .	218
7.34	(Color online) Different sources of systematic errors: pseudo-rapidity distributions using two different discrimination thresholds and different event generators for pp collisions at $\sqrt{s} = 0.9$ TeV. . . . .	218
7.35	(Color online) The left panel shows the unfolded multiplicity distribution of photons from PHOJET and PHOJET + 10% for pp collisions at $\sqrt{s} = 0.9$ GeV, lower half of the left panel shows the ratio of these distributions. In right panel unfolded pseudo-rapidity distribution is shown for both the cases. . . . .	219
7.36	(Color online) Test of unfolding method in simulated data: True multiplicity distributions, the $\gamma$ -like distributions and the unfolded distributions for pp collisions at 0.9 TeV. The lower panels in the figures show the ratios of unfolded to true distributions. . . . .	222

8.1	(Color online) $\bar{p}/p$ ratio at midrapidity as a function of $p_T$ for $p+p$ collisions. The solid lines corresponds to new data from ALICE at LHC [2]. The $\bar{p}/p$ ratio for $\sqrt{s} = 200$ GeV is from the STAR experiment at RHIC [6]. The data for $\sqrt{s} < 200$ GeV are from the ISR [1]. The dashed lines are straight line fits to the $p_T$ dependence of the $\bar{p}/p$ ratios at various $\sqrt{s}$ , assuming the ratios do not depend on $p_T$ for the measured range. . . . .	231
8.2	(Color online) $\bar{p}/p$ ratio at midrapidity as a function of $\sqrt{s}$ for $p+p$ collisions. The experimental data are compared to model calculations from PYTHIA [9], PHOJET [10] and HIJING/B- $\bar{B}$ [11] with default settings. . . . .	232
8.3	(Color online) $\bar{p}/p$ ratio at midrapidity as a function of $\sqrt{s}$ for $p+p$ collisions compared to various implementation of the baryon production schemes in PYTHIA. See text for more details. . . . .	233
8.4	(Color online) Asymmetry for proton and anti-proton production at midrapidity for $p+p$ collisions as a function of $\sqrt{s}$ . The solid line is a fit to the data, with the functional form shown. . . . .	235
8.5	(Color online) Comparison of beam energy of $\bar{p}/p$ ratio at midrapidity for $p+p$ and nucleus-nucleus (A+A) collisions. The solid, dash and dotted lines are fits to the $p+p$ and A+A data inspired by the model based on baryon string junction picture [7, 20]. . . . .	235

# List of Tables

1.1	The resonances measured in high energy experiments; their decay channels, branching ratio and lifetime. . . . .	25
2.1	Summary of sub-detectors of ALICE [7]. . . . .	44
2.2	Trigger level of ALICE detectors . . . . .	57
3.1	The second and third column shows average number of participating nucleons ( $\langle N_{part} \rangle$ ), the average number of binary nucleon-nucleon collisions ( $\langle N_{coll} \rangle$ ) estimated from Glauber model in different collision centrality for Pb-Pb collisions at $\sqrt{s_{NN}} = 2.76$ TeV. The last column shows the measured charged particle pseudo-rapidity density at mid-rapidity in ALICE. . . . .	75
3.2	Number of events analyzed in Pb-Pb collisions at $\sqrt{s_{NN}} = 2.76$ TeV and pp collisions at $\sqrt{s} = 2.76$ TeV . . . . .	77
3.3	Track selection criteria used in Pb-Pb collisions at $\sqrt{s_{NN}} = 2.76$ TeV and pp collisions at $\sqrt{s} = 2.76$ TeV. . . . .	79
3.4	Boltzmann Gibbs Blast-Wave $K^{*0}$ spectra in Pb-Pb collisions at $\sqrt{s_{NN}} = 2.76$ TeV. . . . .	95
3.5	Tsallis fit parameters for the $K^{*0}$ spectra in pp collisions at $\sqrt{s} = 2.76$ TeV. . . . .	97
3.6	$dN/dy$ , $K^{*0}/K^-$ and $\langle p_T \rangle$ of $K^{*0}$ in Pb-Pb collisions $\sqrt{s_{NN}} = 2.76$ TeV and pp collisions at $\sqrt{s} = 2.76$ TeV. . . . .	103
3.7	BG Blast-Wave parameters at $\sqrt{s_{NN}} = 2.76$ TeV . . . . .	109

3.8	Fractional systematic uncertainties (in %) on yield and $\langle p_T \rangle$ in Pb-Pb collisions. . . . .	116
3.9	Fractional systematic uncertainties (in %) on yield and $\langle p_T \rangle$ in pp collisions. . . . .	116
3.10	Fractional systematic uncertainties(in %) on mass and width in Pb-Pb collisions. . . . .	118
3.11	Mass of $K^{*0}$ as a function of $p_T$ within the rapidity interval $-0.5 < y < 0.5$ in Pb-Pb collisions in 0-20% centrality at $\sqrt{s_{NN}} = 2.76$ TeV. .	130
3.12	Mass of $K^{*0}$ as a function of $p_T$ within the rapidity interval $-0.5 < y < 0.5$ in Pb-Pb collisions in 60-80% centrality at $\sqrt{s_{NN}} = 2.76$ TeV. .	130
3.13	Width of $K^{*0}$ as a function of $p_T$ within the rapidity interval $-0.5 < y < 0.5$ in Pb-Pb collisions in 0-20% centrality at $\sqrt{s_{NN}} = 2.76$ TeV. .	131
3.14	Width of $K^{*0}$ as a function of $p_T$ within the rapidity interval $-0.5 < y < 0.5$ in Pb-Pb collisions in 60-80% centrality at $\sqrt{s_{NN}} = 2.76$ TeV. .	131
3.15	Yield of $K^{*0}$ as a function of $p_T$ within the rapidity interval $-0.5 < y < 0.5$ in Pb-Pb collisions in 0-20% centrality at $\sqrt{s_{NN}} = 2.76$ TeV. .	132
3.16	Yield of $K^{*0}$ as a function of $p_T$ within the rapidity interval $-0.5 < y < 0.5$ in Pb-Pb collisions in 20-40% centrality at $\sqrt{s_{NN}} = 2.76$ TeV. .	132
3.17	Yield of $K^{*0}$ as a function of $p_T$ within the rapidity interval $-0.5 < y < 0.5$ in Pb-Pb collisions in 40-60% centrality at $\sqrt{s_{NN}} = 2.76$ TeV. .	133
3.18	Yield of $K^{*0}$ as a function of $p_T$ within the rapidity interval $-0.5 < y < 0.5$ in Pb-Pb collisions in 60-80% centrality at $\sqrt{s_{NN}} = 2.76$ TeV. .	133
3.19	Yield of $K^{*0}$ as a function of $p_T$ within the rapidity interval $-0.5 < y < 0.5$ in minimum bias pp collisions at $\sqrt{s} = 2.76$ TeV. . . . .	134
3.20	Mass of $K^{*0}$ as a function of $p_T$ within the rapidity interval $-0.5 < y < 0.5$ in minimum bias pp collisions at $\sqrt{s} = 2.76$ TeV. . . . .	135
3.21	Width of $K^{*0}$ as a function of $p_T$ within the rapidity interval $-0.5 < y < 0.5$ in minimum bias pp collisions at $\sqrt{s} = 2.76$ TeV. . . . .	136
5.1	Track selection criteria for selecting resonance daughter tracks. . . . .	154

6.1	Track selection criteria for selecting resonance daughter tracks and trigger particle tracks. . . . .	167
6.2	Fit parameters of double gaussian . . . . .	175
7.1	Trigger and vertex reconstruction efficiency . . . . .	190
7.2	Regularization parameters at $\sqrt{s} = 0.9$ TeV. . . . .	204
7.3	Fit parameters for single NBD. . . . .	209
7.4	Fit parameters for double NBD. . . . .	209
7.5	The parameters of the fit functions of Fig 7.27 . . . . .	211
7.6	The magnitude of the sources of systematic errors in multiplicity distribution for pp collisions at $\sqrt{s} = 0.9$ TeV. The values are quoted here for 1-10 multiplicity for all the energies. . . . .	220
7.7	The magnitude of the sources of systematic errors and their contributions to the pseudo-rapidity distributions for pp collisions at $\sqrt{s} = 0.9$ TeV. . . . .	220
7.8	Photon multiplicity for pp collisions at $\sqrt{s} = 0.9$ TeV. . . . .	223
7.9	Photon pseudo-rapidity density for pp collisions at $\sqrt{s} = 0.9$ TeV. . .	224

# Chapter 1

## Introduction

### 1.1 Standard Model

Theories and discoveries since 1930's resulted in providing remarkable insights into the fundamental structure of matter [1]. The attempt to explain the fundamental properties of matter leads to the theory of standard model. It was proposed by Glashow, Salam and Wienberg in 1970 [2, 3, 4]. The standard model is very successful in explaining experimental results with very high precision. According to standard model, the elementary particles can be categorized into 6 quarks, 6 leptons, 4 gauge bosons and the recently discovered Higgs boson. Each group of quarks and leptons can be sub-divided into generations. The six quarks are paired into three generations: the up ( $u$ ) and down ( $d$ ) quark are from the first generation; the charm ( $c$ ) and strange ( $s$ ) are from second generation; and the top ( $t$ ) and bottom ( $b$ ) are the third generation. Similar to quarks the leptons are also arranged into three generations: the electron ( $e$ ) and electron neutrino ( $\nu_e$ ); the muon ( $\mu$ ) and muon neutrino ( $\nu_\mu$ ); the tau ( $\tau$ ) and tau neutrino ( $\nu_\tau$ ). Each quarks and leptons also have their corresponding anti-particle.

There are four fundamental forces at work in the universe namely the strong force, the weak force, the electromagnetic force and the gravitational force. These

fundamental forces result from the exchange of mediator particles called gauge bosons. Each of the fundamental force has a mediator – (1) the strong force is mediated by the exchange of gluons ( $g$ ), (2) the weak force is carried by  $W^\pm$  and  $Z^0$  bosons, (3) the photon ( $\gamma$ ) is responsible for the electromagnetic force and (4) the graviton (not yet discovered) is conjectured to be the corresponding carrier for gravitational force. The gravity does not fit comfortably into the standard model. Since the gravity is the weakest force among all the interactions, it's effect in the particle physics is assumed to be negligible. The schematic diagram of standard model is shown in Fig. 1.1. The

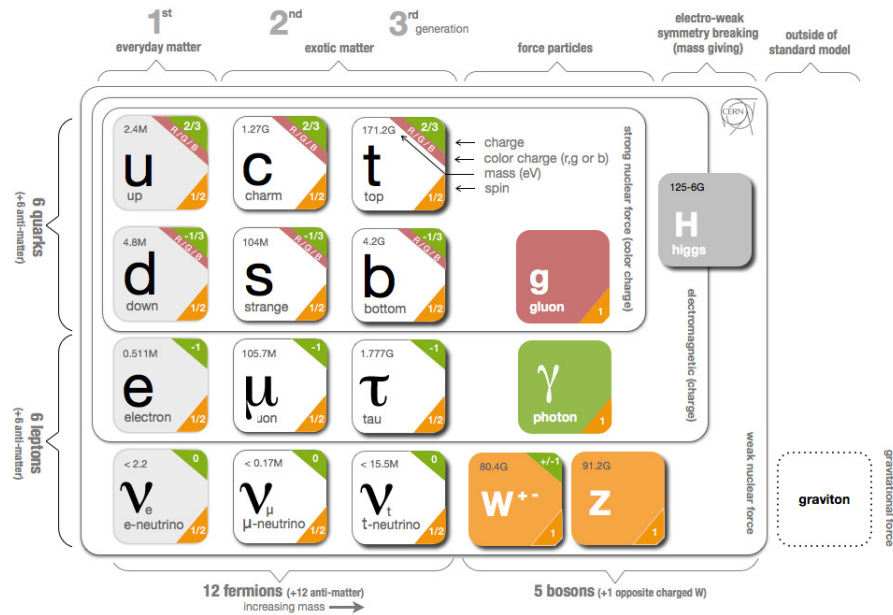


Figure 1.1: (Color online) The schematic representation of standard model. Figure has been taken from [5].

the standard model incorporates the strong, weak and electromagnetic forces and their carrier particles. It explains how these forces act on all the matter particles. The standard model predicts the existence of a particle called Higgs boson [6, 7] which is responsible for the generation of mass for the subatomic particles. The ATLAS [8] and CMS [9] experiments at the CERN LHC announced the experimental evidence of

such particle around the mass region of 126 GeV. Recently on 8th October 2013, the Nobel prize was awarded to Francois Englert and Peter Higgs for their contribution to the theory that lead to the understanding of mechanism for the generation of mass of sub-atomic particles. So far the Standard model accurately described the phenomena within its domain, but still it can not explain the origin of dark matter, matter anti-matter asymmetry etc.

## 1.2 Quantum Chromodynamics (QCD)

Out of the four fundamental interactions as discussed above the strong interaction is described by the theory called Quantum Chromodynamics (QCD). The QCD is formulated in terms of elementary fields, the quarks and gluons. The force between the two quarks is mediated by the exchange of gluons. The quarks and gluons carry a color charge. The color charges are conserved in all physical processes. The interaction potential in QCD can be approximately written as,

$$V(r) \sim -\alpha_s/r + kr \tag{1.1}$$

where  $\alpha_s$  is the strong coupling constant and  $k$  is the color string tension constant. The strong coupling constant is given by,

$$\alpha_s(Q^2) \sim \frac{12\pi}{(33 - 2n_f) \times \ln(Q^2/\Lambda_{QCD}^2)} \tag{1.2}$$

where  $Q^2$  is the momentum transfer,  $n_f$  is the number of quark flavors and  $\Lambda$  is the scale parameter. For small momentum transfer or at large distances, the value of  $\alpha_s$  is large. It increases as the distance between the quark increases and hence the quarks can not be separated. This property is known as quark confinement. It is responsible for binding of quarks inside the hadrons. The quark anti-quark pair bind together to form a meson, while three quarks bind to form a baryon. Now if the momentum transfer between the quarks is large or the distance between them is small, the coupling between them becomes small and the quarks behave like a free non-interacting particle. This is called Asymptotic freedom [10]. In case of hard

processes where the momentum transfer is large, the QCD calculations can be done perturbatively. But in case of soft processes where the momentum transfer is small, the perturbative calculations are not valid. The soft processes are the dominant process in the universe. The QCD can be solved non-perturbatively by lattice QCD approach where the calculation is done on a discrete space time lattice [11]. The lattice QCD calculations predicts transition from a confined hadron to a deconfined partonic matter. It was an idea of T. D. Lee [12] that it might be possible to create a high density nuclear matter containing asymptotically free quarks. Such a matter of free quarks and gluons are named as Quark Gluon Plasma (QGP) [11].

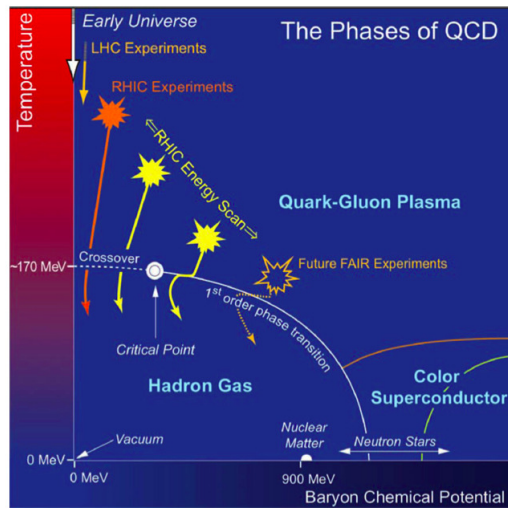


Figure 1.2: (Color online) Schematic representation of QCD phase diagram. Figure has been taken from [16].

### 1.3 QCD phase diagram

The lattice QCD predicts a transition from a confined hadronic phase to a deconfined partonic phase at a temperature of about 154-170 MeV [14, 15]. The Fig. 1.2 shows schematically the QCD phase diagram for the hadronic and partonic matter. The transition from a confined state to a deconfined QGP is expected to happen at either

high temperature or high baryon chemical potential. The QGP is supposed to be existed in the early stages of universe after the big bang. The relativistic heavy ion collision [17] experiments are designed to search for the signatures for such a deconfined state of quarks and gluons and study its properties. With the present technology we can achieve an energy scale similar to micro-second after the big bang where a QGP state was expected to be formed.

## 1.4 Heavy Ion Collision

In a heavy ion collision experiment two heavy nuclei collide at relativistic velocities. Due to very high velocity they are Lorentz contracted along the direction of motion and appears like a pan cake. The Fig. 1.3 describes schematically different stages in a heavy ion collision. The space-time ( $z - t$ ) evolution of heavy ion collision is shown in Fig. 1.4. The heavy ions collide at  $z, t = 0$ . The energy carried by the incoming hadrons are deposited within a small region in space in a short duration of time. The energy density at the collision center is sufficiently high and it can form a strongly interacting matter consisting of deconfined quarks and gluons, called quark gluon plasma (QGP). Model calculations indicate that beyond a critical energy density of  $\sim 1 \text{ GeV}/\text{fm}^3$  (or temperature  $\sim 200 \text{ MeV}$ ) matter can exist in a QGP phase. Initially the QGP may not be in thermal equilibrium, but subsequent equilibration

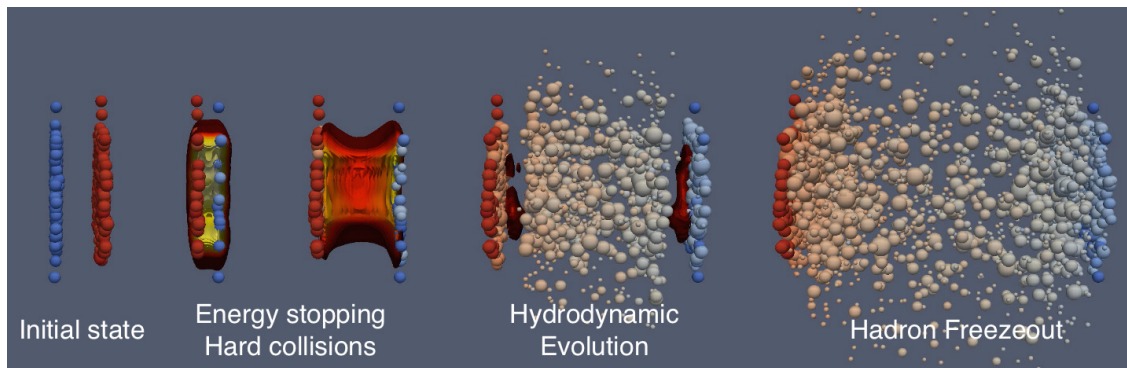


Figure 1.3: (Color online) Schematic picture of a heavy ion collision. Figure has been taken from [19].

may bring it to a local thermal equilibrium at some proper time  $\tau_0$ . The plasma then may behave like a hydrodynamic fluid. Now as the system expands its temperature drops down and at a later proper time the hadronization takes place. The corresponding temperature is called the critical temperature ( $T_c$ ). As the temperature of the system falls below a freeze out temperature called chemical freeze out temperature ( $T_{ch}$ ), the inelastic collision among the constituents ceases. At this stage the chemical composition of the produced particles get fixed. After the chemical freeze out the constituents can interact among themselves via elastic scattering which may further change the shape of their transverse momentum spectra. When the mean free path of the hadrons exceeds the dynamical size of the system, the elastic interaction among the hadrons ceases. This is called kinetic freeze out and the corresponding temperature is known as kinetic freeze out temperature ( $T_{fo}$ ). After that the hadrons streams freely to the detector and get detected.

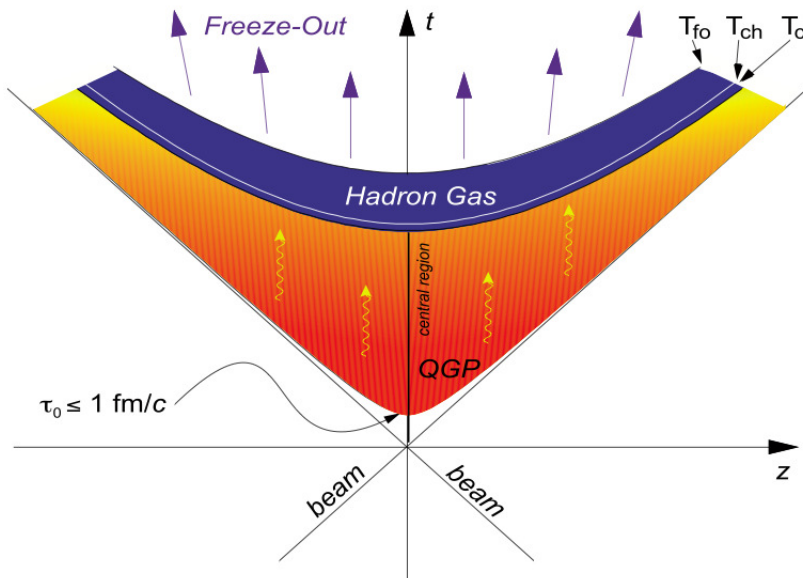


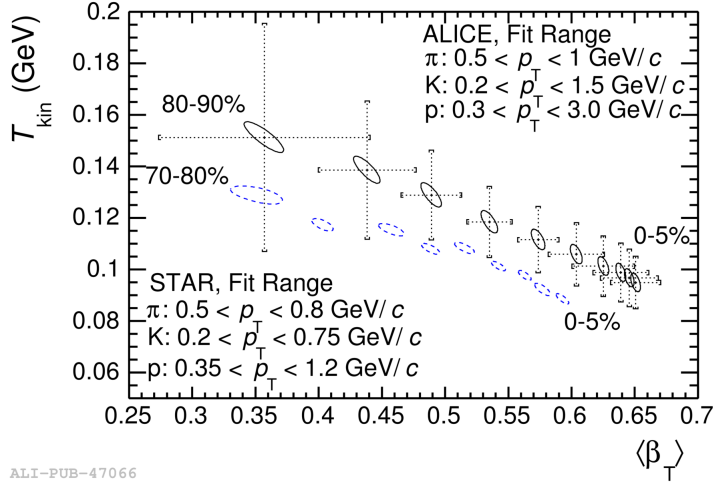
Figure 1.4: (Color online) Schematic representation of space time evolution in a heavy ion collision.

## 1.5 Experimental facilities for heavy ion collisions

The experimental facilities for heavy ion collisions started at the Brookhaven Alternating Gradient Synchrotron (AGS) and CERN Super Proton Synchrotron (SPS) around 1980's. The fixed target experiments at the AGS and SPS have explored the energy range of 2 to 158 GeV per nucleon to characterize the transition from a hadronic matter to a partonic matter. The Relativistic Heavy Ion Collider (RHIC) at BNL can collide heavy ion from a center of mass energy of 7.7 GeV up to 200 GeV. The observations from RHIC show many evidences of formation of a hot and dense QCD matter in heavy ion collisions. The plan of beam energy scan (BES) program at RHIC is to explore the QCD phase diagram, find the QCD critical point [18]. The experimental facilities at CERN Large Hadron Collider (LHC) significantly extends temperature and kinematic ranges for the study of QGP. The LHC is designed to collide lead ions up to a center of mass energy of 5.5 TeV per nucleon. In 2010 the LHC has taken data in lead-lead collision at a center of mass energy of 2.76 TeV per nucleon. This opens a new opportunity to study the QCD matter at extreme energy densities and temperatures. In the coming decades the Facility for Antiproton and Ion Research (FAIR) will allow to access the QCD phase diagram in the region of large baryon density. This thesis is based on the data from A Large Ion Collider Experiment (ALICE) at the LHC. Further details on experimental setup is discussed in Chapter 2.

## 1.6 Quark Gluon Plasma (QGP)

The quark gluon plasma which is expected to be formed in heavy ion collisions could not be detected directly. But the informations carried out by the produced particles may be used to the find its signature. Some of the signatures namely the jet quenching, nuclear modification factors,  $J/\Psi$  suppression, strangeness enhancement etc. will be discussed in the following section.



ALI-PUB-47066

Figure 1.5: (Color online)  $T_{kin}$  vs.  $\beta_T$  extracted by a simultaneous fit to the pion, kaon and proton spectra (measured in ALICE [21] and STAR [22] experiment) to a Blast Wave function [25].

### 1.6.1 Hadron yield and spectra

In a heavy ion collision, the chemical abundances of produced hadrons get fixed at the chemical freeze out. The hadrons continue to interact among themselves (only change the shape of their momentum distribution) until kinetic freeze out and then stream freely towards the detector. In an experiment we can measure the hadron yield as a function of its transverse momentum ( $p_T$ ). The measurement of  $p_T$  spectrum of produced particles can give the information of the system at the kinetic freeze out. The particle  $p_T$  spectra can be fitted with a Blast-Wave function [25] inspired from hydrodynamic models. Such models assume a system having a freeze out temperature ( $T_{kin}$ ) and moving with a collective expansion velocity ( $\beta_T$ ). The Fig. 1.5 shows  $T_{kin}$  vs.  $\beta_T$  extracted by the simultaneous fit to the pion, kaon and proton spectra in Pb-Pb collisions at  $\sqrt{s_{NN}} = 2.76$  TeV in ALICE [21] and in Au-Au collisions at  $\sqrt{s_{NN}} = 200$  GeV in STAR [22]. This shows that the system created in central collisions expands faster than peripheral collisions and freezes out at lower temperature. One can get the  $p_T$  integrated yield of the produced hadrons based on statistical

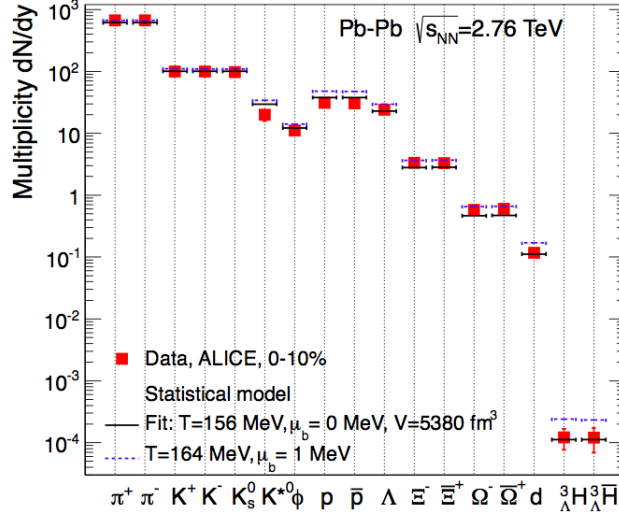


Figure 1.6: (Color online) Fit of the hadron yields measured in ALICE [21] with statistical hadronization model [18]. The  $K^{*0}$  is not included in fit.

equilibrium models [18] which assumes the chemical equilibrium at the freeze out and compare with experimentally measured hadron yields. The Fig. 1.6 describes the comparison of hadron yields measured in Pb-Pb collisions at  $\sqrt{s_{NN}} = 2.76$  TeV with such a statistical thermal model. Overall the equilibrium thermal model explains the data both at the RHIC and LHC energies. However, the proton yield could not be explained by the thermal model based on grand canonical ensemble. The yield of  $K^{*0}$  is not included in the thermal model fit and the prediction is different from the measurement. The  $K^{*0}$  production in Pb-Pb and pp collisions forms a part of this thesis. Further details will be discussed in Chapter 3. Although there are alternative formulations [24, 25] of thermal model to explain the hadron yields at the LHC.

## 1.6.2 Jet quenching

A strong evidence of QGP formation is the jet quenching phenomena [26] in heavy ion collisions. A jet is a high  $p_T$  parton which fragments into a cluster of hadrons, all moving in approximately the same direction. In pp or  $e^+e^-$  collisions, one observes

two jet structures with back to back momenta as shown schematically in Fig. 1.7. These are called dijets. In a typical heavy ion collision if the dijets are produced

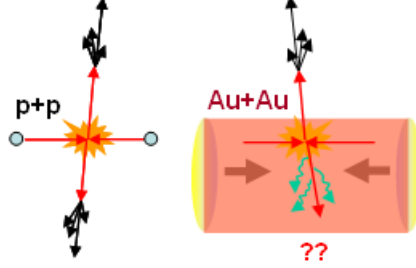


Figure 1.7: (Color online) Schematic representation jet quenching in heavy ion collisions.

near the surface (surface biased) of the medium, then one of the jet is more probable to escape the medium without interaction and fragments in the vacuum. Whereas the other one has more probability to traverse through the hot and dense medium and lose most of its energy or may even completely absorbed into the medium before fragmenting to hadrons. The asymmetry in the dijet production is one the signatures of the formation of a QGP state of matter. The Fig. 1.8 shows two particle azimuthal correlation in pp, Au-Au and d-Au collisions measured by STAR experiment at  $\sqrt{s_{NN}} = 200$  GeV [27]. The double peak structure, at  $\delta\phi = 0$  (near side) and  $\delta\phi = \pi$  (away side) is observed in minimum bias pp and central d-Au collisions. However, in Au-Au collisions the peak in the away side is strongly suppressed. The strong suppression in the away side peak is the experimental evidence of jet-quenching. The jet-quenching behavior is also observed at LHC energies. The Fig.1.9 shows the event display of a highly asymmetric dijet event in Pb-Pb collisions at  $\sqrt{s_{NN}} = 2.76$  TeV in the ATLAS experiment [28]. It shows one jet with a transverse energy  $E_T > 100$  GeV and there is no observation of the recoiled jet in the opposite azimuth direction.

### 1.6.3 Nuclear modification factor ( $R_{AA}$ )

To find the signature of QGP in heavy ion collision, a system is needed for baseline study, such as proton-proton collisions where no QGP is expected to be formed. For this purpose a variable called nuclear modification factor ( $R_{AA}$ ) is defined which is the

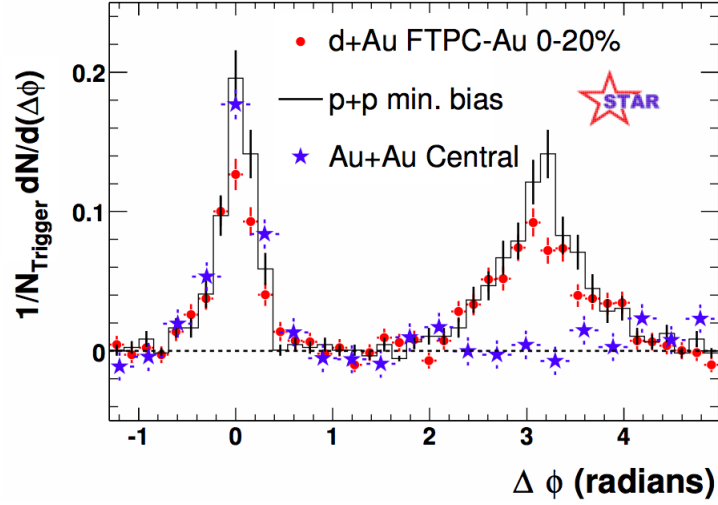


Figure 1.8: (Color online) Dijet azimuthal correlation at  $\sqrt{s_{NN}} = 200$  GeV in pp, d-Au and Au-Au collisions measured in STAR experiment [27].

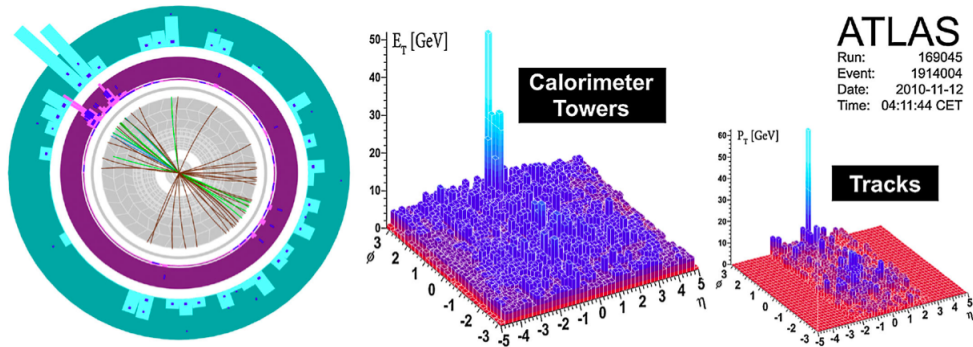


Figure 1.9: (Color online) Dijet asymmetry observed in Pb-Pb collisions at  $\sqrt{s_{NN}} = 2.76$  TeV in ATLAS experiment [28].

ratio of the yield in heavy ion collision to that in proton-proton collision normalized to binary nucleon-nucleon collisions,

$$R_{AA} = \frac{1}{\langle T_{AA} \rangle} \times \frac{(d^2N/dydp_T)_{AA}}{(d^2\sigma/dydp_T)_{pp}} \quad (1.3)$$

where  $\langle T_{AA} \rangle (= \langle N_{coll} \rangle / \sigma_{NN})$  is average nuclear thickness function,  $\langle N_{coll} \rangle$  is the average number of binary nucleon-nucleon collisions calculated using MC Glauber simulations and  $\sigma_{NN}$  is the inelastic pp cross-section. If the nucleus-nucleus collision is a simple superposition of nucleon-nucleon collision, then the value of  $R_{AA}$  should be unity at high  $p_T$ . If it's value is less than unity then it will indicate the effect of strongly interacting matter produced in heavy ion collisions. One of the advantage of this variable is that many systematic uncertainties present in the measurement get cancelled when both the data (AA and pp) are taken in same experiment and same energy. The left panel of Fig. 1.10 shows the results of  $R_{AA}$  of charged hadron at

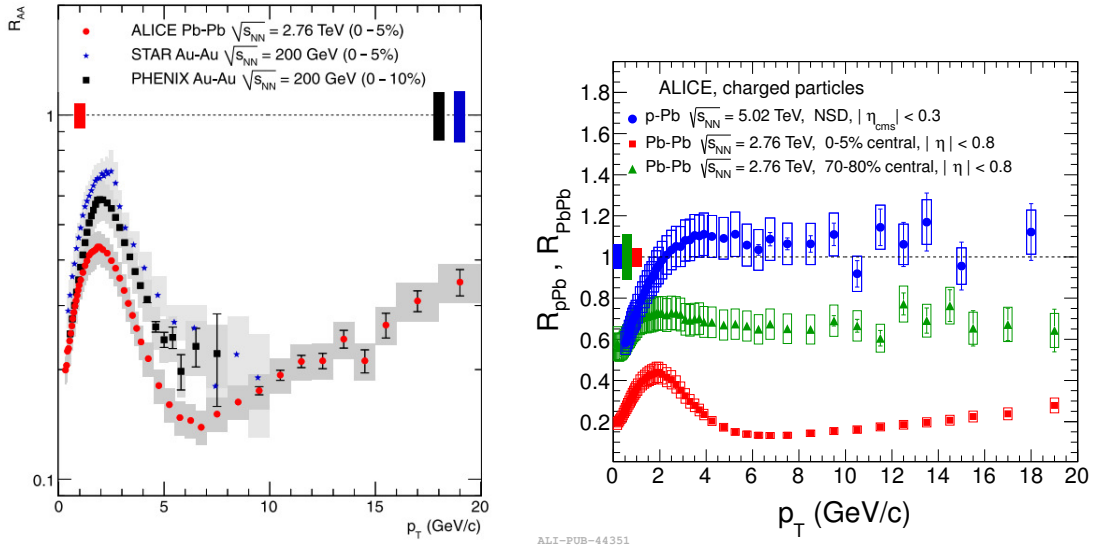


Figure 1.10: (Color online) Nuclear modification factor in Pb-Pb at  $\sqrt{s_{NN}} = 2.76$  TeV [29] and p-Pb [32] collisions at  $\sqrt{s_{NN}} = 5.02$  TeV. The results on the left panel are compared with the measurements at RHIC [30, 31].

ALICE for Pb-Pb collisions at  $\sqrt{s_{NN}} = 2.76$  TeV [29]. It is compared to that measured at RHIC for Au-Au collisions at  $\sqrt{s_{NN}} = 200$  GeV [30, 31]. The suppression of yield

at high transverse momentum suggests strong parton energy loss and the presence of strongly interacting medium. The suppression is found to be larger at LHC than RHIC energies. The right panel of Fig. 1.10 shows the comparison of  $R_{AA}$  of charged hadrons in Pb-Pb collisions at  $\sqrt{s_{NN}} = 2.76$  TeV to  $R_{pPb}$ <sup>1</sup> in p-Pb collisions at  $\sqrt{s_{NN}} = 5.02$  TeV [32]. It is observed that the suppression is small in peripheral than in central Pb-Pb collisions. The  $R_{pPb}$  is close to unity for transverse momentum greater than 2 GeV/c. This further emphasize that the observation in Pb-Pb collisions are due to final state effects and due to formation of a hot and dense QGP medium in the collisions. In this thesis we will discuss the nuclear modification factor for resonance particles like  $K^{*0}$  meson and will compare it to those for  $\phi$  meson and inclusive charged hadrons.

#### 1.6.4 J/ $\Psi$ suppression

The quarkoniums (or bottomoniums) are the bound states of quark anti-quark pairs like  $c\bar{c}$  (or  $b\bar{b}$ ). They are created in the initial stage of the collision. In 1986 Matsui and Satz suggested [33] that the production of J/ $\Psi$ , which is a bound state of  $c\bar{c}$  quarks, will be suppressed in heavy ion collisions with respect to pp collisions. If QGP is formed in heavy ion collisions, the J/ $\Psi$  production will be inhibited due to the screening potential. In presence of QGP, the color charge of a quark is screened due to Debye screening. Hence the  $c\bar{c}$  pair could not be able to form a J/ $\Psi$ . This is called J/ $\Psi$  suppression. The observation from SPS and RHIC [35] shows the suppression of J/ $\Psi$  in heavy ion collision which is attributed to the presence of hot and dense matter. The J/ $\Psi$  suppression is also reported by ALICE in Pb-Pb collisions at  $\sqrt{s_{NN}} = 2.76$  TeV [34] and shown in Fig. 1.11. The nuclear modification factor ( $R_{AA}$ ) of J/ $\Psi$  measured in ALICE is larger than that measured in SPS and RHIC [35] at most central collisions but the  $R_{AA}$  does not exhibit significant centrality dependence at LHC energies. The higher values of J/ $\Psi$   $R_{AA}$  at LHC can be attributed to the recombination process in J/ $\Psi$  production.

---

<sup>1</sup>Nuclear modification factor for p-Pb collisions.

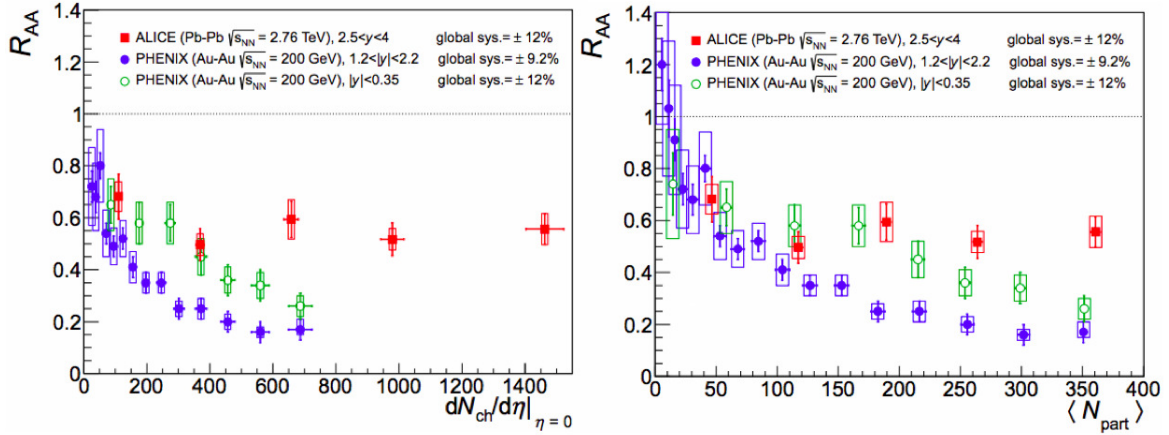


Figure 1.11: (Color online) Nuclear modification factor  $R_{AA}$  of  $J/\Psi$  for Pb-Pb collisions measured in ALICE at  $\sqrt{s_{NN}} = 2.76$  TeV [34]. The results are compared with the measurement from RHIC [35].

### 1.6.5 Strangeness enhancement

In heavy-ion and proton-proton collisions the net strangeness before the collision is zero. The strangeness are produced in the course of collision. The available production channels for  $s\bar{s}$  pair formation ( $q\bar{q} \rightarrow s\bar{s}$  and  $gg \rightarrow s\bar{s}$ ) in the QGP is high because of high gluon density, gluon fusion and annihilation of light  $q\bar{q}$  pairs than pp interactions where QGP is not expected to be formed. The gluonic channel has about 80% contribution to the total production for strange quarks [36]. The strangeness enhancement factor (measured in experiment) is defined as the ratio of yield of a strange particle per participating nucleon in the heavy ion collisions to that in pp collisions. The Fig. 1.12 shows the enhancement plot for multi-strange hadrons in Pb-Pb collisions at  $\sqrt{s_{NN}} = 2.76$  TeV measured in ALICE [37] and it is compared with the results from lower energy experiments at SPS [38] and RHIC [39]. The strangeness enhancement is observed to decrease from SPS to RHIC to LHC energies for all the multi-strange species. However the enhancement is observed in heavy ion collisions but it is uncertain whether or not the enhancement is due to the increased strangeness production in QGP or due to the canonical suppression [40] in pp collisions.

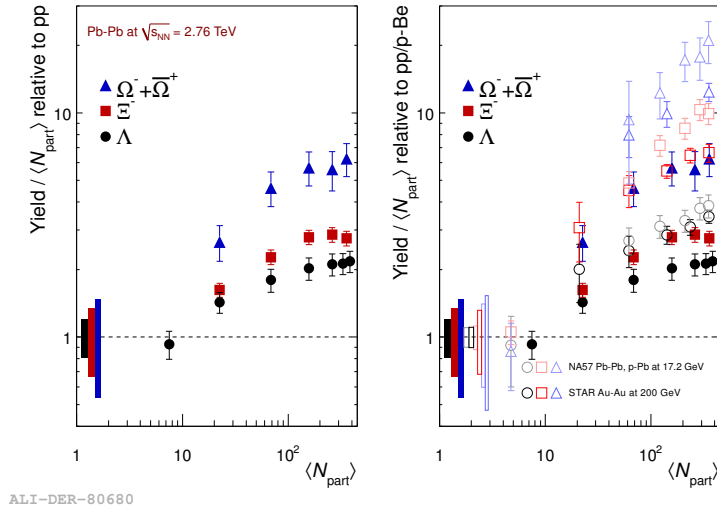


Figure 1.12: (Color online) Strangeness enhancement for multi-strange hadrons measured in SPS [38], RHIC [39] and LHC [37] energies.

### 1.6.6 Elliptic flow

If a heavy ion collision occurs at a non-zero impact parameter, as shown in Fig. 1.13, the participant region where the most collision occurs do not possess azimuthal symmetry. Multiple interactions among the constituents translate this spatial anisotropy into the momentum anisotropy of the produced particles [2]. The observed momentum anisotropy is called collective flow. In non-central heavy ion collisions, the azimuthal distribution of produced particles can be expanded in terms of Fourier series [12, 13],

$$\frac{dN}{d\phi} \propto 1 + \sum_{n=1}^{\infty} v_n \cos[n(\phi - \Psi)] \quad (1.4)$$

where  $\phi$  is the azimuthal angle of the produced particles and  $\Psi$  is the reaction plane angle which is defined by the plane containing the impact parameter between the two nuclei and the beam axis. The second order Fourier coefficient  $v_2$  is called elliptic flow. The  $v_2$  of charged particles and hadrons have been measured in many heavy ion experiments. The Fig. 1.14 shows the of  $v_2$  of  $\pi$ ,  $K$  and  $p$  measured in ALICE for Pb-Pb collisions at  $\sqrt{s_{NN}} = 2.76$  TeV [44]. The  $v_2$  is compared with the results from STAR [45] and PHENIX [46] experiments. It is observed that the  $v_2$  at low transverse momentum for LHC and RHIC energies are similar which is consistent

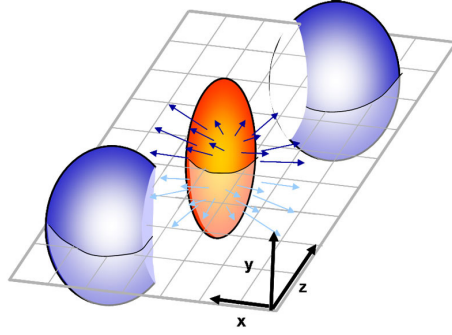
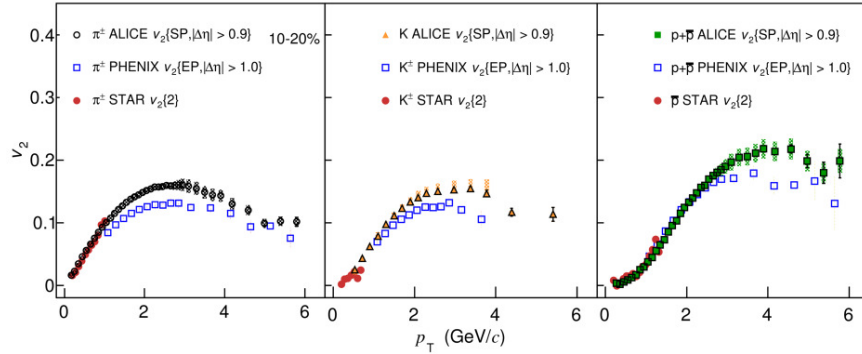


Figure 1.13: (Color online) Schematic representation of elliptic flow in a non-central heavy ion collision.

with predictions from hydrodynamic models. On the other hand the integrated  $v_2$  at the LHC is about 30% higher compared with RHIC which could be effect of radial flow at higher energies [44]. The left panel of Fig. 1.15 reports the  $v_2$  of  $\pi$ ,  $K$ ,  $K_S^0$ ,



ALI-PUB-82574

Figure 1.14: (Color online) Comparison of  $v_2$  of identified hadrons measured in ALICE [44], STAR [45] and PHENIX experiments [46].

$p$ ,  $\phi$ ,  $\Lambda$ ,  $\Xi$  and  $\Omega$  in Pb-Pb collisions at  $\sqrt{s_{NN}} = 2.76$  TeV measured in ALICE. A distinct mass ordering is observed in the low  $p_T$  ( $< 2-3$  GeV/ $c$ ), which is attributed to the interplay between elliptic and radial flow that lowers the value of  $v_2$  for heavy particles and shifts them to higher values of  $p_T$ . Such a mass ordering in  $v_2$  is also observed in previous measurements at RHIC [45]. The right panel of Fig. 1.15 shows the scaling of  $v_2$  with number of constituent quarks. In the intermediate  $p_T$  (2 -

6 GeV/c), there was evidence of constituent quark scaling at RHIC indicating the coalescence to be the dominant mechanism for hadronization. However the data from ALICE exhibit deviation from NCQ scaling at the level of  $\pm 20\%$ . In this thesis we will present the first results of  $K^{*0} v_2$  in Pb-Pb collisions at  $\sqrt{s_{NN}} = 2.76$  TeV.

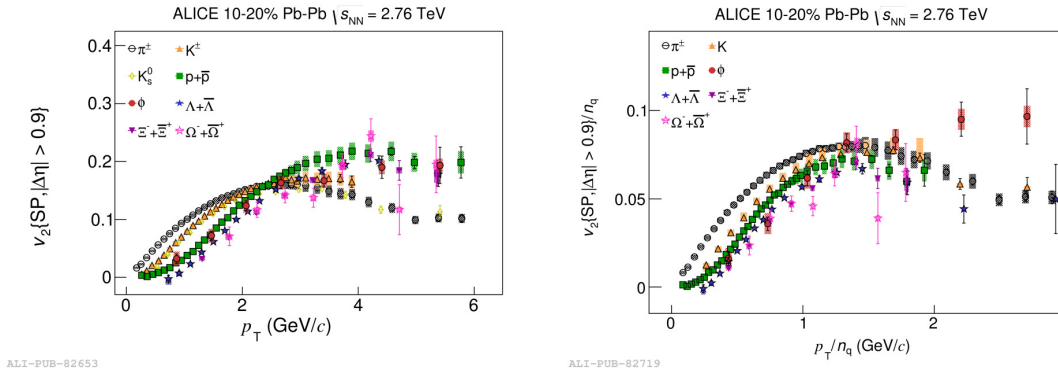


Figure 1.15: (Color online) Left panel:  $v_2$  of identified hadron for Pb-Pb collisions measured in ALICE [44]. Right panel: number of quark scaling for the identified hadrons measured in ALICE.

## 1.7 pp collisions

The proton proton (pp) collisions are very important for the measurements of global characteristics. The pp collisions are mostly dominated by soft interactions (small momentum transfer) and useful to study QCD in non-perturbative regime and to constraint phenomenological models and event generators. Such studies are essential for the understanding of backgrounds for measurements of hard and rare interactions. Also the measurements (such as yield and  $p_T$  spectra) in pp collision are used as a baseline study for the heavy ion collisions.

An inelastic pp collisions can be categorized into three different event classes, Non-diffractive (ND), Single-diffractive (SD) and Double-diffractive (DD). Thus the total inelastic cross-section is given by,

$$\sigma_{INEL} = \sigma_{ND} + \sigma_{SD} + \sigma_{DD} \quad (1.5)$$

In an SD event, one of the colliding particle fragments (e.g.  $p + p \rightarrow p + X$ ), whereas in a DD event both the colliding particle fragments (e.g.  $p + p \rightarrow X + X$ ). In case of ND events none of the colliding particle fragments. The excitation of one or both the protons can be thought as an exchange of multi-gluons which is called Pomerons [47]. The Fig. 1.16 shows pseudorapidity density distribution in a ND, SD and DD events. In case of ND events, the distribution is maximum at mid-rapidity and falls symmetrically on both sides. For SD events one of the projectile ending up at beam rapidity while the other one fragments into the forward rapidities. For DD events both the projectile fragments giving peaks at forward rapidities and a deep in the mid-rapidity region. Due to the limited capabilities in an experiment, the events

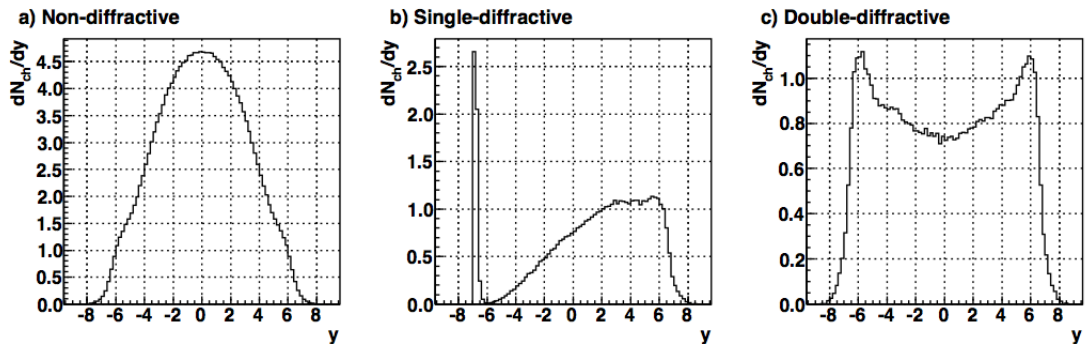


Figure 1.16: Rapidity distribution of ND, SD and DD processes from PYTHIA event generator. This figure has been taken from [48].

are usually published in two different classes – (1) inelastic ( $\text{INEL} = \text{ND} + \text{SD} + \text{DD}$ ) and non-single diffractive ( $\text{NSD} = \text{ND} + \text{DD}$ ).

The multiplicity and pseudorapidity distributions are the basic global observables measured in pp collisions. It is found that the multiplicity distributions can be described by a negative binomial distribution (NBD) function,

$$P_{NBD}(m, k; n) = \frac{\Gamma(n+k)}{\Gamma(n+1)\Gamma(k)} \frac{(m/k)^n}{(m/k+1)^{n+k}} \quad (1.6)$$

where  $m = \langle n \rangle$  is the average multiplicity ( $n$ );  $k$  is a parameter describes the shape of the distribution. If  $k \rightarrow \infty$ , the NBD describes a Poisson distribution, whereas

for  $k = 1$  it becomes a Geometric function. While at lower energies multiplicity distributions are fairly explained by a single NBD function, but it is not sufficient to explain high energy data. The measurement by UA5 experiment [49] at  $\sqrt{s} = 900$  GeV shows a deviation of data from the NBD. This led to a two component model described by a combination of two NBD functions [50],

$$P_{double\ NBD}(W, m_1, k_1, m_2, k_2; n) = WP_{NBD}^1(m_1, k_1; n) + (1 - W)P_{NBD}^2(m_2, k_2; n) \quad (1.7)$$

where  $W$  is a weight factor which indicates the contribution from soft processes and  $(1 - W)$  gives the same for semi-hard processes.

In 1969, Feynman postulated [51] that the average multiplicity of the produced particles are proportional to the logarithmic of the center of mass energy,

$$\langle N \rangle \propto \ln \sqrt{s} \quad (1.8)$$

Based on Feynman scaling Koba, Nielsen and Oleson derived that the multiplicity distribution should obey KNO scaling [52] if they are plotted in term of KNO variable,

$$\Psi(n) = \langle n \rangle P(n) \quad (1.9)$$

Recently the multiplicity distributions are published by LHC experiments. The measurement from ALICE at mid-rapidity for  $\sqrt{s} = 0.9$  and 2.36 TeV [53] shows a mild deviation from KNO scaling, possibly due to the increasing fraction of events with the highest multiplicity.

The pseudorapidity distribution ( $dN/d\eta$ ) are one of the global observables measured in pp collisions. In high energy collisions, the particles near beam or target rapidity were thought to be governed by limiting fragmentation hypothesis [54]. The limiting fragmentation behavior can be understood from the measurement of  $dN/d\eta$ . According to this hypothesis the produced particles in the rest frame of one of the colliding hadrons will approach a limiting distribution. The projectile hadron when seen in the frame of target is Lorentz contracted and passes through the target. Due to excitation the target then fragments into a final state distribution of particles. The particles near the central rapidity are expected to form a plateau which is independent of energy. The  $dN/d\eta$  of charged particles have been measured in pp( $p\bar{p}$ )

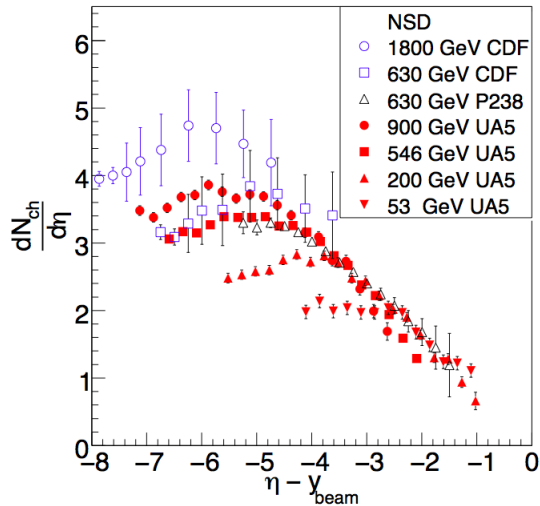


Figure 1.17: (Color online) Pseudorapidity distribution of charged particles as a function of  $\eta - y_{beam}$  for  $pp(p\bar{p})$  collisions. This Figure has been taken from [55].

collisions over a wide range of energy [49]. When viewed in the target frame of reference, these data exhibits a longitudinal scaling. The Fig. 1.17 describes pseudorapidity distribution as a function of  $\eta - y_{beam}$  ( $y_{beam}$  being the beam rapidity). It shows the limiting fragmentation behavior for the charged particles over a wide range of energies. In this thesis we will present the multiplicity and pseudorapidity distribution of inclusive photons produced in  $pp$  collisions at LHC. The results will be confronted to several model calculations and attempts will be made to study the limiting fragmentation phenomena.

## 1.8 Event generators

The event generators are used to generate simulated events as in the real experiments. Although the event generators are limited by the knowledge of existing underlying physics, but it has a vital role in various aspects of high energy physics. The results from event generators are used to obtain an understanding of the real data. It is widely used for preparing analysis strategies and implementing the needed analysis code, as well as for estimating the detector acceptance and efficiency corrections.

Further it can be used for designing and optimizing detectors. Out of the many event generators, we will discuss briefly PYTHIA, PHOJET, HIJING, HIJING B- $\bar{B}$  and AMPT that have been used in the analysis presented in this thesis.

### 1.8.1 PYTHIA

PYTHIA [56, 57, 58] is an event generator which combines the collisions between  $e^+$ ,  $e^-$ ,  $p$  and  $\bar{p}$ . It combines hard processes and various phenomenological models for initial and final state parton showers, multiple parton-parton interactions, beam remnants, string fragmentation and particle decays. The different stages of a pp collision in PYTHIA is schematically shown in Fig. 1.18. Initially two hadrons, coming towards each other, are described by parton distribution function  $f_i(x, Q^2)$ . The parton distribution function gives the probability to find a parton  $i$  inside beam particle, carrying a fraction  $x$  of the total momentum of the hadron. The parton distribution function is also dependent on the momentum  $Q^2$  that characterises the hard processes. For hard interactions ( $p_T > 2$  GeV/c) the parton scattering are described by perturbative QCD. The parton-parton cross section of a given processes  $ij \rightarrow k$  is given by,

$$\sigma_{ij \rightarrow k} = \int dx_1 \int dx_2 f_i^1(x_1, Q^2) f_j^2(x_2, Q^2) \hat{\sigma}_{ij \rightarrow k} \quad (1.10)$$

where  $\hat{\sigma}_{ij \rightarrow k}$  is the hard scattering cross section for the  $k^{th}$  sub-process possible between incoming partons  $i$  and  $j$ ;  $f_i^1(x_1, Q^2)$  and  $f_j^2(x_2, Q^2)$  are the parton distribution functions. Since the derivation of a parton distribution from first principles does not exist, the PYTHIA relies on some parameterization where experimental data are used in conjunction with the evolution equations for the  $Q^2$  dependence. In PYTHIA one shower initiator parton from each of the beam starts off a sequence of branchings such as  $q \rightarrow qg$ , which build up initial state shower. One incoming parton from each of the two showers enters into the hard processes, where there a number of outgoing partons are produced. The outgoing partons may go through multiple interactions to build up final state showers. When the shower initiators are taken out of the beam particles, the beam remnant is left which may have an internal structure and

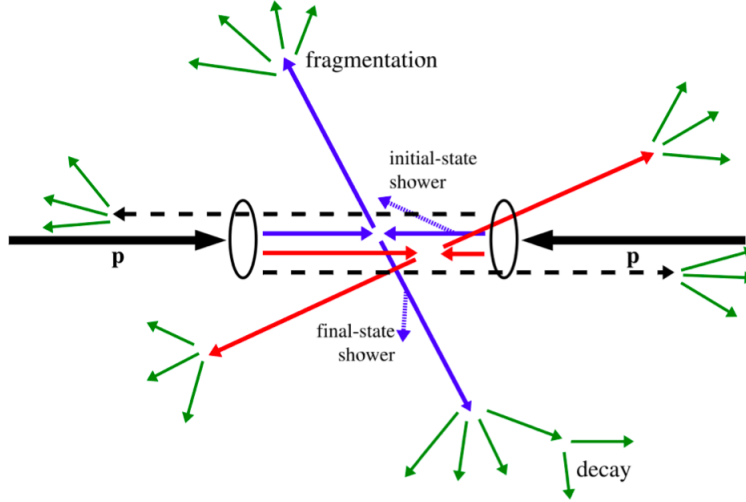


Figure 1.18: (Color online) A schematic diagram of a pp collision in PYTHIA. Figure has been taken from [48].

a net color charge that relates it to rest of the final state. The QCD confinement ensures that the outgoing partons are not observable, but instead they fragment into color neutral hadrons. The hadronization is carried out by Lund string fragmentation model. Finally many of the produced hadrons those are unstable decayed.

## 1.8.2 PHOJET

PHOJET [59, 60] is a two component model which describes the high energy collisions with a soft and hard component. In PHOJET, the soft interactions are described by a Dual Parton Model (DPM) [15], whereas the hard interactions are calculated by perturbative QCD like in PYTHIA. The total cross-section can be written as:

$$\sigma_{total} = \sigma_{soft} + \sigma_{hard} \quad (1.11)$$

The PHOJET uses the DPM for combining phenomenologically the non-perturbative topological expansions of QCD with generally accepted theoretical principles like duality, unitarity, Regge behavior and the parton structure of hadrons. The mechanism of Pomeron exchange is at the heart of the DPM. According to the DPM each exchanged pomeron gives rise to two color neutral chains stretching between the quarks

and diquarks for the baryons, or quarks and anti-quarks for the mesons. In the case of the leading Pomeron exchange, these chains stretch between valence quarks (or anti-quarks) whereas for the other exchanges the chains will end on valence and sea quarks from the initial hadrons. The pomeron exchanged cross section for a pure soft interaction can be parameterized by,

$$\sigma_{soft} = 37.8 s^{0.076} mb \quad (1.12)$$

The soft cross section increases as a power of center of mass energy ( $s$ ), but the total cross section increases with  $(\ln s)^2$ . So the  $\sigma_{soft}$  becomes larger than  $\sigma_{total}$  as  $s \rightarrow \infty$ , which is violation of unitarity bound. So to preserve unitarity bound multiple-pomeron exchanges are taken into account.

The hard cross section are calculated for  $p_T > 2$  GeV/c. It is given by,

$$\sigma_{hard} = \sum_{i,j \rightarrow k,l} \int \int \int dx_1 dx_2 d\hat{t} x_1 F_i(x_1, Q^2) x_2 F_j(x_2, Q^2) \times \frac{1}{x_1 x_2} \pi M^2 \frac{\alpha_s^2(Q^2)}{s^s} \quad (1.13)$$

where  $F_i(x_1, Q^2)$  are the parton distributions,  $M = M_{i,j \rightarrow k,l}$  is the matrix element for the hard parton-parton scattering scattering  $i, j \rightarrow k, l$  and  $\alpha_s^2(Q^2)$  is the strong coupling constant at the scale  $Q^2$ . Here also for increasing  $s$ ,  $\sigma_{hard} > \sigma_{total}$  will appear and a mechanism of multiple parton scattering is adapted to preserve unitarity. In addition the PHOJET allows the possibility of adding initial and final parton showering. The fragmentation both for soft and hard interactions are governed by Lund fragmentation model as in PYTHIA.

### 1.8.3 HIJING

Perturbative QCD predicts jet production from parton scatterings in high energy hadronic interactions. Hard or semi-hard parton scatterings with  $p_T$  of a few GeV are expected to dominate high energy heavy-ion collisions. The Heavy Ion Jet Interaction Generator (HIJING) [15] was developed by combining the pQCD inspired models of jet production using the Lund model for jet fragmentation. The HIJING model has been developed with special emphasis on the role of mini jets in pp, pA

and AA interactions. The model includes multiple mini-jet production with initial and final state radiation. The soft processes in HIJING are guided by Lund FRITOF model and dual parton model (DPM). The hard processes are inspired by the perturbative QCD as implemented in PYTHIA. Binary scattering with Glauber geometry for multiple interactions are used to simulate pA and AA collisions. Two important features of HIJING are jet quenching and nuclear shadowing. Jet quenching is modeled by an assumed energy loss  $dE/dz$  of partons traversing the produced dense matter. Shadowing describes the modification of the free nucleon parton density in the nucleus.

#### 1.8.4 HIJING B- $\bar{B}$

The nuclear mass number ( $A$ ) dependence of baryon stopping and the transfer of baryon to central rapidity are not correctly described by multiparticle production models such as HIJING, FRITOF and DPM which are based on quark-diquark string picture for excited baryons. The concept of baryon junction [7] naturally arises when writing the QCD gauge invariant operator for a baryon, being the vertex which links the three color flux lines flowing from the valence quarks. The novel mechanism of baryon transport motivated by the Regge theory [16] has been implemented in the form of an event generator HIJING/B- $\bar{B}$  [11]. The junction is expected to play a dynamical role through the Regge exchange of junction states in high energy collisions. The junction exchange could provide a natural mechanism for the transport of baryon number [17] into the central rapidity region. Further details on this model can be found in Ref. [7, 11].

#### 1.8.5 AMPT

A MultiPhase Transport (AMPT) [38] is an extension of HIJING and it uses HIJING for generation of initial conditions while changing the treatment of the resulting collision evolution. The Zhangs Parton Cascade Model (ZPC) [16] is then used for partonic (quarks and gluons) scatterings and A Relativistic Transport Model (ART) [17]

is used for the hadronic scatterings after the freeze out. The multiphase design of AMPT makes it suited for studies of collective phenomena e.g., anisotropic transverse flow. Further details on AMPT is discussed in Chapter 4.

## 1.9 Thesis Motivation

### 1.9.1 Resonance production in Pb-Pb and pp collisions at LHC energies

Resonances	Decay channel	Branching ratio	Lifetime ( $\tau$ ) fm/c
$\rho^0$ (770)	$\pi^+\pi^-$	1	1.1
$\Delta$ (1232)	$p\pi$	1	1.6
$f^0$ (980)	$\pi^+\pi^-$	2/3	2.6
$K^{*0}$ (896)	$K\pi$	2/3	4
$\Sigma^*$ (1385)	$\Lambda\pi$	0.88	5.5
$\Lambda^*$ (1520)	$pK$	0.45	12.6
$\phi$ (1020)	$K^+K^-$	0.49	45

Table 1.1: The resonances measured in high energy experiments; their decay channels, branching ratio and lifetime.

The resonances are very short lived particles. They decayed through strong interaction within roughly  $\sim 10^{-23}$  secs (or a few fm/c). The width ( $\Gamma$ ) and lifetime ( $\tau$ ) of the resonances are related by uncertainty relation,  $\Gamma\tau \sim \hbar$ . The table 1.1 reports most of the resonances [4] that can be measured in heavy ion collisions. They have lifetime within the range 1.1 to 45 fm/c, which covers the typical lifetime of the fireball produced in heavy ion collisions. Hence they can be used for studying the evolution of the interacting medium formed in heavy ion collisions. For the present study we have chosen the  $K^{*0}$  resonance which is a vector meson ( $J = 1$ ). In fact the  $K^{*0}$  is chosen because of its short lifetime  $\sim 4$  fm/c which is comparable to that

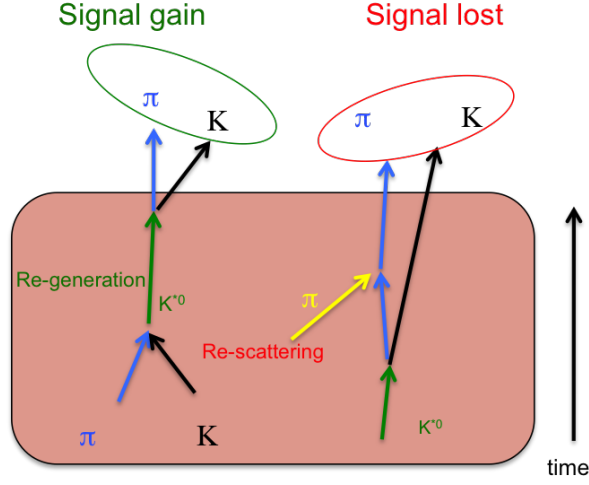


Figure 1.19: (Color online) Schematic representation of re-scattering and re-generation in heavy ion collision taking an example of  $K^{*0}$  resonance.

of the fireball ( $\sim 10$  fm/c). Thus its decay products are prone to re-scattering and re-generation processes in the hadronic phase of the medium. Due to short lifetime, the decay products of  $K^{*0}$ , the kaons and pions, may be re-scattered by the other hadrons in the medium as shown in Fig. 1.19. This re-scattering is dependent on the pion-pion, pion-kaon and kaon-kaon scattering cross section [18, 19]. The resonances can not be detected directly in an experiment. They are identified by reconstructing the invariant mass through their decay products. If the momentum of one of the decay daughters is changed by re-scattering, the resonance can not be reconstructed and the signal is said to be lost. Model calculations [31] suggest that such re-scattering is most probable for low momentum resonances. High momentum resonances are more likely escape the medium and hence may not be affected by re-scattering. Further the hadrons in the medium can scatter pseudo-elastically and re-generate some resonances in the medium (as shown in Fig. 1.19). Such re-generation process can increase the resonance yield. These competing processes, the re-scattering and re-generation, will decide the final yield of the resonance. The re-scattering and re-generation effect can be understood better through resonance to non-resonance ratio (such as  $K^{*0}/K^-$ ) in AA and pp collisions. A naive expectation of re-scattering and re-generation effect

on  $K^{*0}/K^-$  ratio is qualitatively shown in Fig. 1.20. If there is only re-scattering effect present in the hadronic phase of heavy ion collision, then this ratio should be smaller than pp collision and follow the blue line as a function of collision centrality. Thus the suppression in central collision should be more than peripheral collision. For re-generation only case the ratio should be above the pp measurement and follow the red line. The experimental measurement of collision centrality dependence  $K^{*0}/K^-$  ratio in heavy ion with respect to measurement in pp collisions is sensitive to the nature of the hadronic phase. Thus this ratio can be used to extract the lifetime of the hadronic phase in heavy ion collision.

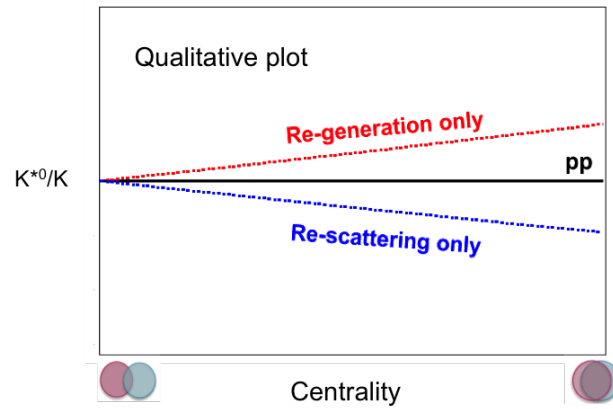


Figure 1.20: (Color online) Qualitative plot showing the effect of re-scattering and re-generation only processes on  $K^{*0}/K^-$  ratio in heavy ion collision with respect to pp collision.

In this thesis we will present the mass, invariant mass distribution width and yield of  $K^{*0}$  in Pb-Pb collisions at  $\sqrt{s_{NN}} = 2.76$  TeV and in pp collisions at  $\sqrt{s} = 2.76$  TeV. The mass and invariant mass width of  $K^{*0}$  may be affected by in-medium effects in heavy ion collision. Further due to the re-scattering or re-generation processes the  $p_T$  spectra and hence the mean transverse momentum ( $\langle p_T \rangle$ ) of the  $K^{*0}$  may be affected. The  $K^{*0} \langle p_T \rangle$  will be compared with other identified hadrons to understand such effect. The STAR experiment at RHIC have measured the production of  $K^{*0}$  resonance in Au-Au and Cu-Cu collisions at  $\sqrt{s_{NN}} = 62.4$  and 200 GeV [74, 75]. The observation at RHIC up to  $\sqrt{s_{NN}} = 200$  GeV suggests a dominance of re-scattering effect. The present reach of center of mass energy at LHC ( $\sqrt{s_{NN}} = 2.76$  TeV) is about

13 times more than that at RHIC. Thus the study of  $K^{*0}$  resonance at LHC energies will be very interesting. The measurement can shed light on the subject whether the re-scattering process will dominate at higher energies or the re-generation will come in to play a dominant role at higher energies.

The nuclear modification factor ( $R_{AA}$  and  $R_{CP}$ ) can be used to study the effect of strongly interacting medium formed in heavy ion collision. The  $R_{CP}$  of  $\Lambda$  baryon and  $K_S^0$  meson have been studied [74] and found to follow different trend as a function of  $p_T$ . It is not clear whether the difference is because of the mass or the species. The  $K_S^0$  is a vector meson and  $\Lambda$  a baryon while the  $K^{*0}$  is a vector meson but its mass is closer to the  $\Lambda$  baryon. Thus the  $K^{*0}$  will play a vital role in disentangling the mass and particle species dependence in nuclear modification factor.

Since the re-scattering and re-generation mostly affects low  $p_T$  particles, the  $v_2$  of  $K^{*0}$  may also be used to understand the effect of hadronic phase. In this thesis we will present the measurement of  $v_2$  of  $K^{*0}$  in Pb-Pb collisions at  $\sqrt{s_{NN}} = 2.76$  TeV.

The in-medium effects [3] on resonance properties (mass, invariant mass distribution width and yield) can also be understood by studying its production with respect to a jet or leading particle. The study of properties resonances in the same side and away side of a jet can distinguish between in-vacuum and in-medium effects, if the jets are assumed to be surfaced biased. The enhanced cross section of jets at LHC energies makes such study more promising. Since the  $K^{*0}$  meson have a small lifetime, it is expected to be affected by in-medium effects in heavy ion collisions. In this thesis we will present the results of  $K^{*0}$ -jet correlation in pp collisions at  $\sqrt{s} = 7$  TeV. This study can be used as a baseline for future analysis in heavy ion collisions.

## 1.9.2 Inclusive photon production in pp collisions at LHC energies

The measurement of inclusive photon production in high energy collisions is complementary to the charged hadron measurement. The inclusive photon at forward rapidity have been measured for a long time from lower SPS energies to RHIC and it

provided measurement of multiplicity, rapidity and azimuthal distributions of photons in lower energies [77]. The Fig. 1.21 shows the photon pseudorapidity distribution in different centrality classes at forward rapidity in Au-Au and Cu-Cu collision at  $\sqrt{s_{NN}} = 62.4$  [78] and 200 GeV [79] measured in STAR experiment at RHIC. The Fig. 1.22 describes the limiting fragmentation behavior of inclusive photons and charged particles which shows an energy dependent limiting fragmentation behavior. The Photon Multiplicity Detector (PMD) [27] was build and installed in the ALICE at the LHC to study the behavior of photons at forward rapidities. The measurement at forward rapidity extends our knowledge of particle production towards higher rapidities. The

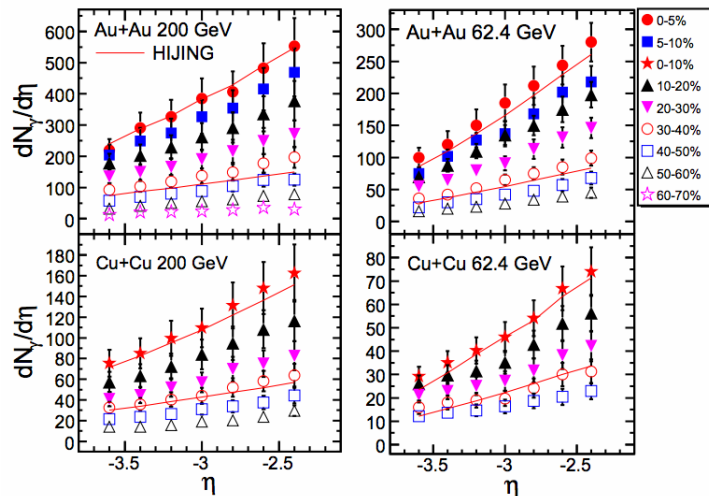


Figure 1.21: (Color online) Photon pseudorapidity distribution in Au-Au collisions at  $\sqrt{s} = 200$  GeV measured in STAR experiment [79].

ALICE has taken data in pp collisions in center of mass energies of 0.9 and 2.36 and 7 TeV [53]. The mean multiplicity at mid-rapidity have been observed to increase as  $s^{0.11}$  with the beam energy ( $s$ ). The left panel of Fig 1.23 represents the charged hadron multiplicity distribution (at central rapidity) and the right panel the pseudorapidity distribution for pp collisions measured in ALICE at  $\sqrt{s} = 0.9$  TeV. The multiplicity distribution is explained by the PHOJET model above multiplicity 10, whereas the PYTHIA tunes are not able to describe the distribution. The pseudora-

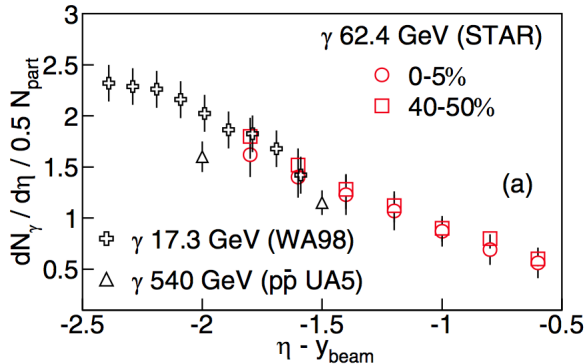


Figure 1.22: (Color online) Scaling of photon pseudorapidity distribution in Au-Au collisions at  $\sqrt{s} = 62.4$  GeV in STAR experiment [78].

pidity distribution measured in ALICE are comparable to the measurement done by other experiments UA5 [81] and CMS [82].

In this thesis, we will present the measurement of photon multiplicity and pseudorapidity distribution at forward pseudorapidity in pp collisions at  $\sqrt{s} = 0.9$  TeV. The measurement of inclusive photons from PMD ( $2.3 < \eta < 3.9$ ) will extend the mid-rapidity measurement by 1.6 unit in  $\eta$ . The measurement will be compared with event generators like PYTHIA and PHOJET. Such comparison of photon multiplicity and pseudorapidity distributions can be used to constraint the underlying physics in the event generators. The photon multiplicity measurement at  $\sqrt{s} = 0.9$  TeV along with that at 2.76 and 7 TeV will be used to study the KNO-scaling behavior at forward rapidities. The multiplicity distribution will be fitted to NBD and double NBD functions to extract the contribution from soft and hard processes in photon production. The mean multiplicity will be used to find the energy dependence of average photon multiplicity at forward pseudorapidity. Finally the pseudorapidity distribution will be used to study the limiting fragmentation behavior of photons.

### 1.9.3 Energy dependence of anti-proton to proton ratio

The ratio of anti-proton to proton can be used to probe the mechanism baryon production and baryon number transport. Recently the ALICE has measured the  $\bar{p}/p$

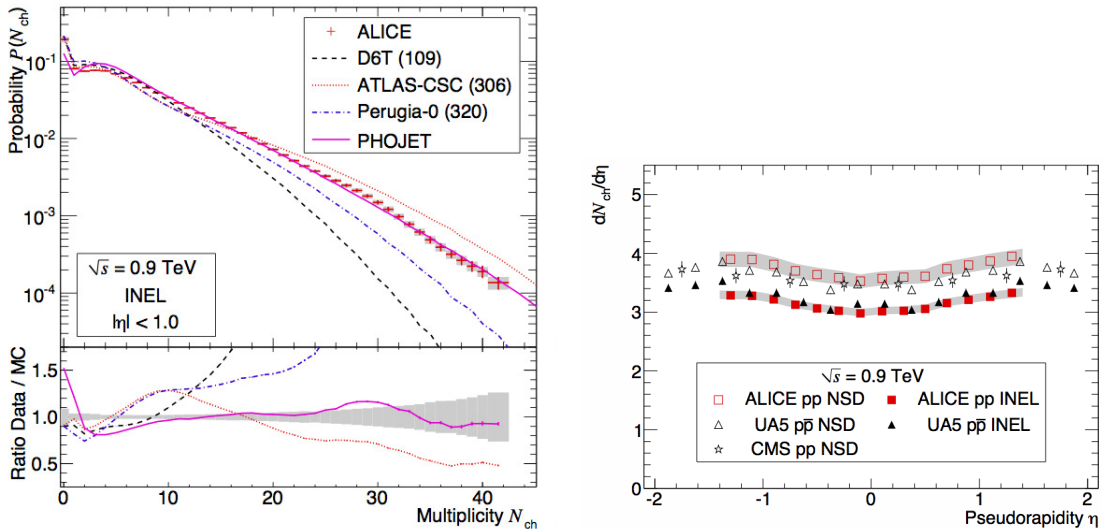


Figure 1.23: (Color online) Left panel: Charged hadron multiplicity in pp collisions at  $\sqrt{s} = 0.9$  TeV measured in ALICE [53]. Right panel: measurement of pseudorapidity distribution of charged hadrons in ALICE [53], UA5 [81] and CMS [82].

ratio in pp collisions at  $\sqrt{s} = 0.9, 2.76$  and  $7$  TeV [84]. The comparison of the measurement  $\bar{p}/p$  ratio in data to various models can enhance our knowledge of baryon production. In this thesis, we have compiled  $\bar{p}/p$  ratio measured at  $\sqrt{s} = 23, 31, 45, 53$  GeV at ISR [85],  $\sqrt{s} = 62.4$  and  $200$  GeV at RHIC [86] and  $\sqrt{s} = 0.9, 2.76$  and  $7$  TeV at the LHC and compared the results with the predictions from models like PYTHIA, PHOJET and HIJING B- $\bar{B}$ . The baryon production are not similar in these models. This study will help in understanding the baryon production mechanism and baryon transport at mid-rapidity in high energy collisions.

## 1.10 Organization of the thesis

The work presented in this thesis deals with the data taken by ALICE at the LHC. Also it contains phenomenological works with various models to support physics observations in experimental data. The Chapter 1 gives an introduction to the heavy ion collisions and motivation for the present study to understand the particle production

at LHC energies. The Chapter 2 gives a brief description of the experimental setup of the ALICE detector at the CERN LHC with special emphasis on detectors like TPC and PMD used in the analysis of data presented in this thesis. In Chapter 3 we have presented the results of mass, invariant mass distribution width, transverse momentum spectra, invariant yield and mean transverse momentum of  $K^{*0}$  meson in Pb-Pb collisions at  $\sqrt{s_{NN}} = 2.76$  TeV and pp collisions at  $\sqrt{s} = 2.76$  TeV. Further the particle ratios relative to kaon and nuclear modification factors are estimated from the measurement. In Chapter 4 we studied AMPT model to demonstrate the effect of hadronic phase on  $K^{*0}$  production in heavy ion collision. The Chapter 5 gives the preliminary results of elliptic flow measurement of  $K^{*0}$  in Pb-Pb collisions at  $\sqrt{s_{NN}} = 2.76$  TeV. In Chapter 6 we studied another interesting analysis of  $K^{*0}$ -hadron correlation in pp collisions at  $\sqrt{s} = 7$  TeV. This will form the baseline for similar measurements in Pb-Pb collisions in future. In Chapter 7, we present the first measurement of photon multiplicity and pseudorapidity distribution in pp collisions at  $\sqrt{s} = 0.9$  TeV using the data collected by the PMD in ALICE. We discussed the method of unfolding employed to correct the detector acceptance and efficiency. The inclusive photon multiplicity distributions will be compared to several models to understand the underlying physics mechanism. The Chapter 8 discusses the study of anti-proton to proton ratio in pp collisions using various models. Finally the chapter 9 gives a summary of this thesis.

# Bibliography

- [1] David Griffiths, Introduction to Elementary Particles, Wiley-Vch.
- [2] S. L. Glashow, Nucl. Phys. 22, 579 (1961).
- [3] A. Salam and J.C. Ward, Phys. Lett. 13, 168 (1964).
- [4] S. Weinberg, Phys. Rev. Lett. 19, 1264 (1967).
- [5] CERN document server: cds.cern.ch
- [6] P. W. Higgs, Phys. Lett. 12, 132 (1964); P. W. Higgs, Phys. Rev. Lett. 13, 508 (1964).
- [7] F. Englert and R. Brout, Phys. Rev. Lett. 13, 321 (1964).
- [8] G. Aad *et al.* (ATLAS Collaboration), Phys. Lett B 716, 1 (2012).
- [9] W. Adam *et al.* (CMS Collaboration), Phys. Lett B 716, 30 (2012).
- [10] D. J. Gross, F. Wilczek, Phys. Rev. Lett. 30, 1343 (1973); H.D. Politzer, Phys. Rev. Lett. 30, 1346 (1973).
- [11] K. G. Wilson, Phys. Rev. D 10, 2445 (1974).
- [12] Report of the Workshop on BeV/nucleon Collisions of Heavy Ions- How and Why, Bear Mountain, New York, Nov. 29 - Dec 1, 1974 (BNL-AUI, 1975); T. D. Lee and G. C. Wick, Phys. Rev. D9 2291 (1974).
- [13] R. Rapp and E. Shuryak, Phys. Rev. Lett. 86, 2980 (2001).

- [14] F. Karsch, Nucl. Phys. A 698, 199 (2002).
- [15] R. V. Gavai and S. Gupta Phys. Rev. D 71, 114014 (2005).
- [16] The Frontiers of Nuclear Science, 2007 NSAC Long Range Plan:  
<http://www.sc.doe.gov/np/nsac/docs/Nuclear-Science.Low-Res.pdf>
- [17] G. E. Brown and M. Rho, Phys. Rev. Lett. 66, 2720 (1991).
- [18] M. A. Stephanov, Phys. Rev. Lett. 102, 032301 (2009); M. Cheng *et al.*, phys. Rev. D 79, 074505 (2009).
- [19] Models and Data Analysis Initiative (MADAI) <https://madai-public.cs.unc.edu/>
- [20] E. Schnedermann, J. Sollfrank and U. Heinz, Phys. Rev. C 48, 2462 (1993).
- [21] B. Abelev *et al.* (ALICE Collaboration), Phys. Rev. Lett. 109, 252301 (2012).
- [22] J. Adams *et al.* (STAR Collaboration), Nucl. Phys. A 757, 102 (2005).
- [23] J. Stachel, A. Andronic, P. Braun-Munzinger, K. Redlich, J. Phys.: Conf. Ser. 509, 012019 (2014).
- [24] M. Petran and J. Rafelski, Phys. Rev. C 88, 021901 (2013).
- [25] S. Chatterjee, R. M. Godbole and S. Gupta, Phys. Lett. B 727, 554 (2013).
- [26] J. D. Bjorken. Energy loss of energetic partons in quark-gluon plasma: Possible extinction of high momentum jets in hadron - hadron collisions. FERMILAB-PUB-82-059-THY; M. Gyulassy and M. Plumer, Phys. Lett. B 243, 432 (1990).
- [27] J. Adams *et al.* (STAR Collaboration), Nucl. Phys. A 757,102 (2005).
- [28] G. Aad *et al.* (ATLAS Collaboration), Phys. Rev. Lett. 105, 252303 (2010).
- [29] K. Aamodt, *et al.*, (ALICE Collaboration), Phys. Lett. B 696, 30, (2011).
- [30] J. Adams, *et al.*, STAR Collaboration, Phys. Rev. Lett. 91 172302, (2003).
- [31] S. S. Adler, *et al.*, (PHENIX Collaboration), Phys. Rev. C 69, 034910 (2004).

- [32] B. Abelev, *et al.*, (ALICE Collaboration), Phys. Rev. Lett. 110, 082302 (2013).
- [33] T. Matsui and H. Satz, Phys. Lett. B 178, 416 (1986).
- [34] B. Abelev, *et al.*, (ALICE Collaboration), Phys. Rev. Lett. 109, 072301 (2012).
- [35] A. Adare, *et al.* (PHENIX Collaboration), Phys. Rev. Lett. 98, 232301 (2007);  
A. Adare, *et al.* (PHENIX Collaboration), Phys. Rev. C84, 054912 (2011); S. S.  
Adler, *et al.* (PHENIX Collaboration), Phys. Rev. C 71, 049901 (2005).
- [36] P. Koch, B. Muller and J. Rafelski, Phys. Rept. 142, 167 (1986).
- [37] B. Abelev *et al.* (ALICE Collaboration), Phys. Lett. B 728, 216 (2013), (erratum  
in preparation); B. Abelev *et al.* (ALICE Collaboration), Phys. Rev. Lett. 111,  
222301 (2013).
- [38] F. Antinori, *et al.*, (NA57 Collaboration), J. Phys. G 32, 427 (2006); F. Antinori,  
*et al.*, (NA57 Collaboration), J. Phys. G 37, 045105 (2010).
- [39] B. I. Abelev, *et al.*, (STAR Collaboration), Phys. Rev. C 77 044908, (2008).
- [40] A. Tounsi, A. Mischke and K. Redlich, Nucl. Phys. A 715, 565 (2003).
- [41] J. Y. Ollitrault, Phys. Rev. D 46, 229 (1992).
- [42] S. Voloshin and Y. Zhang, Z. Phys. C 70, 665 (1996).
- [43] A. M. Poskanzer and S. A. Voloshin, Phys. Rev. C 58, 1671 (1998).
- [44] K. Aamodt, *et al.* (ALICE Collaboration), Phys. Rev. Lett. 105, 252302 (2010);  
ALICE Collaboration, arXiv:1405.4632.
- [45] J. Adams, *et al.* (STAR Collaboration), Phys. Rev. C 72, 014904 (2005).
- [46] A. Adare, *et al.* (PHENIX Collaboration), Phys. Rev. C 85, 064914 (2012).
- [47] S. Nussinov, Phys. Rev. Lett. 34, 1286 (1975); S. Nussinov, Phys. Rev. D 14, 246  
(1976).

- [48] J. F. Grosse-Oetringhaus, PhD thesis, University of Munster, Germany, (2009).
- [49] UA5 Collaboration, Phys. Lett. B 160, 193 (1985); UA5 Collaboration, Z. Phys. C 32, 153 (1986).
- [50] A. Giovannini and R. Ugoccioni, Phys. Rev. D 59, 094020 (1999) [Erratum-ibid. D 69 (2004) 059903].
- [51] R. P. Feynman, Phys. Rev. Lett. 23 (1969) 1415.
- [52] Z. Koba, H. B. Nielsen and P. Olesen, Nucl. Phys. B 40, 317 (1972).
- [53] K. Aamodt *et al.* (ALICE Collaboration), Eur. Phys. J C 65, 111 (2010); K. Aamodt *et al.* (ALICE Collaboration), Eur. Phys. J C 68, 89 (2010).
- [54] J. Benecke, T.T. Chou, C.N. Yang and E. Yen, Phys. Rev. 188, 2159 (1969).
- [55] A. K. Dash, PhD thesis, (<http://www.hbni.ac.in/phdthesis/11phdthesis.htm>).
- [56] T. Sjostrand, Comput. Phys. Commun. 82, 74 (1994).
- [57] T. Sjostrand, S. Mrenna, P. Skands, J. High Energy Phys., 05, 026 (2006).
- [58] PYTHIA 6.4, Physics and Manual, hep-ph/0603175, FERMILAB-PUB-06-052-CD-T, March (2006).
- [59] R. Engel, Z. Phys. C 66, 203 (1995).
- [60] R. Engel, J. Ranft, S. Roesler, Phys. Rev. D 52, 1459 (1995).
- [61] A. Capella *et al.*, Phys. Lett. 81B(1), 68 (1979); A. Capella and J. T. T. Van, Phys. Lett. 93B (1,2), 146 (1980); A. Capella and J. T. T. Van, Z. Phys. C 10, 249 (1981); A. Capella *et al.* Phys. Rep. 236(4,5), 225 (1994).
- [62] M. Gyulassy, X. N. Wang, Phys. Rev. C80, 024906 (2009).
- [63] D. Kharzeev, Phys. Lett. B 378, 238 (1996).

- [64] G. C. Rossi, G. Veneziano, Nucl. Phys. B 123, 507 (1977); Phys. Rep. 63, 153 (1980).
- [65] S. E. Vance, M. Gyulassy and X. N. Wang, Phys. Lett. B 443, 45 (1998).
- [66] Boris Kopeliovich and Bogdan Povh, Phys. Lett. B 446, 321 (1999).
- [67] B. Zhang, C. M. Ko, B. A. Li and Z. Lin, Phys. Rev. C 61, 067901 (2000).
- [68] B. Zhang, Comp. Phys. Comm. 109, 193 (1998).
- [69] B. A. Li and C. M. Ko, Phys. Rev. C 52, 2037 (1995).
- [70] J. Beringer *et al.* (Particle Data Group), Phys. Rev. D 86, 01001 (2012).
- [71] S. D. Protopopescu, M. Alston-Garnjost, A. Barbaro-Galtieri, S. M. Flatte, J. H. Friedman, T. A. Lasinski, G. R. Lynch and M. S. Rabin *et al.*, Phys. Rev. D 7, 1279 (1973).
- [72] M. J. Matison, A. Barbaro-Galtieri, M. Alston-Garnjost, S. M. Flatte, J. H. Friedman, G. R. Lynch, M. S. Rabin and F. T. Solmitz, Phys. Rev. D 9, 1872 (1974).
- [73] M. Bleicher *et al.* J. Phys. G 25, 1859 (1999).
- [74] J. Adams *et al.* (STAR Collaboration), Phys. Rev. C 71, 064902 (2005); M. M. Aggarwal *et al.* (STAR Collaboration), Phys. Rev. C 84, 034909 (2011).
- [75]  $K^*(892)$  resonance production in Au+Au and p+p collisions at the relativistic heavy ion collider. PhD thesis of Hibin Zhang, Yale University (2004) for STAR Collaboration; Study of  $K^{*0}$  resonance production in relativistic heavy ion collision at RHIC. PhD thesis of Sadhana Dash, HBNI (2010) for STAR Collaboration.
- [76] C. Markert *et al.*, Phys. Lett. B, 669 (2008).
- [77] B. Mohanty, Pramana J. of Physics 60, 613 (2003).

- [78] J. Adams *et al.* (STAR Collaboration), Phys. Rev. Lett. 95, 062301 (2005); B. Back *et al.* (PHOBOS Collaboration), Phys. Rev. Lett. 91, 052303 (2003).
- [79] B. I. Abelev, *et al.*, (STAR Collaboration), Nucl Phys A 832 (2010).
- [80] ALICE Technical Design Report of PMD, CERN /LHCC 2003nn ALICE TDR nn (August 2003).
- [81] G. J. Alner *et al.* (UA5 Collaboration), Z. Phys. C 33, 1 (1986).
- [82] V. Khachatryan *et al.* (CMS Collaboration), Phys. Rev. Lett. 105, 022002 (2010).
- [83] G. Aad *et al.* (ATLAS Collaboration), Phys. Lett. B 688, 21 (2010).
- [84] K. Aamodt *et al.*, (ALICE Collaboration) arXiv:1006.5432.
- [85] British-Scandinavian Collaboration, B. Alper *et al.*, Nucl. Phys. B 100, 237 (1975).
- [86] STAR Collaboration, B.I. Abelev *et al.*, Phys. Rev. C 81, 024911 (2010)and the references therein; BRAHMS Collaboration, I. G. Bearden *et al.*, Phys. Rev. Lett. 93, 102301 (2004).
- [87] Steven Weinberg, The First Three Minutes: A Modern View of the Origin of the Universe, Basic Books, 1977.
- [88] C. Y. Wong, Introduction to High Energy Heavy Ion Collisions, World Scientific.

# Chapter 2

## The Experimental Setup

### 2.1 Large Hadron Collider at CERN

The Large Hadron Collider (LHC) at CERN [1, 2, 3] is the largest and most powerful particle accelerator in the world. It was installed in a 27 km long underground tunnel at depth of about 50 - 150 m across the Switzerland and France border. The LHC is divided into eight octants ( Fig. 2.1 ) and each octant contain 154 dipole magnets. The particles are injected to the LHC ring from the point 2 and point 8. The radio frequency system (RF) accelerates the beam at the point 4. The beam crosses only at four points 1, 2, 5 and 8. The beam dumping system is located at point 6. At point 3 and 7, the collimation system cleans the beam by removing the particles that have either too large spatial spread from the bunch center are too fast or too slow. Cleaning prevents the particles from being lost in an uncontrolled fashion within the accelerator.

The protons (or the ions) are produced at LINAC 2 (or LINAC 3) and then it enters into the BOOSTER (LIER) which is 157 m in circumference. The BOOSTER (LIER) can accelerate proton (ion) beam up to the energy of 1.4 MeV (72 MeV/nucleon). Then the beam is sent to the Proton Synchrotron (PS) which is 628 m in circumfer-

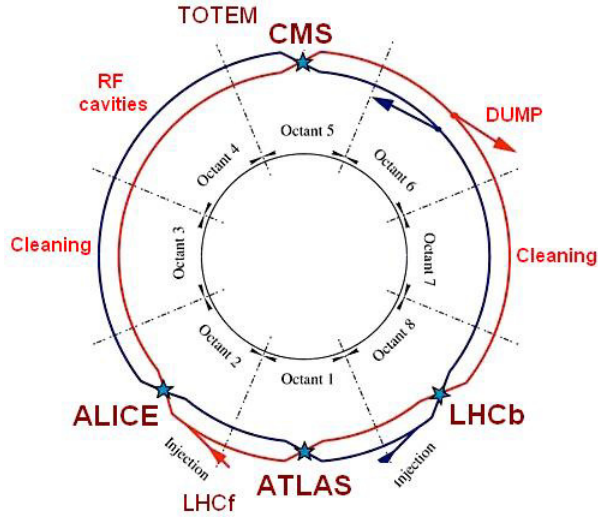


Figure 2.1: (Color online) Octants of LHC.

ence and the energy of each protons (ions) reach up to 25 GeV (5.9 GeV/nucleon). The packet of protons (ions) are then channel into the Super Proton Synchrotron (SPS), 7 km in circumference, for further acceleration. At SPS the energy of protons (ions) can reach up to 450 GeV (177 GeV/nucleon). The protons (ions) are then split into bunches going in either direction of the LHC main ring. Here the protons (or ions) are accelerated to the desired energies. The schematic diagram of the CERN accelerator complex is shown in Fig. 2.2. The LHC is designed to collide two proton beams up to a center of mass energy of 14 TeV and two heavy ions up to 5.5 TeV per nucleon. There are six parallel experimental setup installed at the LHC, namely A Large Ion Collider Experiment (ALICE) [4], A Toroidal LHC ApparatuS (ATLAS) [5], Compact Muon Solenoid (CMS) [6], Large Hadron Collider beauty (LHCb) [7], Large Hadron Collider forward (LHCf) [8] and TOTAl Elastic and diffractive cross section Measurement (TOTEM) [9] experiment. The ALICE [4, 10] is specialized for heavy-ion collision experiment. The aim of the ALICE is to explore the properties of a strongly interacting matter, called Quark Gluon Plasma (QGP) [11], formed under extreme temperature and energy densities. The ALICE can also study the proton-proton collisions, which acts as a baseline for the heavy-ion measurements. This thesis is based on the ALICE experiment and the details will be described in

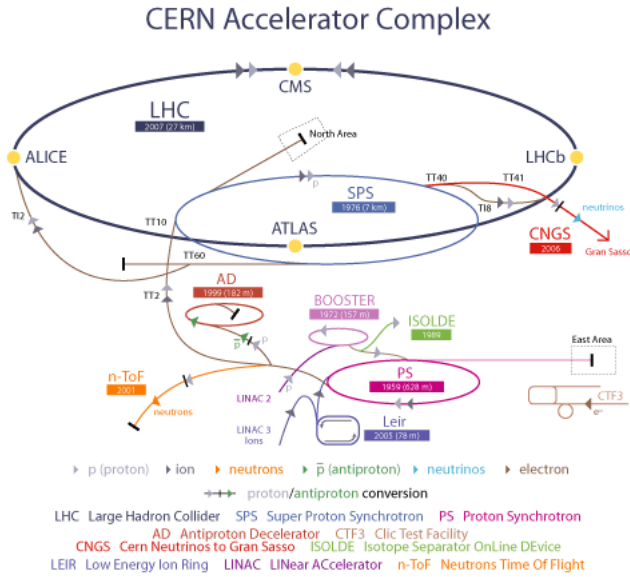


Figure 2.2: (Color online) CERN accelerator complex at the LHC.

the next section.

ATLAS and CMS are the experiments dominantly for the purpose of wide range of physics in proton-proton collisions. The aim of these experiments is to search for the Higgs boson, physics beyond Standard Model, e.g. search for Super Symmetric particles (SUSY), evidence of extra dimensions etc. The LHCb experiment focusses on the physics of CP violation in the heavy b-quark system. The LHCf experiment studies the production of particles very close to the beam direction (forward rapidity) in proton-proton collisions. The TOTEM experiment measures total cross section, elastic scattering and diffractive processes in proton-proton collisions.

## 2.2 ALICE at the LHC

A Large Ion Collider Experiment (ALICE) at CERN LHC is an experiment dedicated to the heavy-ion collisions to study the strongly interacting matter at extreme energy densities produced in such collisions. The ALICE detector (Fig. 2.3) is installed within a L3 magnet (taken from the LEP experiment) of maximal strength of 0.5 T. The ALICE detector has a dimension  $16 \times 16 \times 26 \text{ m}^3$  and weight approximately 10,000

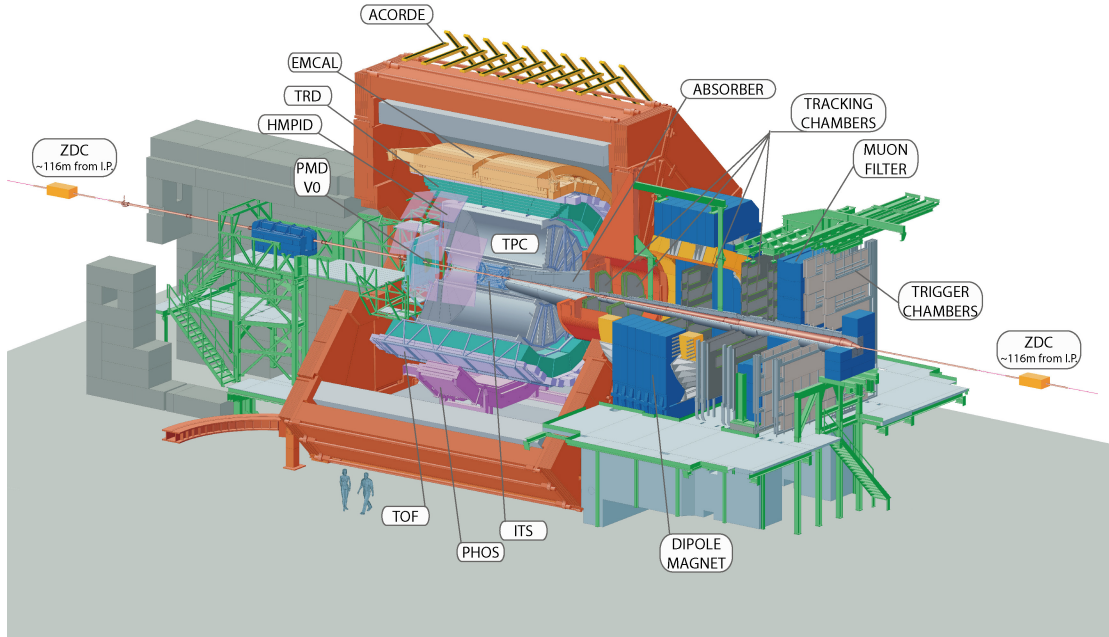


Figure 2.3: (Color online) Schematic diagram of the ALICE detector.

t. The co-ordinate system of ALICE detector is shown in Fig. 2.4. The interaction point (IP) is at the origin  $(0, 0, 0)$ . The X-axis lying along the horizontal plane of the ALICE detector. The Y-axis, which is perpendicular to the X-axis and beam direction, pointing upwards. The Z-axis is along the beam direction. The polar angle  $\theta$  increases from  $-Z$  to  $+Z$  direction and the azimuthal angle  $\varphi$  increases clockwise from X-axis, passing through Y-axis and finally back to X-axis. This is for an observer standing at negative Z and looking towards the IP. The ALICE consists of a central barrel, a muon spectrometer and forward detectors. It has an efficient and robust tracking system over a large momentum starting from  $100 \text{ MeV}/c$  to  $100 \text{ GeV}/c$ , which allows to study over a regime of soft physics ( $p_T < 2 \text{ GeV}/c$ ) to intermediate  $p_T$  and jets regime ( $p_T > 10 \text{ GeV}/c$ ). This is achieved because of very low material budget to reduce multiple scattering at low  $p_T$ . The main feature of the ALICE detector is its excellent capability of particle identification using specific energy loss, time of flight, transition and Cherenkov radiation, electromagnetic calorimetry and muon

spectrometry. The Fig. 2.5 demonstrates the momentum ranges in which different detectors are able to identify different particles. The pion-kaon and proton-kaon separation can be achieved using the detectors Inner Tracking System (ITS), Time Projection Chamber (TPC), Time Of Flight (TOF) and High Momentum Particle Identification (HMPID) [7].

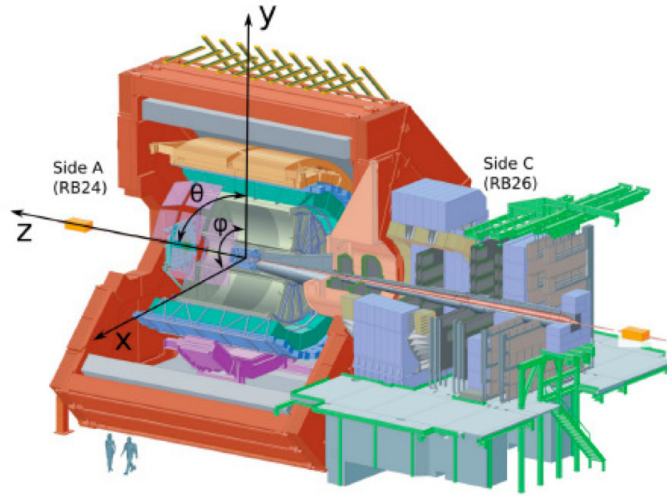


Figure 2.4: (Color online) The Co-ordinate system of ALICE detector.

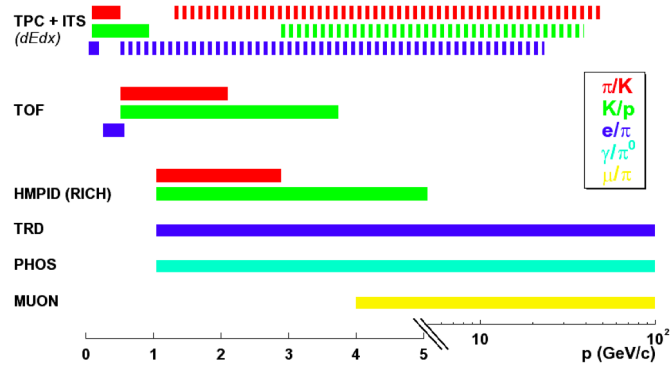


Figure 2.5: (Color online) Momentum ranges in which different detectors are able to identify different particles.

A summary of all the sub-detectors is given in Table 2.1. In this thesis, the minimum bias events are selected by using a combination of VZERO and Silicon Pixel

Detector (SPD). The multiplicity measured by VZERO is used for the estimation of centrality in Pb-Pb collisions. The primary vertex is reconstructed with the information of hits in ITS and TPC. These detectors (ITS and TPC) are also used for reconstructing the tracks. Further for the identification of charged hadrons the TPC and TOF are used. The PMD is used to identify event by event spatial distribution of photons.

Detectors	Position (cm)	Acceptance ( $\eta$ )	Acceptance ( $\phi$ )	technology	purpose
SPD (layer1, 2)	3.9, 7.6	$\pm 2, \pm 1.4$	full	Si Pixel	tracking, vertex
SDD (layer 3, 4)	15.0, 23.9	$\pm 0.9, \pm 0.9$	full	Si drift	tracking, PID
SSD (layer 5, 6)	38, 43	$\pm 0.97, \pm 0.1$	full	Si strip	tracking, PID
TPC (IORC, OROC)	85, 247	$\pm 0.9$	full	Ne drift, MWPC	tracking, PID
TRD	290, 368	$\pm 0.8$	full	TR, Xe drift, MWPC	tracking, $e^\pm$ id
TOF	370, 399	$\pm 0.9$	full	MRPC	PID
PHOS	460, 478	$\pm 0.12$	220, 320	PbWO <sub>4</sub>	photons
EMCAL	430, 455	$\pm 0.7$	80, 187	Pb, scint	photons, jets
HMPID	490	$\pm 0.6$	1, 59	C <sub>6</sub> F <sub>14</sub> , <i>RICH</i> , <i>MWPC</i>	PID
ACORDE	850	$\pm 1.3$	30, 150	scint.	cosmics
FMD	320	$3.6 < \eta < 5.0$	full	Si strip	charged particle
	80	$1.7 < \eta < 3.7$	full	Si strip	
	-70	$-3.4 < \eta < -1.7$	full	Si strip	
PMD	367	$2.3 < \eta < 3.9$	full	Pb+PC	photons
ZDC	$\pm 113$ m	$\eta > 8.8$	full	W+quartz	forward neutrons
	$\pm 113$ m	$6.5 < \eta < 7.5$	$\phi < 10$	brass, quartz	forward protons
	7.3 m	$4.8 < \eta < 5.7$	$\phi < 32$	Pb, quartz	photons
V0	340	$2.8 < \eta < 5.1$	full	scint.	time, vertex
	-90	$-3.7 < \eta < -1.7$	full	scint.	
T0	370	$4.6 < \eta < 4.9$	full	quartz	time, vertex
	-70	$-3.3 < \eta < -3.0$	full	quartz	
MCH	-14.2, -5.4 m	$-4.0 < \eta < -2.5$	full	MWPC	muon tracking
MTR	-17.1, 16.1 m	$-4.0 < \eta < -2.5$	full	RPC	muon trigger

Table 2.1: Summary of sub-detectors of ALICE [7].

## 2.3 Central Barrel Detectors

The central barrel is embedded in the large L3 solenoidal magnet and it covers the polar angle  $45^\circ$  to  $135^\circ$  ( $|\eta| < 0.9$ ) over the full azimuth. It consists of an Inner Tracking System (ITS) [13], Time Projection Chamber (TPC) [14], Transition Radiation Detectors (TRD) [15], Time Of Flight (TOF) detectors [16], Cherenkov counters (HMPID) [17], Photon Spectrometer (PHOS) [18], Electro Magnetic Calorimeter (EMCAL) [19] and the ALICE Cosmic Ray Detector (ACORDE) [20]

### 2.3.1 Inner Tracking System (ITS)

The Inner Tracking System (ITS) [13] has six cylindrical layers of high resolution position sensitive silicon based detectors. Starting from the beam pipe radially outwards it consist of two Silicon Pixel Detectors (SPD), two Silicon Drift Detectors (SDD) and two Silicon Strip Detectors (SSD) as shown in Fig. 2.6. The ITS provides precise information of primary and secondary vertices. Also it could provide particle identification at small transverse momenta with resolution 10-12%.

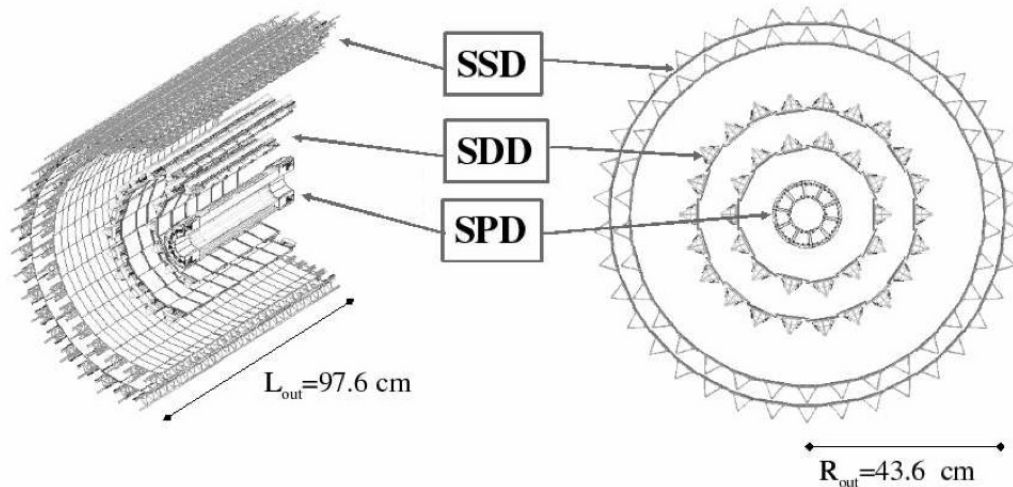


Figure 2.6: Layout of ITS detector [10].

The SPD is the inner most detector in the ITS. It plays an important role in the determination of primary and secondary vertex. It can operate at very high track densities about  $50 \text{ tracks}/\text{cm}^3$  and relatively high radiation levels. The basic component of SPD are the hybrid silicon pixels in the form of a two dimensional matrix of reverse-biased silicon detector diodes. Each diode is connected through a conductive solder bump to a contact on a read out chip that corresponds to the input of readout cell. The SPD contains 1200 readout pixel chips and a total of  $10^7$  cells. The SPD is also capable of generating a prompt trigger based on an internal Fast-OR. Each pixel chip provides a Fast-OR digital pulse whenever a pixel or a group of them detects a particle signal above the threshold.

The SDD are the two intermediate layers (3rd and 4th) of the ITS. On the 3rd layer of ITS there are 14 ladders with 6 modules each and on the 4th layer there are 22 ladders with 8 modules. The ladders and modules are assembled in order to ensure a full angular coverage. It can give high precision position information (a position resolution of  $35 \mu\text{m}$ ) and the information of the energy loss ( $dE/dx$ ) which can be used for particle identification.

The SSD's are the outermost layers of the ITS. It is very crucial in matching the tracks from the TPC to the ITS. The SSD is composed of 1698 modules, each one consist of a 1536 strip double sided silicon sensor connected through a aluminium kapton micro-cables to the front end electronics. It can provide a two dimensional measurement of the track position. In addition it can provide the  $dE/dx$  information.

### 2.3.2 Time Projection Chamber (TPC)

The TPC [14] is the heart of the ALICE detector. It is used for track reconstruction and particle identification. The TPC (Fig. 2.7) has a cylindrical shape of length 5 m with an inner and outer radius of approximately 80 and 250 cm respectively. In between the inner and outer containment vessel, it has a mixture of  $\text{Ne}/\text{CO}_2/\text{N}_2$  (90%/10%/5%) gas with an active volume of  $90 \text{ m}^3$  and a high voltage drift electrode in the center. The drift electrode is kept at a voltage of 100 kV and it divides the gas volume in two regions with a length of 250 cm each. This results in a drift field of 400

V/cm. For the signal readout Multi Wire Proportional Chambers (MWPC) at the end plates are used. Each of the two endplates has 36 readout chambers arranged in 18 sectors. Each sector contains an Inner Readout Chamber (IROC) and an Outer Readout Chamber (OROC).

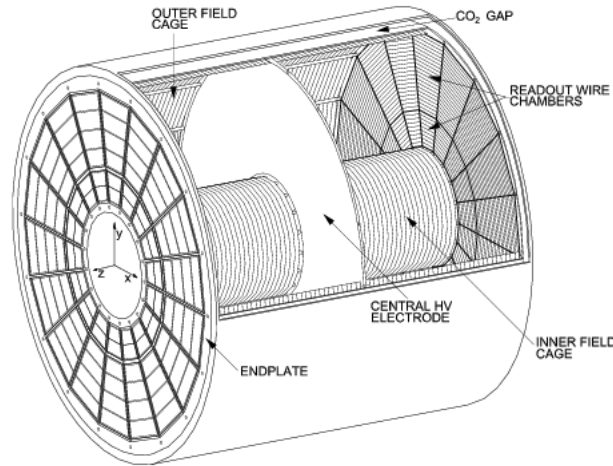


Figure 2.7: Layout of TPC [10].

The working principle of TPC is schematically shown in Fig. 2.8. As the charged particles traverse through the gas of TPC, it ionizes the gas. The electrons created by the ionization drifts along the electric field. The magnetic field is oriented parallel to the electric field and thus the drifting electrons are not influenced by it. At the end of drift path, the electrons are amplified by an avalanche process around the anode wires.

From 3-dimensional space points, the tracks can be reconstructed in TPC and the transverse momentum can be obtained from the curvature of the track. The TPC can reconstruct a primary track of momentum 100 MeV/c up to 100 GeV/c. The Fig. 2.9 shows the tracks reconstructed in TPC in Pb-Pb collisions at  $\sqrt{s_{NN}} = 2.76$  TeV during 2010. Another important task of TPC is to provide particle identification. The particle identification is performed by the simultaneous measurement of the specific energy loss, charge and momentum of each particle that traverse through the detector. The energy loss in TPC is described by the Bethe-Bloch formula which

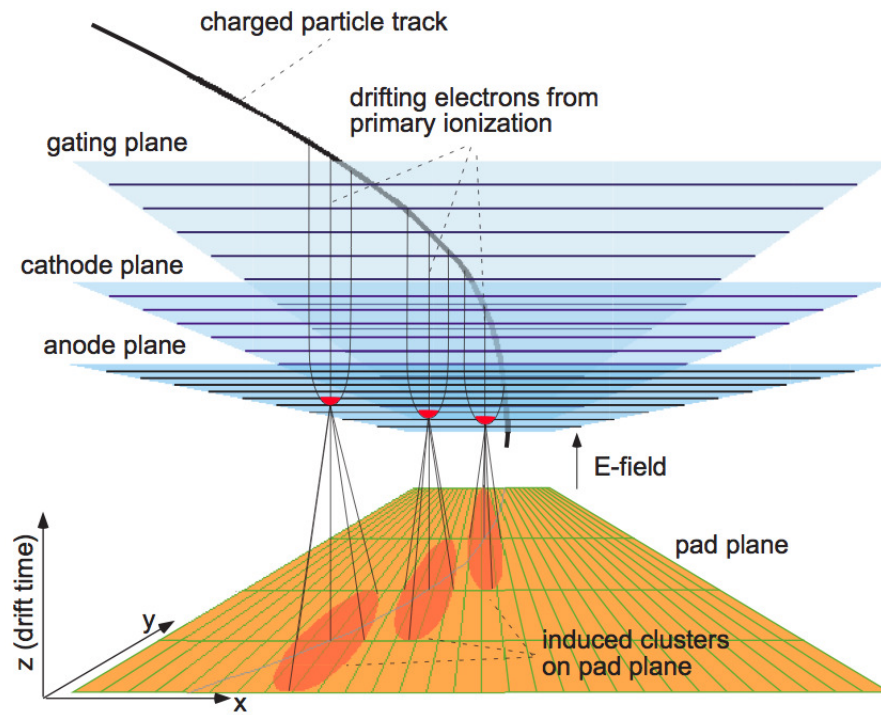


Figure 2.8: (Color online) Working principle of TPC [21].



Figure 2.9: (Color online) Event display of the tracks reconstructed inside TPC in Pb-Pb collisions at  $\sqrt{s_{NN}} = 2.76$  TeV during 2010.

is parameterized by a function originally proposed by ALEPH collaboration [6].

$$f(\beta\gamma) = \frac{P_1}{\beta^{P_4}} (P_2 - \beta^{P_4} - \ln(p_3 + \frac{1}{(\beta\gamma)^{P_5}})), \quad (2.1)$$

where  $P_1$  to  $P_5$  are the fit parameters extracted for each data taking period [23].  $\beta$  is the particle velocity and  $\gamma$  is the Lorentz factor. The Fig. 2.10 shows the  $dE/dx$  vs momentum in Pb-Pb collisions at  $\sqrt{s_{NN}} = 2.76$  TeV measured in the TPC. The lines corresponds to the parameterization 2.1 ( $dE/dx_{expected}$ ). At low  $p_T$  ( $< 1$  GeV/c), the

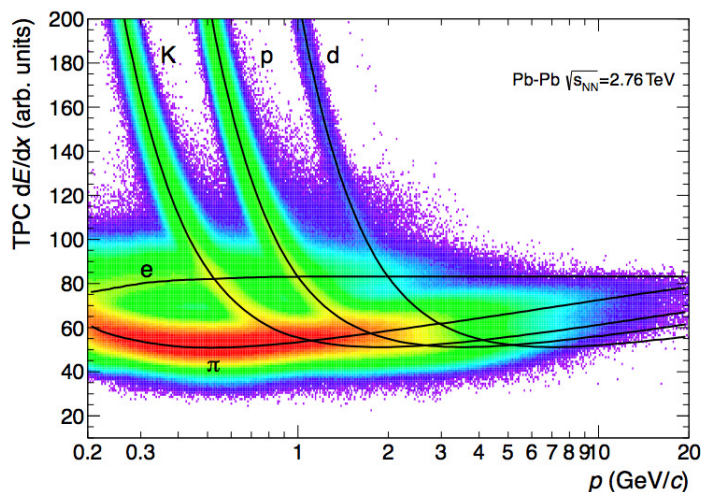


Figure 2.10: (Color online) The measurement of energy loss  $dE/dx$  vs momentum using TPC in Pb-Pb collisions at  $\sqrt{s_{NN}} = 2.76$  TeV [7].

particles can be identified on a track by track basis, while at higher momenta particles can be separated on a statistical basis via multi-gaussian fits to the difference between the  $dE/dx$  measured and  $dE/dx$  parameterized by 2.1 ( $dE/dx_{measured} - dE/dx_{expected}$ ). Another approach to identify the particles is via an  $N\sigma$  cut, which is defined in terms of resolution as,

$$N\sigma_{TPC} = \frac{dE/dx_{measured} - dE/dx_{expected}}{\sigma_{TPC}^{PID}} \quad (2.2)$$

where

- $dE/dx_{measured}$  is the energy loss of the tracks measured in TPC;
- $dE/dx_{expected}$  is the expected energy loss of the tracks using a parameterization of modified Bethe Bloch function [6, 7];

–  $\sigma_{TPC}^{PID}$  PID resolution of the TPC which is about 5.2% in pp collisions and 6.5% in central Pb–Pb collisions.

### 2.3.3 Transition Radiation Detector (TRD)

The TRD [15] consist of a radiator and Multi Wire Proportional Chamber (MWPC) placed around the TPC at radial distance of 2.9 to 3.68 m ( $|\eta| < 0.84$ ) over the full azimuthal angle. It was installed in ALICE to improve the electron detection for  $p_T > 1$  GeV/c. The working principle of TRD is based on the phenomena of transition radiation (TR) emitted by a relativistic charged particle passing through a medium of different dielectric constants. The high energy electrons that crosses the threshold for transition radiation ( $\gamma \sim 1000$ ) can produce about 1.45 X-ray photons in the energy range of 1 to 30 keV. Since the TR photons are in the keV range they

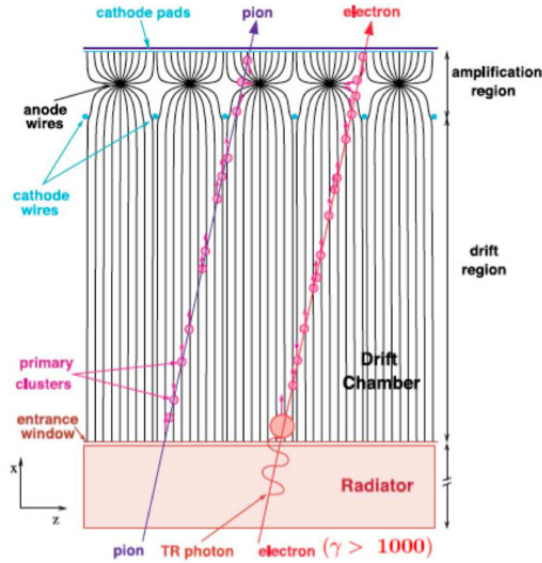


Figure 2.11: (Color online) Working principle of TRD [10].

are detected by the gaseous detector. To optimize the absorption of X-rays a gas mixture of Xe/CO<sub>2</sub> (85/15) is used. The pion being heavier do not emit TR below momentum  $\sim 100$  GeV/c. The working principle of TRD is shown schematically in Fig. 2.11. Since the TRD is very efficient in distinguishing the electrons from pions

with an efficiency of about 100%, this allows for the better measurement of  $J/\Psi$  production through di-electron channel. The TRD is also designed to derive a fast trigger (L1) for charged particles with high momentum.

### 2.3.4 Time of Flight (TOF)

The TOF [16] is a gas based Multigap Resistive Plate Chamber (MRPC) and placed around the TRD at a radial distance of 2.70 to 3.99 m (within  $\eta < 0.9$ ) covering polar angles  $45^0$  to  $135^0$ . The basic unit of TOF is 10 gap-MRPC strip. Each strip has an active area of  $120 \times 7.4 \text{ cm}^2$  and it is sub-divided into two rows of 48 pads of size  $3.5 \times 2.5 \text{ cm}^2$ . When a charged particle ionize the gas, the high electric field amplifies the ionization through electron avalanche, which are stopped due to the resistive plates. The total signal is the sum of all the signals from all gaps. The time jitter of the signal depends on the width of individual gap. The TOF has an ability to detect particles with 99.9% efficiency and a time resolution about 85 ps in Pb–Pb collisions and 120 ps in pp collisions. The particles in TOF can be identified by an  $N\sigma$  cut, which is defined by,

$$N\sigma_{TOF} = \frac{time_{measured} - time_{expected}}{\sigma_{TOF}^{PID}} \quad (2.3)$$

where

- $time_{measured}$  is the flight time of the particle measured by an algorithm of TOF and T0 detector;

- $time_{expected}$  is the flight time computed during the central tracking procedure;

- $\sigma_{TOF}^{PID}$  is the PID resolution of the TOF detector which is about 120 ps for pp collisions and 85 ps for Pb-Pb collisions;

The TOF can provide more than  $2\sigma$   $\pi/K$  separation up to momentum 3 GeV/c and  $3\sigma$   $K/p$  separation up to 4 GeV/c in Pb-Pb collisions at  $\sqrt{s_{NN}} = 2.76 \text{ TeV}$ .

### 2.3.5 High Momentum Particle Identification (HMPID)

The HMPID [17] is a ring imaging Cherenkov detector with a radiator liquid  $C_6F_{14}$  (perfluorohexane). When a charged particle passes through the detector the electromagnetic radiation is emitted in a cone. The Cherenkov photons emitted by a fast charged particle traversing the radiator, are detected by a photon counter consists of  $10\text{ m}^2$  of active CsI photo cathode area. The aim of the HMPID detector is to enhance the capability of particle identification beyond the momentum interval achievable by ionization energy loss (in TPC) and time of flight measurements (in TOF). It is optimized to discriminate  $\pi/K$  up to momentum  $3\text{ GeV}/c$  to  $5\text{ GeV}/c$ .

### 2.3.6 PHOton Spectrometer (PHOS)

PHOS [18] is a high resolution electro-magnetic calorimeter. It is located at a radial distance of  $4.6\text{ m}$  with an azimuthal acceptance  $220^\circ$  to  $320^\circ$  ( $|\eta| < 0.12$ ). It consist of lead tungsten crystals ( $PbWO_4$ ). It has 5 modules with 3584 crystals in each. There is a set of Multi-Wire Proportional Chambers infront of PHOS to reject the charged particles, called the Charged Particle Veto (CPV). The aim of the PHOS detector is to detect the direct photons,  $\pi^0$  and  $\eta$  mesons.

### 2.3.7 Electro Magnetic Calorimeter (EMCAL)

The ElectroMagnetic Calorimeter [19] was installed to enhance the measurement of jets and high  $p_T$  photons and electron identification. It is located at a radial distance of  $4.5\text{ m}$  from the beam line opposite to the PHOS and covers an azimuthal angle of  $80^\circ$  to  $187^\circ$  ( $|\eta| < 0.7$ ) which is about 23% of the phase space of the central region. Although it has an acceptance larger than PHOS, it has lower granularity and resolution. It can provide the measurement of transverse energy ( $E_T$ ) in the region from  $100\text{ MeV}$  to  $100\text{ GeV}$ . It also provides a fast and efficient trigger (L0 and L1) for hard jets, photons and electrons.

### 2.3.8 ALICE Cosmic Ray Detector (ACORDE)

The ALICE Cosmic Ray Detector (ACORDE) [20] provides a trigger for the cosmic rays. It is located at a radial distance of 8.5 m ( $\eta < 1.3$ ) over the azimuthal angle  $-60^\circ$  to  $60^\circ$ . It consists of an array of 60 plastic scintillators placed on the top of L3 magnet with an effective area of  $190 \times 20 \text{ cm}^2$ . It provides a fast L0 trigger signal during the commising, calibration and alignment of some ALICE tracking detectors.

### 2.3.9 Muon Spectrometer

The Muon spectrometer [24] is located in the negative Z-direction of the ALICE detector. It has an acceptance from polar angle of  $171^\circ$  to  $181^\circ$  ( $-4 < \eta < -2.5$ ) over the full azimuth coverage for muons with  $p_T > 4 \text{ GeV}/c$ . The cut off is due to the fact that muons have to pass through the front absorber made of carbon, concrete and steel. The muons are successively measured by five tracking stations with two planes each made of very thin, highly granular cathode strip tracking stations. A dipole magnet is located outside the L3 magnet which allows the muon momenta to be reconstructed. An iron wall of 1.2 m acts as a further muon filter after which two trigger stations with two planes (each of resistive plate chambers) are located. The whole spectrometer is shielded by means of a dense absorber tube against particles emerging from the beam pipe. The main task of the muon spectrometer is to measure the quarkonia ( $J/\Psi$ ,  $\Psi'$ ,  $\Upsilon$ ,  $\Upsilon'$ ,  $\Upsilon''$ ) through their di-muon decay channel.

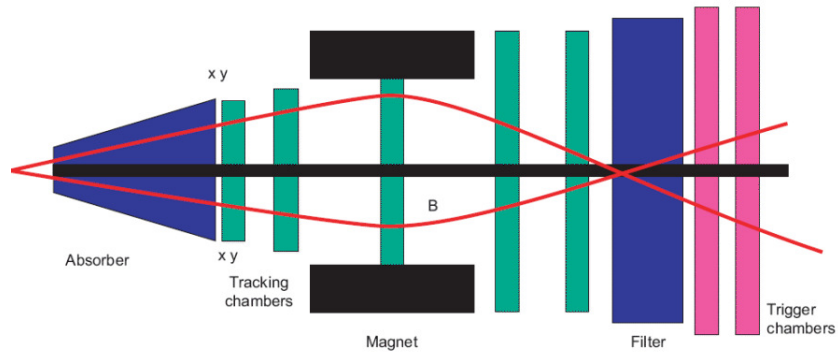


Figure 2.12: (Color online) The lay out of Muon spectrometer [24].

## 2.4 Forward detectors

The forward detectors consist of Zero Degree Calorimeter (ZDC) [25], Forward Multiplicity Detector (FMD) [26], Photon Multiplicity Detector (PMD) [27, 28], VZERO and TZERO [26] detectors. These detectors will be discussed in the sub-sections below, with a special emphasis on PMD, as results from this detector forms a major part of this thesis work.

### 2.4.1 Zero Degree Calorimeter (ZDC)

The Zero Degree Calorimeters (ZDC) [25] are located on either side of IP at a distance of 116 m. The spectator nucleons that leaves the interaction point along the beam direction are separated by the LHC magnets. The hadronic ZDC consist of neutron detector (ZN) and the proton detector (ZP). Spectator protons are spatially separated from the neutrons by the magnet in the LHC beam line. The ZN is placed between the beam pipes at  $0^0$  with respect to the LHC axis, while the ZP is placed externally to the outgoing beam pipe on the side where positive particles are deflected. There is an electromagnetic calorimeter (ZEM) located at forward rapidity at a distance of 7.25 m from the IP. ZDC can be used for the determination of centrality in heavy-ion collisions and also for triggering at level 1 (L1). It can be used to estimate the reaction plane in nuclear collisions.

### 2.4.2 Forward Multiplicity Detector (FMD)

The Forward Multiplicity Detector (FMD) [26] is located at high rapidities ( $-3.4 < \eta < -1.7$  and  $1.7 < \eta < 5.0$ ) with full azimuthal coverage. It is used to determine the multiplicity of charged particles and the reaction plane [7]. It consists of five rings, three inner rings and two outer rings. The five rings are located at a distance of 3.2 m, 0.83 m, 0.75 m, 0.63 m and -0.75 m from the IP . The inner and outer rings are segmented into 20 and 40 sectors in  $\phi$  respectively. Each of the sectors of inner and outer rings are segmented into 512 and 256 strips of silicon detectors.

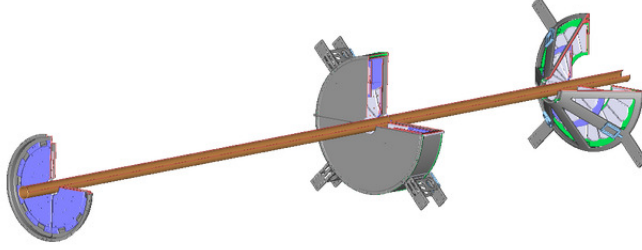


Figure 2.13: The lay out of FMD in GEANT3.

### 2.4.3 Photon Multiplicity Detector (PMD)

The PMD [27, 28] is installed to measure the multiplicity of photons produced in pp and Pb-Pb collisions in the forward rapidity. It can also be used for the determination of reaction plane [7]. It is located at a distance of 3.67 m from the interaction point in the A side of the ALICE and it covers a pseudo-rapidity  $2.3 < \eta < 3.9$  with full azimuth. The PMD consists of two planes (charged particle veto and preshower) separated by a  $3X_0$  thick converter (1.5 cm Pb and 0.5 cm Stainless Steel). Each plane consist of 24 unit modules. More details will be discussed in the section 2.7.

### 2.4.4 VZERO (V0)

The VZERO (V0) [26] detectors are the plastic scintillator detectors located asymmetrically on both sides of the interaction point. It covers the full azimuth within  $2.8 < \eta < 5.1$  (V0-A) and  $-3.7 < \eta < -1.7$  (V0-C). The V0-A is at a distance of 3.4 m from the IP, whereas the V0-C at a distance of 0.9 m on the opposite side. The detectors are segmented in 32 counters distributed in 4 rings. Each ring is divided into 8 sectors. The time resolution is about 1 ns. It is mainly used for triggering and rejection of beam gas events through its timing information. It is also used for the determination of centrality in Pb-Pb collisions.

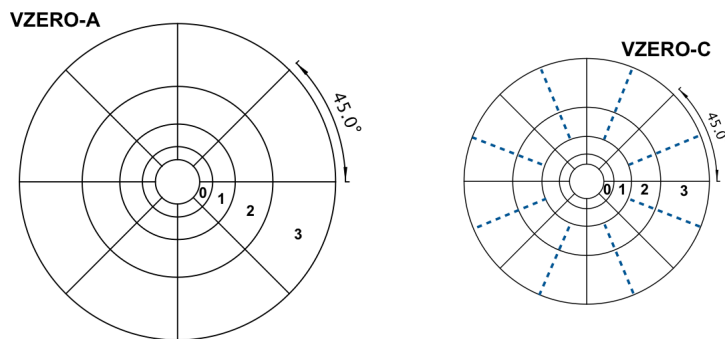


Figure 2.14: VZERO-A and VZERO-C.

### 2.4.5 TZERO (T0)

The TZERO (T0) [26] detector consist of two arrays of Cherenkov counters, called T0A and T0C. The T0A is located at a distance of 3.75 m from the IP, opposite to the Muon spectrometer covering the range of  $4.61 < \eta < 5.92$ . The other component T0C is located on the opposite side of T0A at a distance of 7.27 m from the IP with coverage  $-3.28 < \eta < -2.97$ . The T0 detector can measure the collision time with a precision of 25 ps. This time is used as a reference time for the TOF to measure the flight time of particles. The T0 can also send a pre-trigger to the TRD. It can also generate minimum bias and multiplicity triggers.

## 2.5 Online and Trigger

### 2.5.1 CTP

The ALICE trigger system consist of Central Trigger Processor (CTP) [29, 30] and a High Level Trigger (HLT) [29, 30]. The CTP is a low level hardware trigger and HLT is a software trigger. The CTP consist of 24 Local Trigger Units (LTU) for each detector system. The CTP receives and process trigger signal from trigger detectors (Table 2.2). The first level trigger is called the L0 which is delivered after  $1.2 \mu s$ , the second level is called L1 delivered after  $6.5 \mu s$  and the final trigger L2 is delivered after  $100 \mu s$ . After the L2 trigger the event is stored. The output of the CTP goes

to the LTUs of each detectors and then to the front end electronics of the detector via Low Voltage Differential Signaling (LVDS) cables and optical fibres. The CTP forms 50 independent trigger classes combining 24 L0 inputs, 24 L1 inputs and 12 L2 inputs [30].

Detectors	Trigger level
SPD	L0
TRD	L1
TOF	L0
PHOS	L0
EMCAL	L0/L1
ACORDE	L0
V0	L0
T0	L0
ZDC	L1
MTR	L0

Table 2.2: Trigger level of ALICE detectors

## 2.5.2 HLT

The High Level Trigger (HLT) [30] permits a firmware and software filtering mechanism to select interesting events. The HLT receives the raw data via 454 Detector Data Links (DDL). Then it performs the basic calibration and extracts hits and clusters. Then the event is reconstructed for each detector individually. After that the selection of event is performed with the reconstructed physics observables. The HLT also perform compression on data allowing to reach a sustained rate to disk of more than 4 Gb/s. The same rate is maintained during transferring the data to tape support in CERN computer center.

## 2.5.3 DAQ

The ALICE Data Acquisition system (DAQ) [29, 30] handles the data flow from the detector electronics to the permanent storage. A first layer of computers the Local

Data Concentrators (LDCs) read out the events from the optical Detector Data Link (DDLs). The DDLs are point to point links at 2 Gb/s and up to 12 of them can be connected to the same LDC. The LDCs assemble the data into the sub-events and then shipped to Global Data Collectors (GDCs). The GDCs recorded the events to a Transient Data Storage (TDS) and then it is migrated to the tape (PDS) in the storage.

## 2.6 Offline and computing

The offline project [31] is the development and operation of the framework for the data processing.

### 2.6.1 Data processing

During the data processing in pp collisions, the following four activities proceed in parallel on the raw data:

- Copy to the CASTOR [32] tapes.
- Export to the Tier-1 centres to have a second distributed copy on highly-reliable storage media and to prepare for the successive reconstruction passes that will be processed in the Tier-1 centres;
- First pass is processing at the Tier-0 centre. This includes: reconstruction, production of calibration and alignment constants and scheduled analysis;
- Fast processing of selected sets of data mainly calibration, alignment, reconstruction and analysis on the CERN Analysis Facility (CAF).

Similarly during Pb–Pb collisions, the steps are the following:

- Registration of the RAW data in CASTOR;
- Partial export to the Tier-1 centres to allow remote users to examine the data locally;
- Partial first pass processing at the Tier-0 centre to provide rapid feedback on the offline chain;

– Fast processing, mainly calibration, alignment, reconstruction and analysis on the CAF.

During the first pass reconstruction, high precision alignment and calibration data are produced as well as a first set of Event Summary Data (ESD) and Analysis Object Data (AOD). The feedback derived from the first pass, including analysis, is used to tune the code for the second pass processing. One full copy of the raw data is stored at the CERN, and the second one is shared among the TIER 1's outside CERN. Subsequent data reduction, analysis and Monte Carlo production is a collective operation where all Tiers participate, with Tier-2s being particularly active for Monte Carlo and end-user analysis.

## **2.6.2 ALICE Grid**

The concept of ALICE Grid is introduced to process the huge amount of data distributed among computing resources. ALICE developed a set of middlewired services, the AliEn [33], as a user interface to connect to the Grid. AliEn Web Services play the central role in enabling AliEn as a distributed computing environment. The user interacts with them by exchanging SOAP (Simple Object Access Protocol) [10] messages and they constantly exchange messages between themselves behaving like a true Web of collaborating services. The distributed computing infrastructure serving the LHC experimental program is coordinated by the Worldwide LHC Computing Grid (WLCG). The WLCG is highly hierarchical by nature. All real data originate from CERN, with a very large computing centre called Tier-0. Large regional computing centres, called Tier-1, share with CERN the role of a safe storage of the data. Smaller centres, called Tier-2, are logically clustered around the Tier-1s. The main difference between the two is the availability of high reliability mass storage media at Tier-1s. The major role of Tier-2s is simulation and end-user analysis. Smaller centre, corresponding to departmental computing centre and sometimes called Tier-3s, contribute to the computing resources but there is no definite role or definition for them.

### 2.6.3 AliRoot simulation framework

The AliRoot offline framework [31] is based on the Object Oriented techniques for simulation, reconstruction, calibration, alignment, visualization and analysis. It uses the ROOT [34] system as a foundation on which the framework and all applications are built. It has been in continuous development since 1998. The simulation framework is schematically shown in Fig. 2.15 and briefly described below:

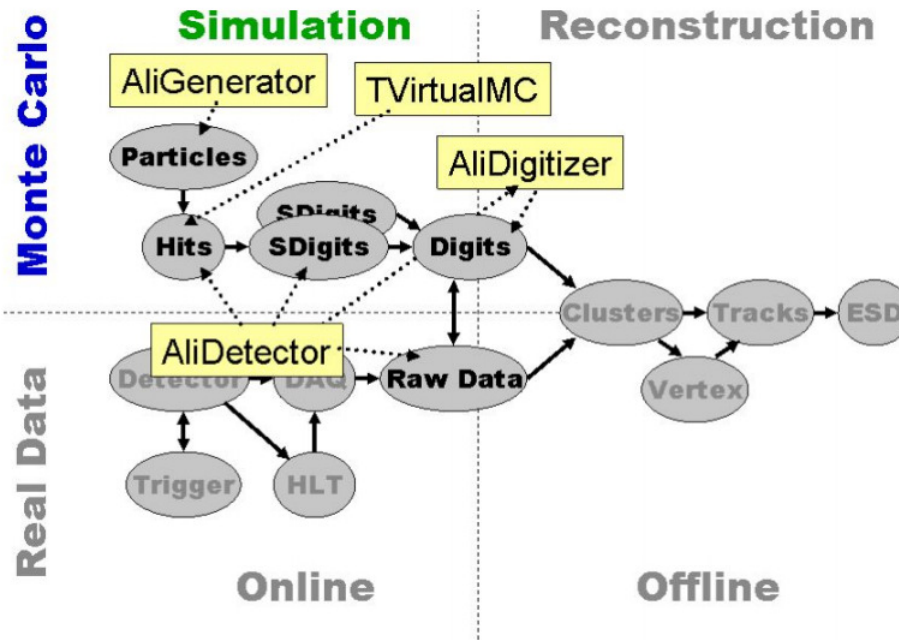


Figure 2.15: (Color online) Data Processing Framework in ALIROOT.

#### Event generation

– The data is produced by the monte carlo event generators. The framework provides the interface to the event generators such as PYTHIA [9], PHOJET [10], HIJING [15], AMPT [38], DPMJET [39] etc. The data produced by the event generators are stored in a tree with the full information of the generated particle type, its momentum and charge and mother-decay daughter relationship.

#### Detector response

– The generated particles are propagated through the detector material. The response of the detectors to each crossing particles is simulated using a monte carlo

transport package. The available transport packages are GEANT3 [10], GEANT4 [41] and FLUKA [42]. The ALICE detector is described in great detail (services and support structures, absorbers, shielding, beam pipe, flanges and pumps) in the transport packages. During the propagation, the particles undergo all possible interactions which they would undergo during the real experiment. The information of hits or the energy deposition at a given point and time are stored for each detector. The information is complemented by the so-called track references corresponding to the location where the particles are crossing user defined reference planes. The hits are converted into digits taking into account the detector and associated electronics response function. Finally, the digits are stored in the specific hardware format of each detector as raw data.

### **Alignment framework**

– The framework also takes care of the misalignment in positioning the part of detectors from their ideal position. When the simulation program is started, the ideal geometry is generated by the compiled code or read from the Offline Conditioned Data Base (OCDB), where it was saved in a previous run. Several objects are marked as alignable, that is the geometrical modeller is ready to accept modifications to their position, even if they were obtained by replication. The framework then reads the alignment objects which contain the adjustments in the position of the alignable objects. The particle transport is then performed in the modified geometry. During the reconstruction of the real data, the best alignment objects are loaded from the OCDB. During first pass reconstruction, the alignment objects are taken from the survey data. For subsequent reconstruction passes, the alignment objects are produced by the alignment algorithms optimizing the reconstruction quality during processing of raw data.

### **Calibration framework**

The calibration framework is similar to the alignment one. The initial calibration constants come either from the detector properties as measured during construction, or from algorithms running online during data-taking aimed at providing a partial calibration sufficient for the first-pass data reconstruction. During the reconstruction

itself, better calibration constants can be calculated and stored in the OCDB.

### **Reconstruction framework**

– During the reconstruction of raw data (or simulated data) . The first step in the reconstruction procedure is the generation of clusters from digits. Afterwards, during tracking the clusters are combined to form the most probable path of the particle through the detectors.

The track reconstruction is done using a Kalman filter algorithm [43]. The seeding is done twice once under the assumption that the track is originated from the primary vertex and once that it originates somewhere else. In the next step the seeds are combined in the outermost pad rows in TPC with the nearby clusters going inwards to a track under the constraint that the particle originates from the primary vertex. This process is repeated, each time choosing in addition pad rows closer to the primary vertex. This process is continued until the innermost pad row of the TPC is reached.

After finishing the initial tracking in TPC, the tracks are propagated outwards to the ITS layers. The tracks are then reconstructed for the six layers in the ITS going inwards to the primary vertex. After the combined ITS and TPC fit of the track, the algorithm is reversed and proceed outwards using the seeds from the already reconstructed tracks. Then the tracks are re-calculated in the TPC to remove improperly assigned points. After that the tracking follows the track beyond TPC and assigns space point in the TRD, TOF, HMPID and in EMCAL or PHOS. Finally a last inversion of the Kalman filter is performed and the final track parameters are calculated once assuming the track parameters are originating from the primary vertex and the other time without.

The primary vertex reconstruction is done mainly using the clusters in the SPD. At first the two layers of SPD, close in azimuthal and transverse direction, are selected. From the Z coordinates the a first estimate of the Z-position of the primary vertex position is done by linear extrapolation. Then the same procedure is performed in the transverse xy plane, which can only give a rough estimate because of the bending of the track in the transverse plane due to magnetic field. Considering the small distance from the interaction point the x and y coordinates can be determined with

adequate precision. In pp collisions, a Z-vertex resolutions of  $150 \mu\text{m}$  can be reached, whereas in Pb–Pb it can reach to  $10 \mu\text{m}$ .

The secondary vertex reconstruction is done from the tracks with parameter sets obtained by not assuming the primary vertex as their origin. This is done by combining the oppositely charged tracks. A pair is accepted as potential secondary vertex if it satisfies certain criteria based on distance of closest approach (DCA) and the topology of two tracks for decay.

The output of the reconstruction is stored as Event Summary Data (ESD). It has a complete information of each event. For analysis purpose, not all the informations in ESD are needed. So the ESDs are further reduced to the Analysis Object Data (AOD) format.

### **Analysis**

The analysis framework is developed to analyse the reconstructed or simulated data. As the first step, the analysis framework extracts a subset of the Datasets from the File Catalogue using meta-data selection. Then the framework negotiates with dedicated Grid services balancing between local data access and data replication. Once the distribution is decided, the analysis framework creates sub-jobs. The framework collects and merges available results from all terminated sub-jobs on request. An analysis object associated with the analysis task remains persistent in the Grid environment so the user can go offline and reload an analysis task at a later date, check the status, merge current results, or resubmit the same task with a modified analysis code.

## **2.7 Details of PMD**

The Photon Multiplicity Detector is build and installed at the LHC to study the production of photons in the forward rapidity. As most of the photons are coming from the decay of neutral pions, it gives a complimentary information to that of the charged particle. The physics goal of the PMD are the following:

1. Measurement of global observables like multiplicity, pseudo-rapidity distribu-

tions are useful in understanding particle production mechanism. PMD can extend our understanding of particle production in forward rapidities.

2. Measurement of azimuthal anisotropy and flow of photons can be used to probe the thermalization of the medium formed in heavy-ion collisions. We can study the elliptic flow of photons using PMD [44]. Since PMD has a large  $\eta$ -gap with the central detectors, it can be used to estimate the reaction plane [7]. The information of reaction plane can be used to estimate the azimuthal anisotropy of charged hadrons at mid rapidity.

3. Signals of chiral-symmetry restoration (e.g. disoriented chiral condensate) can be studied through the measurement of  $N_\gamma/N_{charged}$  in a common phase space.

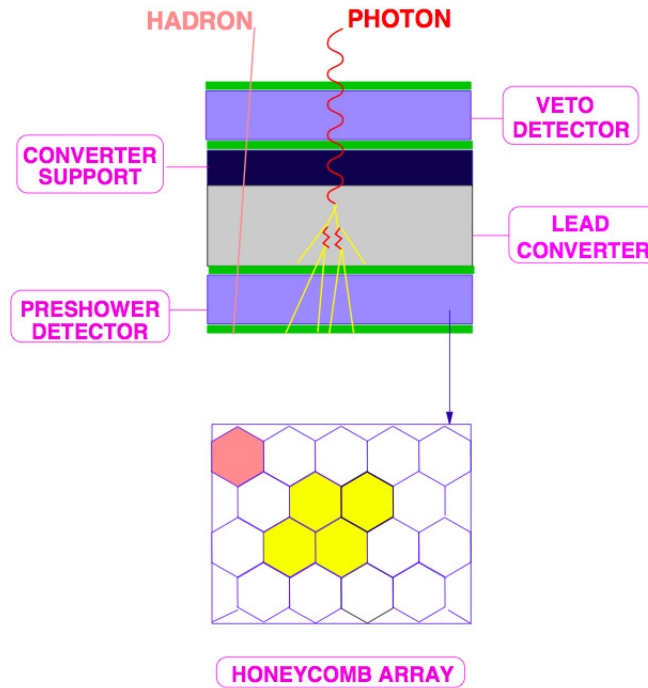


Figure 2.16: (Color online) Working principle of PMD [27, 28].

### 2.7.1 Working principle of PMD

The PMD consist of two planes, the Charged Particle Veto (CPV) and preshower (PRE) plane with an intermediate Pb converter. The active volume of PMD consist

of a gas mixture Ar/CO<sub>2</sub> (70/30). The working principle of PMD is shown schematically in Fig. 2.16. When a photon passes through the PMD, it interacts with the converter plates and produce electromagnetic shower via bremstrahlung radiation and pair production. Then the electromagnetic shower hits the detector and deposite its energy in the sensitive medium (Ar/CO<sub>2</sub>) of PMD. The photon can affect more than one cell of PMD. On the other side, the charged hadrons affect only single cell and produce a signal representing minimum-ionizing particles. So the energy deposited by photons is more compared to charged particles in PMD. The thickness of the converter is optimized such that the conversion probability of photons is high and the transverse shower spread is small to minimize the shower overlap in the high multiplicity environment.

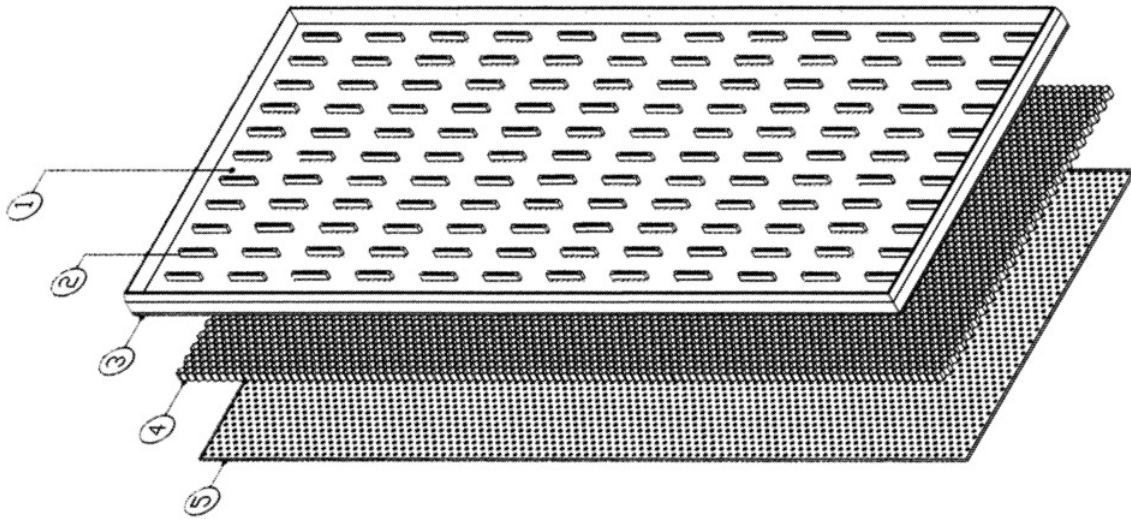


Figure 2.17: Schematic picture of a unit module in PMD. (1) Top PCB, (2) 32-pin connectors, (3) edge frame, (4) honeycomb cells and (5) bottom PCB [27, 28].

## 2.7.2 Construction of PMD

The PMD consists of the following mechanical parts:

- two planes, the preshower and the charged particle veto;
- lead converter plate;
- support assembly.

Each plane of PMD contain 24 unit modules. A schematic picture of an unit module is shown in Fig. 2.17. Each module has 4608 number of honeycomb structured cells. There are two kind of unit modules, the long type and short type. The long type (short type) has an array of 96 rows and 48 columns (48 rows and 96 columns) with a dimension  $41.9 \times 24.25 \text{ cm}^2$  ( $48.25 \times 21 \text{ cm}^2$ ). Each honeycomb cell has a depth of 5 mm and cross-section  $0.23 \text{ cm}^2$ . The Fig. 2.18 shows one such honeycomb cell.

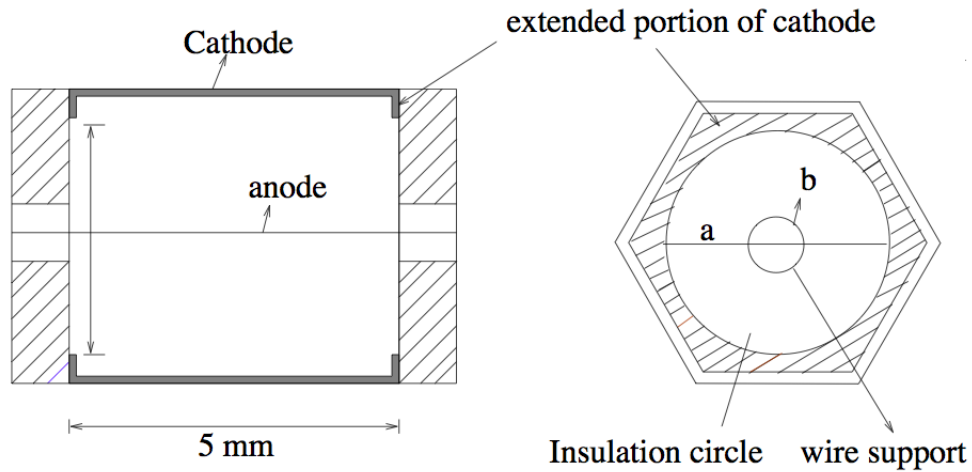


Figure 2.18: Cell of PMD [28].

Each unit module is covered by gold plated Printed Circuit Boards (PCBs) from both sides, each having 4608 insulation circles of 2 mm diameter. The top PCB consist of electronic boards, solder islands at center of each cell with a 0.4 mm gold-plated through-hole. Signal tracks from a group of 32 cells are brought to a 32-pin connector. The bottom PCB have only soldering islands without signal tracks, serving as anchor points. A gold-plated tungsten wire of diameter  $20 \mu\text{m}$  is inserted through the center of each cell and a proper tension is applied in the wire during soldering. The unit modules are kept in a air tight container which is made of 2 mm thick stainless

steel material. There are two nozzles for the gas inlet and outlet. There are 1.5 cm thick ( $3X_0$  radiation length) lead plates sandwiched between each modules. The lead plates are of two different types according to the unit modules. The long type has a dimension  $49.05\text{ cm} \times 21.7\text{ cm}$  and the short one has  $42.5\text{ cm} \times 25.15\text{ cm}$ . There is a 5 mm stainless steel plate to support the lead converter plates and modules. The left panel of Fig. 2.19 shows the real pictures of PMD (looking towards the IP) in data taking configuration and the right panel shows the same in the parking position during the technical shut down in 2012.

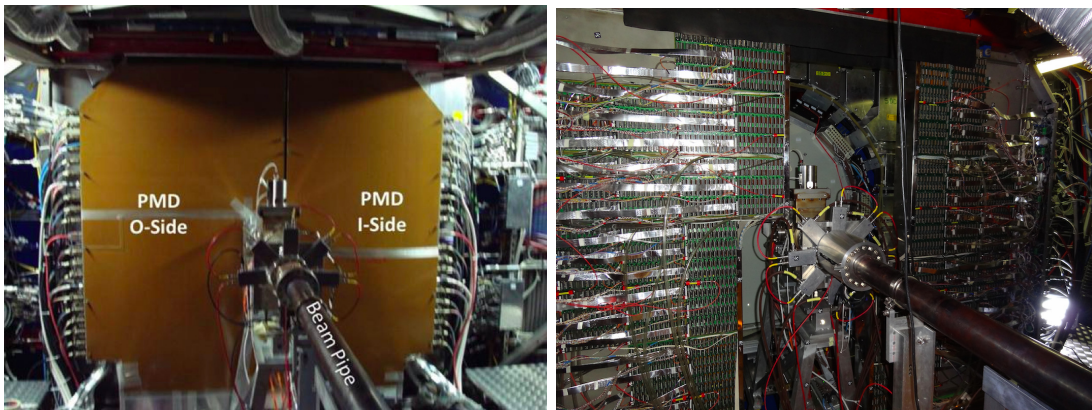


Figure 2.19: (Color online) Left panel: Picture of PMD (looking towards the IP) in data taking configuration. Right panel: PMD in parking position during 2012 technical shut down.

### 2.7.3 Front End Electronics and readout

The Front End Electronics (FEE) for the readout of the PMD signals is based on a 16-channel Multiplexed ANAlog Signal (MANAS) processor chips. The FEE boards are connected to the unit modules through flexible kapton cables. The signals from the PMD are then processed and digitized in Multi Chip Module (MCM). The signals are then send to the Translator Boards (TB). From TB the signals are then transferred to the Cluster ReadOut Concentrator (CROCUS) system via Patch Bus (PB) cables and further to the Data Acquisition System (DAQ) via Detector Data Link (DDL). A

schematic view of the FEE of the PMD is shown in Fig. 2.20. The readout of signal is structured in three levels, are briefly described below:

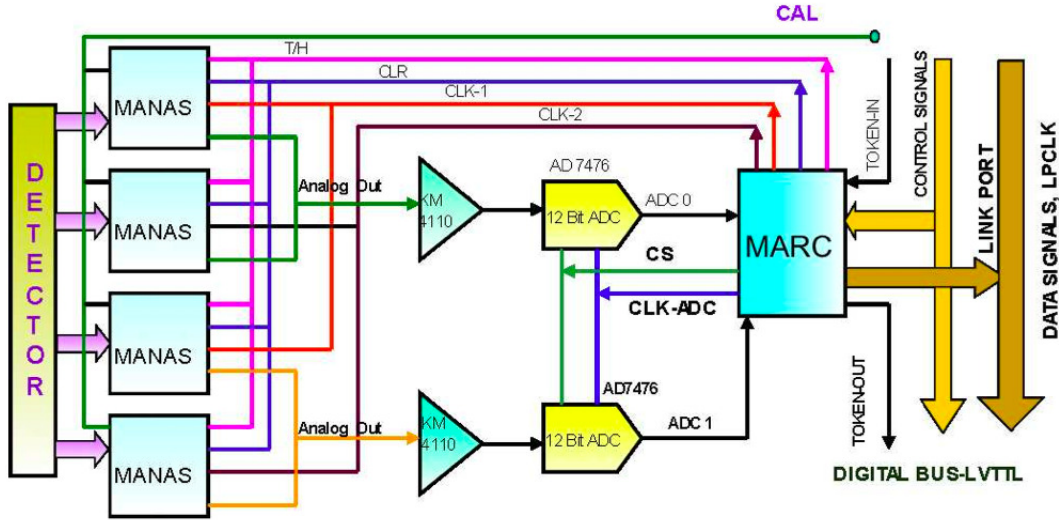


Figure 2.20: (Color online) Front end electronics of PMD [31].

1) Multi Chip Module (MCM): The MCM contains a digital readout chip called Muon Arm Readout Chip (MARC) which controls 4 MANAS chips and two 12-bits ADC. It can handle 64 analog inputs. It can perform analog processing, ADC conversion, pedestal subtraction, zero suppression, data formatting and transmission to the digital signal processor via digital local bus.

2) Digital Signal Processor (DSP): The local buses collect the data from MCMs. A maximum 24 MCMs can be connected to a bus. Several buses run through each chamber, making the data available to the DSPs located on the edge of the detector. Each DSP can handle up to 6 buses.

3) CROCUS: The DSPs are handled through a cluster readout system called Cluster ReadOut Concentrator (CROCUS). The CROCUS gathers and concentrate informations coded on FEE and pass to the Detector Acquisition system (DAQ). Each CROCUS crate can handle 50 patch-buses (PB). Each PB can handle one chain of FEE. Each readout chain has 12 FEE boards. Each module has 6 chains. The PRE and CPV plane has 72 chains each.

# Bibliography

- [1] T. S. Pettersson (ed.) and P. Lefevre (ed.), CERN-AC-95-05 LHC (1995).
- [2] LHC Design Report Volume I + II, CERN-2004-003-V-2 (2004).
- [3] M. Benedict, P. Collier, V. Mertens, J. Poole, and K. Schindl, LHC Design Report, volume III (2004).
- [4] Technical Proposal for A Large Ion Collider Experiment at the CERN LHC, CERN/LHCC 95-71 (1995).
- [5] ATLAS Technical Proposal, CERN/LHCC 94-43 (1994).
- [6] The Compact Muon Solenoid Technical Proposal, CERN/LHCC 94-38 (1994).
- [7] LHCb Technical Proposal, CERN/LHCC 98-4 (1998).
- [8] Technical Proposal for the CERN LHCf Experiment, CERN/LHCC 2005-032 (2005).
- [9] TOTEM Technical Proposal, CERN/LHCC 99-7 (1999).
- [10] K. Aamodt *et al.* (ALICE Collaboration), JINST **3**, S08002 (2008).
- [11] R. Rapp and E. Shuryak, Phys. Rev. Lett. 86, 2980 (2001).
- [12] K. Aamodt *et al.* (ALICE Collaboration), arXiv:1402.4476.
- [13] ALICE Inner Tracking System (ITS): Technical Design Report, CERN-LHCC-99-012, <http://edms.cern.ch/file/398932/1>.

- [14] ALICE Time Projection Chamber: Technical Design Report, CERN-LHCC-2000-001, <http://cdsweb.cern.ch/record/451098>.
- [15] A. Andronic *et al.* (ALICE TRD Collaboration), Electron identification performance with ALICE TRD prototypes, Nucl. Instrum. Meth. A 522 (2004) 40; C. Adler *et al.* (ALICE Collaboration), Electron / Pion Identification with ALICE TRD Prototypes using a Neural Network Algorithm, Nucl. Instrum. Meth. A 552 (2005) 364. A. Wilk, Particle Identification using a Neural Network Algorithm in the ALICE TRD, Ph.D. Thesis, University of Munster, (2009).
- [16] ALICE Time-Of-Flight system (TOF): Technical Design Report, CERN-LHCC-2000-012; <http://cdsweb.cern.ch/record/430132>; ALICE Time-Of-Flight system (TOF): addendum to the technical design report, CERN-LHCC-2002-016, <http://cdsweb.cern.ch/record/545834>.
- [17] ALICE high-momentum particle identification: Technical Design Report, CERN-LHCC-98-019, <http://cdsweb.cern.ch/record/381431>.
- [18] ALICE Technical Design Report of the Photon Spectrometer (PHOS), CERN/LHCC 99-4 (1999), <https://edms.cern.ch/document/398934/1>.
- [19] ALICE electromagnetic calorimeter: addendum to the ALICE technical proposal, CERN-LHCC-2006-014, <http://cdsweb.cern.ch/record/932676>.
- [20] Cosmic ray physics with the ALICE detectors, Czech. J. Phys. 55 (2005) B801; A. Fernandez *et al.*, ACORDE a cosmic ray detector for ALICE, Nucl. Instrum. Meth. A572, 102 (2007).
- [21] M. Knichel, PhD thesis, GSI Darmstadt (2009).
- [22] W. Blum, W. Riegler and L. Ronaldi, Particle Detection With Drift Chambers, 2nd ed.(Springer-Verlag, 2008), <http://www.springer.com/physics/elementary/book/978-3-540-76683-4>.
- [23] A. Kalweit, PhD thesis, GSI Darmstadt (2012).

- [24] ALICE dimuon forward spectrometer: Technical Design Report, CERN-LHCC-99-022; <http://cdsweb.cern.ch/record/401974>; ALICE dimuon forward spectrometer: addendum to the Technical Design Report, CERN-LHCC-2000-046, <http://cdsweb.cern.ch/record/494265>.
- [25] ALICE Zero-Degree Calorimeter (ZDC): Technical Design Report, CERN-LHCC-99-005, <http://cdsweb.cern.ch/record/381433>.
- [26] ALICE forward detectors: FMD, T0 and V0: Technical Design Report, CERN-LHCC-2004-025, <http://cdsweb.cern.ch/record/781854>.
- [27] ALICE Photon Multiplicity Detector (PMD): Technical Design Report, CERN-LHCC-99-032; <http://cdsweb.cern.ch/record/451099>; ALICE Photon Multiplicity Detector (PMD): addendum to the technical design report, CERN-LHCC-2003-038, <http://cdsweb.cern.ch/record/642177>.
- [28] ALICE Technical Design Report on Photon Multiplicity Detector, Addendum-1, CERN/LHCC 2003-038 (2003).
- [29] F. Bergsma *et al.*, CERN ALICE DAQ Group, ALICE DAQ and ECS users guide, ALICE Internal Note ALICE-INT-2005-015, <http://cdsweb.cern.ch/record/960457>.
- [30] ALICE Collaboration, ALICE Technical Design Report of the Trigger, Data Acquisition, High-Level Trigger, Control System, CERN/LHCC 2003/062 (2004), <https://edms.cern.ch/document/456354/2>.
- [31] The ALICE experiment offline project, <http://www.cern.ch/ALICE/Projects/offline/aliroot/Welcome.html>
- [32] J. Durand, O. Barring, S. Ponce and B. Couturier, CASTOR: Operational issues and new developments, in Interlaken, Computing in high-energy physics and nuclear physics, 1221-1226 (2004).
- [33] P. Saiz *et al.*, AliEn ALICE environment on the GRID, Nucl. Instrum. Meth. A502, 437 (2003); AliEn home page, <http://alien.cern.ch/>.

- [34] R. Brun and F. Rademakers, ROOT: An object oriented data analysis framework, Nucl. Instrum. Meth. A 389, 81 (1997).
- [35] H. -U. Bengtsson and T. Sjostrand, The Lund Monte Carlo for hadronic processes: Pythia version 4.8, Comput. Phys. Commun. 46, 43 (1987).
- [36] R. Engel, Photoproduction within the two-component dual parton model. 1. Amplitudes and cross-sections, Z. Phys. C 66 (1995) 203. R. Engel and J. Ranft, Hadronic photon-photon interactions at high energies, Phys. Rev. D 54 (1996) 4244.
- [37] M. Gyulassy, X. N. Wang, Phys. Rev. C80, 024906 (2009).
- [38] Z. W. Lin, C. M. Co, B. A. Li, B. Zhang and S. Pal, Phys. Rev. C72, 064901 (2005).
- [39] J. Ranft: New features in DPMJET version II.5, Siegen preprint, 1999.
- [40] R. Brun, F. Bruyant, M. Maire, A. C. McPherson and P. Zancarini, GEANT3 user guide, CERN data handling division DD/EE/84-1 (1985), <http://wwwinfo.cern.ch/asdoc/geantold/GEANTMAIN.html>.
- [41] S. Agostinelli *et al.*, Geant4, a simulation toolkit, Nucl. Instrum. Meth. A506, 250 (2003), CERN-IT-2002-003, <http://cdsweb.cern.ch/record/602040>; <http://wwwinfo.cern.ch/asd/geant4/geant4.html>.
- [42] A. Fasso *et al.*, FLUKA: present status and future developments, Proceedings of the IV International Conference on Calorimeters and their Applications, World Scientific, Singapore (1994).
- [43] P. Billoir, Progressive track recognition with a Kalman like fitting procedure, Comput. Phys. Commun. 57, 390 (1989).
- [44] R. Singh, PhD thesis, University of Jammu (2014).
- [45] F. Carminati *et al.* (ALICE Collaboration), ALICE: Physics Performance Report, Volume I, J. Phys. G 30, 1517 (2004).

- [46] B. Alessandro *et al.* (ALICE Collaboration]) ALICE: Physics Performance Report, Volume II, J. Phys. G 32, 1295 (2006).
- [47] A. K. Dash, PhD thesis, (<http://www.hbni.ac.in/phdthesis/11phdthesis.htm>).
- [48] S. K. Prasad, PhD thesis, Calcutta University, (2010).
- [49] M. M. Mondal, PhD thesis, Calcutta University, (2010).
- [50] N. Sharma, PhD thesis, University of Panjub, (2012).
- [51] S. De, PhD thesis, Home Bhabha National Institute, (2014).
- [52] J. F. Grosse-Oetringhaus, PhD thesis, University of Munster, Germany, (2009).

# Chapter 3

## $K^{*0}$ Resonance Production in Pb–Pb and pp collisions

This chapter discusses the results of  $K^{*0}$  resonance production in Pb–Pb and pp collisions at  $\sqrt{s_{NN}} = 2.76$  TeV. Specifically it presents the results of invariant yield of neutral  $K^*$  meson and other derived observables to address physics mechanism behind resonance production.

### 3.1 Introduction

The production of resonances in heavy-ion collisions [2] is expected to be sensitive to the properties of strongly interacting matter [1] produced in these collisions. The resonance production may be affected by the onset of deconfined phase of quarks and gluons called the quark gluon plasma (QGP). The Large Hadron Collider (LHC) at CERN can provide collisions of heavy nuclei at center of mass energies up to 5.5 TeV per nucleon, where such a QGP can be formed. The resonance like  $K^*(892)^0$  meson is of particular interest because it has a small lifetime ( $\sim 4$  fm/c) compared to the one of the fireball ( $\sim 10$  fm/c at LHC [3]). So the characteristic properties of  $K^{*0}$  such as its mass, invariant mass distribution width and yield could be modified

relative to systems where there is no QGP (like small systems of minimum bias pp collisions). Due to short lifetime, decay particles of resonances may undergo re-scattering and re-generation effects. These are the two most important process which a typical resonance could undergo. Since the resonance  $K^{*0}$  contains a strange quark, it may also provide some information regarding the strangeness enhancement for the system. The recent measurements by STAR experiment [4, 5, 6, 7] suggest that the re-scattering of  $K^{*0}$  decay products is dominant over the  $K^{*0}$  re-generation. In this chapter we will study the effect of re-scattering, re-generation and strangeness production at LHC energies with the help of  $K^{*0}$  meson produced in Pb-Pb and pp collisions at center mass energy of 2.76 TeV.

## 3.2 Data Set

The analysis is done from minimum-bias data in Pb–Pb collisions at  $\sqrt{s_{NN}} = 2.76$  TeV and in pp collisions at  $\sqrt{s} = 2.76$  TeV recorded by the ALICE detector [8] in the year of 2010 and 2011 respectively.

Centrality	$\langle N_{part} \rangle$	$\langle N_{coll} \rangle$	$dN_{ch}/d\eta_{ y <0.5}$
Pb–Pb : 0-20 %	$308.20 \pm 3.40$	$1210 \pm 127$	$1207 \pm 46$
Pb–Pb : 20-40 %	$157.30 \pm 3.40$	$438.4 \pm 42.0$	$538 \pm 19$
Pb–Pb : 40-60 %	$68.76 \pm 2.40$	$127.7 \pm 11.0$	$205 \pm 8$
Pb–Pb : 60-80 %	$22.57 \pm 1.05$	$26.71 \pm 2.0$	$56 \pm 3$

Table 3.1: The second and third column shows average number of participating nucleons ( $\langle N_{part} \rangle$ ), the average number of binary nucleon-nucleon collisions ( $\langle N_{coll} \rangle$ ) estimated from Glauber model in different collision centrality for Pb-Pb collisions at  $\sqrt{s_{NN}} = 2.76$  TeV. The last column shows the measured charged particle pseudo-rapidity density at mid-rapidity in ALICE.

### 3.3 Event Selection

The minimum bias events are selected for the analysis which requires a single hit either in the SPD detector or in any one of the VZERO detectors. It is equivalent to selecting events having at least one particle approximately 8 units in pseudo-rapidity. The effect of beam induced background is reduced with the timing information from the VZERO detector and cut on the primary vertex position. The primary vertex are reconstructed using either the hits in SPD or by using the tracks of TPC and ITS. The Z-position of vertex is selected in the analysis presented here to be between  $\pm 10$  cm from the interaction point to ensure uniform detector acceptance, because events with Z- position of vertex far from the interaction point will cause a loss in the acceptance. The Z - position of vertex distribution in Pb–Pb and pp collisions are shown in Fig. 3.1. The full width at half maximum of the Z - position of vertex distribution is 13.2 cm and 12.4 cm in Pb–Pb and pp collisions respectively. The Z-vertex distribution in Pb–Pb and pp collisions is slightly different. This may be due to the effect of LHC beam displacement off the Z-axis. It has been explicitly considered in the primary vertex reconstruction [9].

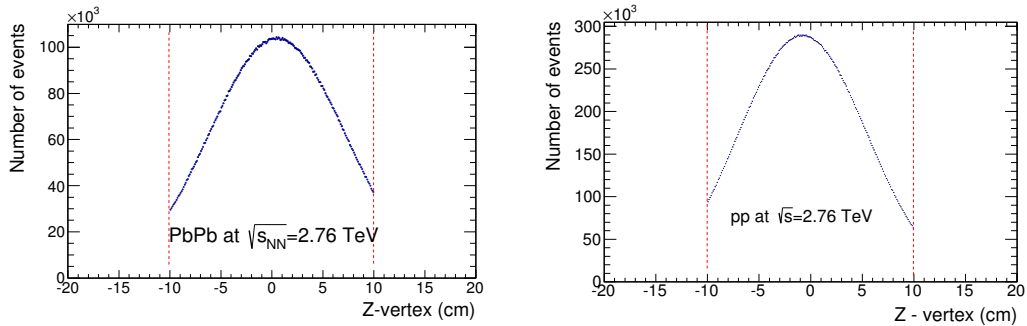


Figure 3.1: (Color online) The Z- position of vertex in Pb–Pb at  $\sqrt{s_{NN}} = 2.76$  TeV and pp collisions at  $\sqrt{s} = 2.76$  TeV.

For the analysis in Pb–Pb collisions the centrality is determined using the VZERO amplitude distribution (Fig. 3.2). It is fitted with a Glauber Monte Carlo model to compute the fraction of the hadronic cross section corresponding to any given range of VZERO amplitude. The method of selecting the centrality is described in reference

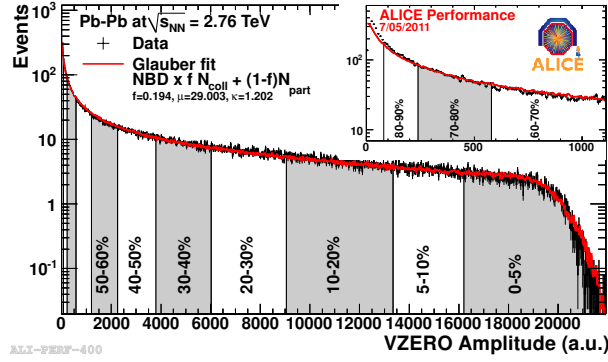


Figure 3.2: (Color online) Centrality selection using the amplitude of VZERO detector in Pb-Pb collisions at  $\sqrt{s_{NN}} = 2.76$  TeV [10].

[10]. The analysis in Pb-Pb collisions are done in four different centrality classes: 0-20%, 20-40%, 40-60% and 60-80%. The mean number of participating nucleons ( $\langle N_{part} \rangle$ ), mean number of binary collisions ( $\langle N_{coll} \rangle$ ) and charged particle multiplicity measured in  $|y| < 0.5$  for each centrality classes are given in Table 3.1 and the number of minimum bias events analyzed in Pb-Pb and pp collisions are given in Table 3.2.

System	Number of events (Million)
Pb-Pb : 0-20 %	3.05
Pb-Pb : 20-40 %	3.05
Pb-Pb : 40-60 %	3.05
Pb-Pb : 60-80 %	3.06
pp : Min. Bias	57

Table 3.2: Number of events analyzed in Pb-Pb collisions at  $\sqrt{s_{NN}} = 2.76$  TeV and pp collisions at  $\sqrt{s} = 2.76$  TeV .

### 3.4 Track Selection

The  $K^{*0}$  production is measured through the hadronic decay channel ( $K^{*0} \rightarrow \pi^- K^+$  and  $\overline{K}^{*0} \rightarrow \pi^+ K^-$ ) (branching ratio is 66 % in  $K^\pm \pi^\mp$  channel [4]) at mid-rapidity ( $-0.5 < y < 0.5$ ) in both Pb–Pb and pp collisions. The analysis is done by taking the average of  $K^{*0}$  and  $\overline{K}^{*0}$  and in the text it is denoted by  $K^{*0}$ . The analysis is done by selecting the good quality global tracks. The global tracking is done using the detectors ITS and TPC. A Kalman filter algorithm [12, 13] is applied for tracking. A refit is performed with the reconstructed tracks where the tracks are refitted inwards from the outermost layers of TPC to the innermost layers of ITS and are prolonged to the reconstructed primary vertex and vice-versa. The tracks which pass the TPC and ITS refit are accepted in the analysis. Since the  $K^{*0}$  has a very small lifetime, the decay daughters seem to originate from the interaction point. For the present analysis, the kaon and pion tracks are selected from the primary tracks by applying a cut on distance of closest approach (DCA) to the primary vertex on the XY and Z plane. The cut on the  $DCA_{XY}$  is implemented as a function of  $p_T$ , i.e.,  $(DCA)_{XY}(p_T) < 0.0182 + 0.035p_T^{-1.01}$  cm. The magnitude of  $DCA_Z$  is required to be less than 2 cm. The above cuts on DCA reduces the contribution from the secondaries which may come from the weak decay of strange hadrons and interaction with the detector material. To maintain a reasonable momentum resolution a cut on transverse momentum  $p_T > 0.15$  GeV/c is applied. The good quality tracks are selected by requiring a minimum 70 clusters inside TPC out of 159 possible with a minimum  $\chi^2$  of the fit per cluster less than equal to 4 and at least one hit in the inner sector of the SPD. The tracks with kinks (tracks those decayed to muon and neutrino, e.g.,  $K^\pm \rightarrow \mu^\pm + \nu_\mu$ ) are rejected through topological cut in the analysis. To reduce the acceptance drop, an  $|\eta|$  cut of 0.8 on the daughters of  $K^{*0}$  is required, which is well within the acceptance of TPC. The track selection cuts are given in Table 3.3.

Cut name	Cut values
$p_T$ range	$0.15 < p_T < 20 \text{ GeV}/c$
$\eta$ range	$-0.8 < \eta < 0.8$
TPC and ITS refit	yes
Reject kink daughters	yes
Minimum TPC clusters	70
TPC $\chi^2$ / number of clusters	4
Minimum number of cluster in SPD	1
$(DCA)_{XY}(p_T)$	$< 0.0182 + 0.035p_T^{-1.01} \text{ cm}$
$(DCA)_z$	$< 2 \text{ cm}$
Pair rapidity	$-0.5 < y_{pair} < 0.5$

Table 3.3: Track selection criteria used in Pb-Pb collisions at  $\sqrt{s_{NN}} = 2.76 \text{ TeV}$  and pp collisions at  $\sqrt{s} = 2.76 \text{ TeV}$ .

### 3.5 PID Selection

Pions and kaons are identified using the Time Projection Chamber (TPC). The particle identification in TPC is based on the specific energy loss ( $dE/dx$ ) of each particle inside the medium of the TPC. The value of  $dE/dx$  is extracted using a minimum 20 up to a maximum possible 159 clusters assigned to a track. Because of ionization fluctuation and edge effects (clusters near the boundary of TPC), it is not possible to measure accurately the average of  $dE/dx$ . Thus, the  $\langle dE/dx \rangle$  is calculated by taking the truncated mean of lowest 60% of the measured clusters (removing 40% largest ionization clusters). The measured  $dE/dx$  is then compared with the expectation from a modified Bethe Bloch parameterization [14, 15] for a given particle species. The deviation from the expected  $dE/dx$  value is expressed in units of energy resolution of the TPC, which is 5% for isolated tracks and 6.5% for central collisions. In TPC, kaons can be distinguished from pions up to momenta  $p < 0.7 \text{ GeV}/c$  and protons from pions and kaons up to  $p < 1 \text{ GeV}/c$ . In both Pb-Pb and pp analysis, pions and kaons are considered within two standard deviation ( $2\sigma$ ) from the expected  $dE/dx$  values for each particle species over all momenta. Such a PID selec-

tion may introduce contamination in the signal and the effect of which is discussed in the section 3.6.3. The  $dE/dx$  as a function of momenta for each particle species is shown in Fig. 3.3. The solid black line shows the expected curve of energy loss from parameterized Bethe Bloch [14, 15] function for each particle species.

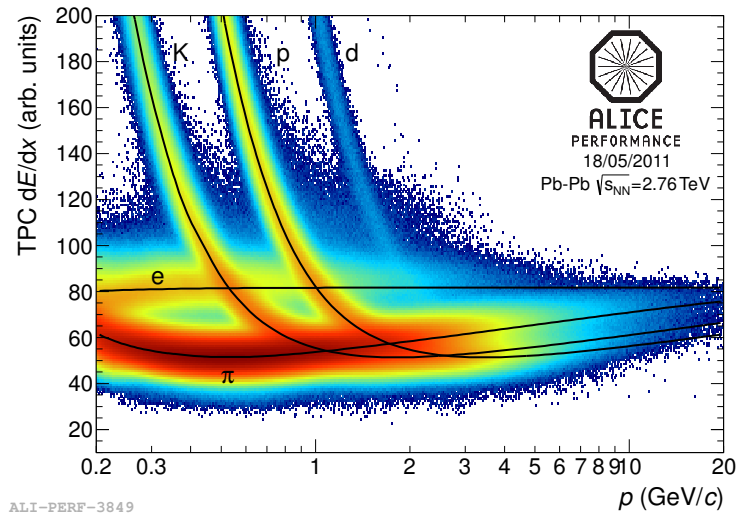


Figure 3.3: (Color online)  $dE/dx$  measured in the TPC as a function of momentum for different particle species in Pb–Pb collision at  $\sqrt{s_{NN}} = 2.76$  TeV. The solid black curves represent the modified Bethe-Bloch parameterization [14, 15]

### 3.6 Signal reconstruction

In a relativistic heavy ion collision, it is difficult to build the  $K^{*0}$  signal by selecting accurately the corresponding pion and kaon daughters, as they are indistinguishable from the other primary tracks in an event. We reconstruct the invariant mass of  $K^{*0}$  by taking the opposite signed pion and kaon pairs from the same event as defined by the equation below:

$$M_{\pi K} = \sqrt{(E_{\pi} + E_K)^2 - (\vec{p}_{\pi} + \vec{p}_K)^2} \quad (3.1)$$

where  $E_{\pi} = \sqrt{m_{\pi}^2 + p_{\pi}^2}$  and  $E_K = \sqrt{m_K^2 + p_K^2}$ .

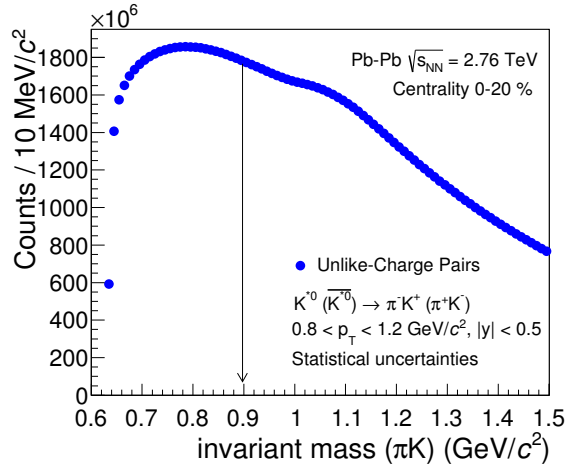


Figure 3.4: (Color online) Unlike charged same event  $\pi K$  invariant mass distribution in 0-20% centrality in Pb–Pb collisions at  $\sqrt{s_{NN}} = 2.76$  TeV. The arrow indicates the PDG value of the mass ( $0.896 \text{ GeV}/c^2$ ) of  $K^{*0}$ .

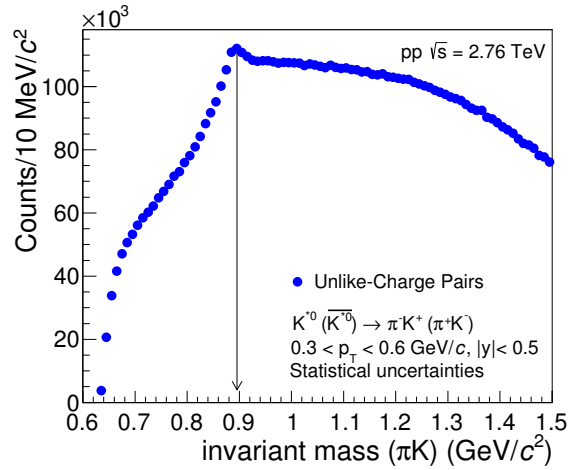


Figure 3.5: (Color online) Unlike charged same event  $\pi K$  invariant mass distribution in minimum bias pp collisions at  $\sqrt{s} = 2.76$  TeV. The arrow indicates the PDG value of the mass ( $0.896 \text{ GeV}/c^2$ ) of  $K^{*0}$ .

However such a event wise construct also includes the background combinations of  $\pi K$  pairs not originating from  $K^{*0}$ . The Fig. 3.4 shows the  $\pi K$  invariant mass distribution in same event in Pb–Pb collision at  $\sqrt{s_{NN}} = 2.76$  TeV, while the Fig. 3.5 shows the same in pp collisions at  $\sqrt{s} = 2.76$  TeV. Due to huge uncorrelated background the signal is not visible in Pb–Pb collisions. To observe the signal we need to subtract the combinatorial background from the same event  $\pi K$  pairs distribution. The combinatorial background estimated using two different methods, event mixing method [16, 17] and like sign method, will be described in the section below.

### 3.6.1 Event mixing method

In event mixing technique, first the event samples are divided in several bins of Z-vertex, centrality percentile from VZERO and event plane angle. This is done in order to keep the event characteristics as similar as possible. For the construction of mixed event background, we have taken 10 bins in Z - vertex (-10 to 10 cm), 10 bins in centrality (0 to 100%) and 12 bins in event plane angle (0 to  $2\pi$ ) for the analysis in Pb–Pb collisions. The distribution of centrality percentile and event plane angle are shown in Fig. 3.6. Then the  $\pi K$  pairs from 5 different events are mixed. The 5 events have the difference in Z-vertex position within 1 cm, difference in centrality percentile within 10 and difference in event plane angle within 20 degree. For the analysis in pp collisions, the binning in event plane angle is not required and the binning in centrality percentile is replaced by the binning in charged particle multiplicity in the TPC. The mixed event distribution statistics is about five times higher than that of the same event distribution. Then the mixed event distribution is normalized in the region of invariant mass of 1.1 to 1.3 GeV/ $c^2$  ( $4 \Gamma^1$  away from the signal), where the pairs are very unlikely to be correlated. The  $K^{*0}$  signal is obtained after the subtraction of normalized mixed event invariant mass distribution from the same event distribution. The following formula shows the process of subtracting the mixed event unlike sign  $\pi K$  pairs from the same event unlike sign  $\pi K$  pairs,

---

<sup>1</sup>the full width at half maximum of  $K^{*0}$  invariant mass distribution

$$N_{K^*0} = N_{K_1^+\pi_1^-} + N_{K_1^-\pi_1^+} - S \times \sum_{i=2}^6 (N_{K_1^+\pi_i^-} + N_{K_1^-\pi_i^+} + N_{K_i^+\pi_1^-} + N_{K_i^-\pi_1^+}), \quad (3.2)$$

where  $S$  is the normalization factor, which is equal to the ratio of the integral of the same event distribution to the mixed event distribution (such a distribution shown in left panel of Fig. 3.7) in the invariant mass range of 1.1 to 1.3  $GeV/c^2$ . The typical value of the normalization factor  $S$  is about 0.22.

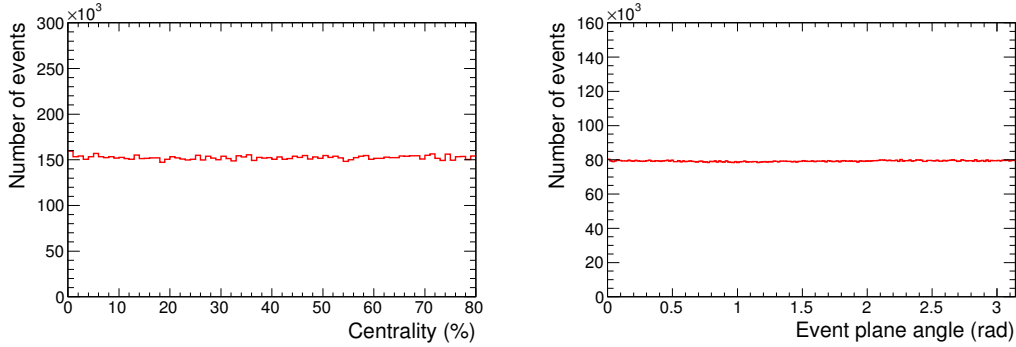


Figure 3.6: Distribution of centrality percentile (left panel) and event plane angle (right panel) in Pb–Pb collision at  $\sqrt{s_{NN}} = 2.76$  TeV.

### 3.6.2 Like sign method

Apart from the mixed event method, there is another method to subtract the background is through the like sign method. In this technique, the combinatorial background is constructed through the invariant mass of pions and kaons of same charge from same event. Since the number of positive and negative particles produced in relativistic heavy ion collisions are not same, the combinatorial background is constructed by taking the geometric mean of number of like sign pairs as shown in equation below

$$N_{K^*0} = N_{K_1^+\pi_1^-} + N_{K_1^-\pi_1^+} - 2 \times \sqrt{N_{K_1^+\pi_1^+} \times N_{K_1^-\pi_1^-}}, \quad (3.3)$$

An example of like sign subtraction is shown in Fig. 3.7.

### 3.6.3 Residual background

Even after the subtraction of combinatorial background, a certain amount of residual backgrounds remain under the  $K^{*0}$  signal (right panel of Fig. 3.7). This residual background may come from the following sources:

1. correlated real  $\pi$  K pairs from particle decays.
2. effect of elliptic flow.
3. correlated but mis-identified  $\pi$  K pairs.

Some particles ( such as  $K_1(1400) \rightarrow K\rho \rightarrow K\pi\pi$ ,  $K^*(1410) \rightarrow K\rho \rightarrow K\pi\pi$ ,  $K_2(1770) \rightarrow K\pi\pi$ , etc ) may decay into oppositely charged  $\pi$  K pairs. The invariant mass calculated from these  $\pi$  K pairs may contribute to the residual background under the  $K^{*0}$  signal. The residual background may come from misidentification of daughter

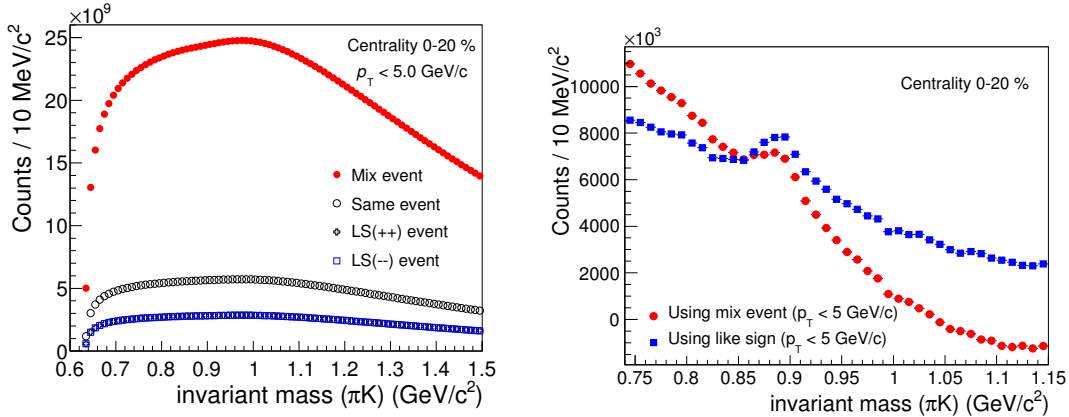


Figure 3.7: (Color online) Left panel:  $\pi$ K invariant mass distribution constructed using unlike charge pairs from the same event, unlike charged pair from mixed (different) events and taking like charge pairs from the same event in 0-20% central Pb–Pb collisions at  $\sqrt{s_{NN}} = 2.76$  TeV. Right panel:  $\pi$  K invariant mass distribution after the subtraction of normalized unlike charged mixed event distribution and like charged distribution from unlike charged same event distribution.

particles. If we select a pion (kaon) candidate with momenta larger than 0.7 GeV/c may be mis-identified as a kaon (pion) candidate. Due to the mis-identification of

decay daughters the signal of  $\rho, \eta$  and  $\omega$  can contribute in the signal region of  $K^{*0}$ . The invariant mass calculated from this mis-identified pairs could not be subtracted away by mixed event background and it remains as a residual background. Compared to mixed event method, the like sign method has the advantage that there is no effect of elliptic flow in the residual background. But the like sign technique has larger statistical uncertainties than mixed event technique. The Fig. 3.7 shows the comparison of the  $\pi$  K invariant mass distribution from event-mixing background subtraction and like sign background subtraction for the collision centrality 0 – 20%. The signal/background in mixed event subtracted case is 0.00133, while in like sign subtracted case 0.00114. So the signal/background ratio from mixed event subtracted case is 1.16 times higher than that in like sign subtracted case. In the present analysis, the combinatorial background is taken from mixed event technique, while the like sign technique is used to study the systematics associated with signal extraction.

### 3.7 Mass and Width

Since the  $K^{*0}$  is a vector meson with spin  $J = 1$ , the invariant mass of  $K^{*0}$  is fitted with a relativistic p-wave Breit Wigner [4] and a residual background function

$$RBW = BW \times PS + RBKG, \quad (3.4)$$

where

$$BW = \frac{M_{K\pi}\Gamma M}{(M_{K\pi}^2 - M^2) + M^2\Gamma^2}, \quad (3.5)$$

$$PS = \frac{M_{K\pi}}{\sqrt{M_{K\pi}^2 + p_T^2}} \times \exp\left(-\frac{\sqrt{M_{K\pi}^2 + p_T^2}}{T}\right), \quad (3.6)$$

$$RBKG = AM_{K\pi}^2 + BM_{K\pi} + C. \quad (3.7)$$

Where PS accounts for the phase space and T is the freeze out temperature,  $M$  and  $\Gamma$  are the mass and invariant mass width of  $K^{*0}$ . The residual background function ( $RBKG$ ) is taken as a polynomial of second order in  $K\pi$  invariant mass ( $M_{K\pi}$ ). The phase space factor is introduced to take into account the effect of direct production of  $K^{*0}$  through the scattering of pions and kaons, present in the medium, through the channel  $K\pi \rightarrow K^{*0} \rightarrow K\pi$ . T is fixed to 156 MeV; this is approximately equal to the chemical freeze out temperature extracted from the yields of produced hadrons [18]. Variation of T by  $\pm 30$  MeV does not produce any significant variation in mass of  $K^{*0}$ .

The top panel of Fig. 3.8 shows the unlike charged same event and mixed event  $\pi K$  invariant mass distribution for the range  $0.3 < p_T < 0.8$  and  $2.5 < p_T < 3.0$  GeV/c in 0-20 % centrality in Pb–Pb collisions. The mixed event distribution is normalized in the region of invariant mass between 1.1 to 1.3 GeV/ $c^2$ . The signal is obtained by subtracting the combinatorial background from the  $\pi K$  invariant mass distribution. The bottom panel in Fig. 3.8 shows the event mixing subtracted  $\pi K$  invariant mass distributions fitted with a p-wave relativistic Breit Wigner function. The red solid line indicates the function given in equation 3.4. The magenta dashed line corresponds to the residual background which is chosen as the polynomial function of second order in  $\pi K$  invariant mass. The left panel of Fig. 3.9 describes same event and mixed event  $\pi K$  invariant mass distribution over the range  $0.3 < p_T < 0.6$  GeV/c for pp collisions. The invariant mass distribution after the mixed event background subtraction is shown on the right panel of Fig. 3.9. Here also the data is fitted with a p-wave relativistic Breit Wigner function and a residual background function. The mass and width of  $K^{*0}$  are extracted from the Breit Wigner fitting parameters. The statistical uncertainties in mass and width are obtained from the errors given in fitting using the ROOT package [15].

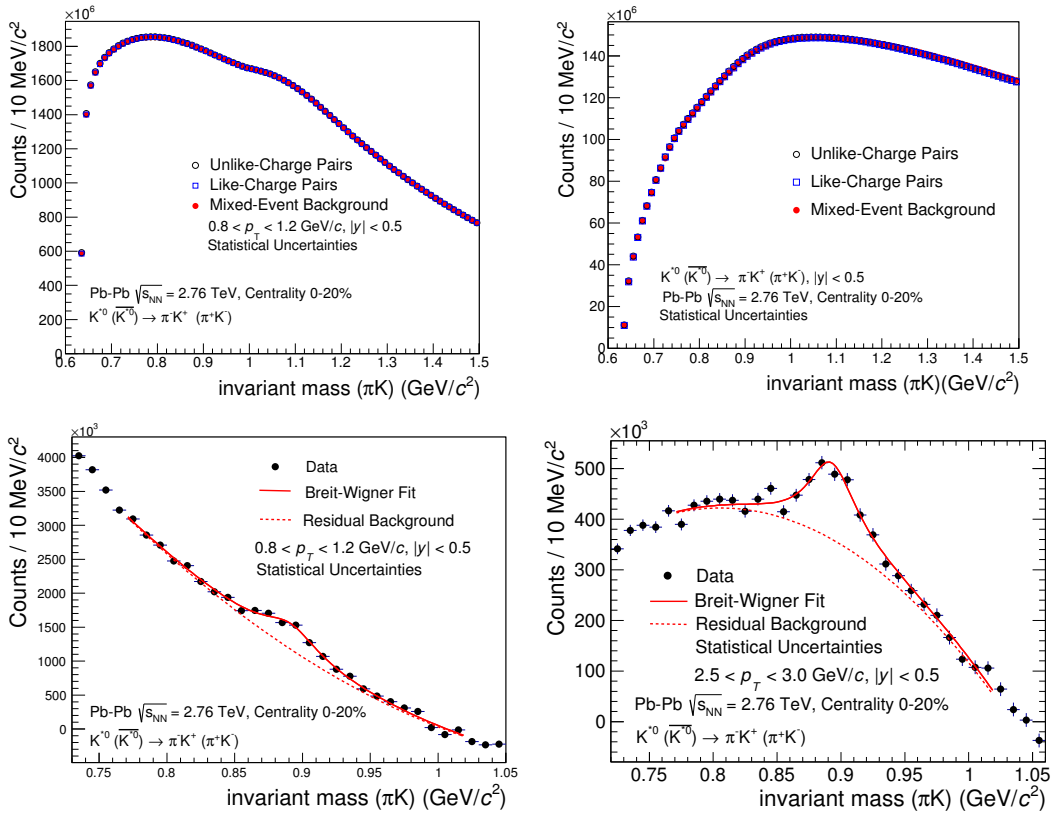


Figure 3.8: (Color online) Top panel: same event and mixed event  $\pi K$  invariant mass distribution over the range  $0.8 < p_T < 1.2$  GeV/c and  $2.5 < p_T < 3.0$  GeV/c for Pb–Pb collisions in 0-20 % centrality at  $\sqrt{s_{NN}} = 2.76$  TeV. Bottom panel: mixed event background subtracted  $\pi K$  pair invariant mass distributions, which is fitted with a p-wave relativistic Breit Wigner function. The uncertainties are statistical only.

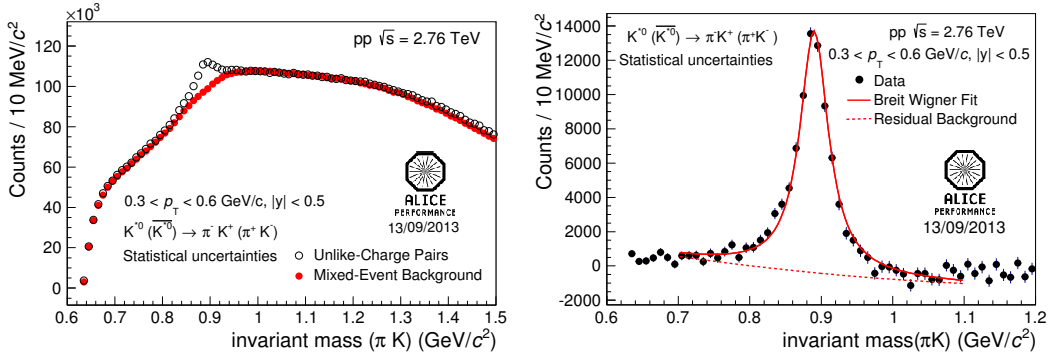


Figure 3.9: (Color online) Left panel: same event and mixed event  $\pi K$  invariant mass distribution over the range  $0.3 < p_T < 0.6$  GeV/c for pp collisions at  $\sqrt{s} = 2.76$  TeV. Right panel: mixed event background subtracted  $\pi K$  pair invariant mass distributions, which is fitted with a p-wave relativistic Breit Wigner function. The uncertainties are statistical only.

### 3.8 Yield extraction

The  $K^{*0}$  signal is obtained by subtracting the combinatorial mixed event background from the same event pair distribution. For the extraction of  $K^{*0}$  yield in a transverse momentum bin, the signal is fitted with a non-relativistic Breit Wigner function,

$$\frac{Y}{2\pi} \times \frac{\Gamma}{(M_{K\pi} - M)^2 + \frac{\Gamma^2}{4}} + AM_{K\pi}^2 + BM_{K\pi} + C. \quad (3.8)$$

Where  $M$  and  $\Gamma$  are the mass and width of the  $K^{*0}$ . The parameter  $Y$  gives the Breit Wigner area. The residual background function is taken as a polynomial of second order in  $\pi K$  invariant mass ( $M_{K\pi}$ ). Since the p-wave relativistic Breit Wigner function has more parameters than the non-relativistic Breit Wigner function, the later is used for the yield extraction to reduce the statistical uncertainty for the yield after fit. For the same reason, the width of resonance is kept fixed to the PDG ( $\Gamma = 0.048$  GeV/c<sup>2</sup>) value [4]. The yield are extracted from both the p-wave relativistic and non-relativistic Breit Wigner function and the difference between them added in the systematic error on the yields. Also the yield are extracted keeping the width as a free parameter in

the fitting. The difference in yields with and without keeping the width parameter free is taken as a part of systematic error on the yields. Alternatively, the yield is also calculated by bin counting method. In the bin counting method the mixed event subtracted same event invariant mass histogram is integrated in the region of invariant mass 0.77 to 1.04  $GeV/c^2$ . Then we take the integral of residual background function in the same range and subtract it from the same event histogram integral. The difference in yields between different methods of yield extraction (function integration and bin counting) are added in the systematic uncertainties.

### 3.9 Efficiency and branching ratio correction

The raw yield of  $K^{*0}$  has to be corrected for the loss due to the detector acceptance, efficiency and the choice of track parameters made to improve the signal over the background. The reconstruction efficiency  $\times$  acceptance (denoted by  $\epsilon$ ) of the detector for  $K^{*0}$  is calculated using the Monte Carlo simulation HIJING [15] for Pb–Pb collisions and PYTHIA [9] for pp collisions. The generated  $K^{*0}$  from monte carlo events within a rapidity interval of  $y < |0.5|$  are passed through the ALICE detector simulation in GEANT3 [10]. The number of  $K^{*0}$  that are reconstructed after passing through detector simulation and the same choices of track parameters as used in real data to the input number of  $K^{*0}$  within the same rapidity interval gives the reconstruction efficiency  $\times$  acceptance.

$$\epsilon(p_T) = \frac{N_{Reconstructed}(p_T)}{N_{Generated}(p_T)} \quad (3.9)$$

Further, this correction factor is scaled to according to the selection criteria used on the TPC energy for particle identification corresponds to the efficiency ( $e_{n\sigma}$ ) of the offline PID selection.

$$\epsilon = \frac{e}{e_{n\sigma}} \quad (3.10)$$

where  $e_{n\sigma}$  is defined by the equation 3.11 considering two tracks of the decay daughter (also assuming the distribution of the energy loss of particles in the medium of TPC

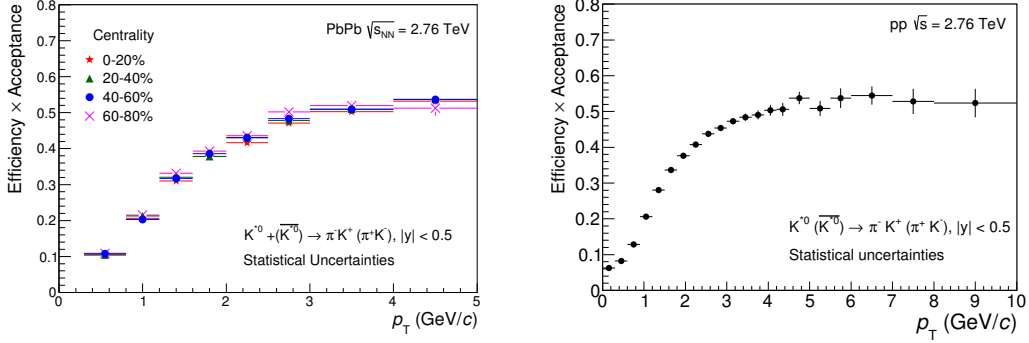


Figure 3.10: (Color online) Efficiency  $\times$  Acceptance of  $K^{*0}$  meson as a function of  $p_T$  in Pb–Pb (left panel) at  $\sqrt{s_{NN}} = 2.76$  TeV and pp collisions at  $\sqrt{s} = 2.76$  TeV (right panel).

as a gaussian)

$$e_{n\sigma} = \left( \frac{2}{\sqrt{\pi}} \int_0^{n/\sqrt{2}} e^{-t^2} dt \right)^2 \quad (3.11)$$

So,  $e_{2\sigma} = 0.911$  for  $2\sigma$  and  $e_{1.5\sigma} = 0.750$  for  $1.5\sigma$  selection placed on the measured  $dE/dx$  of TPC from the theoretical value.

The transverse momentum dependence of the efficiency in Pb–Pb and pp collisions are shown in Fig. 3.10. The efficiency of  $K^{*0}$  has a strong dependence on transverse momentum at low  $p_T$  but it has no dependence on centrality in Pb–Pb collisions. The efficiency of  $K^{*0}$  in Pb–Pb collisions is slightly smaller than that in pp collisions.

The  $K^{*0}$  meson decays to  $K\pi$  ( $K^\pm\pi^\mp$  and  $K^0\pi^0$ ) channel with a branching ratio of 100% [4]. Considering the isospin conservations,  $2/3$  of the  $K^{*0}$  mesons can decay into the channel with oppositely charged daughters while  $1/3$  decay into the channel with neutral daughters. So the yield of  $K^{*0}$  needs to be corrected for branching ratio  $2/3$ , since we could measure only in the channel with charged daughters.

## 3.10 Results

### 3.10.1 Mass and Width

The mass and width of  $K^{*0}$  are obtained from fitting the invariant mass distributions in various momentum bins with a p-wave relativistic Breit Wigner function as described in section 1.7. The Fig. 3.11 and 3.12 show the mass and invariant mass distribution width of  $K^{*0}$  as a function of transverse momentum in Pb–Pb collisions at  $\sqrt{s_{NN}} = 2.76$  TeV in four different collision centralities.

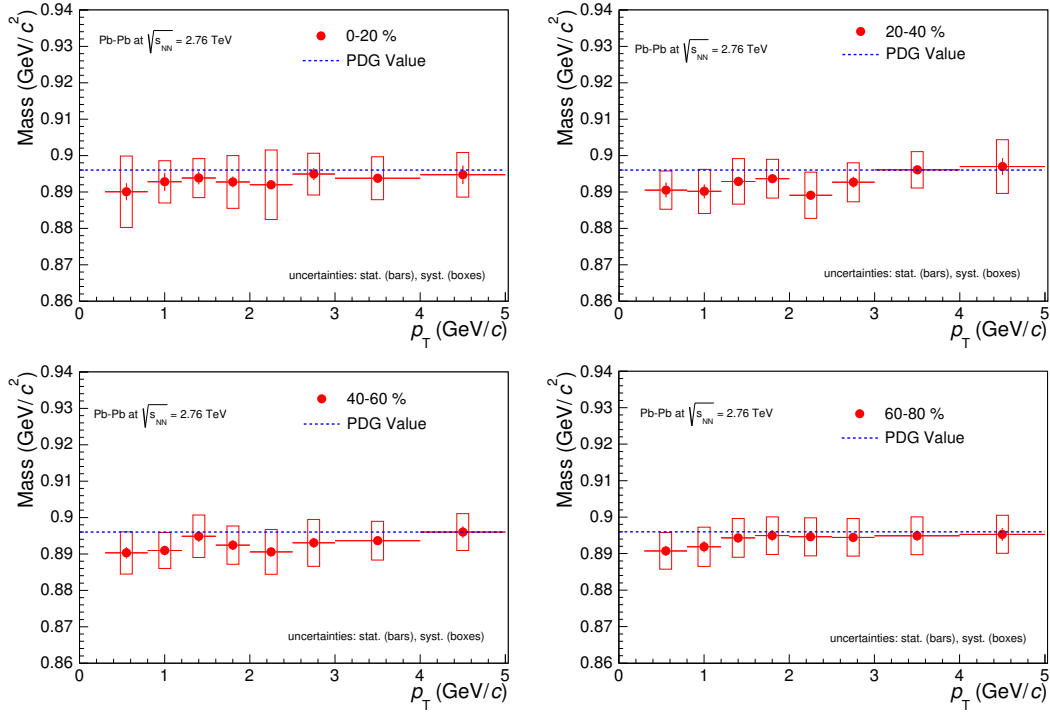


Figure 3.11: (Color online)  $K^{*0}$  mass as a function of  $p_T$  for Pb–Pb collisions at  $\sqrt{s_{NN}} = 2.76$  TeV in four different collision centralities. The blue dotted line represents the PDG value  $896.0 \text{ MeV}/c^2$  for the mass of  $K^{*0}$ .

The blue dotted line is the PDG value. We observed that the mass and invariant mass distribution width of  $K^{*0}$  are consistent with the PDG value within the systematic uncertainties. The mass and invariant mass distribution width of  $K^{*0}$  is compared with the results in minimum bias pp collisions and with HIJING (0-20%)

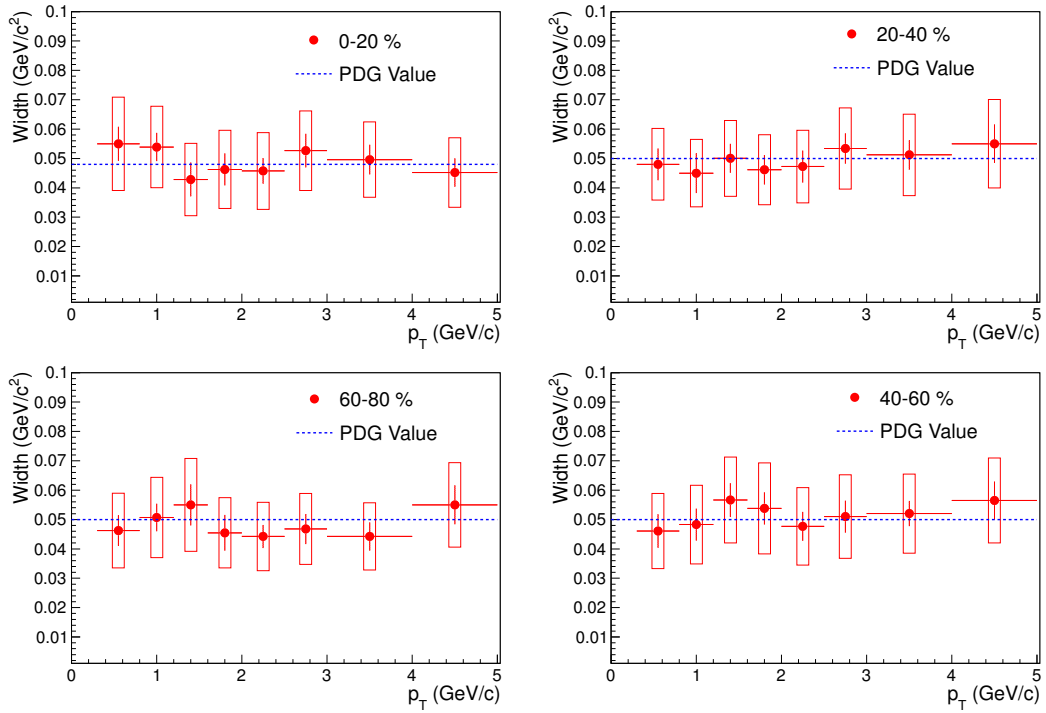


Figure 3.12: (Color online)  $K^{*0}$  invariant mass distribution width as a function of  $p_T$  for Pb–Pb collisions at  $\sqrt{s_{NN}} = 2.76$  TeV in four different collision centralities. The blue dotted line represents the PDG value 48  $\text{MeV}/c^2$  for the invariant mass width of  $K^{*0}$ .

monte carlo simulations in Fig. 3.13. The mass and invariant mass distribution width of  $K^{*0}$  from Pb–Pb, pp collisions and monte carlo HIJING simulations are consistent with the PDG value. A few MeV deviation of mass of  $K^{*0}$  is observed in pp collisions at the lowest  $p_T$ . This may be due to the effect of energy loss of decay daughters of  $K^{*0}$  inside the medium of TPC.

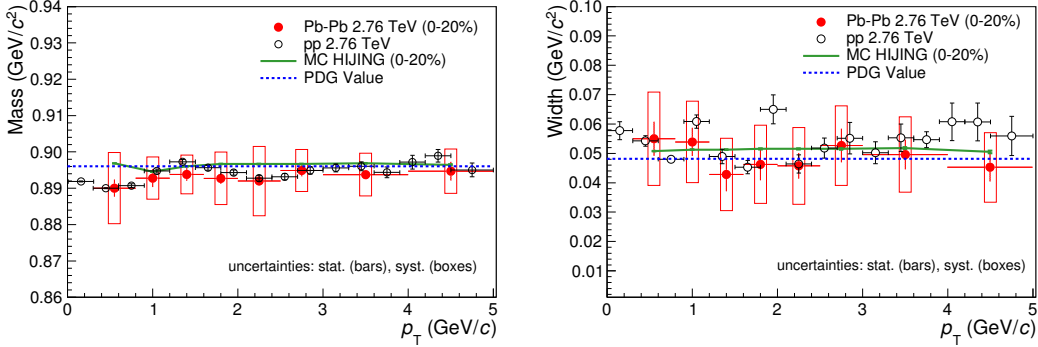


Figure 3.13: (Color online)  $K^{*0}$  mass and width as a function of  $p_T$  for Pb–Pb collisions in 0-20% collision centrality at  $\sqrt{s_{NN}} = 2.76$  TeV. The mass and width is compared with the results in pp collisions  $\sqrt{s} = 2.76$  TeV and MC HIJING (0-20%) simulations. The blue dotted line indicates the PDG value.

### 3.10.2 Transverse momentum distribution

The raw yield of  $K^{*0}$  are computed from the fitted Breit Wigner function in each  $p_T$  bin for different collision centralities in Pb–Pb collisions and for minimum bias pp interactions. The raw spectra are corrected for the efficiency of reconstructing the daughter particle tracks, acceptance of the detector and branching ratio. The spectra in Pb–Pb collisions for different centralities are obtained using the following formula

$$\frac{d^2 N}{dp_T dy} = \frac{N_{raw\ counts}}{N_{evt} \times BR \times dp_T \times dy \times \epsilon}, \quad (3.12)$$

where

- $N_{evt}$  is the number of events for a centrality bin,
- $N_{raw\ counts}$  is the raw yield of  $K^{*0}$  in a momentum bin,

- BR is the branching ratio,
- $dp_T$  is the width of the momentum bin,
- $dy$  is the width of rapidity,
- and  $\epsilon$  is the reconstruction efficiency  $\times$  acceptance of  $K^{*0}$ .

The Fig. 3.14 shows the corrected spectra for  $K^{*0}$  in four different centrality bins in Pb–Pb collisions. The dashed lines denote the Boltzmann Gibbs Blast-Wave function [25], used to extrapolate the  $K^{*0}$  yield and mean transverse momentum in the un-measured region. In the Boltzmann Gibbs Blast-Wave model, the invariant yield of produced particle is given as,

$$\frac{d^2N}{dp_T dy} \propto p_T \times \int_0^R r dr m_T I_0(p_T \sinh \rho / T_{kin}) K_1(m_T \cosh \rho / T_{kin}), \quad (3.13)$$

where the velocity profile  $\rho$  is described by

$$\rho = \tanh^{-1} \left( \left( \frac{r}{R} \right)^n \beta_S \right) \quad (3.14)$$

Here,  $m_T = \sqrt{m^2 + p_T^2}$  is the transverse mass,  $I_0$  and  $K_1$  are the modified Bessel functions,  $r$  is the radial distance in the transverse plane,  $R$  is the radius of the fireball and  $\beta_S$  is the transverse expansion velocity at the surface,  $T_{kin}$  is the temperature of the kinetic freeze-out surface of the produced particle and  $n$  is the exponent in the velocity profile. The corrected spectra are fitted using the equation 3.13 and the fit parameters are given in Table 3.4.

For pp collisions, the spectra is further corrected by vertex reconstruction efficiency and event losses due to trigger and vertex selection. The correction due to the inelastic trigger selection is found from the ALICE van der Meer scans [23]

$$C_{trigger} = 0.881.$$

The correction of signal due to cut on primary vertex is done using the MC PYTHIA. Since the Z-vertex distribution in data and MC does not match (Fig. 3.15), an extra correction factor is introduced. So, the correction factor due to vertex selection is

$$C_{vertex} = \frac{C_{Zvertex}}{\epsilon_{|Z|<10}}$$

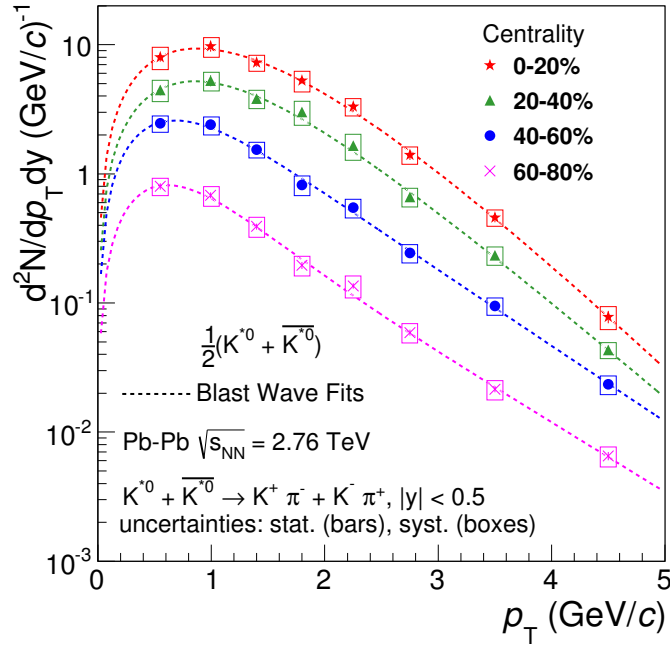


Figure 3.14: (Color online) Transverse momentum spectra of  $K^{*0}$  in various centralities in Pb–Pb collisions at  $\sqrt{s_{NN}} = 2.76$  TeV. The bars denotes the statistical uncertainties, while the boxes are the systematic uncertainties. The dashed line is the fitted Boltzmann Gibbs Blast-Wave function.

Pb–Pb at $\sqrt{s_{NN}} = 2.76$ TeV (BG Blast-Wave parameters)				
Centrality	$T$ (GeV)	$\beta_s$ (c)	$n$	$\chi^2/ndf$
0-20%	$0.117 \pm 0.087$	$0.887 \pm 0.092$	$0.875 \pm 0.277$	0.280
20-40%	$0.202 \pm 0.141$	$0.765 \pm 0.026$	$0.724 \pm 0.644$	0.371
40-60%	$0.280 \pm 0.096$	$0.743 \pm 0.097$	$2.417 \pm 1.460$	0.411
60-80%	$0.249 \pm 0.065$	$0.818 \pm 0.043$	$3.802 \pm 1.929$	0.476

Table 3.4: Boltzmann Gibbs Blast-Wave  $K^{*0}$  spectra in Pb–Pb collisions at  $\sqrt{s_{NN}} = 2.76$  TeV.

where  $C_{Zvertex} = \left(\frac{N_{|Z|<10}^{MC}}{N_{gVtx}^{MC}}\right) / \left(\frac{N_{|Z|<10}^{Data}}{N_{gVtx}^{Data}}\right) = 0.939/0.888 = 1.057$ ;

–  $N_{|Z|<10}^{MC}$  is the number of events in MC after a cut on primary Z -vertex position  $|v_Z| < 10$  cm;

–  $N_{|Z|<10}^{Data}$  is the number of events in data after a cut on primary Z -vertex position  $|v_Z| < 10$  cm;

–  $N_{gVtx}^{MC}$  is the number of events in MC having a reconstructed vertex;

–  $N_{gVtx}^{Data}$  is the number of events in data having a reconstructed vertex;

This factor  $C_{Zvertex}$  takes into account the difference in Z-vertex distribution in MC and data and  $\epsilon_{|Z|<10} = \text{number of } K^{*0} \text{ after primary Z-vertex selection} / \text{number of } K^{*0} \text{ after minimum bias trigger selection} = 0.94$ ; So the overall correction factor is  $C_{vertex} = \frac{C_{Zvertex}}{\epsilon_{|Z|<10}} = 1.057/0.940 = 1.123$ .

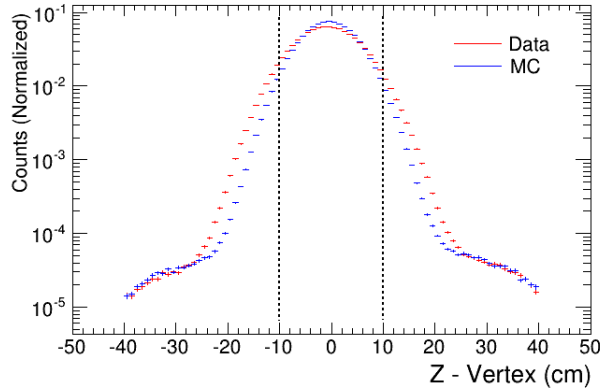


Figure 3.15: (Color online) Z-position of the vertex distribution in data and MC in pp collisions at  $\sqrt{s} = 2.76$  TeV.

The corrected  $K^{*0}$  spectra in pp collisions is obtained by the following equation

$$\frac{d^2 N}{dp_T dy} = \frac{N_{raw\ counts} \times C_{trigger} \times C_{vertex}}{N_{Phys\ Sel} \times dp_T \times dy \times BR \times \epsilon}, \quad (3.15)$$

where

–  $N_{raw\ counts}$  is the raw yield of  $K^{*0}$ ,

–  $N_{Phys\ Sel}$  number of events after physics selection<sup>2</sup>,

<sup>2</sup>the number of events after the CINT1B trigger selection.

- $C_{vertex}$  is the vertex correction factor,
- $C_{trigger}$  is the correction to inelastic trigger class,
- BR is the branching ratio of  $K^{*0}$ ,
- $dp_T$  is the width of the momentum bin,
- $dy$  is the width of rapidity,
- and  $\epsilon$  is the detector acceptance  $\times$  efficiency.

The corrected spectra of  $K^{*0}$  is shown in Fig. 3.16, which is fitted with a Tsallis function [26]. Here also the fit is used to extrapolate the yield and mean transverse momentum in the un-measured region. In Tsallis statistics the invariant yield of produced particle is given as,

$$\frac{d^2N}{dp_T dy} = p_T \times \frac{(n-1)(n-2)}{nT + [nT + m(n-2)]} \times \frac{dN}{dy} \times \left(1 + \frac{m_T - m}{nT}\right)^n, \quad (3.16)$$

where  $m_T = \sqrt{m^2 + p_T^2}$ . This Tsallis function describes both the exponential shape at low  $p_T$  and power law distribution at high  $p_T$ .  $T$  is the inverse slope parameter and  $n$  is the exponent. The spectra is fitted using the equation 3.16 and the fit parameters are given in Table 3.5.

pp at $\sqrt{s} = 2.76$ TeV (Tsallis parameters)			
System	$T$ (GeV)	$n$	$\chi^2/ndf$
pp: MB	$0.248 \pm 0.005$	$7.40 \pm 0.16$	0.25

Table 3.5: Tsallis fit parameters for the  $K^{*0}$  spectra in pp collisions at  $\sqrt{s} = 2.76$  TeV.

### 3.10.3 $K^{*0}$ -meson yield per unit rapidity

The yield of  $K^{*0}$  per unit rapidity ( $dN/dy$ ) is calculated by integrating the spectra in the measured range and integral of the fit in the extrapolated region. The low- $p_T$  extrapolation region ( $p_T < 0.3$  GeV/c) accounts for 5% of the total  $K^{*0}$  yield, while the high  $p_T$  region ( $p_T > 5$  GeV/c) accounts for 0.1 % in Pb–Pb collisions. In pp

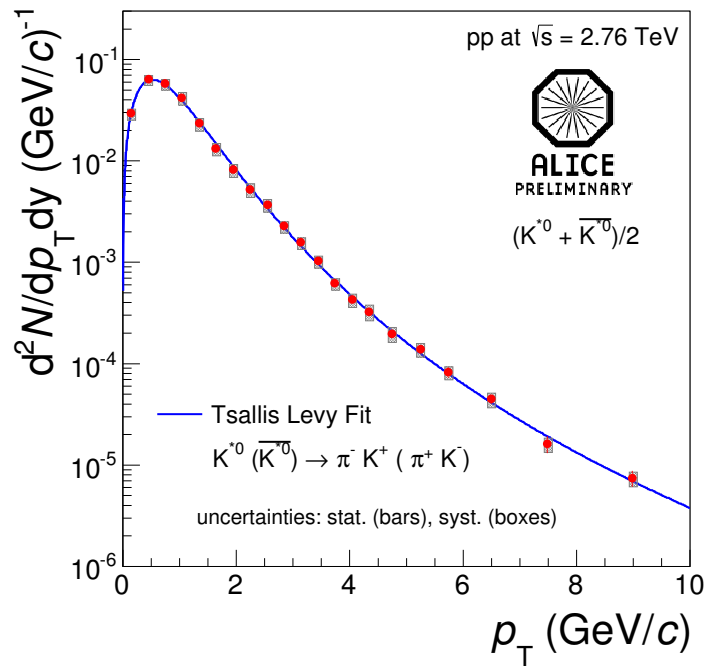


Figure 3.16: (Color online) Transverse momentum spectra of  $K^{*0}$  in minimum bias pp collisions at  $\sqrt{s} = 2.76$  TeV. The bars denotes the statistical uncertainties, while the boxes are the systematic uncertainties. The dashed line is the fitted with a Tsallis function.

collisions, the extrapolation is only at high  $p_T$  ( $p_T > 10$  GeV/c), which accounts for 0.01% of the total  $K^{*0}$  yield. The default value of  $dN/dy$  is calculated using the following equation,

$$dN/dy = I_{low} + I_{hist} + I_{high} \quad (3.17)$$

where  $I_{low} = \int_0^{0.3} f(p_T) dp_T$ ,  $I_{high} = \int_{5.0}^{30} f(p_T) dp_T$ , and  $I_{hist}$  denotes the integral of the histogram in the measured region for the Pb–Pb collisions, while for pp collisions the extrapolation is only for the high  $p_T$  region ( $p_T > 10$  GeV/c) and  $f(p_T)$  is either the Boltzmann Gibbs Blast-Wave or the Tsallis function for Pb-Pb and pp collisions respectively. The statistical uncertainties in extrapolated regions are assumed to be fully correlated with the statistical uncertainties in the measured region and the statistical uncertainty in the  $dN/dy$  are calculated using the equation below

$$\sigma_{dN/dy} = \sigma_{I_{low}} + \sigma_{I_{hist}} + \sigma_{I_{high}} \quad (3.18)$$

where  $\sigma_{I_{low}}$  and  $\sigma_{I_{high}}$  are calculated using the function `IntegralError()` in ROOT [15] package.

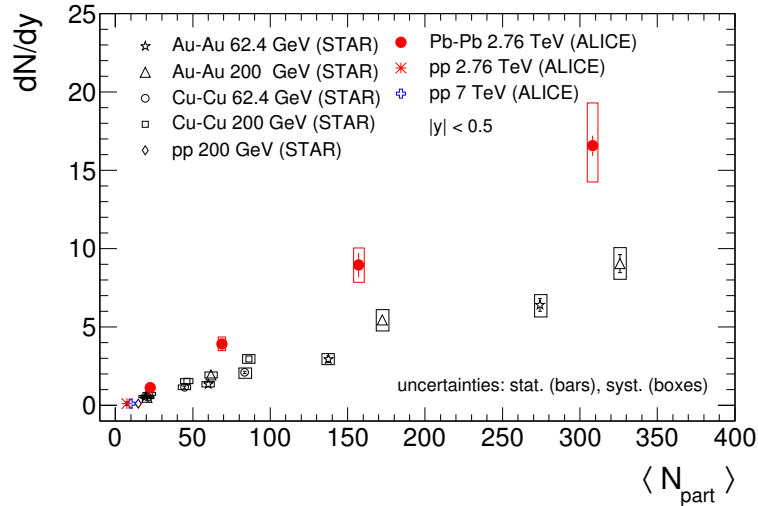


Figure 3.17: (Color online)  $dN/dy$  of  $K^{*0}$  meson as a function of number of participant in Pb–Pb collisions at  $\sqrt{s_{NN}} = 2.76$  TeV and pp collisions at  $\sqrt{s} = 7$  TeV [32]. The results are compared with the measurements from STAR experiment [4, 5].

The  $dN/dy$  is also obtained by integrating only the fitting function (either BG Blast-Wave or Tsallis function). The difference in  $dN/dy$  calculated from fit function only with default value (equation 1.16) is added in the systematic error on the  $dN/dy$ . The Fig. 3.17 shows  $dN/dy$  as a function of number of participants in Pb–Pb and pp collisions. The results are compared with the measurements at lower energy from the STAR experiment [4, 5]. The value of the  $dN/dy$  increases as one goes from peripheral to the central collisions. Also, the  $dN/dy$  increases with the increase in beam energy.

### 3.10.4 $K^{*0}$ -meson $\langle p_T \rangle$

The average transverse momentum of  $K^{*0}$  is defined as

$$\langle p_T \rangle = \frac{\int p_T f(p_T) dp_T}{\int f(p_T) dp_T}, \quad (3.19)$$

where  $f(p_T)$  is either the Boltzmann Gibbs Blast-Wave function taken to calculate the  $\langle p_T \rangle$  value for the extrapolation region in Pb–Pb collisions, or the Tsallis Levy function used for the same in pp collisions. The default value of the  $\langle p_T \rangle$  is calculated using the following formula

$$\langle p_T \rangle = \frac{\langle p_T \rangle_{low} I_{low} + \sum_i \bar{p}_T^i dp_T^i I_i + \langle p_T \rangle_{high} I_{high}}{I_{low} + I_{hist} + I_{high}} \quad (3.20)$$

where  $\bar{p}_T^i$  is the bin centre,  $dp_T^i$  is the bin width and  $I_i$  is the yield in the  $i^{th}$   $p_T$  bin.

The statistical uncertainty in  $\langle p_T \rangle$  is calculated using the following equation

$$\sigma_{\langle p_T \rangle} = \frac{\langle p_T \rangle_{low} \sigma_{I_{low}} + \sqrt{\sum_i (\bar{p}_T^i dp_T^i \sigma_{I_i})^2} + \langle p_T \rangle_{high} \sigma_{I_{high}}}{I_{low} + I_{hist} + I_{high}} \quad (3.21)$$

The  $\langle p_T \rangle$  is also calculated from the fitting function only. The difference in the value  $\langle p_T \rangle$  using only fit function with the default value (equation 1.19) is added in the systematic error on  $\langle p_T \rangle$ . The Fig. 3.18 shows the mean transverse momentum as a function of number of participant nucleons. The  $K^{*0}$  results in Pb–Pb collisions are compared with results at  $\sqrt{s} = 2.76$  and 7 TeV [32] and also with the measurements

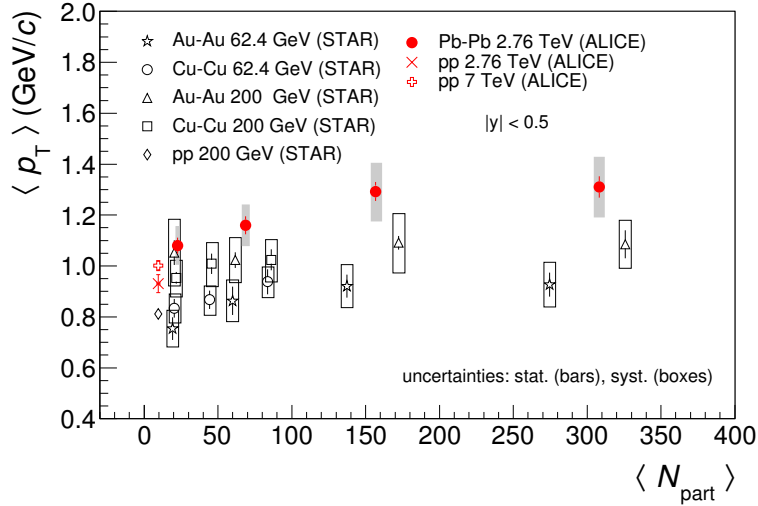


Figure 3.18: (Color online)  $\langle p_T \rangle$  of  $K^{*0}$  meson as a function of number of participants in Pb–Pb collisions at  $\sqrt{s_{NN}} = 2.76$  TeV and pp collisions at  $\sqrt{s} = 2.76$  and 7 TeV [32]. The results are compared with measurements from STAR experiment [4, 5].

from STAR experiment [4, 5] at RHIC. The  $\langle p_T \rangle$  of  $K^{*0}$  in central Pb–Pb collisions is found to be higher than the peripheral Pb–Pb and minimum bias pp collisions. Similar centrality dependence is observed in measurements at RHIC. The  $\langle p_T \rangle$  of  $K^{*0}$  at LHC energies are about 15% higher than that measured at RHIC energies which is consistent with the increase in the radial boost of produced particles at higher energies [21]. The  $\langle p_T \rangle$  of  $K^{*0}$  is also compared with the measurements of  $\pi^-$ ,  $K^-$  and  $\bar{p}$  [21] in Fig. 3.19. It shows that the  $\langle p_T \rangle$  increases with the mass of the hadron, which indicates the hydrodynamic like behaviour of the system that the lighter particles will move faster than the heavier one. The  $\langle p_T \rangle$  of particles measured in pp collisions at  $\sqrt{s} = 0.9, 2.76$  and 7 TeV are shown in Fig. 3.20. The results are compared with the measurements from STAR experiment [4, 5] at  $\sqrt{s} = 200$  GeV. The red dashed line indicates the parameterization from the ISR experiment [34]. We observe the rise in  $\langle p_T \rangle$  with the increase in beam energy, which can be understood through the effect of color reconnections [27] between the strings produced in multiple parton interactions. The  $\langle p_T \rangle$  of  $K^{*0}$  is in agreement with the trend for other particles

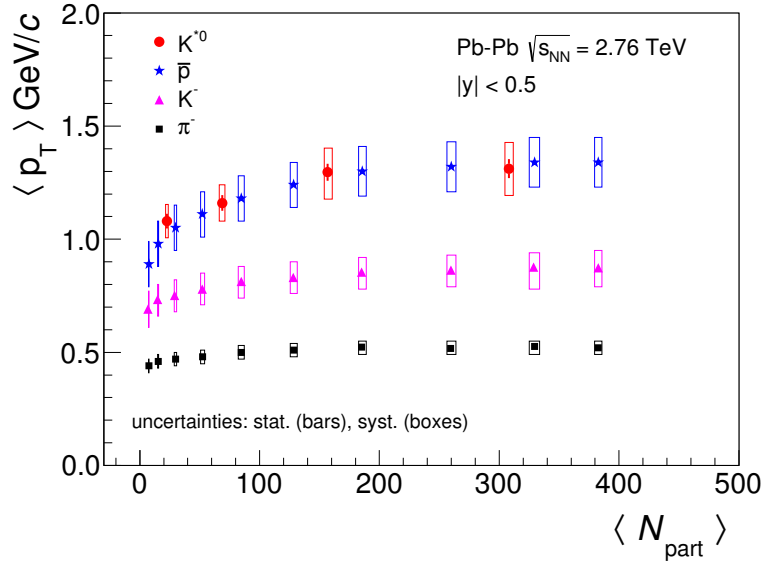


Figure 3.19: (Color online) Comparison of  $\langle p_T \rangle$  of  $K^{*0}$  meson with  $\pi$ ,  $K$  and  $p$  in Pb-Pb collisions at  $\sqrt{s_{NN}} = 2.76$  TeV [21].

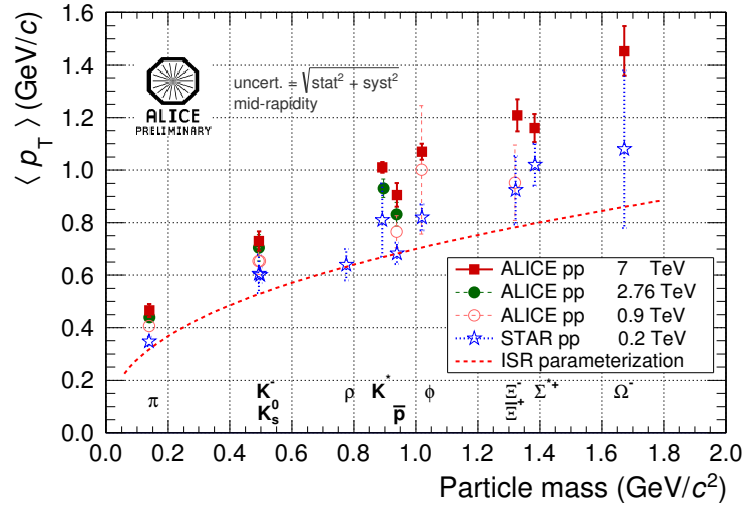


Figure 3.20: (Color online)  $\langle p_T \rangle$  as a function of particle mass in pp collisions [34, 4, 32].

in pp collisions.

System	$\langle N_{part} \rangle$	$dN/dy$	$K^{*0}/K^-$	$\langle p_T \rangle (GeV/c)$
Pb-Pb:0-20%	308.1±3.7	16.6 ± 0.6±2.5	0.19±0.01±0.03	1.31±0.04±0.11
Pb-Pb:20-40%	157.2±3.1	9.0±0.8±1.1	0.23±0.01±0.03	1.29±0.04±0.01
Pb-Pb:40-60%	68.6±2.0	3.9±0.3±0.4	0.27±0.02±0.04	1.16±0.03±0.08
Pb-Pb:60-80%	22.52±0.77	1.13±0.08±0.10	0.30±0.02±0.04	1.08±0.03±0.07
pp:MB	2.0	0.075±0.002±0.010	0.075±0.002±0.010	0.933 ±0.005±0.035

Table 3.6:  $dN/dy$ ,  $K^{*0}/K^-$  and  $\langle p_T \rangle$  of  $K^{*0}$  in Pb-Pb collisions  $\sqrt{s_{NN}} = 2.76$  TeV and pp collisions at  $\sqrt{s} = 2.76$  TeV.

### 3.10.5 Particle ratio:

The lifetime of  $K^{*0}$  is comparable to that of fireball produced in heavy-ion collisions, hence the decay daughters are affected by the late stage hadronic interactions. The decay daughters could be re-scattered by other hadrons in the medium, causing a change in the momentum of the decay daughters and we will not be able to reconstruct back the  $K^{*0}$ . Therefore, the signal is lost due to the re-scattering and the  $K^{*0}$  yield will be decreased. In the other scenario, the pions and kaons in the hadronic medium may go through pseudo-elastic interactions, producing the  $K^{*0}$ . In this case the  $K^{*0}$  yield will be increased. These two competing processes, re-scattering and re-generation, can be understood through the resonance to non-resonance ratio such as  $K^{*0}/K^-$ . This ratio can be studied as a function of centrality in heavy-ion collisions and compared with the results from pp collisions, where the decay daughter of resonances are expected to be less affected by hadronic interactions. Qualitatively if the re-scattering effect is dominant in the hadronic medium, one would naively expect the  $K^{*0}/K^-$  ratio to be decreased in more central collisions compared to the peripheral A+A and minimum bias pp collisions while the dominance of re-generation effect will increase the  $K^{*0}/K^-$  ratio in central collisions with respect to the peripheral

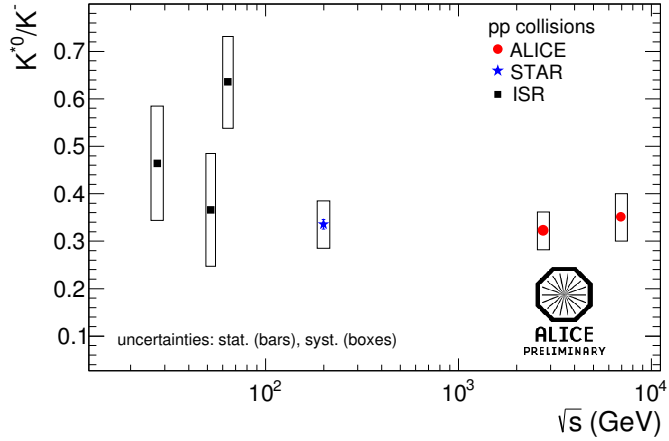


Figure 3.21: (Color online)  $K^{*0}/K^-$  as a function of beam energy in pp collisions. The solid red symbols are the measurements in ALICE, the solid black squares are the measurements in SPS [19] and the blue star denotes the measurements in STAR [4, 5]. open boxes denote the systematic uncertainties and the bars denote the statistical uncertainties.

A+A and pp collisions. We have extracted  $K^{*0}/K^-$  ratio in four different centrality bins in Pb–Pb collisions and also in minimum bias pp interactions. Fig. 3.21 shows the  $K^{*0}/K^-$  ratio as a function of beam energy in pp collisions. The  $K^{*0}/K^-$  ratio in pp collisions at  $\sqrt{s} = 2.76$  TeV is compared with the results at 7 TeV and also with lower energy measurements at SPS [19] and RHIC [4, 5]. The  $K^{*0}/K^-$  ratio is found to be independent of beam energy in pp collisions. The  $K^{*0}/K^-$  ratio as a function of beam energy in heavy-ion and pp collisions are shown in Fig. 3.22. The results are compared with the earlier measurements from SPS [19], RHIC [4, 5] and ALICE [32]. The ratio is also compared with the calculation from a Thermal model [18] at a given chemical freeze out temperature of 156 MeV. The value of  $K^{*0}/K^-$  ratio in Pb–Pb collisions is smaller than that in pp collisions and thermal model expectation. It demonstrates the effect of hadronic re-scattering in heavy ion collisions. From HBT [3, 24] studies, it is observed that the radii of the fireball increases approximately linearly with the  $(dN_{ch}/d\eta)^{1/3}$ . So the variable  $(dN_{ch}/d\eta)^{1/3}$  can be used as a proxy to the radius of the system formed in heavy ion collisions. The Fig. 3.23 shows the  $K^{*0}/K^-$  ratio as a

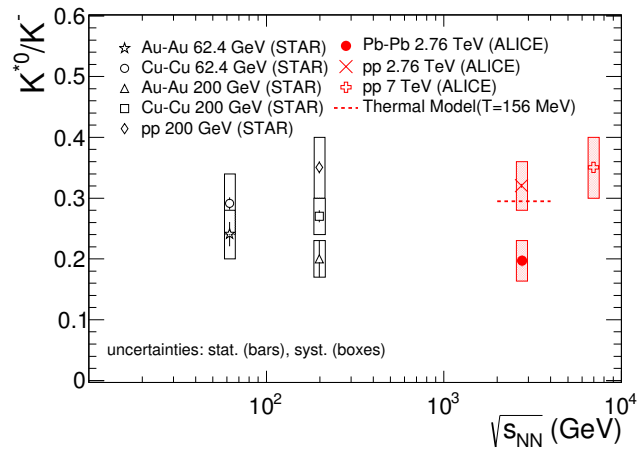


Figure 3.22: (Color online)  $K^{*0}/K^-$  as a function of beam energy in A+A and pp collisions [4, 32]. The solid red symbols are the measurements in ALICE, the solid black squares are the measurements in SPS [19] and the blue star denotes the measurements in STAR [4, 5]. open boxes denote the systematic uncertainties and the bars denote the statistical uncertainties.

function of  $(dN_{ch}/d\eta)^{1/3}$ . If one assumes that the strength of re-scattering related to

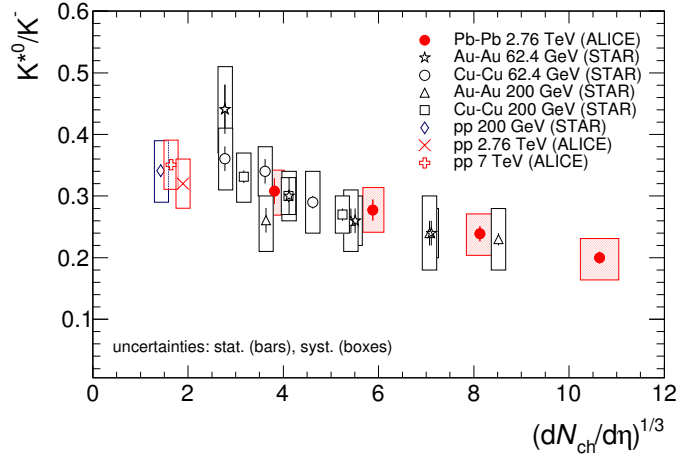


Figure 3.23: (Color online)  $K^{*0}/K^-$  ratio as a function of  $(dN_{ch}/d\eta)^{1/3}$ . The results are compared with the measurements in pp collisions at  $\sqrt{s} = 2.76$  TeV and 7 TeV [32] in ALICE. Also the results are compared with the lower energy measurements at STAR experiment [4, 5]. The open boxes denote the systematic uncertainties and the bars denote the statistical uncertainties.

the distance travelled by the decay products through the hadronic medium, then one naively expects  $K^{*0}/K^-$  to decrease exponentially with  $(dN_{ch}/d\eta)^{1/3}$ . The observed dependence of  $K^{*0}/K^-$  ratio is consistent with the expected behaviour. The decrease in  $K^{*0}/K^-$  ratio for more central collisions may be due to the dominance of the re-scattering of decay daughters over the re-generation of  $K^{*0}$  in more central collisions. Also, the indication of further decrease in  $K^{*0}/K^-$  ratio at the highest  $(dN_{ch}/d\eta)^{1/3}$  may be attributed to a larger fireball size (and lifetime) accessible at LHC energies. The  $K^{*0}/K^-$  ratio is also compared with the  $\phi/K^-$  ratio in Fig. 3.24. The  $K^{*0}$  and  $\phi$  meson have almost similar mass, same spin but different lifetime and quark content. The  $\phi/K^-$  ratio does not show any dependence on collision centrality which is consistent considering that the lifetime of  $\phi$  mesons is 10 times larger than that of  $K^{*0}$  and hence the former is expected to be not affected by the re-scattering effects. The quark content of  $\phi$ -meson is  $s\bar{s}$ , while that of  $K^{*0}$  is  $d\bar{s}$ . So the  $\phi/K^{*0}$  ratio may

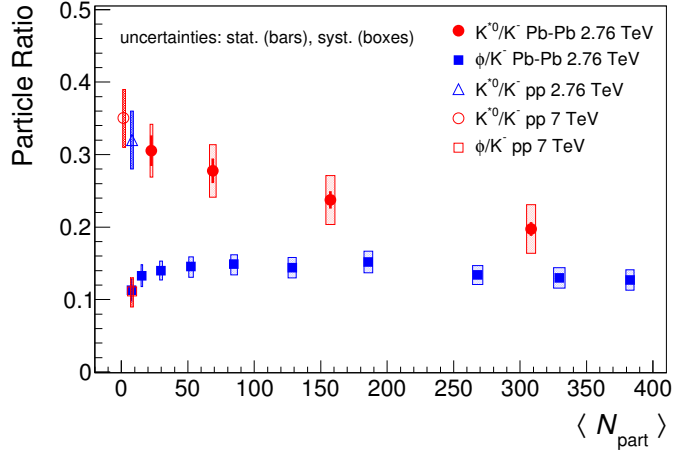


Figure 3.24: (Color online)  $K^{*0}/K^-$  and  $\phi/K^-$  ratio as a function of mean number of participating nucleons. The results are compared with the measurements in pp collisions at  $\sqrt{s} = 2.76$  TeV and 7 TeV [32]. the open boxes denote the systematic uncertainties and the bars denote the statistical uncertainties.

give some indication on strangeness enhancement at LHC energies. The Fig. 3.26 shows the  $\phi/K^{*0}$  ratio as a function of  $(dN_{ch}/d\eta)^{1/3}$  in Pb–Pb collisions. The results are compared with the measurement in pp collisions at  $\sqrt{s} = 7$  TeV and measurements at lower energies in STAR experiment [4, 5].

### 3.10.6 Study of spectral shapes

The decrease in  $K^{*0}/K^-$  ratio as a function of collision centrality and smaller value with respect to pp collisions and Thermal model expectation indicates the dominance of re-scattering effects over the re-generation. The UrQMD [31] calculation for RHIC energies predicts the ratio to be dependent on transverse momentum and to be lower in low  $p_T$ . To study the  $p_T$  dependence of  $K^{*0}$  suppression, the spectral shape of  $K^{*0}$  is studied with the predictions from the Boltzmann Gibbs Blast-Wave function. The ALICE [21] has measured the freeze out temperature ( $T_{kinetic}$ ), the velocity profile exponent ( $n$ ) and radial flow velocity of the surface ( $\beta_s$ ) through the combined fit of  $\pi^\pm$ ,  $K^\pm$  and  $p(\bar{p})$  spectra. The combined fit describes the  $\pi^\pm$ ,  $K^\pm$  and  $p(\bar{p})$  spectra

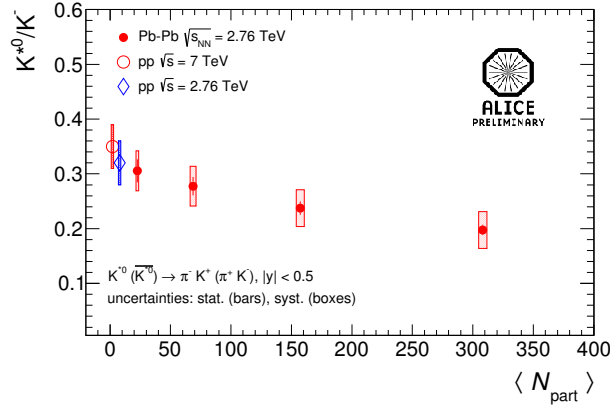


Figure 3.25: (Color online)  $K^{*0}/K^-$  ratio as a function of mean number of participating nucleons. The results are compared with the measurements in pp collisions at  $\sqrt{s} = 2.76$  TeV and 7 TeV [32]. The open boxes denote the systematic uncertainties and the bars denote the statistical uncertainties.

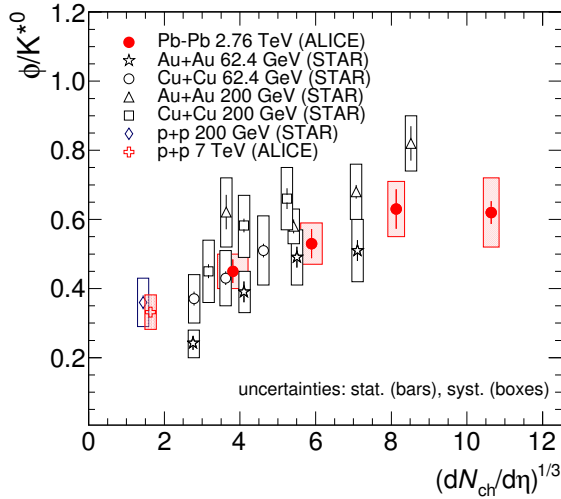


Figure 3.26: (Color online)  $\phi/K^{*0}$  ratio as a function of  $(dN_{ch}/d\eta)^{1/3}$ . The results are compared with the measurements in pp collisions at  $\sqrt{s} = 2.76$  TeV and 7 TeV [32] in ALICE. Also the results are compared with the lower energy measurements at STAR experiment [4, 5]. The open boxes denote the systematic uncertainties and the bars denote the statistical uncertainties.

well below  $p_T < 3 \text{ GeV}/c$ . The following parameters (Table 3.7) are taken for 0-20 % and 60-80 % centrality from the above reference:

Centrality %	$T_{kinetic}(GeV)$	$\beta_s (c)$	$n$
Pb-Pb : 0-20	0.097	0.88	0.73
Pb-Pb : 60-80	0.13	0.80	1.38

Table 3.7: BG Blast-Wave parameters at  $\sqrt{s_{NN}} = 2.76 \text{ TeV}$

First we generate the Blast-Wave spectra for  $K^{*0}$  using the above parameters and then normalize this spectra using the  $K^{*0}/K^-$  ratio from a Thermal model [18] with a chemical freeze-out temperature of 156 MeV, such that the integral of the predicted spectra gives the expected yield of  $K^{*0}$  at the chemical freeze-out. So, the normalization factor is the yield of  $K^-$  in Pb-Pb collisions measured in ALICE [21] multiplied by the  $K^{*0}/K^-$  ratio from Thermal model [18]. Mathematically,

$$normalization\ factor = Y(K^-)_{Pb-Pb} \times Y\left(\frac{K^{*0}}{K^-}\right)_{ThermalModel} \quad (3.22)$$

The Fig. 3.27 shows the comparison of  $K^{*0}$  spectra with the above mentioned normalized Blast-Wave predictions for the 0 – 20% central and 60 – 80% peripheral Pb-Pb collisions. The ratio between the predicted spectra and data is shown in the bottom panel. It is observed that the data is about a factor of 0.6 below the Blast-Wave predictions and there is no dependence on the transverse momentum up to  $p_T < 2 \text{ GeV}/c$  for the central collisions as expected from UrQMD calculation. For the peripheral collisions, the Blast-Wave prediction reproduces the spectral shape of  $K^{*0}$ . Since  $\phi$  meson is expected to be not affected by the hadronic interactions, we have also generated similar Blast-Wave predictions for the  $\phi$  meson and compared to the data. We observe that the spectral shape of  $\phi$  meson is well described by the Blast-Wave predictions.

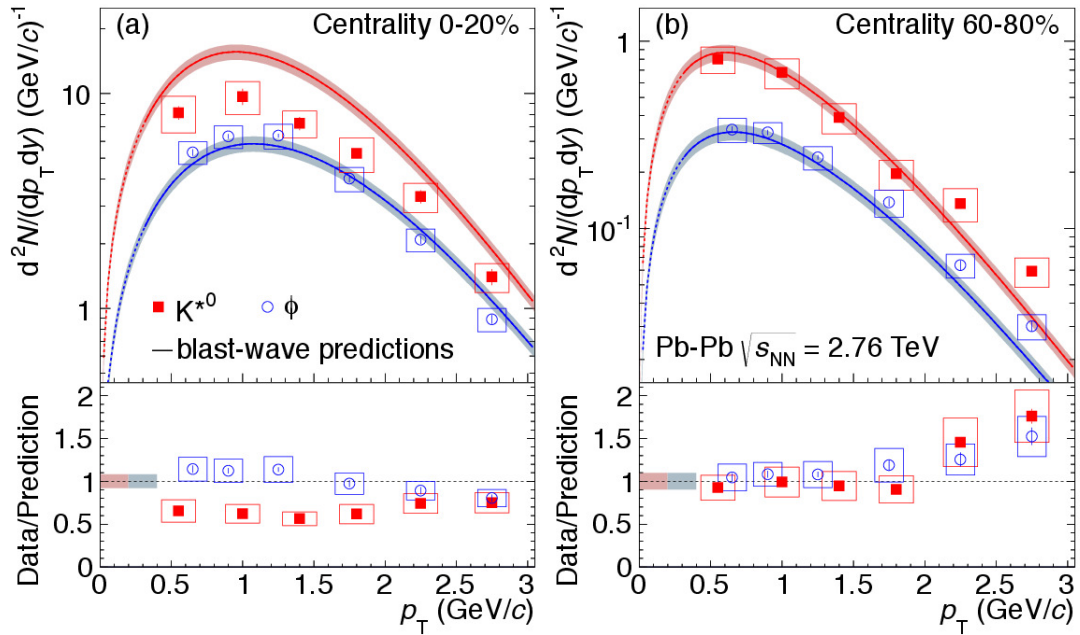


Figure 3.27: (Color online) Comparison of spectral shape of  $K^{*0}$  and  $\phi$  with respect to Boltzmann Gibbs Blast-Wave predictions. The open boxes denote the systematic uncertainties and the bars denote the statistical uncertainties.

### 3.10.7 Nuclear modification factor ( $R_{CP}$ and $R_{AA}$ )

The nuclear modification factor  $R_{CP}$  (central to peripheral) and  $R_{AA}$  (scaled to pp data) are the variables to study the effect of the medium formed in heavy-ion collisions. They are very sensitive to the system size and density of the medium produced in such collisions. The nuclear modification factor  $R_{CP}$ , the ratio of the yields in the central collision to that in the peripheral collision normalized with the binary collision, is mathematically defined as

$$R_{CP} = \frac{N_{coll}^{peripheral}}{N_{coll}^{central}} \times \frac{(d^2N/dydp_T)_{central}}{(d^2N/dydp_T)_{peripheral}} \quad (3.23)$$

Here one assumes that the in-medium effects in peripheral collisions is similar to what happens in pp collisions. Another way of representing the nuclear modification factor through  $R_{AA}$ , where the yields in the heavy-ion collisions normalized to that in the pp collisions, is defined as

$$R_{AA} = \frac{1}{\langle T_{AA} \rangle} \times \frac{(d^2N/dydp_T)_{AA}}{(d^2\sigma/dydp_T)_{pp}} \quad (3.24)$$

Where  $\langle T_{AA} \rangle (= \langle N_{coll} \rangle / \sigma_{NN})$  is average nuclear thickness function,  $\langle N_{coll} \rangle$  is the average number of binary nucleon-nucleon collisions calculated using MC Glauber simulations and  $\sigma_{NN}$  is the inelastic pp cross-section is taken to be  $62.4 \pm 2.4_{-4.0}^{+1.2}$  mb [23]. Fig. 3.28 shows the  $R_{CP}$  for  $K^{*0}$  meson. The value of  $R_{CP}$  is much lower than unity, indicating the effect of strongly interacting matter produced in heavy-ion collisions. Further, it is compared with that of the  $\Lambda$  baryon,  $K_S^0$  and  $\phi$  meson. It is observed that at low  $p_T$  ( $< 2$  GeV/c)  $R_{CP}$  of  $K^{*0}$  is smaller than that of  $\Lambda$ ,  $K_S^0$  and  $\phi$ . This may be due to the effect of hadronic re-scattering dominantly at low  $p_T$ . At intermediate  $p_T$  ( $> 2$  GeV/c) the  $R_{CP}$  of  $K^{*0}$  follows the trend of the  $K_S^0$  meson. Such a behavior is expected in the intermediate momentum region from a quark recombination model [35] of particle production. The  $R_{AA}$  for  $K^{*0}$  meson for four different centrality bins are shown in Fig. 3.29. It is compared with that of charged hadrons [36] and  $\phi$  mesons. The  $R_{AA}$  of  $K^{*0}$  is found to be decreasing as one goes from peripheral to central collisions. It is observed that for central collisions at low  $p_T$  the  $R_{AA}$  of  $K^{*0}$  is significantly lower than charged hadrons, dominated by

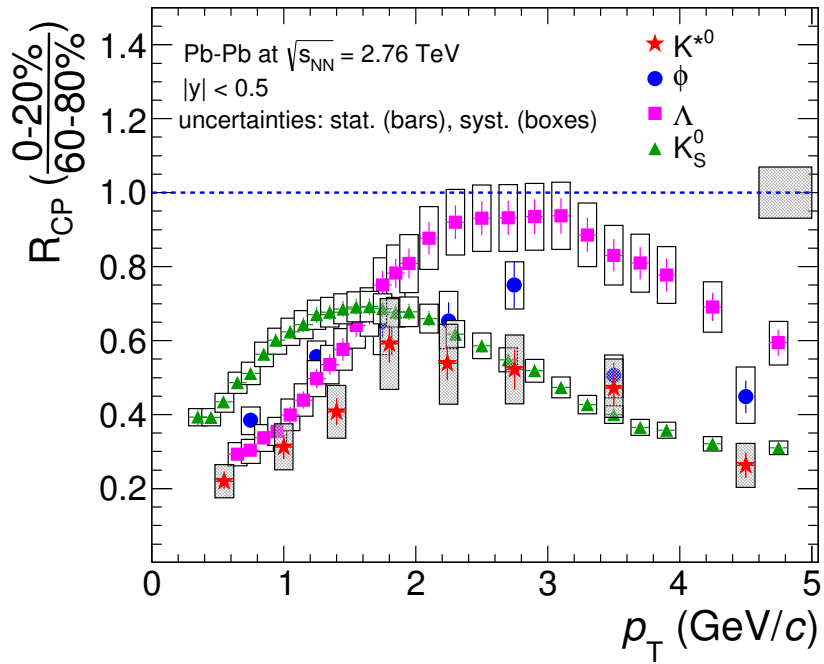


Figure 3.28: (Color online) Nuclear modification factor  $R_{CP}$  of  $K^{*0}$  as a function of  $p_T$ .

The results are compared with that of  $\Lambda$  baryon,  $K_S^0$  and  $\phi$  meson [43].

pions, and comparable with charged hadrons and  $\phi$  mesons at intermediate  $p_T$ . This is likely to be the effect of additional hadronic re-scattering for the decay daughters of  $K^{*0}$  at low transverse momentum.

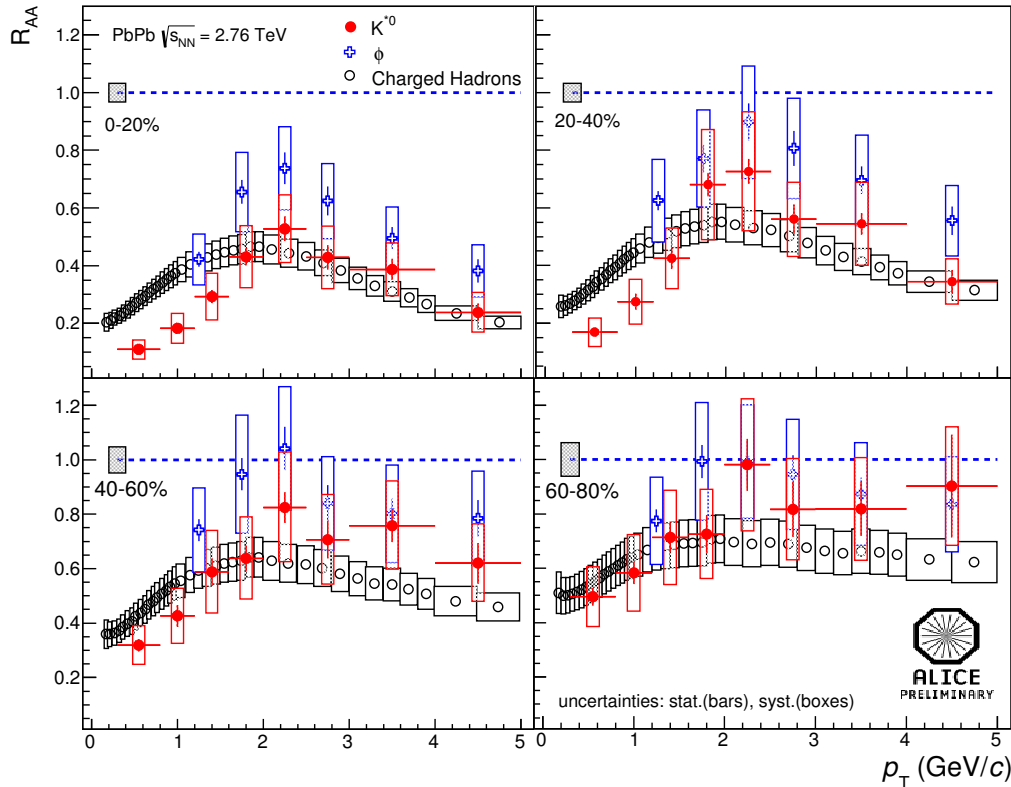


Figure 3.29: (Color online) Nuclear modification factor  $R_{AA}$  of  $K^{*0}$  as a function of  $p_T$ . It is compared with the results of charged hadrons [36] and  $\phi$  meson [43]. The error bars on the charged hadrons are the systematic uncertainties only. For  $K^{*0}$  and  $\phi$ , the open boxes denote the systematic uncertainties and the bars denote the statistical uncertainties.

### 3.11 Systematic uncertainties

For the extraction of systematic error we have followed the prescription as discussed in [38]. Let us consider two cases, one is the measurement with default settings and other is the alternative systematic measurements (e.g. track quality cut variations).

The yield in the default case is called as  $Y_{def}$  with statistical uncertainty  $\sigma_{def}$  and the yield for the alternate systematic case is called as  $Y_{sys}$  with statistical uncertainty  $\sigma_{sys}$ , then the difference between the yields is denoted as  $\Delta = Y_{def} - Y_{sys}$  and the difference of their statistical uncertainties is  $\sigma = \sigma_{def} - \sigma_{sys}$ .

We define a factor  $n = \sigma/\Delta$ ;

The cases where  $n \leq 1$  are rejected. That means the cases where the alternative measurements are consistent with the statistical uncertainties are not considered in the calculation of systematic uncertainties. The main sources of systematic uncertainty in the analysis in Pb-Pb and pp collisions are presented below:

### 3.11.1 Uncertainty from signal extraction background

Due to the misidentification in pion and kaon selection as discussed in section 3.6, the shape of the residual background after the mixed event background subtraction varies with  $p_T$ . To estimate the effect of the shape of the residual background, different methods has been used for raw  $K^{*0}$  yield extraction.

1. Varying fit function range for residual background.
2. Using different fit function for residual background
  - 1st order polynomial
  - 2nd order polynomial
  - 3rd order polynomial

### 3.11.2 Uncertainty from yield extraction method

The yield of  $K^{*0}$  is measured by integrating the Breit Wigner function. The yield is also extracted by bin counting method, in which the integral of the residual background is subtracted from the histogram integral of the signal. The yield is extracted by keeping the width of the Breit Wigner function as a free and fixed parameter. Also by using different functions, relativistic and non-relativistic Breit Wigner function.

### 3.11.3 Uncertainty in particle identification

The kaons and pions are selected using the cut of less than 2 standard deviation ( $\sigma$ ) from the expected energy loss in TPC. For systematic study, the number of  $|\sigma|$  is varied:

1.  $|N\sigma| < 1.5$
2.  $|N\sigma| < 2.5$

### 3.11.4 Uncertainty from track cut variations

The good quality tracks are selected by applying the set of cuts as described in section 1.4. The systematic check in track selection is done by varying the cut on the minimum number of clusters required in TPC and the distance to closest approach values associated with the tracks. A detailed analysis has been done in reference [37] and we have taken the uncertainty as 10% from the above reference.

### 3.11.5 Uncertainty from material budget

For the uncertainty in material budget in ALICE, a detailed study has been done in the reference [36]. We have taken it from this reference as 1%.

### 3.11.6 Total systematic uncertainty

For the total systematic uncertainty all the above sources are added in quadrature. The relative fractional systematic uncertainties for all the above sources are shown in Fig. 3.31. The black dotted line represents the final systematic uncertainty in the  $K^{*0}$  yield. The average systematic uncertainties on the yield and  $\langle p_T \rangle$  are given in Table 3.8 and 3.9 for Pb–Pb and pp collisions respectively.

Cut variations	$d^2N/dp_T dy$	$dN/dy$	$\langle p_T \rangle$
varying fit range	9.9	6.2	5.7
varying residual background	5.8	2.1	2.2
varying normalization region	2.2	1.0	0.01
varying fit functions	5.2	2.7	1.8
yield extraction procedures	2.5	1.4	1.2
particle identification cuts	2.7	1.2	1.1
track selection cuts	10.0	10.0	–
material budget	1.0	1.0	1.0
$p_T$ extrapolation function	–	1.2	2.1
Centrality selection	2.7	2.7	–
Total	17.3	12.2	7.2

Table 3.8: Fractional systematic uncertainties (in %) on yield and  $\langle p_T \rangle$  in Pb-Pb collisions.

Cut variations	$d^2N/dp_T dy$	$dN/dy$	$\langle p_T \rangle$
varying fit range	6.19	4.03	3.19
varying residual background	2.33	1.01	0.02
varying normalization region	1.12	0.1	0.01
varying fit functions	3.04	2.1	1.8
yield extraction procedures	1.00	0.8	0.3
particle identification cuts	3.07	3.07	3.07
track selection cuts	10.0	10.0	10.0
material budget	1.07	1.07	–
$p_T$ extrapolation function	–	0.01	–
Total	13.7	13.3	3.75

Table 3.9: Fractional systematic uncertainties (in %) on yield and  $\langle p_T \rangle$  in pp collisions.

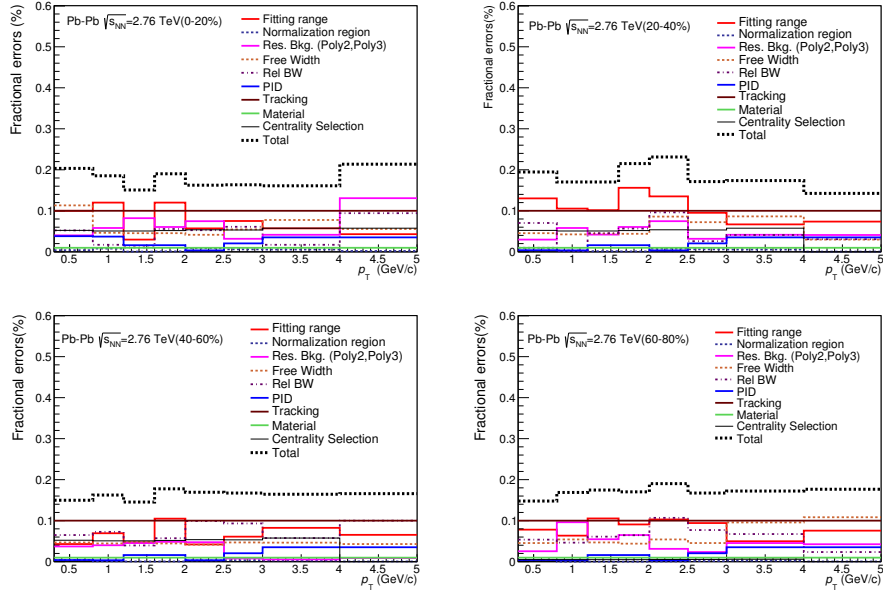


Figure 3.30: (Color online) Fractional systematic errors (in %) in the  $p_T$  spectra of  $K^{*0}$  in Pb–Pb collisions at  $\sqrt{s_{NN}} = 2.76$  TeV. Different sources of errors are denoted by different lines of different colors.

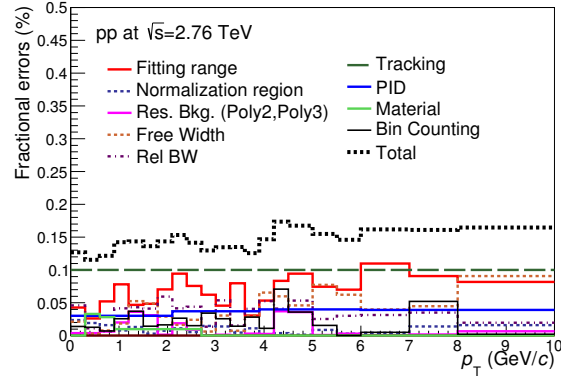


Figure 3.31: (Color online) Fractional systematic errors (in %) in the  $p_T$  spectra of  $K^{*0}$  in pp collisions at  $\sqrt{s} = 2.76$  TeV. Different sources of errors are denoted by different lines of different colors.

Cut variations	mass	width
varying fit range	0.40	18.2
varying residual background	0.30	15.7
varying normalization region	0.01	1.0
varying fit functions	0.3	10.0
particle identification cuts	0.2	4.4
track selection cuts	0.3	3.0
material budget	0.1	–
Total	0.6	26.4

Table 3.10: Fractional systematic uncertainties(in %) on mass and width in Pb-Pb collisions.

### 3.11.7 Systematic uncertainties in mass and width

The sources of systematic uncertainties in mass and width are the following:

1. fitting range variation
2. normalization region variation
3. residual background variation
4. different combinatorial background
5. track quality selections
6. PID selections
7. material budget.

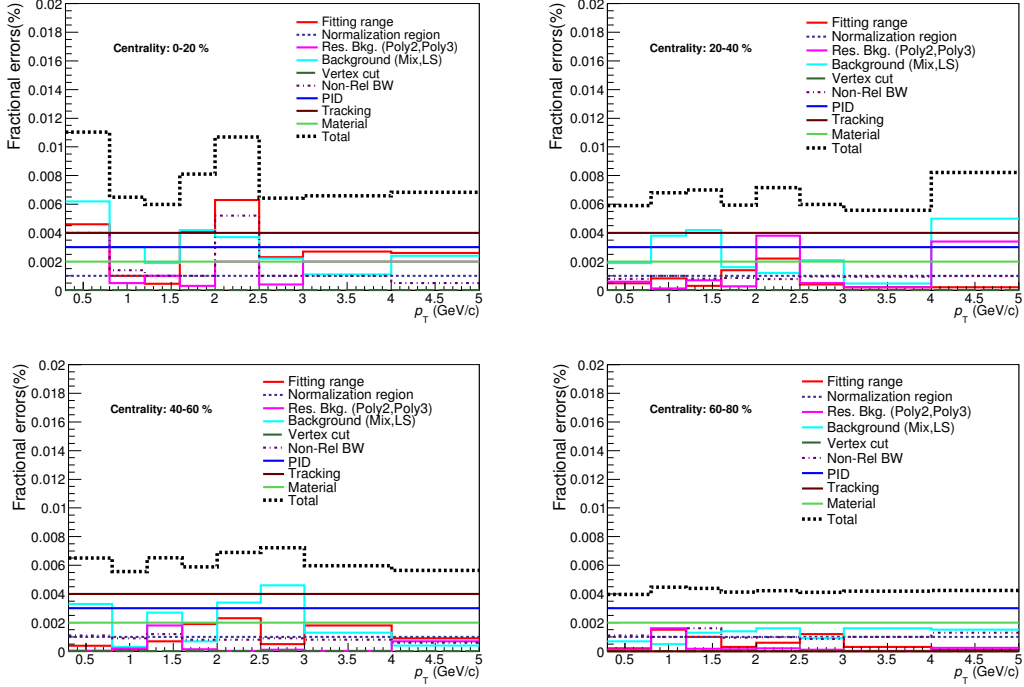


Figure 3.32: (Color online) Fractional systematic uncertainties (in %) in mass of  $K^{*0}$ .

### 3.12 Summary

In summary, we have obtained the mass, invariant mass distribution width and yield of  $K^{*0}$  in Pb–Pb and pp collisions at LHC energies at center mass energy of 2.76 TeV. The mass and invariant mass distribution width of  $K^{*0}$  is consistent with the PDG value. The  $K^{*0}/K^-$  ratio is obtained in different centrality classes in Pb–Pb and minimum bias pp collisions. The  $K^{*0}/K^-$  ratio is studied as a function of centrality and center of mass energy. The ratio in Pb–Pb collisions is smaller than that in pp collisions, showing the effect of hadronic re-scattering in heavy ion collisions. The  $K^{*0}/K^-$  ratio has a weak dependence on centrality, while the  $\phi/K^-$  ratio does not. It implies the dominance of hadronic re-scattering in more central collisions. The  $K^{*0}/K^-$  ratio is found to decrease with increase  $(dN_{ch}/d\eta)^{1/3}$ , which is equivalent to previously discussed centrality dependence. The comparison with Boltzmann Gibbs Blast-Wave model predictions implies the suppression of  $K^{*0}$  below  $p_T < 3.0$  GeV/c. The  $\langle p_T \rangle$  of  $K^{*0}$  in Pb–Pb and pp collisions are compared with the results of other

identified hadrons measured in ALICE and with lower energy measurements at RHIC. The increase in  $\langle p_T \rangle$  of  $K^{*0}$  in Pb–Pb collisions for LHC energies with respect to the RHIC is consistent with the increase in the increase in radial boost at higher energies. The increase in  $\langle p_T \rangle$  in pp collisions can be understood through the effect of color reconnections in multiple parton interactions. We have obtained the nuclear modification factor  $R_{CP}$  and  $R_{AA}$  of  $K^{*0}$ . The  $R_{CP}$  of  $K^{*0}$  is lower than that of  $\Lambda$ ,  $K_S^0$  and  $\phi$  at low  $p_T$ , where the effect of re-scattering is expected to be dominating, while it follows the trend of  $K_S^0$  meson in the intermediate  $p_T$  expected from a quark recombination model. The  $R_{AA}$  of  $K^{*0}$  is compared with charged hadrons measured in ALICE and  $\phi$  meson. The drop in  $R_{AA}$  of  $K^{*0}$  with respect to charged hadrons at low  $p_T$  for most central collisions may be due to the re-scattering effect.

# Bibliography

- [1] G. E. Brown and M. Rho, Phys. Rev. Lett. 66, 2720 (1991).
- [2] R. Rapp and E. Shuryak, Phys. Rev. Lett. 86, 2980 (2001).
- [3] K. Aamodt *et al.* (ALICE Collaboration), Phys. Lett. B 696, 328 (2011).
- [4] J. Adams *et al.* (STAR Collaboration), Phys. Rev. C 71, 064902 (2005).
- [5] M. M. Aggarwal *et al.* (STAR Collaboration), Phys. Rev. C 84, 034909 (2011).
- [6] Study of  $K^{*0}$  resonance production in relativistic heavy ion collision at RHIC. PhD thesis of Sadhana Dash, HBNI (2010) for STAR Collaboration.
- [7]  $K^*(892)$  resonance production in Au+Au and p+p collisions at the relativistic heavy ion collider. PhD thesis of Hibin Zhang, Yale University (2004) for STAR Collaboration.
- [8] K. Aamodt *et al.* (ALICE Collaboration), J. Inst. 3, S08002 (2008).
- [9] A. Badala *et al.*, ALICE Internal Note, ALICE/INT-2001-26.
- [10] B. Abelev *et al.* (ALICE Collaboration), Phys. Rev. C 88, 044909 (2013).
- [11] J. Beringer *et al.* (Particle Data Group), Phys. Rev. D 86, 01001 (2012).
- [12] R. E. Kalman, Trans ASME, J. Bas. Eng. 82 D, (1960).
- [13] B. Alessandro *et al.* (ALICE Collaboration), J. Phys. G 32, 1295 (2006).

- [14] W. Blum, W. Riegler and L. Ronaldi, Particle Detection with Drift Chambers, 2nd edition, vol 448, (Springer, Berlin 2008).
- [15] K. Aamodt *et al.* (ALICE Collaboration), Eur. Phys. J. C 71, 1655 (2011).
- [16] D. Drijard *et al.*, Nucl. Instr. Meth. A225, 367 (1984).
- [17] D. L'Hote, Nucl. Instr. Meth. A 337, 544 (1994).
- [18] J. Stachel, A. Andronic, P. Braun-Munzinger and K. Redlich, Proc. of Strangeness in Quark Matter 2013 conference (2013), 1311.4662.
- [19] R. Brun and F. Rademaker, "ROOT: An object oriented data analysis framework", Nucl. Instr. Meth. A 389, 81 (1997) ([www.root.cern.ch](http://www.root.cern.ch)).
- [20] B. Abelev *et al.* (ALICE Collaboration), Phys. Rev. C 88, 044909 (2013).
- [21] B. Abelev *et al.* (ALICE Collaboration), Phys. Rev. C 88, 044910 (2013).
- [22] B. Abelev *et al.* (ALICE Collaboration), Phys. Rev. Lett. 109, 252301 (2012).
- [23] B. Abelev *et al.* (ALICE Collaboration), Phys. Rev. C 88, 044909 (2013).
- [24] M. Lisa *et al.*, Annu. Rev. Nucl. Part. Sci. 55, 357 (2005).
- [25] E. Schnedermann, J. Sollfrank and U. Heinz, Phys. Rev. C 48, 2462 (1993).
- [26] C. Tsallis, J. Stat. Phys. 52, 479 (1988).
- [27] P.Z. Skands, Phys. Rev. D 82, 074018 (2010).
- [28] R. Brun *et al.*, GEANT3 User Guide (CERN Data Handling Division) DD/EE/841.
- [29] X. N. Wang and M. Gyulassy, Phys. Rev. D 44, 3501 (1991).
- [30] T. Sjostrand, S. Mrenna and P. Skands, PYTHIA 6.4 physics and manual J. High Energy Phys. 05, 026 (2006).
- [31] M. Bleicher *et al.* J. Phys. G 25, 1859 (1999).

- [32] B. Abelev *et al.* (ALICE Collaboration), Eur. Phys. J. C. 72, 2183 (2012).
- [33] S. V. Afanasiev *et al.* (NA49 Collaboration), Phys. Lett. B 491, 59 (2000).
- [34] M. Bourquin and J. M. Gaillard, Nucl. Phys. B 114, 334 (1976).
- [35] R. Fries, V. Greco and P. Sorensen, Annu. Rev. Nucl. Part. Sci 58, 177 (2008).
- [36] B. Abelev *et al.* (ALICE Collaboration), Phys. Lett. B 720, 52 (2013).
- [37] K. Aamodt *et al.* (ALICE Collaboration), Eur. Phys. J. C 71, 1594 (2011).
- [38] R. Barlow, Systematic Errors: facts and fictions, arXiv:hep-ex/0207026.
- [39] S. Singha, ALICE Analysis Note,  $K^{*0}$  resonance production in Pb–Pb collisions at  $\sqrt{s_{NN}}=2.76$  TeV, <https://aliceinfo.cern.ch/Notes/node/82>, <https://aliceinfo.cern.ch/Notes/node/160>, <https://aliceinfo.cern.ch/Notes/node/184>.
- [40] S. Singha, ALICE Analysis Note,  $K^{*0}$  resonance production in pp collisions at  $\sqrt{s}=2.76$  TeV, <https://aliceinfo.cern.ch/Notes/node/219>.
- [41] S. Singha (for ALICE Collaboration), Nucl. Phys. A 904-905, 539c-542c (2013).
- [42] S. Singha (for ALICE Collaboration), Proceedings of science (CPOD 2013) 055.
- [43] V. Riabov, M. Malev, Y. Riabov, ALICE Analysis Note,  $\phi$  resonance production in Pb–Pb collisions at  $\sqrt{s_{NN}}=2.76$  TeV.

## 3.13 Appendix

### 3.13.1 $K^{*0}$ signals in different centrality bins

The following section shows the  $K^{*0}$  signals in various  $p_T$  bins for different collision centrality (Fig 33 to 36)

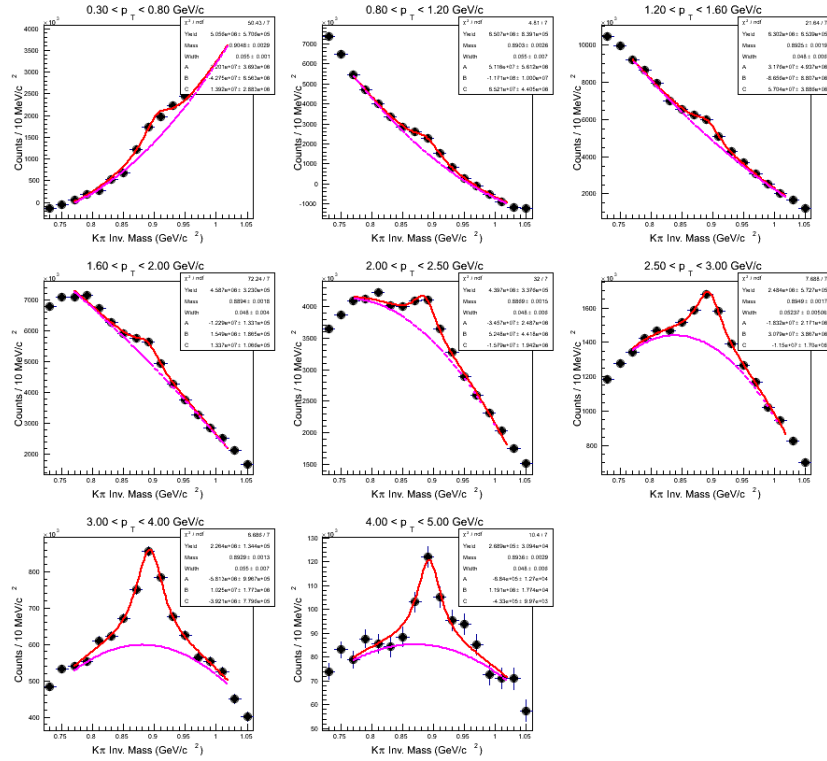


Figure 3.33: (Color online)  $K^{*0}$  signals in various momentum bins within the rapidity interval  $-0.5 < y < 0.5$  in Pb-Pb collisions in 0-20% centrality at  $\sqrt{s_{NN}} = 2.76$  TeV.

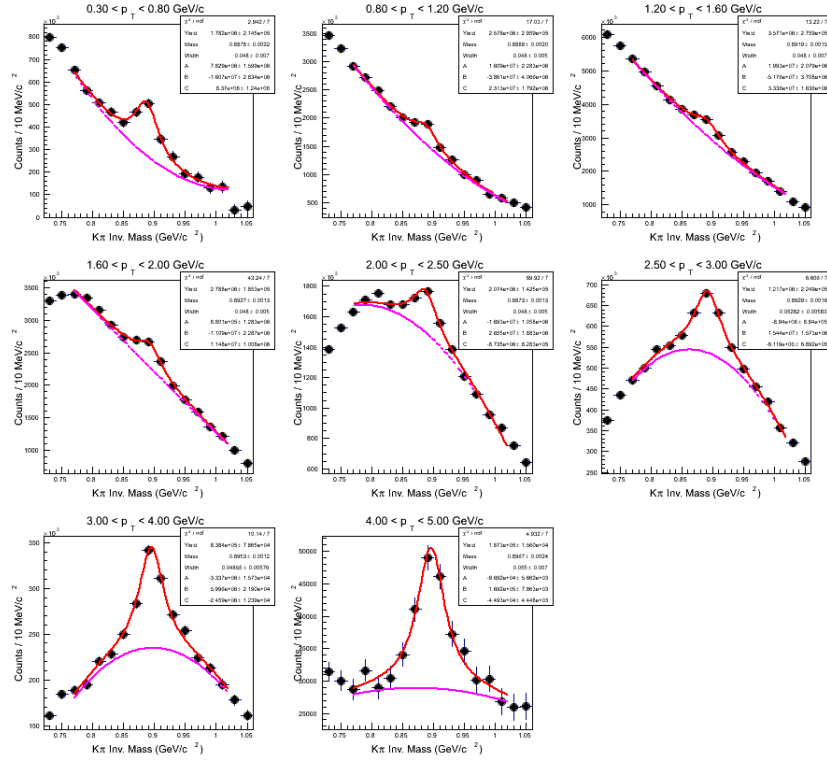


Figure 3.34: (Color online)  $K^*0$  signals in various momentum bins within the rapidity interval  $-0.5 < y < 0.5$  in Pb-Pb collisions in 20-40 % centrality at  $\sqrt{s_{NN}} = 2.76$  TeV.

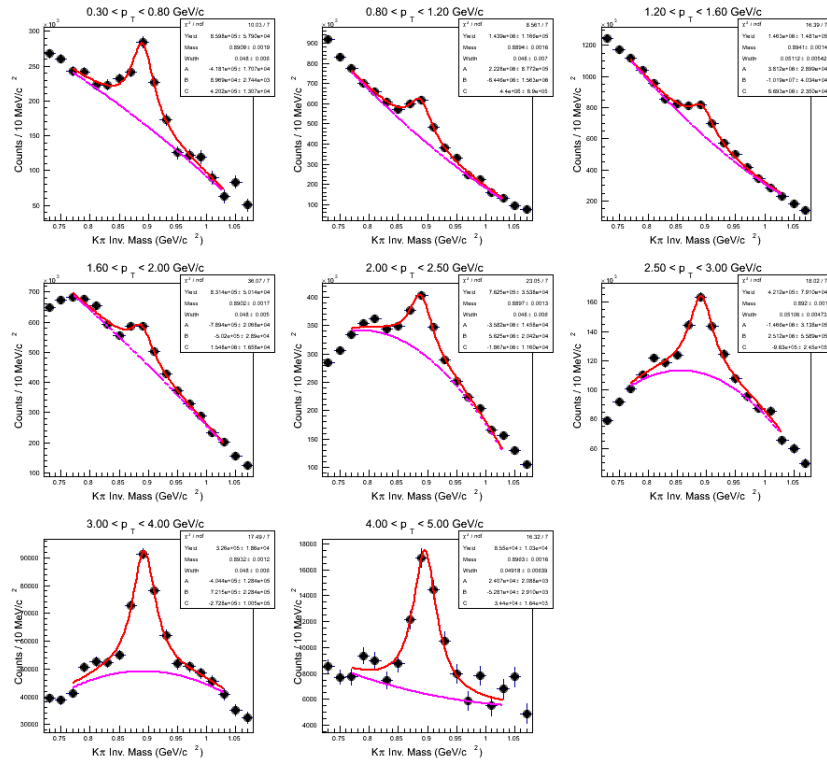


Figure 3.35: (Color online)  $K^*0$  signals in various momentum bins within the rapidity interval  $-0.5 < y < 0.5$  in Pb–Pb collisions in 40–60 % centrality at  $\sqrt{s_{NN}} = 2.76$  TeV.

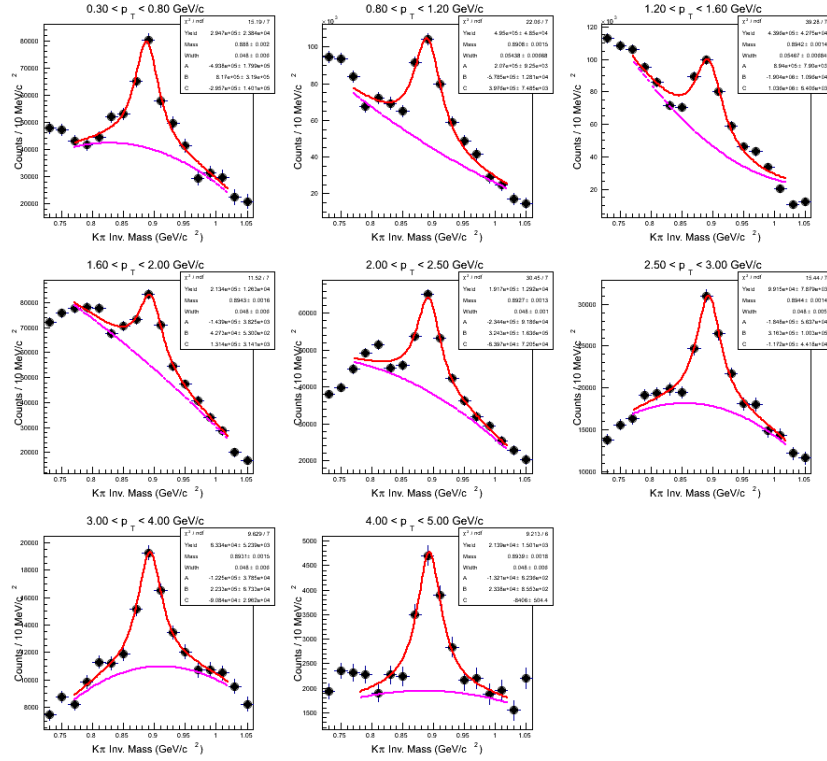


Figure 3.36: (Color online)  $K^{*0}$  signals in various momentum bins within the rapidity interval  $-0.5 < y < 0.5$  in Pb–Pb collisions in 60–80 % centrality at  $\sqrt{s_{NN}} = 2.76$  TeV.

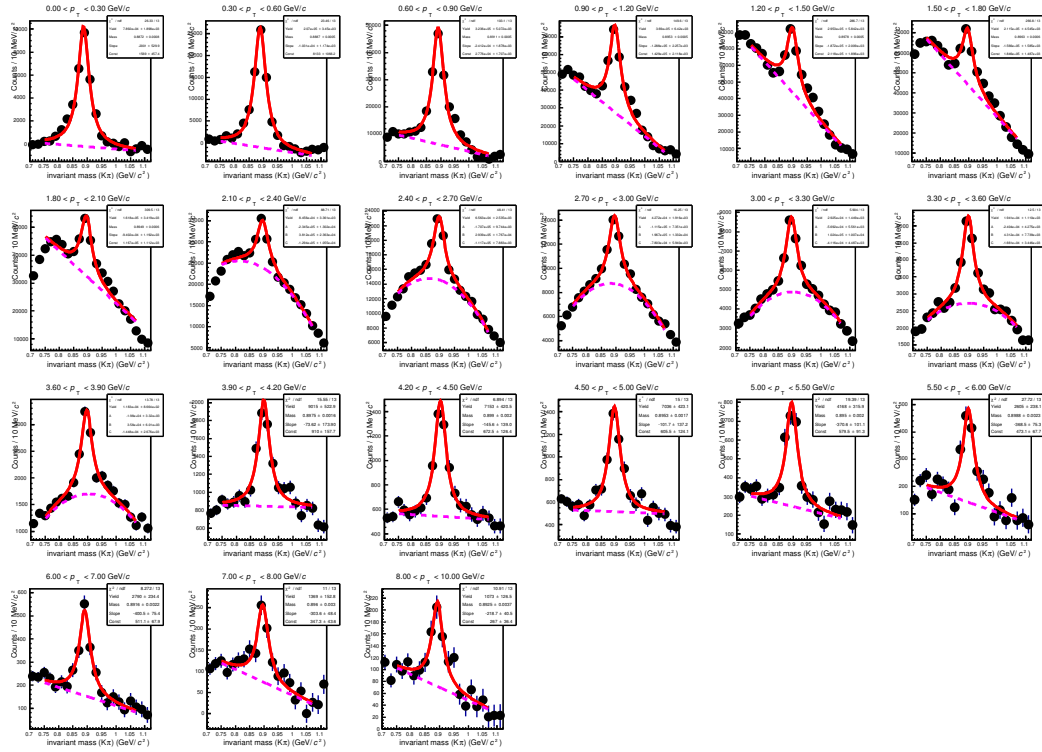


Figure 3.37: (Color online)  $K^{*0}$  signals in various momentum bins within the rapidity interval  $-0.5 < y < 0.5$  in minimum bias pp collisions at  $\sqrt{s} = 2.76$  TeV.

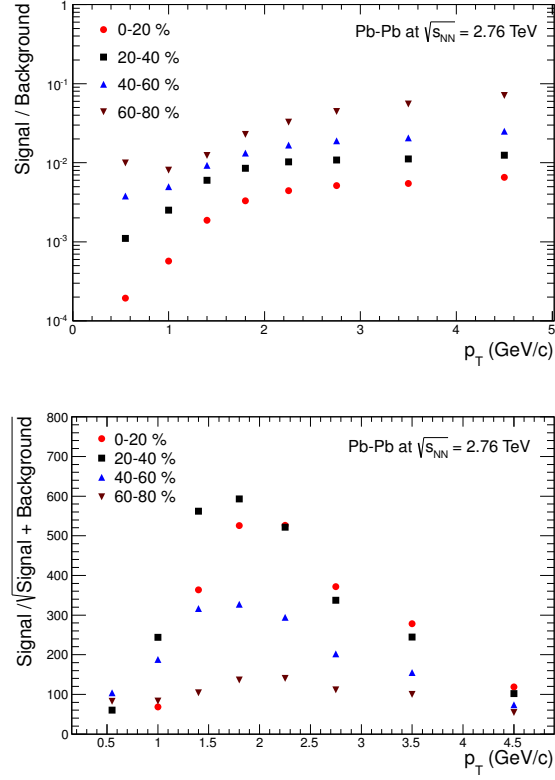


Figure 3.38: (Color online) Signal by background and significance of  $K^{*0}$  meson as a function of  $p_T$  within the rapidity interval  $-0.5 < y < 0.5$  in Pb-Pb collisions at  $\sqrt{s_{NN}} = 2.76$  TeV.

$p_T$ bins (GeV/c)	mass (GeV/c <sup>2</sup> )	stat. uncertainties (GeV/c <sup>2</sup> )	syst. uncertainties (GeV/c <sup>2</sup> )
0.3–0.8	0.8900	0.0023	0.0098
0.8–1.2	0.8928	0.0024	0.0058
1.2–1.6	0.8938	0.0018	0.0053
1.6–2.0	0.8927	0.0015	0.0072
2.0–2.5	0.8919	0.0012	0.0095
2.5–3.0	0.8949	0.0016	0.0057
3.0–4.0	0.8938	0.0013	0.0059
4.0–5.0	0.8947	0.0025	0.0061

Table 3.11: Mass of  $K^{*0}$  as a function of  $p_T$  within the rapidity interval  $-0.5 < y < 0.5$  in Pb–Pb collisions in 0-20% centrality at  $\sqrt{s_{NN}} = 2.76$  TeV.

$p_T$ bins (GeV/c)	mass (GeV/c <sup>2</sup> )	stat. uncertainties (GeV/c <sup>2</sup> )	syst. uncertainties (GeV/c <sup>2</sup> )
0.3–0.8	0.8907	0.0014	0.0050
0.8–1.2	0.8919	0.0016	0.0053
1.2–1.6	0.8943	0.0014	0.0053
1.6–2.0	0.8949	0.0015	0.0051
2.0–2.5	0.8946	0.0011	0.0052
2.5–3.0	0.8944	0.0013	0.0051
3.0–4.0	0.8949	0.0014	0.0052
4.0–5.0	0.8953	0.0017	0.0052

Table 3.12: Mass of  $K^{*0}$  as a function of  $p_T$  within the rapidity interval  $-0.5 < y < 0.5$  in Pb–Pb collisions in 60-80% centrality at  $\sqrt{s_{NN}} = 2.76$  TeV.

$p_T$ bins (GeV/c)	width (GeV/c <sup>2</sup> )	stat. uncertainties (GeV/c <sup>2</sup> )	syst. uncertainties (GeV/c <sup>2</sup> )
0.3–0.8	0.05500	0.00581	0.01590
0.8–1.2	0.05390	0.00483	0.01389
1.2–1.6	0.04284	0.00577	0.01230
1.6–2.0	0.04627	0.00546	0.01330
2.0–2.5	0.04574	0.00438	0.01307
2.5–3.0	0.05266	0.00573	0.01357
3.0–4.0	0.04962	0.00504	0.01283
4.0–5.0	0.04521	0.00488	0.01184

Table 3.13: Width of  $K^{*0}$  as a function of  $p_T$  within the rapidity interval  $-0.5 < y < 0.5$  in Pb–Pb collisions in 0-20% centrality at  $\sqrt{s_{NN}} = 2.76$  TeV.

$p_T$ bins (GeV/c)	width (GeV/c <sup>2</sup> )	stat. uncertainties (GeV/c <sup>2</sup> )	syst. uncertainties (GeV/c <sup>2</sup> )
0.3–0.8	0.04623	0.00526	0.01271
0.8–1.2	0.05070	0.00470	0.01364
1.2–1.6	0.05500	0.00700	0.01579
1.6–2.0	0.04547	0.00607	0.01198
2.0–2.5	0.04422	0.00396	0.01164
2.5–3.0	0.04680	0.00512	0.01206
3.0–4.0	0.04423	0.004786	0.01144
4.0–5.0	0.05500	0.006645	0.01440

Table 3.14: Width of  $K^{*0}$  as a function of  $p_T$  within the rapidity interval  $-0.5 < y < 0.5$  in Pb–Pb collisions in 60-80% centrality at  $\sqrt{s_{NN}} = 2.76$  TeV.

$p_T$ bins (GeV/c)	$d^2N/dp_T dy$ (GeV/c) $^{-1}$	stat. uncertainties (GeV/c) $^{-1}$	syst. uncertainties (GeV/c) $^{-1}$
0.3–0.8	7.989360	1.745180	1.596270
0.8–1.2	9.670140	1.123800	1.698080
1.2–1.6	7.259880	0.682443	1.043240
1.6–2.0	5.257980	0.405854	0.970624
2.0–2.5	3.309280	0.313692	0.514594
2.5–3.0	1.401090	0.162094	0.219551
3.0–4.0	0.458699	0.050149	0.067612
4.0–5.0	0.077891	0.011005	0.015843

Table 3.15: Yield of  $K^{*0}$  as a function of  $p_T$  within the rapidity interval  $-0.5 < y < 0.5$  in Pb–Pb collisions in 0-20% centrality at  $\sqrt{s_{NN}} = 2.76$  TeV.

$p_T$ bins (GeV/c)	$d^2N/dp_T dy$ (GeV/c) $^{-1}$	stat. uncertainties (GeV/c) $^{-1}$	syst. uncertainties (GeV/c) $^{-1}$
0.3–0.8	4.457350	0.537226	0.868293
0.8–1.2	5.243980	0.691521	0.877318
1.2–1.6	3.822450	0.412619	0.629176
1.6–2.0	3.010820	0.174983	0.632573
2.0–2.5	1.649660	0.089025	0.375957
2.5–3.0	0.663316	0.067053	0.108983
3.0–4.0	0.233768	0.014610	0.037870
4.0–5.0	0.043185	0.004948	0.006080

Table 3.16: Yield of  $K^{*0}$  as a function of  $p_T$  within the rapidity interval  $-0.5 < y < 0.5$  in Pb–Pb collisions in 20-40% centrality at  $\sqrt{s_{NN}} = 2.76$  TeV.

$p_T$ bins (GeV/c)	$d^2N/dp_T dy$ (GeV/c) $^{-1}$	stat. uncertainties (GeV/c) $^{-1}$	syst. uncertainties (GeV/c) $^{-1}$
0.3–0.8	2.458620	0.204039	0.363876
0.8–1.2	2.376210	0.279104	0.377580
1.2–1.6	1.540010	0.160104	0.216526
1.6–2.0	0.821582	0.062388	0.142462
2.0–2.5	0.545962	0.032020	0.089865
2.5–3.0	0.243920	0.024386	0.039710
3.0–4.0	0.094801	0.005385	0.014666
4.0–5.0	0.023387	0.001929	0.003906

Table 3.17: Yield of  $K^{*0}$  as a function of  $p_T$  within the rapidity interval  $-0.5 < y < 0.5$  in Pb–Pb collisions in 40-60% centrality at  $\sqrt{s_{NN}} = 2.76$  TeV.

$p_T$ bins (GeV/c)	$d^2N/dp_T dy$ (GeV/c) $^{-1}$	stat. uncertainties (GeV/c) $^{-1}$	syst. uncertainties (GeV/c) $^{-1}$
0.3–0.8	0.799554	0.058756	0.125530
0.8–1.2	0.680117	0.050772	0.119769
1.2–1.6	0.391529	0.028366	0.069888
1.6–2.0	0.195756	0.016458	0.034551
2.0–2.5	0.135746	0.008685	0.026484
2.5–3.0	0.059015	0.004405	0.010227
3.0–4.0	0.021406	0.001494	0.003705
4.0–5.0	0.006516	0.000645	0.001158

Table 3.18: Yield of  $K^{*0}$  as a function of  $p_T$  within the rapidity interval  $-0.5 < y < 0.5$  in Pb–Pb collisions in 60-80% centrality at  $\sqrt{s_{NN}} = 2.76$  TeV.

$p_T$ bins (GeV/c)	$d^2N/dp_T dy$ (GeV/c) $^{-1}$	stat. uncertainties (GeV/c) $^{-1}$	syst. uncertainties (GeV/c) $^{-1}$
0.3–0.6	0.062531	0.001430	0.007222
0.6–0.9	0.056747	0.001356	0.006911
0.9–1.2	0.041446	0.001060	0.005900
1.2–1.5	0.022910	0.000696	0.003292
1.5–1.8	0.013048	0.000453	0.001780
1.8–2.1	0.008046	0.000310	0.001155
2.1–2.4	0.005168	0.000222	0.000793
2.4–2.7	0.003648	0.000156	0.000516
2.7–3.0	0.002223	0.000114	0.000289
3.0–3.3	0.001541	0.000083	0.000207
3.3–3.6	0.001012	0.000063	0.000137
3.6–3.9	0.000608	0.000048	0.000076
3.9–4.2	0.000421	0.000037	0.000062
4.2–4.5	0.000320	0.000030	0.000056
4.5–5.0	0.000194	0.000017	0.000032
5.0–5.5	0.000137	0.000013	0.000021
5.5–6.0	0.000081	0.0000097	0.000011
6.0–7.0	0.000044	0.0000048	0.0000071
7.0–8.0	0.000016	0.0000031	0.0000025
8.0–10.0	0.0000073	0.0000013	0.0000012

Table 3.19: Yield of  $K^{*0}$  as a function of  $p_T$  within the rapidity interval  $-0.5 < y < 0.5$  in minimum bias pp collisions at  $\sqrt{s} = 2.76$  TeV.

$p_T$ bins (GeV/c)	mass (GeV/c <sup>2</sup> )	stat. uncertainties (GeV/c <sup>2</sup> )
0.3–0.6	0.8922	0.00016
0.6–0.9	0.8900	0.00014
0.9–1.2	0.8919	0.00016
1.2–1.5	0.8960	0.00059
1.5–1.8	0.8976	0.00062
1.8–2.1	0.8957	0.00067
2.1–2.4	0.8928	0.00088
2.4–2.7	0.8933	0.00088
2.7–3.0	0.8954	0.00110
3.0–3.3	0.8959	0.00108
3.3–3.6	0.8967	0.00128
3.6–3.9	0.8953	0.00143
3.9–4.2	0.8978	0.00196
4.2–4.5	0.8997	0.00181
4.5–5.0	0.8954	0.00194
5.0–5.5	0.8947	0.00219
5.5–6.0	0.8993	0.00254
6.0–7.0	0.8900	0.00172
7.0–8.0	0.8960	0.00326
8.0–10.0	0.8934	0.00352

Table 3.20: Mass of  $K^{*0}$  as a function of  $p_T$  within the rapidity interval  $-0.5 < y < 0.5$  in minimum bias pp collisions at  $\sqrt{s} = 2.76$  TeV.

$p_T$ bins (GeV/c)	width (GeV/c <sup>2</sup> )	stat. uncertainties (GeV/c <sup>2</sup> )
0.3–0.6	0.04748	0.00221
0.6–0.9	0.04769	0.00237
0.9–1.2	0.05108	0.00206
1.2–1.5	0.04500	0.00105
1.5–1.8	0.04500	0.00051
1.8–2.1	0.04500	0.00038
2.1–2.4	0.04500	0.00074
2.4–2.7	0.04500	0.00709
2.7–3.0	0.04735	0.00608
3.0–3.3	0.04500	0.00850
3.3–3.6	0.04725	0.00570
3.6–3.9	0.04500	0.00620
3.9–4.2	0.05390	0.00894
4.2–4.5	0.05500	0.00940
4.5–5.0	0.05232	0.00847
5.0–5.5	0.05500	0.00819
5.5–6.0	0.05373	0.00664
6.0–7.0	0.04500	0.00996
7.0–8.0	0.04500	0.00763
8.0–10.0	0.05500	0.00928

Table 3.21: Width of  $K^{*0}$  as a function of  $p_T$  within the rapidity interval  $-0.5 < y < 0.5$  in minimum bias pp collisions at  $\sqrt{s} = 2.76$  TeV.

# Chapter 4

## Studying re-scattering in heavy-ion collisions through $K^{*0}$ production using AMPT

In this chapter we will study the effect of hadronic re-scattering in heavy-ion collisions by studying the production of  $K^{*0}$  mesons in A Multi Phase Transport (AMPT) model [1, 2, 3].

### 4.1 Introduction

The hadronic resonances play an important role in studying the properties and evolution of strongly interacting matter formed in heavy-ion collisions [4]. Many resonances have been observed [5, 6, 7, 8, 9] in these collisions such as  $f_2(1270)$ ,  $\rho(770)^0$ ,  $\Delta(1232)^{++}$ ,  $f_0(980)$ ,  $K(892)^{0\pm}$ ,  $\Sigma(1385)$ ,  $\Lambda(1520)$  and  $\phi(1020)$  with lifetimes of 1.1 fm/c, 1.3 fm/c, 1.6 fm/c, 2.6 fm/c, 4 fm/c, 5.5 fm/c, 12.6 fm/c and 44 fm/c, respectively [10]. During the evolution of the system formed in heavy ion collisions two

important temperatures or time-scales comes into picture. One is chemical freeze-out in which the inelastic collision among the constituents are expected to cease and the other is kinetic freeze-out where the distance between the constituents are larger than their mean free path and the elastic collisions among them ceases [11, 12, 13]. If the resonances decay before the kinetic freeze out, they are subjected to be affected by the hadronic re-scattering effects, in which momentum of the decay daughters changed. In experiment, we reconstruct the resonances through the invariant mass method using their decay products. So, if the momentum of the decay products are changed during the hadronic re-scattering, we can not reconstruct back the resonances, as a result the signal is lost. On the other hand the hadrons present in the medium can undergo pseudo-elastic interactions [14] and produce some resonances leading to enhancement of resonance yields. The interplay between these two competing processes, re-scattering and regeneration, finally decides the resonance yield.

Having a small lifetime ( $\sim 4$  fm/c), the decay products of  $K^{*0}$  resonance is expected to be affected by hadronic interactions and thus can be used as a tool to understand effects of hadronic re-scattering in heavy ion collision. In this work, we have used A Multi Phase Transport (AMPT) model [1, 2, 3] to understand the role of hadronic re-scattering through  $K^{*0}$  resonance production.

## 4.2 The AMPT model

The AMPT model [1, 2] has two versions, the default and string melting (SM). Since the default AMPT model reproduces the yield and transverse momentum spectra much better than AMPT-SM, we have chosen the AMPT default for our study. The structure of default AMPT model is shown schematically in Fig 4.1. It has four main components: the initial conditions, the partonic interactions, conversion from partonic to hadronic matter and hadronic interactions. The AMPT model uses the same initial conditions as in HIJING [15]. However, the minijet partons are made to undergo scattering before they are allowed to fragment into hadrons. The scattering among the partons are carried out by a Zhang Parton Cascade (ZPC) [16] model. Then the

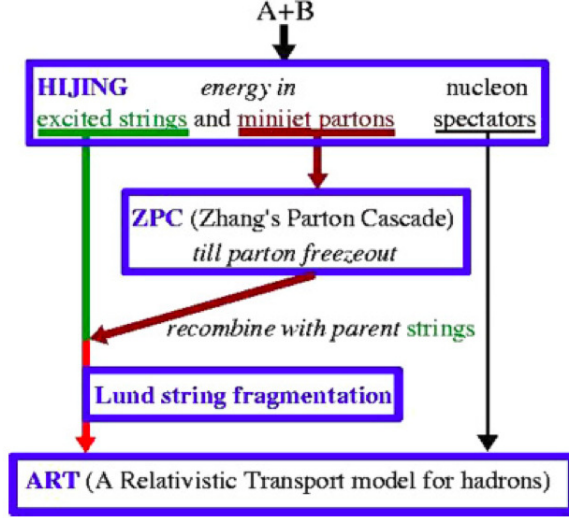


Figure 4.1: (Color online) Schematic diagram of the default AMPT model. Figure has been taken from [1]

partons are recombined with their parent strings when they stop interacting, and the resultant strings are converted to hadrons by Lund string fragmentation model. The evolution of the hadronic matter is described by a hadronic cascade which is based on the A Relativistic Transport (ART) model [17]. Final results are obtained after the termination of hadronic cascade. The termination time of hadronic cascade ( $\tau_{HC}$ ) can be tuned by an input parameter called NTMAX, which is the number of time steps (each step corresponds to 0.2 fm/c) of the hadronic interactions. The default value of NTMAX is 150 which corresponds to a value of  $\tau_{HC} = 30$  fm/c, while NTMAX = 3 effectively turns off the hadronic cascade. We gradually increase the  $\tau_{HC}$  from 0.6 to 30 fm/c to study the effect of hadronic interaction on  $K^{*0}$  production.

### 4.3 Results

In this work, we have generated AMPT events in Au+Au collisions at  $\sqrt{s_{NN}} = 200$  GeV with various NTMAX values corresponding to  $\tau_{HC} = 0.6, 4, 8, 14, 30$  fm/c. We reconstruct the  $K^{*0}$  resonance through its hadronic decay  $K^{*0} \rightarrow K^+\pi^-$ ,  $\bar{K}^{*0} \rightarrow$

$K^- \pi^+$ . The yield and mean transverse momentum of  $K^{*0}$  and yield relative to kaon is estimated using AMPT. The Fig. 4.2 shows time evolution of  $K^*$  for Au+Au collisions

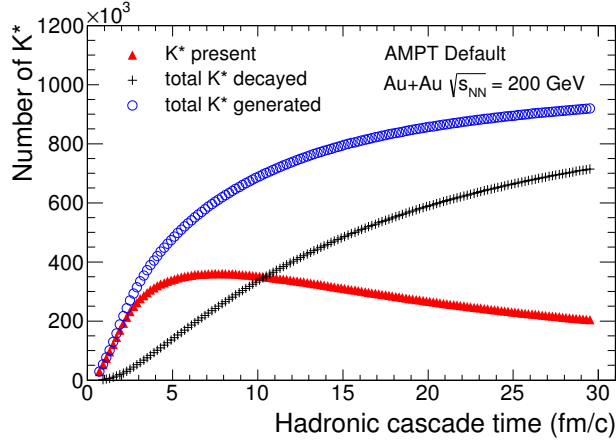


Figure 4.2: (Color online) Number of  $K^*$  as a function of hadronic cascade time in default AMPT model for Au+Au collisions at  $\sqrt{s_{NN}} = 200$  GeV. Red solid triangles corresponds to total  $K^*$  present at any given  $\tau_{HC}$ . Blue open circle corresponds to total  $K^*$  produced and black cross corresponds to total  $K^*$  decayed.

at  $\sqrt{s_{NN}} = 200$  GeV in default AMPT model. The solid red triangles corresponds to total  $K^*$  present at any given  $\tau_{HC}$ . Blue open circle corresponds to total  $K^*$  produced and black cross corresponds to total  $K^*$  decayed at  $\tau_{HC}$ . The decay products of  $K^*$  (the pions and kaons) undergo re-scattering thereby lead to loss in  $K^*$  invariant mass signal. However the regeneration of  $K^*$  can increase the yield with increase in hadronic cascade time but if it is not dominant then regeneration can not compensate for the yield loss in re-scattering. The regeneration of  $K^*$  depends on the cross section  $\sigma_{K\pi}$ , whereas the re-scattering depends on  $\sigma_{\pi\pi}$  and  $\sigma_{K\pi}$ , where  $\sigma_{\pi\pi}$  is considerably larger than  $\sigma_{K\pi}$  [18, 19].

### 4.3.1 Invariant mass distribution

The Fig. 4.3 shows the  $K \pi$  invariant mass distribution in minimum bias (0-80 % of the total cross section) Au+Au collisions at  $\sqrt{s_{NN}} = 200$  GeV using AMPT model.

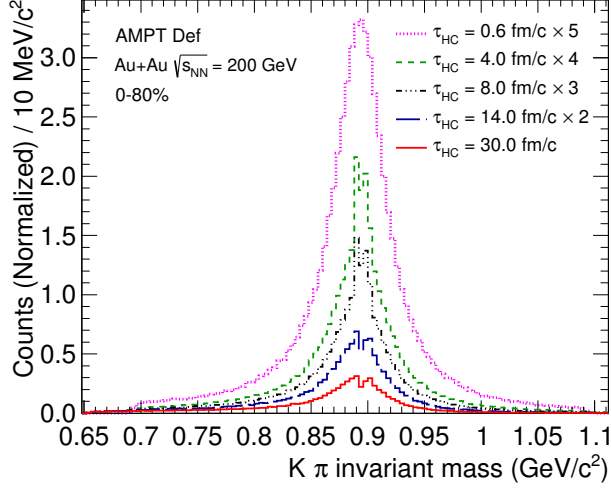


Figure 4.3: (Color online)  $K\pi$  invariant mass distribution in 0-80% minimum bias Au+Au collisions for different termination time of hadron cascade using the default AMPT model. Different lines corresponds to different termination time of hadron cascade.

The termination time of the hadronic cascade time is varied from 0.6 to 30 fm/c (shown by different coloured lines). The number of events in each configuration are kept same in order to make a proper comparison. It is clearly observed that the invariant mass signal decreases with increase in hadronic cascade time. An increase in hadronic cascade time refers to increase in hadronic re-scattering. It is expected because of the change in momentum of the daughters of  $K^{*0}$  ( $\pi$  and K) due to re-scattering. In the next section we will discuss how to quantify the re-scattering effect in heavy-ion collision.

### 4.3.2 Observables for re-scattering

The Fig 4.4 shows the  $dN/dy$  and  $\langle p_T \rangle$  of reconstructed  $K^*$  as a function of hadronic cascade time for 0-80% minimum bias Au+Au collisions at  $\sqrt{s_{NN}} = 200$  GeV. It is observed that the  $dN/dy$  decreases with increase in  $\tau_{HC}$ . Also the  $\langle p_T \rangle$  increases with  $\tau_{HC}$ . It is consistent with the loss of  $K^*$  due to re-scattering. In order to provide signature of re-scattering effect in heavy-ion collisions we need a proper baseline to

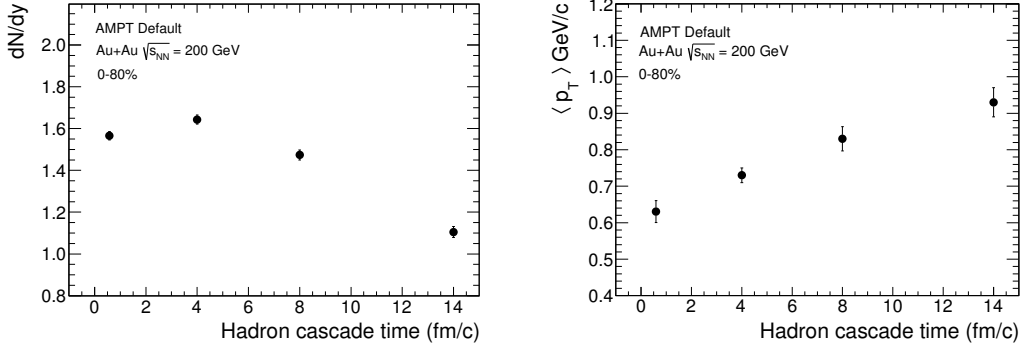


Figure 4.4:  $dN/dy$  and  $\langle p_T \rangle$  of reconstructed  $K^*$  as a function of hadronic cascade time for 0-80% minimum bias Au+Au collisions at  $\sqrt{s_{NN}} = 200$  GeV.

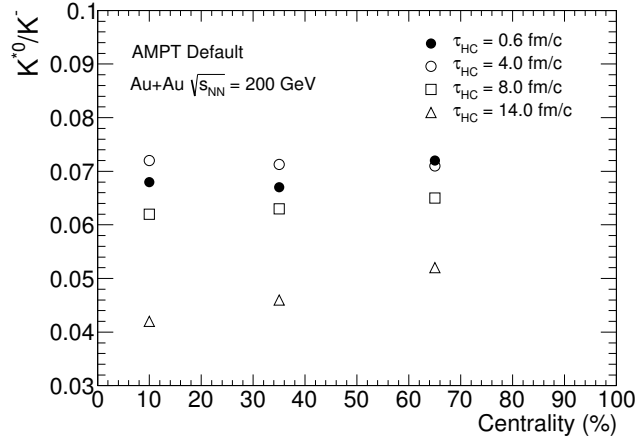


Figure 4.5:  $K^*/K^-$  as a function collision centrality for 0-80% minimum bias Au+Au collisions in AMPT model at  $\sqrt{s_{NN}} = 200$  GeV. Results are shown for different hadron cascade time.

compare. One such observable can be the yield ratio of  $K^*/K^-$ . The Fig 4.5 shows the  $K^*/K^-$  ratio as a function of collision centrality for different  $\tau_{HC}$ . At large hadron cascade time the ratio shows a decrease from peripheral to central collisions. The medium formed in central collisions are expected to live longer and hence the possibility of re-scattering is higher. Hence a clear decrease in the centrality dependence of  $K^*/K^-$  ratio or a decrease in ratio with respect to pp collisions would indicate a dominance of re-scattering in heavy-ion collisions. The Fig 4.6 shows the  $K^{*0}/K^-$

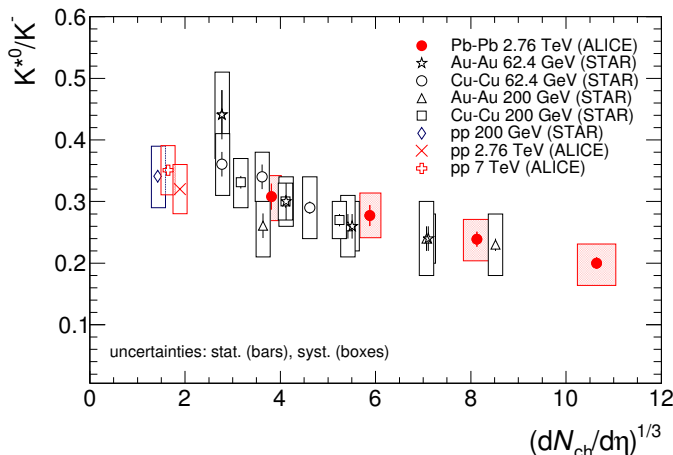


Figure 4.6: (Color online)  $K^{*0}/K^-$  as a function of  $(dN_{ch}/d\eta)^{1/3}$  from experimental data in heavy-ion [5, 6, 7] and p+p collisions [19, 7, 9].

ratio as a function of  $(dN_{ch}/d\eta)^{1/3}$  from Pb+Pb, Au+Au, Cu+Cu and p+p collisions, where  $(dN_{ch}/d\eta)$  is the number of particles per unit pseudorapidity. It is observed that the  $K^{*0}/K^-$  ratio in pp collisions is higher than heavy-ion and there is a clear decrease observed in the centrality dependence in heavy-ion collisions, indicating the presence of hadronic re-scattering.

### 4.3.3 Estimation of hadronic phase time

The suppression of  $K^{*0}/K^-$  ratio in heavy-ion collisions with respect to pp collisions can be used to estimate a lower limit on the difference between chemical and kinetic freeze out in a toy model and under certain assumptions. The experimental observa-

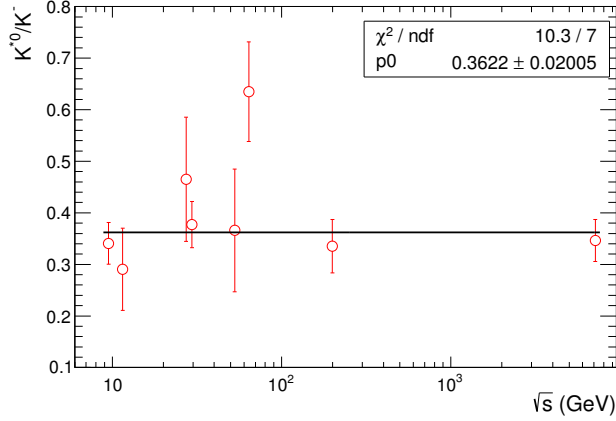


Figure 4.7: (Color online)  $K^{*0}/K^-$  ratio for p+p collisions [19, 7, 9] at various center mass energies. The data are fitted to a straight line.

tion of decrease in  $K^{*0}/K^-$  ratio in more central collisions shows the dominance of re-scattering over the regeneration. So the reaction  $K^{*0} \leftrightarrow K\pi$  is not in balance and the  $K^{*0}/K^-$  ratio in kinetic freeze out can be related to that in chemical freeze out by the following equation,

$$\left(\frac{K^{*0}}{K^-}\right)_{kinetic} = \left(\frac{K^{*0}}{K^-}\right)_{chemical} \times e^{-\tau\Delta t} \quad (4.1)$$

where,  $\tau$  is the lifetime of  $K^{*0}$  ( $\sim 4$  fm/c) and  $\Delta t$  is the time difference between the chemical and kinetic freeze out. Further, we assume that the  $\left(\frac{K^{*0}}{K^-}\right)_{chemical}$  is given by the experimental data in p+p collisions [19, 7, 9] and the heavy-ion data [5, 6, 7] provides the  $\left(\frac{K^{*0}}{K^-}\right)_{kinetic}$ . So the equation 4.1 can be re-written as,

$$\left(\frac{K^{*0}}{K^-}\right)_{pp} = \left(\frac{K^{*0}}{K^-}\right)_{AA} \times e^{-\tau\Delta t} \quad (4.2)$$

where the underlying assumption is

1. all the  $K^{*0}$  decayed before kinetic freeze out are lost due to re-scattering effects;

2. there is no regeneration of  $K^{*0}$  between the chemical and kinetic freeze out.

Thus, the term  $\Delta t$  gives a lower limit of the time difference between chemical and kinetic freeze out. The AMPT model simulation shows that the above two

assumptions could hold to a substantial extent. The value of  $\left(\frac{K^{*0}}{K^-}\right)_{chemical}$  is taken from a global fit (0.36 from Fig. 4.7) to the  $K^{*0}K^-$  ratio in p+p collisions. The  $\left(\frac{K^{*0}}{K^-}\right)_{kinetic}$  values are taken from the heavy-ion data shown in Fig. 4.6. The result of  $\Delta t$  which is boosted by the Lorentz factor ( $\sim 1.38 - 1.57$ ) is shown in Fig. 4.8 for three different collision centralities for various systems. It is observed that the time difference between the chemical and kinetic freeze out increases with both the beam energy and system size as expected. For the most central Au+Au collisions at  $\sqrt{s_{NN}} = 200$  GeV the lower limit of time difference between chemical and kinetic freeze out is about 3.7 fm/c, while for most central Pb+Pb collisions at 2.76 TeV it increases to 4.7 fm/c. The extracted values of  $\Delta t$  are consistent with other estimates [21].

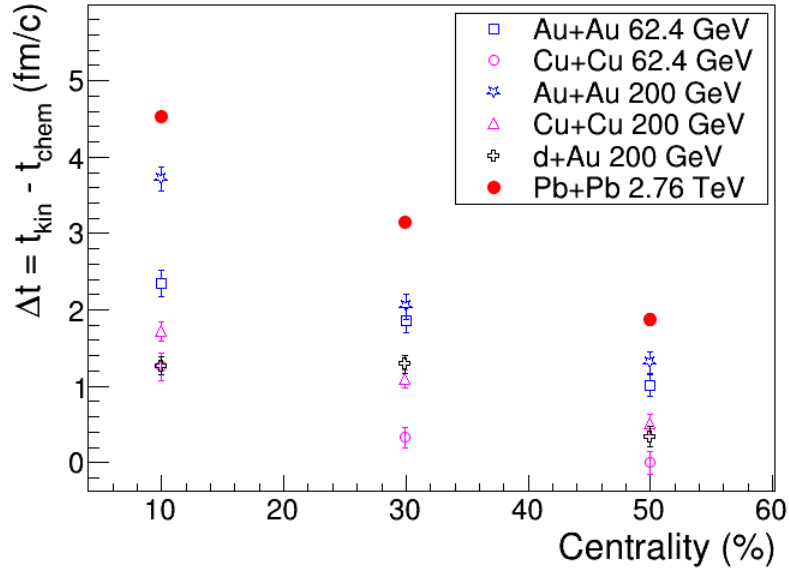


Figure 4.8: (Color online) Estimate of the lower limit of time difference between the chemical and kinetic freeze out for various systems and beam energies using  $K^*/K^-$  ratio.

## 4.4 Summary

In summary, we have provided a detail study of effect of hadronic re-scattering on  $K^{*0}$  production using the AMPT model. The study has been carried out by varying the termination time of the hadronic cascade. Larger the hadronic cascade time more is the re-scattering of the daughters ( $\pi K$ ) of the  $K^{*0}$  meson. We observe that the reconstructed  $K^{*0}$  signal is lost due to re-scattering of the daughters which results in the change in their momentum distributions. There is a clear decrease in  $dN/dy$  of the reconstructed  $K^{*0}$  meson with increase in hadron cascade time and the  $\langle p_T \rangle$  increases with hadron cascade time. We propose an observable  $K^{*0}/K^-$  as a function of collision centrality to study the re-scattering effect in heavy-ion collisions. A clear decrease in the  $K^{*0}/K^-$  ratio with respect to p+p collisions and with increase in collision centrality can be considered as a signature of re-scattering effect in heavy-ion collisions. Within the framework of a toy model, it is possible to use the measured  $K^{*0}/K^-$  ratio in p+p and A+A collisions to estimate the lower limit of the time difference between chemical and kinetic freeze-out. For the most central collisions at RHIC this lower limit of the time difference is found to be about 3.7 fm/c, while it is about 4.7 fm/c at the LHC showing an indication of a longer lived system at higher energies.

# Bibliography

- [1] Z. W. Lin, C. M. Ko, Phys. Rev. C 65, 034904 (2002).
- [2] Z. W. Lin *et al.*, Phys. Rev. C 72, 064901 (2005).
- [3] Z. W. Lin, S.Pal, C.M.Ko, B.A.Li and B.Zhang, Phys. Rev. C 64, 011902 (2001).
- [4] G. E. Brown and M. Rho, Phys. Rev. Lett. 66, 2720 (1991).
- [5] M. M. Aggarwal *et al.* (STAR Collaboration), Phys. Rev. C 84, 034909 (2011).
- [6] B. I. Abelev *et al.* (STAR Collaboration), Phys. Rev. C 78, 044906 (2008).
- [7] J. Adams *et al.* (STAR Collaboration), Phys. Rev. C 71, 064902 (2005).
- [8] B. I. Abelev *et al.* (STAR Collaboration), Phys. Lett. B 673, 183 (2009).
- [9] B. I. Abelev *et al.* (ALICE Collaboration), Eur. Phys. J. C 72, 2183 (2012).
- [10] J. Beringer *et al.* (Particle Data Group), Phys. Rev. D 86, 010001 (2012).
- [11] R. Rapp and E. Shuryak, Phys. Rev. Lett. 86, 2980 (2001).
- [12] C. Song and V. Koch, Phys. Rev. C 55, 3026 (1997).
- [13] J. Rafelski, J. Letessier and G. Torrieri, Phys. Rev. C 64, 054907 (2001)  
[Erratum-ibid. C 65, 069902 (2002)].
- [14] M. Bleicher, J. Aichelin arXiv:0201123v1.
- [15] X. N. Wang and M. Gyulassy, Phys. Rev. D 44, 3501 (1991).

- [16] B. Zhang, *Comp. Phys. Comm.* 109, 193 (1998).
- [17] B. A. Li and C. M. Ko, *Phys. Rev. C* 52, 2037 (1995).
- [18] S. D. Protopopescu, M. Alston-Garnjost, A. Barbaro-Galtieri, S. M. Flatte, J. H. Friedman, T. A. Lasinski, G. R. Lynch and M. S. Rabin *et al.*, *Phys. Rev. D* 7, 1279 (1973).
- [19] M. J. Matison, A. Barbaro-Galtieri, M. Alston-Garnjost, S. M. Flatte, J. H. Friedman, G. R. Lynch, M. S. Rabin and F. T. Solmitz, *Phys. Rev. D* 9, 1872 (1974).
- [20] S. V. Afanasiev *et al.* (NA49 Collaboration), *Phys. Lett. B* 491, 59 (2000).
- [21] J. Adams *et al.* (STAR Collaboration), *Phys. Rev. Lett.* 92, 112301 (2004); J. Adams *et al.* (STAR Collaboration), *Phys. Rev. Lett.* 93, 012301 (2004).

# Chapter 5

## Elliptic flow $K^{*0}$ meson in Pb-Pb collisions at $\sqrt{s_{NN}} = 2.76$ TeV

In this chapter we will discuss the results of elliptic flow analysis of  $K^{*0}$  meson in Pb-Pb collisions at  $\sqrt{s_{NN}} = 2.76$  TeV.

### 5.1 Introduction

In non-central heavy ion collisions [2], the overlap area of two nucleus is not spatially isotropic. This initial spatial anisotropy is transformed into an anisotropy in momentum space because of the pressure gradient developed among the constituents [2]. The elliptic flow coefficient, called  $v_2$  (defined in equation 5.2), is a measure of such anisotropy in momentum space. The  $v_2$  of charged particles and identified hadrons have been measured at RHIC [3, 4, 5, 6] and LHC [7, 8]. It is observed that the  $v_2$  at low transverse momentum at RHIC and LHC is similar which is consistent with the predictions from hydrodynamic models [9, 10]. In particular, the measurement of  $v_2$  of  $K^{*0}$  is important because of its small lifetime which is comparable to that of the medium formed in heavy ion collisions. Thus the decay products of  $K^{*0}$  undergoes re-scattering effect in the hadronic phase and the  $v_2$  of  $K^{*0}$  may be modified [11].

Moreover the mass of  $K^{*0}$  is comparable to that of proton. So the  $v_2$  of  $K^{*0}$  will help in understanding baryon-meson  $v_2$  difference at intermediate transverse momentum ( $\sim 2 < p_T < 6$  GeV/c).

In this thesis, we will present the results of elliptic flow measurement ( $v_2$ ) of  $K^{*0}$  meson in Pb-Pb collisions at  $\sqrt{s_{NN}} = 2.76$  TeV. The  $K^{*0}$   $v_2$  will help us to understand re-scattering effect and baryon-meson difference (number of quark scaling) in  $v_2$  at intermediate  $p_T$ . The method for the estimation of  $v_2$  is discussed in following section.

## 5.2 Analysis Method

The invariant yield of particles produced in heavy ion collisions can be expanded in the form of Fourier series [12, 13],

$$E \frac{d^3 N}{dp^3} = \frac{1}{2\pi} \frac{d^2 N}{p_T dp_T dy} \left( 1 + \sum_{n=1}^{\infty} v_n(p_T, y) \cos[n(\varphi - \Psi_R)] \right) \quad (5.1)$$

where  $E$  is the energy of the particle,  $p$  the momentum,  $p_T$  the transverse momentum,  $\varphi$  the azimuthal angle,  $y$  the rapidity and  $\Psi_R$  is the reaction plane angle. The  $\Psi_R$  is defined by the beam axis and the impact parameter between the colliding nucleus. The  $n^{th}$  order Fourier coefficient  $v_n$  is given by,

$$v_n = \langle \cos[2(\varphi - \Psi_R)] \rangle \quad (5.2)$$

where the average is taken over all particles over all events. The first Fourier coefficient  $v_1$  is called directed flow and the second coefficient  $v_2$  is called elliptic flow. This thesis focusses only on the measurement of  $v_2$ . For the estimation of  $v_2$  of  $K^{*0}$  we have used the Event Plane method [13] which is discussed below.

### 5.2.1 Estimation of event plane

In real heavy ion experiment it is not possible measure the impact parameter between the two nuclei and hence the reaction plane is unknown. We used a method to estimate the reaction plane by using the anisotropy flow itself [13]. Such an estimated reaction

plane is called an event plane. First we construct the event flow vector which is defined as,

$$Q_X = Q_n \cos(n\Psi_n) = \sum_{i=1}^N W_i \cos(n\varphi_i) \quad (5.3)$$

$$Q_Y = Q_n \sin(n\Psi_n) = \sum_{i=1}^N W_i \sin(n\varphi_i) \quad (5.4)$$

where  $W_i$  is the weight and  $N$  is the total number of produced particles in a given acceptance used for flow vector calculation in an event. The  $n^{\text{th}}$  harmonic event plane is given by,

$$\Psi_n = \frac{1}{n} \tan^{-1} \left( \frac{\sum_{i=1}^N W_i \sin(n\varphi_i)}{\sum_{i=1}^N W_i \cos(n\varphi_i)} \right) \quad (5.5)$$

### 5.2.2 Event plane resolution correction

Due to the finite number of particle produced in a heavy ion collision, there is a finite resolution of the estimated event plane angle. Thus the estimated  $v_2$  has to be corrected for such event plane resolution ( $R$ ). Therefore,

$$v_2 = \frac{v_2^{\text{obs}}}{R} = \frac{v_2^{\text{obs}}}{\langle \cos 2(\Psi_2 - \Psi_R) \rangle} \quad (5.6)$$

where  $\Psi_R$  is the true reaction plane angle. The term  $\langle \cos 2(\Psi_2 - \Psi_R) \rangle$  can be written as,

$$\langle \cos 2(\Psi_2 - \Psi_R) \rangle = \frac{\sqrt{\pi}}{2\sqrt{2}} \chi_2 e^{-\chi_2^2/4} [I_0(\chi_2^2/4) + I_1(\chi_2^2/4)] \quad (5.7)$$

where,  $\chi_2 = v_2/\sigma$  with  $\sigma = \sqrt{\frac{1}{2M} \frac{\langle W^2 \rangle}{\langle W \rangle^2}}$ ;  $M$  is the particle multiplicity used in the calculation of flow vector  $Q_n$  and  $I_x$  is the modified Bessel function of order  $x$ .

The drawback of full event plane method is that the same set of tracks are used for the estimation of event plane and  $v_2$ . This may bias the measurement of  $v_2$ . To remove this auto-correlation effect, we have considered different pseudorapidity ( $\eta$ ) regions for the estimation of event plane and  $v_2$ . The event plane is constructed taking the particles within  $0.5 < |\eta| < 0.8$  whereas the  $v_2$  is calculated by using the particles in the range  $|\eta| < 0.5$ .

### 5.2.3 Event plane flattening

Due to the non uniform acceptance of the detectors the distribution of the azimuthal angle is not flat. To correct for this effect we have used a  $\varphi$  weighting procedure to flatten the event plane distribution. In this procedure, each particle  $i$  gets a weight  $W_{\varphi_i}$ ,

$$W_{\varphi_i} = \frac{1}{N_{\varphi_i}} \times \frac{\sum_i^{N_{bins}} N_{\varphi_i}}{N_{bins}} \quad (5.8)$$

where  $\varphi_i$  is the azimuthal angle at which the track  $i$  is emitted and  $N_{\varphi_i}$  is the discrete bin in the histogram that contains  $\varphi_i$ . The obtained weights are then used in the calculation of flow vectors ( $Q_n$ ). For the estimation of  $v_2$ , we have used invariant mass method which is described below.

### 5.2.4 $v_2$ vs. invariant mass method

This method [14] is used to calculate the  $v_2$  of such particles those are identified through their decay products. The steps of this method are the following:

- 1) First calculate  $v_2^{sig.+bkg.}$  as a function of  $\pi$  K invariant mass ( $M_{\pi K}$ ), where  $v_2^{sig.+bkg.} = \langle \cos[2(\varphi - \Psi_2)] \rangle$ .
- 2) Then decompose the  $v_2^{sig.+bkg.}$  as,

$$v_2^{sig.+bkg.} = v_2^{sig.} \frac{sig.}{sig. + bkg.}(M_{\pi K}) + v_2^{bkg.} \frac{bkg.}{sig. + bkg.}(M_{\pi K}) \quad (5.9)$$

where  $sig.$  is the signal yield and  $bkg.$  is the background yield;

$v_2^{sig.}$ ,  $v_2^{bkg.}$  and  $v_2^{sig.+bkg.}$  are the  $v_2$  for signal, background and total particles.

$\frac{sig.}{sig.+bkg.}$  and  $\frac{bkg.}{sig.+bkg.}$  are the ratios as a function of  $\pi$  K invariant mass;

The term  $v_2^{bkg.}$  is parameterized by a polynomial function of invariant mass. The  $v_2$  as a function of  $M_{\pi K}$  is fitted with the equation 5.9 and from fitting  $v_2^{sig.}$  is extracted which is further corrected for the resolution of event plane.

## 5.3 Event selection

The analysis is done using the Pb-Pb data taken by the ALICE detector in the year of 2010. The minimum bias events are selected using the  $MB_{OR}$  trigger which requires a logical OR between the signals from Silicon Pixel Detector (SPD) and VZERO detectors. The beam induced background is reduced using timing information from the VZERO detectors and by a cut on the position of the primary vertex reconstructed by the SPD detector. The analysis is performed within a  $\pm 10$  cm of the Z-position of the primary vertices. The distribution of Z-position of vertex in Pb-Pb collisions is shown in Fig. 6.1. The centrality is estimated using the amplitude of V0 detector.

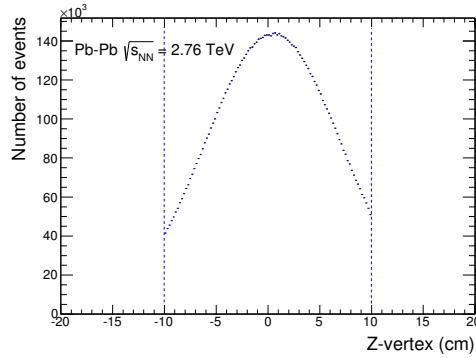


Figure 5.1: Z-position of vertex distribution in 0-80% minimum bias Pb-Pb collisions at  $\sqrt{s_{NN}} = 2.76$  TeV.

## 5.4 Track selection

The  $K^{*0}$  is reconstructed via its hadronic decay channel ( $K^{*0} \rightarrow \pi^- K^+$  and  $\bar{K}^{*0} \rightarrow \pi^+ K^-$  with branching ratio 66% [4]) in the rapidity range  $-0.5 < y < 0.5$  in Pb-Pb collisions at  $\sqrt{s_{NN}} = 2.76$  TeV. The good quality tracks are reconstructed by using the detectors ITS and TPC. A refit is performed with the reconstructed tracks in which the tracks are refitted inwards from the outermost layer of the TPC to the innermost layers of ITS and prolonged to the primary vertex and vice-versa. The

good quality tracks are ensured by requiring a minimum TPC number of clusters as 70 out of possible 159, a minimum  $\chi^2$  of the fit to the TPC clusters as 4 and at least one hit in the inner sector of the SPD. The tracks with kinks (tracks those decayed to muon and neutrino, *eg*,  $K^\pm \rightarrow \mu^\pm + \nu_\mu$ ) are rejected by kink decay topology. In order to reduce the contamination from the secondaries a strict  $p_T$  dependent cut on the  $DCA_{XY}$  ( $DCA_{XY}(p_T) < 0.0182 + 0.0350/pt^{1.01}$  cm) and  $DCA_Z$  ( $DCA_Z < 0.2$  cm) is applied. To maintain a reasonable resolution and reduce acceptance drop, the tracks with transverse momentum greater than 150 MeV/c and pseudorapidity between  $-0.5 < \eta < 0.5$  are selected. The list of track cuts for selecting the resonance decay products are shown in Table 6.1.

Cut name	Resonance tracks
$p_T$ range	$p_T > 0.15 \text{ GeV}/c$
$\eta$ range	$-0.5 < \eta < 0.5$
TPC and ITS refit	yes
Reject kink daughters	yes
Minimum TPC clusters	70
TPC $\chi^2$ / number of clusters	4
Minimum number of cluster in SPD	1
$(DCA)_{XY}(p_T)$	$< 0.0182 + 0.035p_T^{-1.01}$ cm
$(DCA)_z$	$< 2$ cm
Rapidity	$-0.5 < y_{pair} < 0.5$

Table 5.1: Track selection criteria for selecting resonance daughter tracks.

## 5.5 PID selection

The decay products of  $K^{*0}$ , pions and kaons, are identified using the combination of Time Projection Chamber (TPC) and Time of Flight (TOF) detectors. The particles are identified using a cut on a number of standard deviation ( $N\sigma$ ) with respect to

the expectation. For the TPC and TOF the  $N\sigma$  are defined by the equation below:

$$N\sigma_{TPC} = \frac{dE/dx_{measured} - dE/dx_{expected}}{\sigma_{TPC}^{PID}} \quad (5.10)$$

$$N\sigma_{TOF} = \frac{time_{measured} - time_{expected}}{\sigma_{TOF}^{PID}} \quad (5.11)$$

where

- $dE/dx_{measured}$  is the energy loss of the tracks measured in TPC;
- $dE/dx_{expected}$  is the expected energy loss of the tracks using a parameterization of modified Bethe Bloch function [6, 7];
- $\sigma_{TPC}^{PID}$  PID resolution of the TPC which is about 5% for pp collisions;
- $time_{measured}$  is the flight time of the particle measured by an algorithm of TOF and T0 detector;
- $time_{expected}$  is the flight time computed during the central tracking procedure;
- $\sigma_{TOF}^{PID}$  is the PID resolution of the TOF detector which is about 120 ps for pp collisions.

If the tracks does not have a TOF signal, the pions and kaons are identified with within  $5\sigma_{TPC}$ ,  $3\sigma_{TPC}$  and  $2\sigma_{TPC}$  from the Bethe Bloch expectation with momentum  $p < 0.35$  GeV/c,  $0.35 < p < 0.5$  GeV/c and  $p > 0.5$  GeV/c respectively. Further the kaons with  $p > 0.7$  GeV/c are rejected to reduce the contamination. For the tracks with TOF signal, the pions (and kaons) are taken within  $3\sigma_{TOF}$  and  $2\sigma_{TOF}$  for  $p < 1.5$  GeV/c and  $p > 1.5$  GeV/c respectively.

## 5.6 Analysis

The invariant mass of  $K^{*0}$  is reconstructed from the pions and kaons identified by TPC and TOF detectors as discussed in the section 1.2.7 above. In the left panel of Fig. 5.2 the open black circles represent the unlike charged  $\pi$  K invariant mass in same event for 0-80% minimum bias Pb-Pb collisions at  $\sqrt{s_{NN}} = 2.76$  TeV. The solid red line indicates the  $\pi$  K invariant mass from the mixed event. The mixed event distribution is normalized in the invariant mass range of 1.1 to 1.3 GeV/c<sup>2</sup> where the

signal is very unlikely to be correlated. The right panel of Fig. 5.2 shows the signal of  $K^{*0}$  after the combinatorial background subtraction. It is fitted with a Breit-Wigner function and a second order polynomial in invariant mass to take care of residual background,

$$\frac{Y}{2\pi} \times \frac{\Gamma}{(M_{K\pi} - M)^2 + \frac{\Gamma^2}{4}} + AM_{K\pi}^2 + BM_{K\pi} + C, \quad (5.12)$$

where  $M$  and  $\Gamma$  are the mass and invariant mass width of the  $K^{*0}$ . The parameter  $Y$  gives the Breit-Wigner area. The signal and background is obtained in various momentum bins in 0-80% minimum bias Pb-Pb collisions.

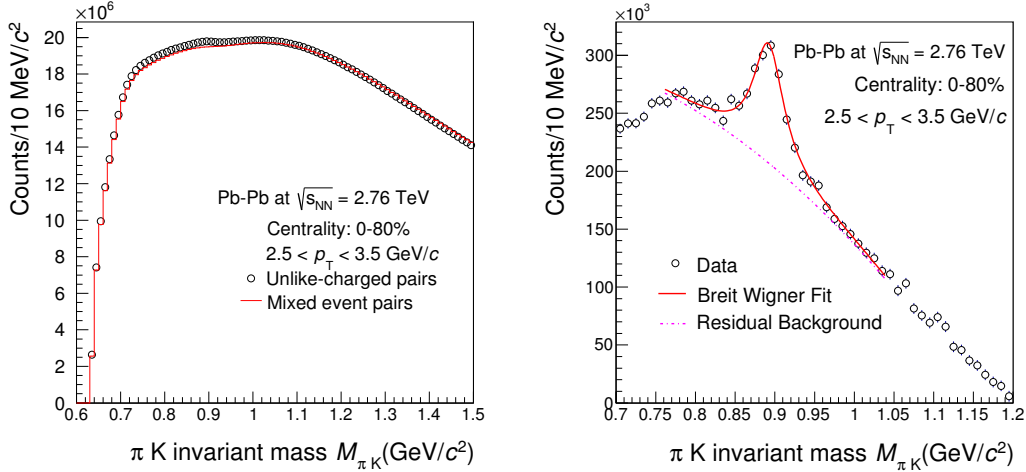


Figure 5.2: (Color online) Left panel: Unlike charged  $\pi$  K invariant mass in same event and mixed event after normalization for 0-80% minimum bias Pb-Pb collisions at  $\sqrt{s_{NN}} = 2.76$  TeV. Right panel: Unlike charged  $\pi$  K invariant mass after combinatorial background subtraction. The data fitted with a Breit Wigner function (solid red line) and a residual background function (dotted magenta line). The uncertainties shown are statistical only.

The event plane angle  $\Psi_2$  is estimated by using equation 5.5. The  $\varphi$  weighting procedure is followed to flatten the event plane angle distribution. The event plane angle distributions for particles within the range  $0.5 < |\eta| < 0.8$  are shown in Fig. 5.3 after applying  $\varphi$  weights. The distribution is fitted with a function,

$$f = p_0[1 + 2p_1\cos(2\Psi_2) + 2p_2\sin(2\Psi_2)], \quad (5.13)$$

where  $p_0$ ,  $p_1$  and  $p_2$  are the free parameters. The small values of  $p_1$  and  $p_2$  indicate that the event plane angle distribution is flat.

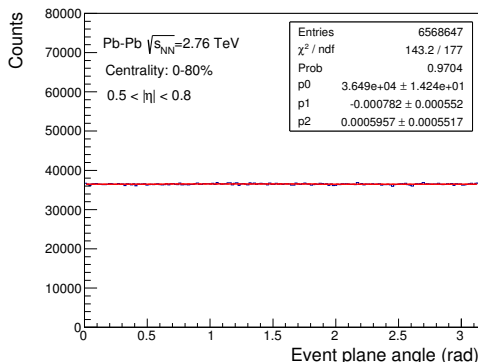


Figure 5.3: (Color online) TPC event plane distribution in 0-80% minimum bias Pb-Pb collisions at  $\sqrt{s_{NN}} = 2.76$  TeV within  $0.5 < |\eta| < 0.8$ . The distribution is fitted with equation 5.13

Then  $v_2$  of the  $\pi$  K pair is estimated by using the event plane ( $\Psi_2$ ). The solid black circle in Fig. 5.4 shows the  $v_2^{sig.+bkg.}$  as a function of  $M_{\pi K}$ . It is fitted with a function (shown by a solid red line) given in equation 5.9. Here the  $v_2^{bkg.}$  is parameterized by a third order polynomial function in  $M_{\pi K}$ . From fitting the  $v_2^{sig.}$  is obtained which is further corrected for the event plane resolution ( $R=0.65$ ) as described in section 1.2.2.

## 5.7 Results

The  $v_2$  of  $K^{*0}$  in 0-80% minimum bias Pb-Pb collisions at  $\sqrt{s_{NN}} = 2.76$  TeV is extracted via invariant mass method. The solid red circles in Fig. 5.5 shows the  $v_2$  of  $K^{*0}$  as a function of transverse momentum  $p_T$ . The uncertainties shown on the plot are statistical only. The  $v_2$  of  $K^{*0}$  is compared with the results of the  $K^{*0}$  meson

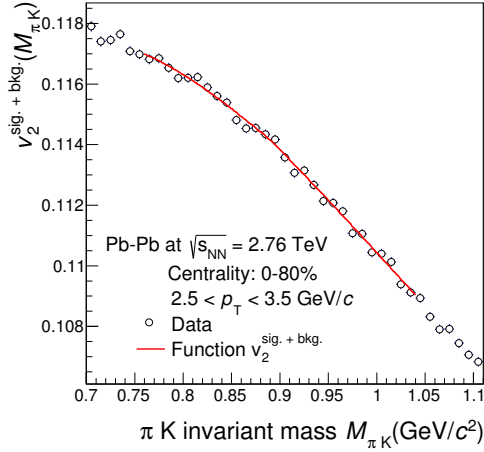


Figure 5.4: (Color online)  $v_2^{sig.+bkg.}$  as a function of  $M_{\pi K}$  for 0-80% minimum bias Pb-Pb collisions at  $\sqrt{s_{NN}} = 2.76$  TeV. The data is fitted with a function given in equation 5.9. The uncertainties shown are statistical only.

from Au+Au collision (Run IV) [19] at  $\sqrt{s_{NN}} = 200$  GeV. The  $v_2$  of  $K^{*0}$  at low  $p_T$  ( $< 3$  GeV/c) in ALICE is smaller than that measured in STAR experiment. This may be due to increasing hadronic re-scattering effects at LHC energies.

## 5.8 Summary

In summary, we have presented first results of  $v_2$  of  $K^{*0}$  meson through invariant mass method in Pb-Pb collisions at  $\sqrt{s_{NN}} = 2.76$  TeV. The results are compared with STAR measurements in Au+Au collisions at  $\sqrt{s_{NN}} = 200$  GeV. We have observed that the  $v_2$  of  $K^{*0}$  at low  $p_T$  at LHC energies is smaller than that measured at RHIC, may indicate an effect of increasing hadronic re-scattering at LHC energies.

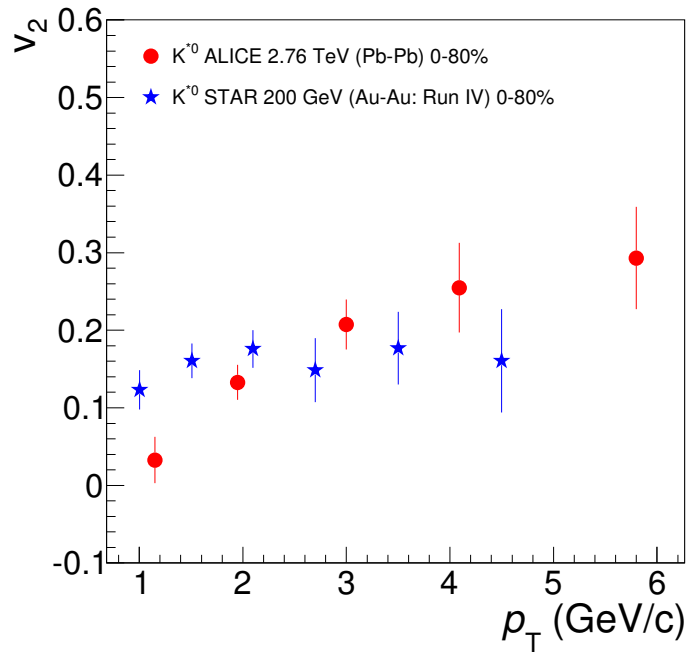


Figure 5.5: (Color online) Preliminary results of  $v_2$  of  $K^{*0}$  as a function of  $p_T$  for 0-80% minimum bias Pb-Pb collisions at  $\sqrt{s_{NN}} = 2.76$  TeV. The results are compared with the  $v_2$  of  $K^{*0}$  measured in STAR experiment. The uncertainties shown are statistical only.

## 5.9 Appendix

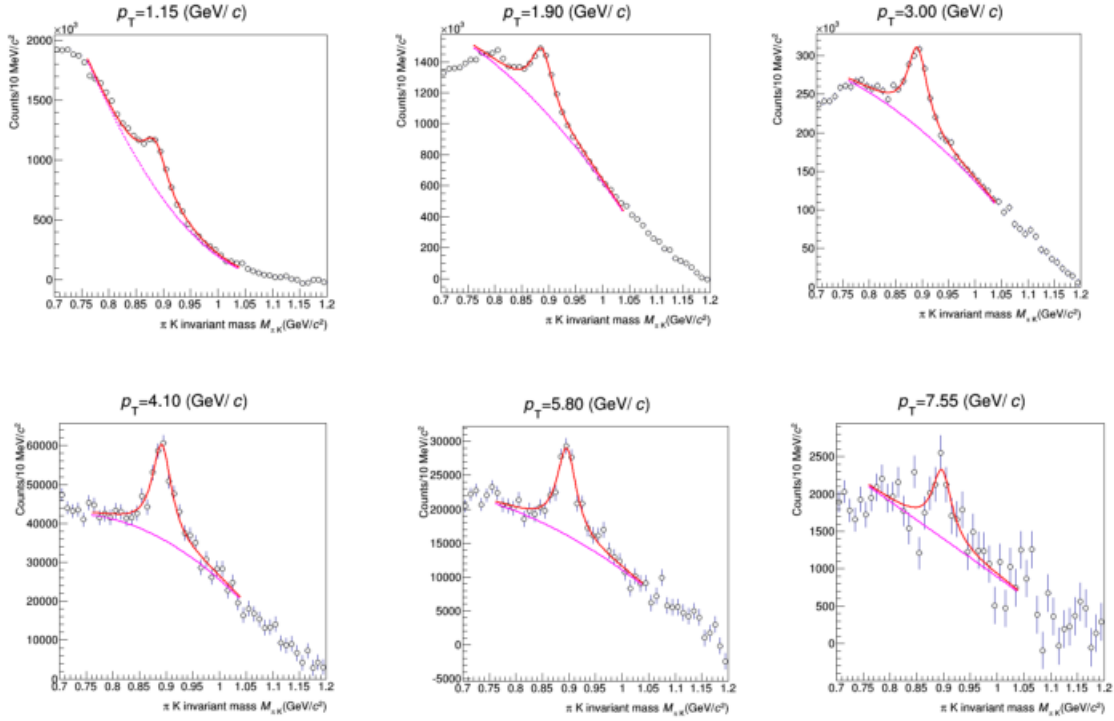


Figure 5.6: (Color online)  $K^{*0}$  signals after mixed event background subtraction in 0-80% minimum bias Pb-Pb collisions at  $\sqrt{s_{NN}} = 2.76$  TeV.

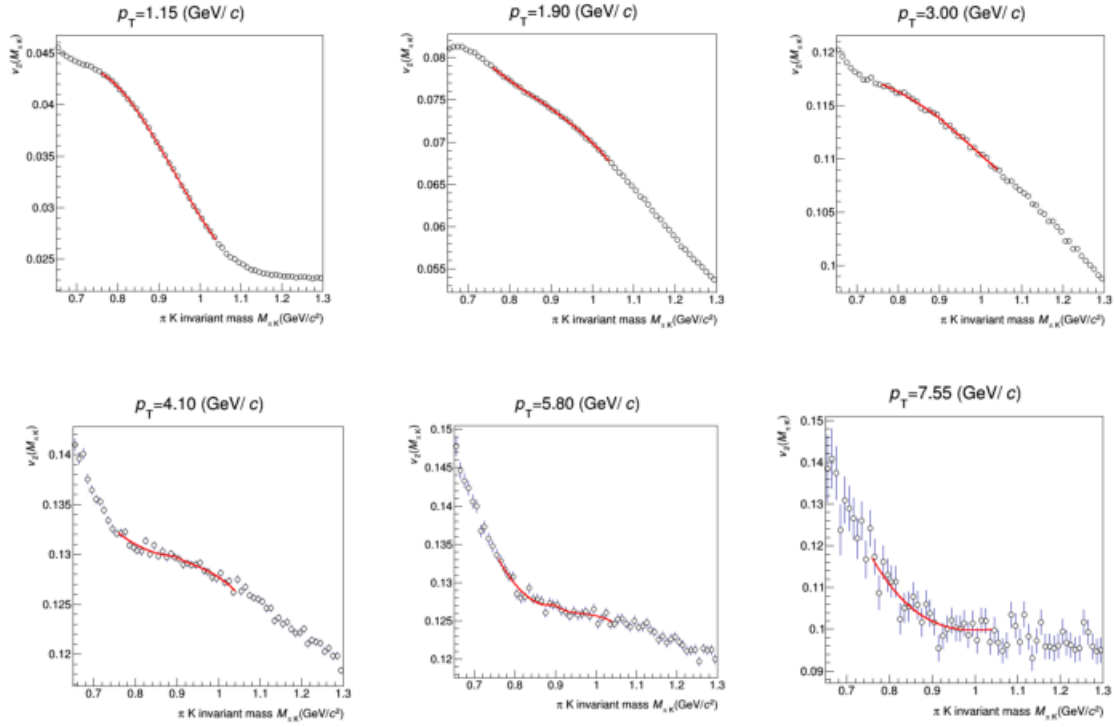


Figure 5.7: (Color online)  $v_2^{sig.+bkg.}$  as a function of  $M_{\pi K}$  for 0-80% minimum bias Pb-Pb collisions at  $\sqrt{s_{NN}} = 2.76$  TeV.

# Bibliography

- [1] G. E Brown and M. Rho, Phys. Rev. Lett. 66, 2720 (1991).
- [2] J. Y. Ollitrault, Phys. Rev. D 46, 229 (1992).
- [3] K. H. Ackermann *et al.* (STAR Collaboration), Phys. Rev. Lett. 86, 402 (2001).
- [4] J. Adams *et al.* (STAR Collaboration), Nucl. Phys. A 757, 102 (2005).
- [5] I. Arsene *et al.* (BRAHMS Collaboration), Nucl. Phys. A757, 1 (2005).
- [6] K. Adcox *et al.* (PHENIX Collaboration), Nucl. Phys. A757, 184 (2005).
- [7] K. Aamodt *et al.* (ALICE Collaboration), Phys. Rev. Lett. 105, 252302 (2010).
- [8] B. Abelev *et al.* (ALICE Collaboration), Phys. Lett. B 719 18 (2013).
- [9] G. Kestin and U. W. Heinz, Eur. Phys. J. C 61, 545 (2009).
- [10] H. Niemi, K. J. Eskola and P. V. Ruuskanen, Phys. Rev. C 79, 024903 (2009).
- [11] C. Nonaka *et al.* Phys Rev C. 69, 031902 (2004).
- [12] S. Voloshin and Y. Zhang, Z. Phys. C 70, 665 (1996).
- [13] A. M. Poskanzer and S. A. Voloshin Phys. Rev. C 58 1671 (1998).
- [14] N. Borghini and J. Y. Ollitrault, Phys. Rev. C 70, 064905 (2004).
- [15] J. Beringer *et al.* [Particle Data Group], Phys. Rev. D **86**, 010001 (2012).

- [16] W. Blum, W. Riegler and L. Ronaldi, Particle Detection With Drift Chambers, 2nd ed. (Springer-Verlag, 2008)
- [17] K. Aamodt *et al.* (ALICE Collaboration), arXiv:1402.4476
- [18] ALICE Collaboration, paper in preparation.
- [19] J. Adams *et al.* (STAR Collaboration), Phys. Rev. C 71, 064902 (2005).

# Chapter 6

## $K^{*0}$ -hadron correlation in pp collisions at $\sqrt{s} = 7$ TeV

In this chapter we will discuss  $K^{*0}$ -hadron correlation analysis in pp collisions at  $\sqrt{s} = 7$  TeV.

### 6.1 Introduction

The resonances are very good probe to study the properties of strongly interacting matter [1] produced in heavy-ion collisions [2] as their lifetime is comparable to the lifetime of the medium formed in such collisions. In particular, the high momentum heavy resonances ( $K^*(892)^0, \phi(1020), \Lambda^*(1520)$ ) can be used to look for in-medium effects [3] through the study of correlation with respect to a jet or a leading particle (particle having highest momentum in an event). The high momentum resonances are likely to be produced early and also escape from the medium sufficiently fast so that they do not have sufficient interaction with the hadronic phase. The resonance-jet correlation in the same side (towards the direction of the jet or leading particle) and away side (opposite to the direction of the jet or leading particle) can distinguish between in-medium and in-vacuum fragmentation with an assumption that the same

side resonance properties and production remain unaffected due to the surface bias (jets are produced near the surface of the medium), while the away side resonances are likely to be interacting with the hot and dense partonic medium. The enhanced cross-section of jets at LHC energies provide sufficient statistics for carrying such correlation studies. We have not considered the low momentum resonances as their properties can be affected by the re-scattering and re-generation effects. It was proposed in [3] that the properties of resonances with transverse momentum  $p_T > 2 \text{ GeV}/c$  and emitted along the away side could be affected by in-medium effects. In this chapter, we will present the analysis of  $K^{*0}$ -hadron correlation with respect to a leading particle in pp collisions. We will study the mass, invariant mass distribution width and yield of  $K^{*0}$  with respect to the emission angle of the leading particle. This analysis will act as a baseline for such study in heavy-ion collisions.

## 6.2 Analysis Details

### 6.2.1 Event selection

The analysis is done using the pp data taken by the ALICE detector at  $\sqrt{s} = 7 \text{ TeV}$  in the year of 2010. The minimum bias events are selected using the  $MB_{OR}$  trigger which requires a logical OR between the signals from Silicon Pixel Detector (SPD) and VZERO detectors. The beam induced background is reduced using timing information from the VZERO detectors and by a cut on the position of the primary vertex reconstructed by the SPD detector. The analysis is performed within a  $\pm 10 \text{ cm}$  of the Z-position of the primary vertices. The distribution of Z-position of vertex in pp collisions is shown in Fig. 6.1.

### 6.2.2 Track selection

The resonance  $K^{*0}$  is reconstructed through its hadronic decay channel ( $K^{*0} \rightarrow \pi^- K^+$  and  $\bar{K}^{*0} \rightarrow \pi^+ K^-$  with branching ratio 66% [4]) in the rapidity range  $-0.5 < y < 0.5$  in pp collisions at  $\sqrt{s} = 7 \text{ TeV}$ . The good quality tracks are reconstructed by using

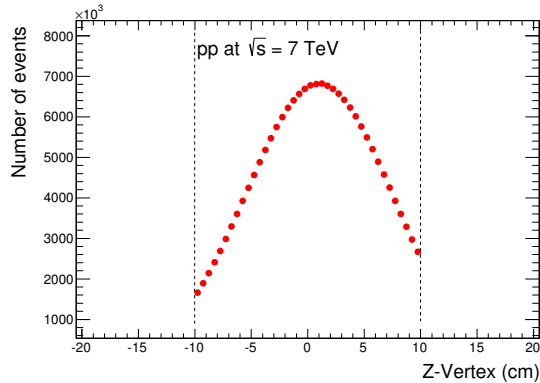


Figure 6.1: (Color online) The Z- position of vertex in pp collisions at  $\sqrt{s} = 7$  TeV.

the detectors ITS and TPC. A refit is performed with the reconstructed tracks in which the tracks are refitted inwards from the outermost layer of the TPC to the innermost layers of ITS and prolonged to the primary vertex and vice-versa. The good quality tracks are ensured by requiring a minimum TPC number of clusters as 70 out of possible 159, a minimum  $\chi^2$  of the fit to the TPC clusters as 4 and at least one hit in the inner sector of the SPD. The tracks with kinks (tracks those decayed to muon and neutrino, *eg*,  $K^\pm \rightarrow \mu^\pm + \nu_\mu$ ) are rejected by kink decay topology. In order to reduce the contamination from the secondaries a strict  $p_T$  dependent cut on the  $DCA_{XY}$  ( $DCA_{XY}(p_T) < 0.0182 + 0.0350/p_T^{1.01}$  cm) and  $DCA_Z$  ( $DCA_Z < 0.2$  cm) is applied. To maintain a reasonable resolution and reduce acceptance drop, the tracks with transverse momentum greater than 150 MeV/c and pseudorapidity between  $-0.8 < \eta < 0.8$  are selected. The list of track cuts for selecting the resonance decay daughters are given in Table 6.1.

### 6.2.3 Leading particle selection

The leading particle is selected as the track having highest transverse momentum in an event. For selecting the leading particle the good quality tracks inside TPC (TPC only tracks) are considered because of their flat azimuthal acceptance as shown in

Cut name	Resonance tracks	Trigger tracks
$p_T$ range	$p_T > 0.15 \text{ GeV}/c$	$p_T > 4 \text{ GeV}/c$
$\eta$ range	$-0.8 < \eta < 0.8$	$-0.8 < \eta < 0.8$
TPC and ITS refit	yes	no
Reject kink daughters	yes	yes
Minimum TPC clusters	70	70
TPC $\chi^2$ / number of clusters	4	4
Minimum number of cluster in SPD	1	–
$(DCA)_{XY}(p_T)$	$< 0.0182 + 0.035p_T^{-1.01} \text{ cm}$	$< 2.4 \text{ cm}$
$(DCA)_Z$	$< 2 \text{ cm}$	$< 3.2 \text{ cm}$
Rapidity	$-0.5 < y_{pair} < 0.5$	$-0.5 < y < 0.5$

Table 6.1: Track selection criteria for selecting resonance daughter tracks and trigger particle tracks.

Fig.6.2. The periodic dips are due to the gap between the 18 sectors of the TPC. To ensure a good quality of the TPC only tracks, a minimum TPC number of cluster of 70 out of possible 159 with a minimum  $\chi^2$  of the fit to the TPC clusters as 4 and no constraint on the number of cluster in the inner most ITS layer is required. Further to maintain flat azimuthal angle distribution, the refitting of the tracks using the ITS is not required. To improve global resolution the tracks with pseudo-rapidity between  $-0.8 < \eta < 0.8$  is considered. The secondary contamination is reduced by requiring a maximum distance to closest approach (DCA) in the xy plane as  $(DCA_{XY})$  2.4 cm and in the Z-direction  $(DCA_Z)$  as 3.2 cm. The set of track cuts for selecting leading particle are given in Table 6.1.

#### 6.2.4 PID selection

The decay products, pions and kaons, are identified using the combination of Time Projection Chamber (TPC) and Time of Flight (TOF) detectors [5]. The particles are identified using a cut on a number of standard deviation ( $N\sigma$ ) with respect to

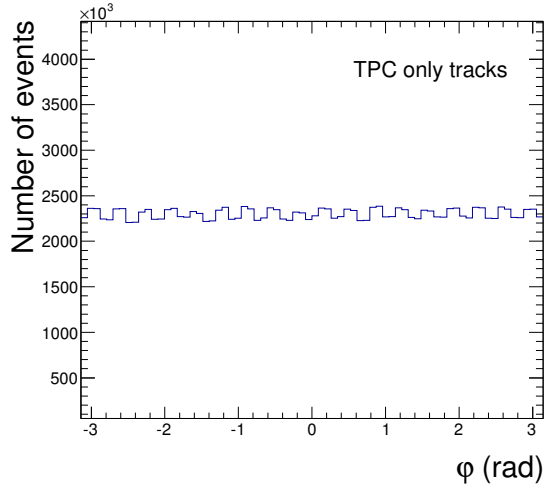


Figure 6.2: The azimuthal-angle distribution of TPC only tracks in pp collisions at  $\sqrt{s} = 7$  TeV.

the expectation. For the TPC and TOF the  $N\sigma$  are defined by the equation below:

$$N\sigma_{TPC} = \frac{dE/dx_{measured} - dE/dx_{expected}}{\sigma_{TPC}^{PID}} \quad (6.1)$$

$$N\sigma_{TOF} = \frac{time_{measured} - time_{expected}}{\sigma_{TOF}^{PID}} \quad (6.2)$$

where

- $dE/dx_{measured}$  is the energy loss of the tracks measured in TPC;
- $dE/dx_{expected}$  is the expected energy loss of the tracks using a parameterization of modified Bethe Bloch function [6, 7];
- $\sigma_{TPC}^{PID}$  PID resolution of the TPC which is about 5% for pp collisions;
- $time_{measured}$  is the flight time of the particle measured by an algorithm of TOF and T0 detector;
- $time_{expected}$  is the flight time computed during the central tracking procedure;
- $\sigma_{TOF}^{PID}$  is the PID resolution of the TOF detector which is about 120 ps for pp collisions.

If the tracks does not have a TOF signal, the pions and kaons are identified with within  $5\sigma_{TPC}$ ,  $3\sigma_{TPC}$  and  $2\sigma_{TPC}$  from the Bethe Bloch expectation with momentum

$p < 0.35$  GeV/c,  $0.35 < p < 0.5$  GeV/c and  $p > 0.5$  GeV/c respectively. Further the kaons with  $p > 0.7$  GeV/c are rejected to reduce the contamination. For the tracks with TOF signal, the pions (and kaons) are taken within  $3 \sigma_{TOF}$  and  $2 \sigma_{TOF}$  for  $p < 1.5$  GeV/c and  $p > 1.5$  GeV/c respectively.

## 6.2.5 Analysis technique

The analysis is done taking the events with leading particle transverse momentum  $p_T > 4.0$  GeV/c. The cut off range of transverse momentum is compromised keeping the event loss in mind. Further, to minimize the re-scattering and re-generation effects, the resonances with  $p_T > 2.0$  GeV/c are considered in the analysis. If the leading particles are the pions and kaons, giving the invariant mass of  $K^{*0}$ , are not considered. We considered the emission angle of the leading particle ( $\varphi_{leading}$ ) as the direction of trigger particle. We divide the full azimuthal angle with respect to the trigger particle in 18  $\Delta\varphi$  bins. The  $K^{*0}$  resonances are reconstructed in different  $\Delta\varphi$  ( $=\varphi_{resonance} - \varphi_{leading}$ ) bins with respect to the leading particle emission angle.

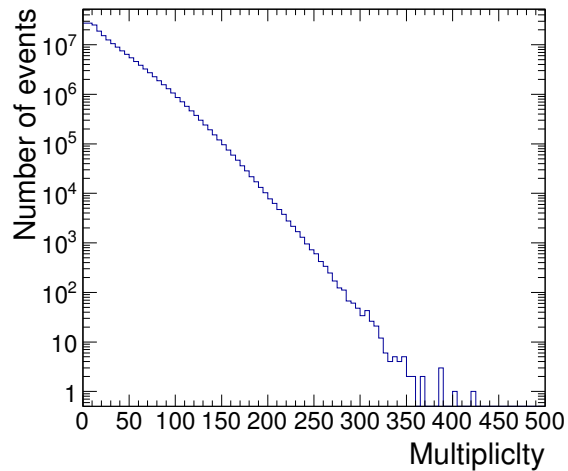


Figure 6.3: Multiplicity distribution of charged particles in TPC for pp collisions at  $\sqrt{s} = 7$  TeV.

### 6.2.6 Signal extraction:

The invariant mass of  $K^{*0}$  is reconstructed using the kaons and pions that are detected by a combination of TPC and TOF detectors. The combinatorial background is constructed using an event mixing technique, where the uncorrelated pions and kaons are taken from two different events having the difference in Z-vertex as 1 cm and difference in charged particle multiplicity as 5. The distribution of charged particles multiplicity in TPC is shown in Fig. 6.3. The mixed event background distribution is then normalized in the range of invariant mass range of 1.1 to 1.3  $GeV/c^2$  ( $4\Gamma^1$  away from the signal), where the pairs are very unlikely to be correlated. Then this mixed event  $K\pi$  invariant mass distribution is subtracted from the same event invariant mass distribution. The same event and normalized mixed event invariant mass distributions before the background subtraction in various  $\Delta\varphi$  bins are shown in Figures 6.4 and 6.5. The  $K^{*0}$  signal, obtained after the subtraction is fitted with a Breit-Wigner and a first order polynomial function in invariant mass (to take care of the residual background) as given in equation 6.3.

$$\frac{Y}{2\pi} \times \frac{\Gamma}{(M_{K\pi} - M)^2 + \frac{\Gamma^2}{4}} + AM_{K\pi}^2 + BM_{K\pi} + C, \quad (6.3)$$

where  $M$  and  $\Gamma$  are the mass and invariant mass width of the  $K^{*0}$ . The parameter  $Y$  gives the Breit-Wigner area. The residual background function is taken as a polynomial of first order in  $\pi K$  invariant mass ( $M_{K\pi}$ ). The signals are obtained in various  $\Delta\varphi$  bins after subtracting the mixed event distribution from the same event distribution are shown in Figures 6.6 and 6.7. The mass, width and yield of  $K^{*0}$  are extracted from the Breit-Wigner fit in 18  $\Delta\varphi$  bins.

## 6.3 Results

The mass and width of  $K^{*0}$  extracted from Breit-Wigner fitting are shown in Figures 6.8 and 6.9 as a function of the azimuthal angle with respect to the leading

---

<sup>1</sup>the full width at half maximum of  $K^{*0}$  invariant mass distribution

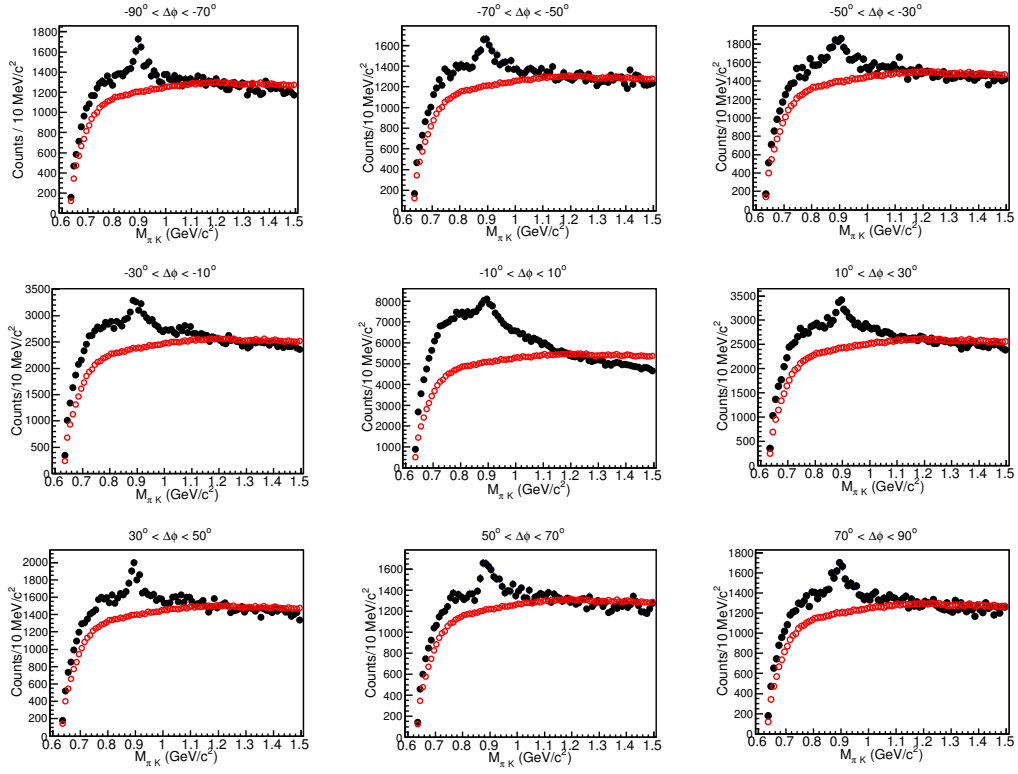


Figure 6.4: (Color online)  $K\pi$  invariant mass distribution in same event (solid black circle) and mixed event (open red circle) after normalization for pp collisions at  $\sqrt{s} = 7$  TeV.

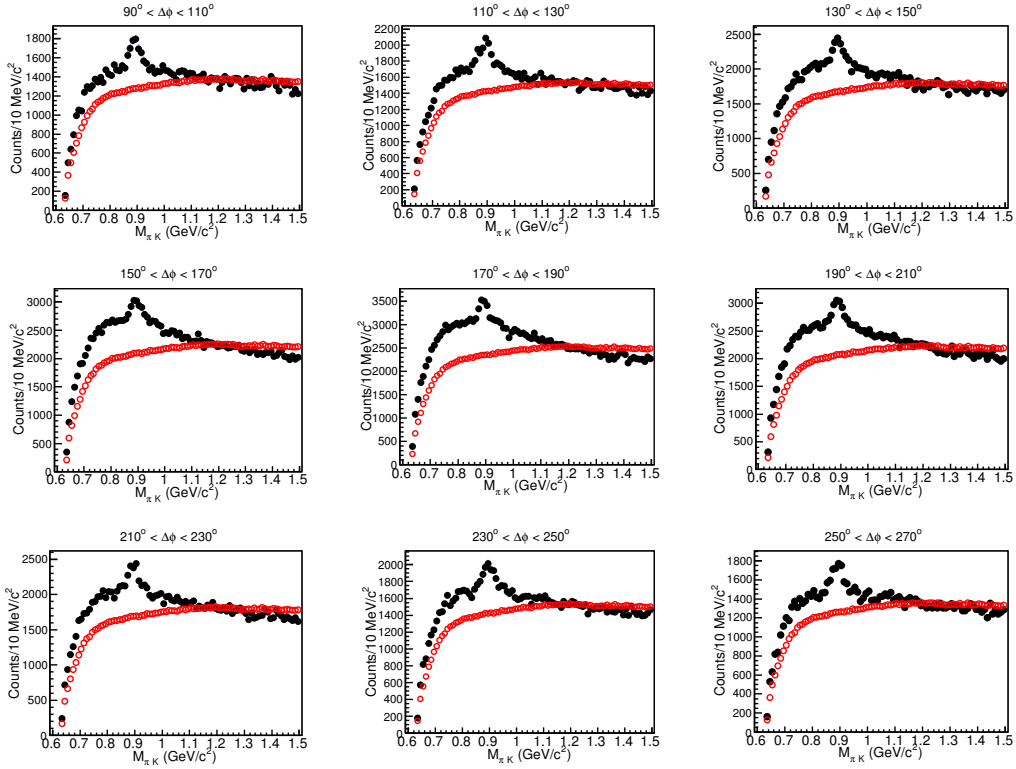


Figure 6.5: (Color online)  $K\pi$  invariant mass distribution in same event (solid black circle) and mixed event (open red circle) after normalization for pp collisions at  $\sqrt{s} = 7$  TeV.

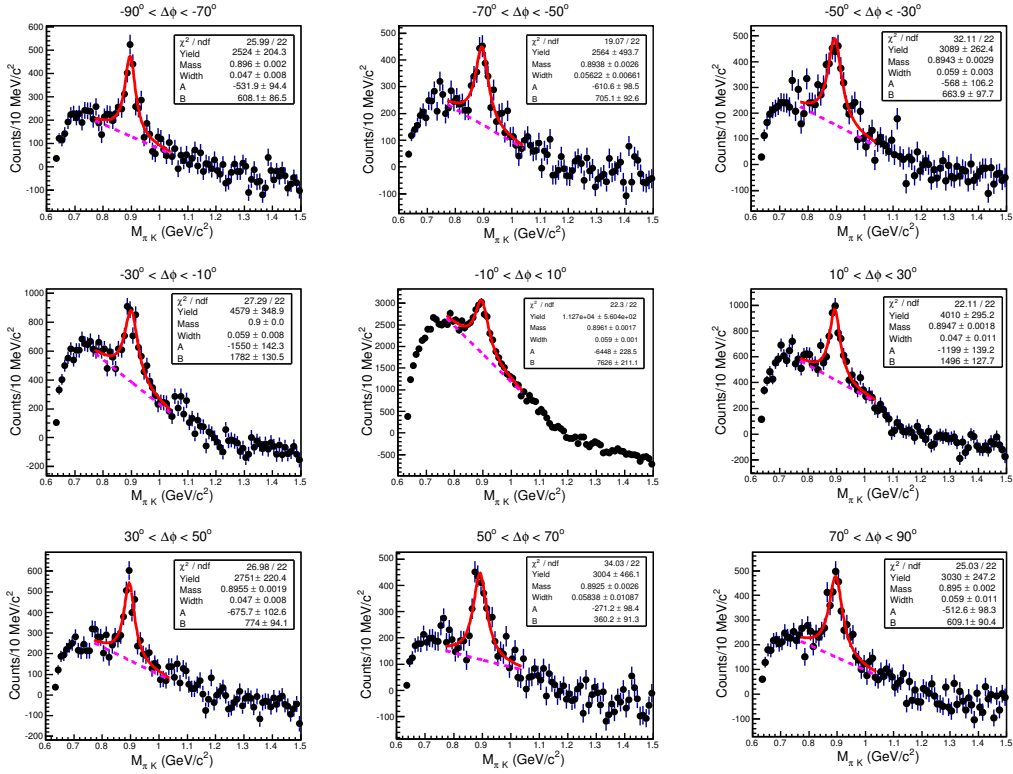


Figure 6.6: (Color online)  $K\pi$  invariant mass distribution after the mixed event background subtraction. The signal is fitted with a Breit Wigner function (solid red line) plus a linear polynomial (dotted magenta line) in invariant mass.

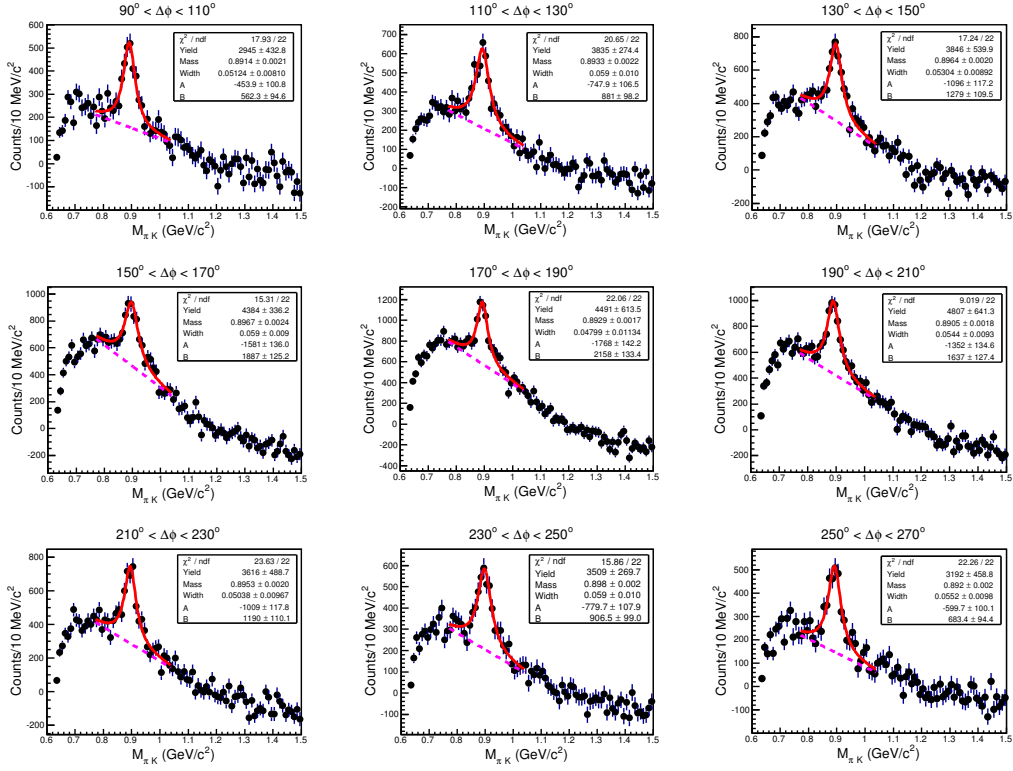


Figure 6.7: (Color online)  $K\pi$  invariant mass distribution after the mixed event background subtraction. The signal is fitted with a Breit Wigner function (solid red line) plus a linear polynomial (dotted magenta line) in invariant mass.

Table 6.2: Fit parameters of double gaussian

	Near side	Away side
Amplitude	$1.42 \times 10^{07} \pm 1.02 \times 10^{06}$	$1.37 \times 10^{07} \pm 2.60 \times 10^{06}$
Mean (rad)	0	180
RMS (rad)	$10.74 \pm 0.55$	$50.35 \pm 8.76$

particle. There is no mass shift and/or width broadening observed in pp collisions. The yield of  $K^{*0}$  as a function of  $\Delta\varphi$  is shown in Figure 6.10. The correlation is fitted with a double gaussian function with mean fixed at 0 and 180 degree.

$$\frac{dN}{d\varphi} = C + A_1 g_1(\Delta\varphi) + A_2 g_2(\Delta\varphi), \quad (6.4)$$

where

$$g(\varphi) = \frac{1}{\sqrt{2\pi}\sigma} \exp\left(-\frac{\Delta\varphi^2}{2\sigma^2}\right), \quad (6.5)$$

The fit parameters (Amplitude, Mean, RMS) in near side and away side are given in Table 1.

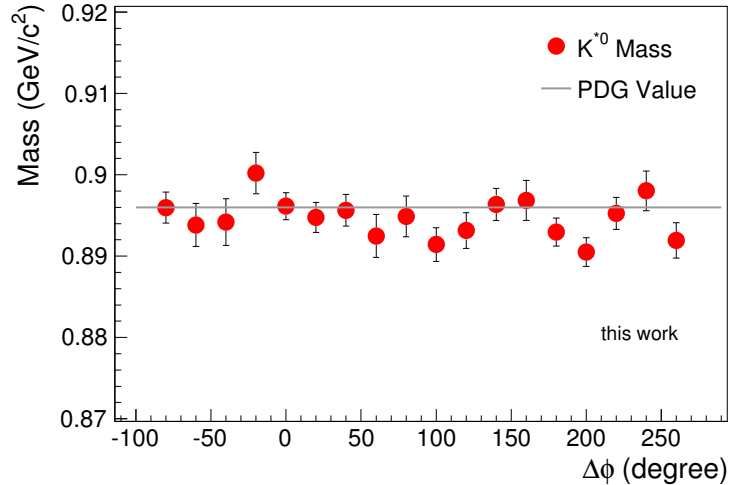


Figure 6.8: (Color online)  $K^{*0}$  mass as a function of azimuthal angle ( $\Delta\phi$ ) with respect to the leading particle. The solid black line is the PDG value.

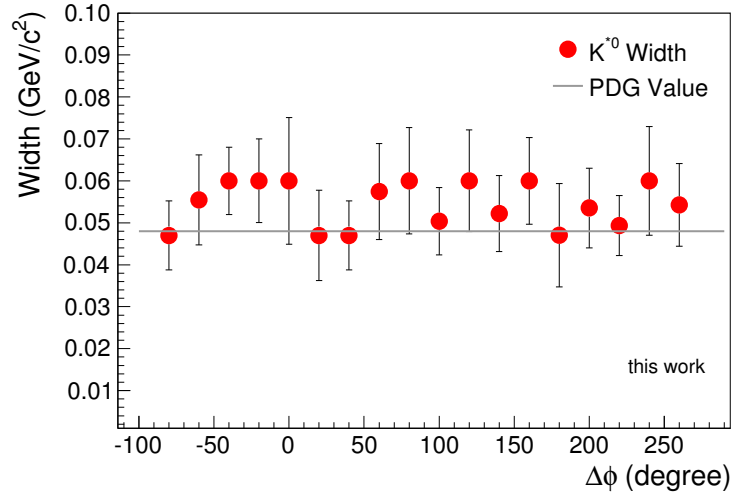


Figure 6.9: (Color online)  $K^{*0}$  width as a function of azimuthal angle ( $\Delta\phi$ ) with respect to the leading particle. The solid black line is the PDG value.

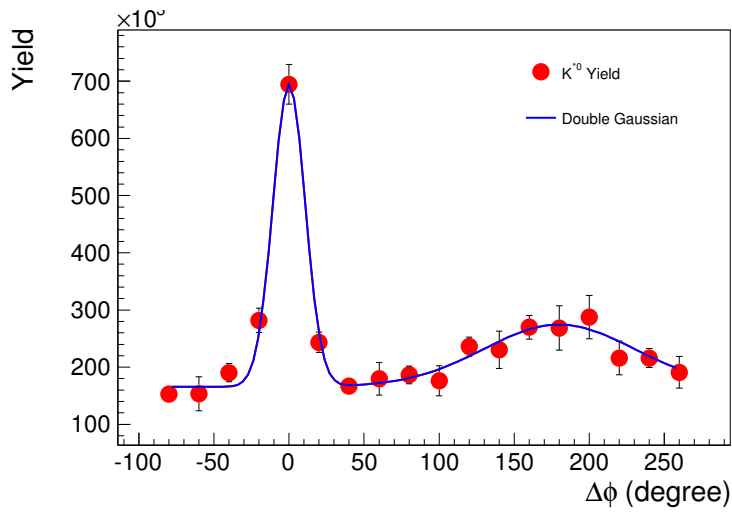


Figure 6.10: (Color online)  $K^{*0}$  yield as a function of azimuthal angle ( $\Delta\phi$ ) with respect to the leading particle. The solid red line is the double gaussian function with fixed mean.

## 6.4 Summary

In summary, we have studied the correlation of  $K^{*0}$  resonance with the leading hadrons in pp collisions at 7 TeV with the ALICE detector at the LHC. We have not observed any mass shift and/or width broadening as a function of the leading particle azimuthal angle. We observe a nice correlation in the  $K^{*0}$  yield as a function of  $\Delta\phi$ . This analysis may act as a baseline study for the future analysis in Pb-Pb collisions.

# Bibliography

- [1] R. Rapp and E. Shuryak, Phys. Rev. Lett. **86**, 2980 (2001).
- [2] G. E. Brown and M. Rho, Phys. Rev. Lett. **66**, 2720 (1991).
- [3] C. Markert *et al.*, Phys. Lett. B**92**, 669 (2008).
- [4] J. Beringer *et al.* [Particle Data Group], Phys. Rev. D **86**, 010001 (2012).
- [5] B. I. Abelev *et al.* [ALICE Collaboration], Eur. Phys. J. C **72**, 2183 (2012).
- [6] W. Blum, W. Riegler and L. Ronaldi, Particle Detection With Drift Chambers, 2nd ed. (Springer-Verlag, 2008).
- [7] K. Aamodt *et al.* (ALICE Collaboration), arXiv:1402.4476.
- [8] S. Singha, A. Badala, INFN Internal Note 2014.

# Chapter 7

## Inclusive Photon Production in pp collisions at $\sqrt{s} = 0.9$ TeV

This chapter discusses the results of inclusive photon production in pp collisions at  $\sqrt{s} = 0.9$  TeV using the Photon Multiplicity Detector (PMD) in ALICE.

### 7.1 Introduction

The Large Hadron Collider (LHC) at CERN gives us an unique opportunity to study the particle production mechanism at unprecedented high energy proton-proton collisions up to 14 TeV over a wide range in rapidity. ALICE [1, 2], CMS [3] and ATLAS [4] have measured the charged particle multiplicity and pseudo-rapidity density from 0.9 TeV to 7 TeV, showing a substantial increase in pseudo-rapidity densities with beam energy. The photon measurement is complimentary to the charged particle as most of the photons are produced as decay products such as photons from  $\pi^0$  decays and charged particle multiplicity is dominated by charged pions. A Photon Multiplicity Detector (PMD) [5] was build and installed at the LHC to study the photon production mechanism at forward pseudo-rapidity ( $2.3 < \eta < 3.9$ ). Simultaneous measurement of photons and charged particles at mid-rapidity and forward rapidity

could provide insight into the particle production mechanism at extremely high energies. Such a measurement have been done at lower energies at RHIC [6, 7], giving us the information of longitudinal scaling of produced particles. In this thesis, we have used the technique of unfolding for the estimation of photon multiplicity and pseudo-rapidity distributions using PMD in pp collisions. We will present the multiplicity and pseudo-rapidity distribution of photons within  $2.3 < \eta < 3.9$  in pp collisions at  $\sqrt{s} = 0.9$  TeV. To understand the particle production mechanism in different rapidity regions, we will compare our photon results at forward rapidity to that of charged particles at mid-rapidity. We will also compare the results with the expectation from various models like PYTHIA [8] and PHOJET [9]. These results will also be used to study the limiting fragmentation behavior at LHC energies.

## 7.2 Detector subsystem used for this analysis

This analysis uses data from the Photon Multiplicity Detector (PMD). The PMD is located at 3.67 meters from the interaction point in the forward z-direction and spans a region of  $2.3 \leq \eta \leq 3.9$ . The PMD uses a preshower principle where a three radiation length thick lead converter<sup>1</sup> is placed between the two highly granular detector array of gas proportional counters. The detector plane facing the interaction point is called the charged particle veto (CPV) plane<sup>2</sup> and the other is called preshower plane. A photon traversing through the lead converter plane produces an electro-magnetic shower in the preshower plane affecting several cells in the detector, whereas the charged particle signal is confined mostly in a single cell. The preshower plane is used for the photon identification in the present analysis.

---

<sup>1</sup>actually lead converter plus steel support frame.

<sup>2</sup>because of limited acceptance the CPV plane of the detector during experimental data taking it is not used in the analysis.

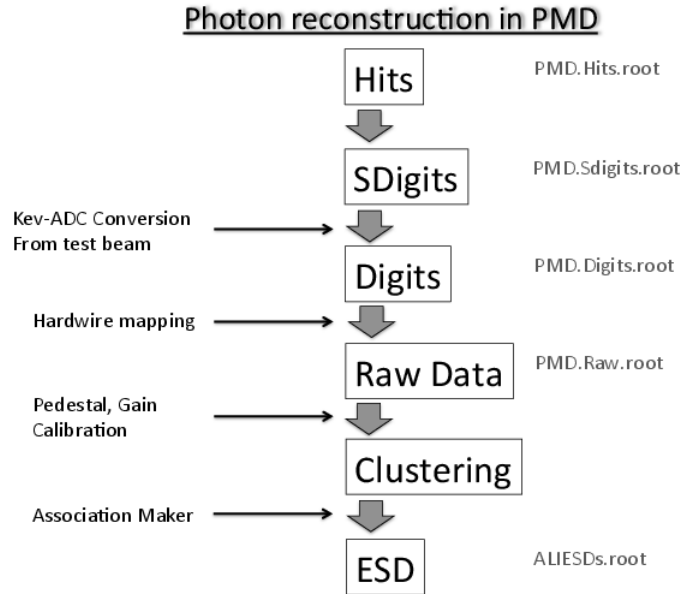


Figure 7.1: Photon reconstruction chain in PMD

### 7.3 Simulation framework

The response of PMD to photons and charged particles has been simulated using the AliRoot package where all the detector systems (along with their services) are described through a GEANT3 framework [10]. The particles produced in event generators have been passed through the detectors in GEANT3 simulations. The steps of photon reconstruction are given in Fig. 7.1 and briefly described below:

- 1) The particles from monte carlo generator produce hits in the cells of PMD (both in CPV and preshower plane) and deposit their energy inside the sensitive medium (gas mixture of Ar and CO<sub>2</sub>) of PMD. The information of energy deposition are stored in a root file (PMD.Hits.root).

- 2) The energy of hits deposited in a cell in an event are then summed and the total energy deposition in each cell is stored in a root file (PMDSDigits.root) in electron-volt units.

– 3) Then the energy stored are digitized through keV-ADC conversion using the data from test beam experiment [11]. The informations are kept in a root file (PMDDigits.root).

– 4) The mapping between the cells of PMD to the electronic channels are done at this step and the digits are converted to a raw data format (PMD.Raw.root).

– 5) At the next step, pedestal is subtracted from raw data and the gain calibration is done. At this stage the signal from a simulated cell resembles that from the actual experimental set up.

– 6) Then the photon clusters are reconstructed from raw data through a clustering algorithm [13]. Clusters are the group of contiguous cells having non-zero energy deposition. In simulation, the clusters can be associated to the incoming photon or hadron track [14].

– 7) After clustering is performed the final file (AliESDs.root) is stored in a root format [15] with the information of number of cells in a cluster, position of the cluster center and total energy deposition of a cluster as in case of real data.

### 7.3.1 Pedestal

The intrinsic electronic noise for each channel give rise to a finite read out value known as pedestal. Pedestal values depend on the design of the electronics and the operating environment. The noise from the front-end electronics and the electronic baseline data for each channel need to be removed. This is done by applying a random trigger to the PMD prior to a real physics run. Then the mean and RMS values of pedestal for each channel is produced from a large number of events. The Fig. 7.2 shows such a distribution of mean and RMS of pedestal obtained in test beam experiment [11] with PMD modules at the CERN-PS (Proton Synchrotron). The signals that are above a threshold ( $\sim 8$  RMS) are passed to the next step. This process is called

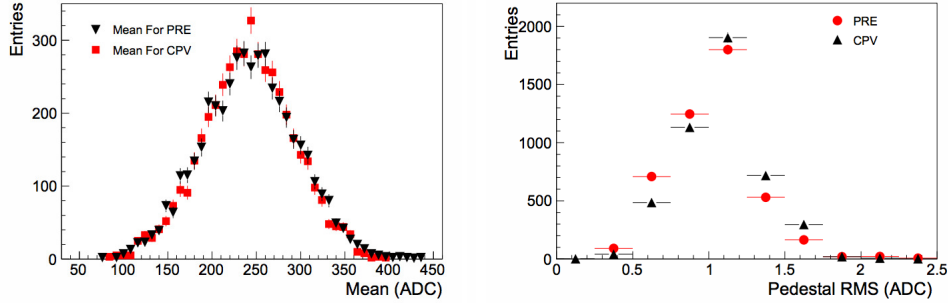


Figure 7.2: (Color online) Variation of mean (left panel) and RMS (right panel) of pedestal in a module. The results obtained in test beam experiment [11] with prototype PMD module at the CERN-PS.

zero suppression. In PMD the data is always recorded in zero-suppressed mode. The pedestal subtraction is performed during the offline analysis. The information of electronic baseline for each cell of PMD is then send to the Offline Conditioned Data Base (OCDB). The information of pedestal is fetched from the OCDB and subtracted from the real data during the first reconstruction level.

### 7.3.2 Hot/Noisy cell removal

In ideal case the response of each of the cells of PMD should be identical. But in real case, the hit frequency in some cells averaged over a large number of events is relatively high compared to other cells. The left panel of Fig 7.3 shows the hit frequency distribution of the cells of module 20 (Fig.7.16) in PMD. For some cells the hit frequency is high compared to nearby cells and those cells are observed to have lower ADC. These are called hot/noisy cells and need to be removed before the reconstruction. The method of removal of hot/noisy cell are briefly described below:

First we read the raw data and divide the  $\eta$  range of PMD in several  $\delta\eta$ -region of width 0.1 between  $2.3 < \eta < 3.9$ . Then we count the number of hits in each cell in each of  $\delta\eta$  bin. Such a distribution of hits in cells is shown in Fig 7.4. The hits distribution is then fitted with a gaussian function and we obtain a mean and RMS

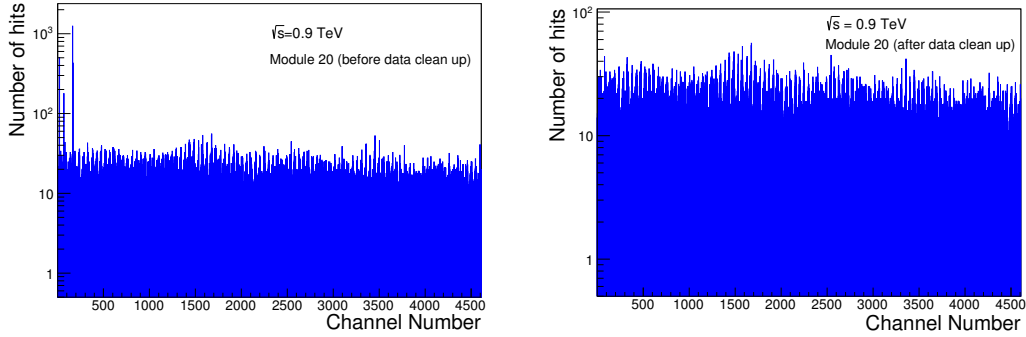


Figure 7.3: (Color online) The number of hits distribution in each channel in a module of PMD for pp collisions at  $\sqrt{s} = 0.9$  TeV. Left panel: before the data clean up. Right panel: after data clean up.

of hits distribution for each  $\delta\eta$  bin. Then we choose a cut-off value ( $= \text{mean} + 5 \times \text{RMS}$ ). After that we compare the hit frequency distribution of each cell with this cut-off value. Any cell, corresponding to a value higher than the cut-off are termed as noisy cell. The information about these noisy cells is then passed to the OCDB. Then during the reconstruction procedure, information from OCDB is fetched and the noisy cells are removed. The distribution of hit frequency after the hot channel removal are shown in the right panel of Fig 7.3.

### 7.3.3 Clustering

A number of contiguous cells having non-zero energy deposition are termed as clusters. The clusters are separated by the cells having no energy deposition. During the data reconstruction the clustering of cells are done via a clustering algorithm [13]. Since, in pp collisions, the occupancy<sup>3</sup> is very low ( $< 0.5\%$  at 0.9 GeV see Fig. 7.15), we expect the overlap of clusters to be rare. Therefore in this analysis a clustering algorithm with continuous cell search is employed to find the clusters. This is called crude clustering. But in Pb–Pb collisions, where the occupancy is very high and one should divide such crude clusters into small clusters. This is to account for the overlap

---

<sup>3</sup>see section 7.5.4

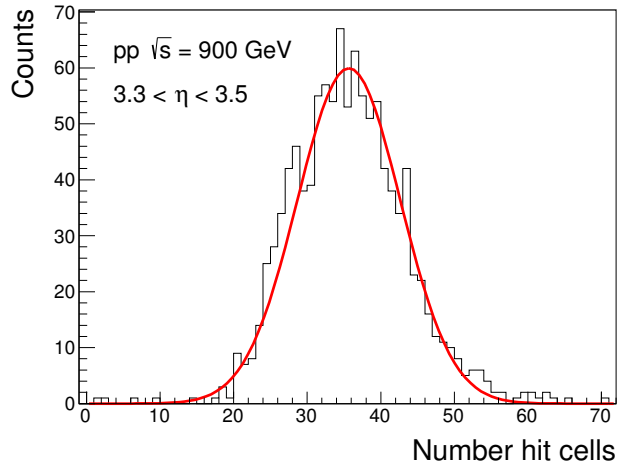


Figure 7.4: (Color online) The number of hits distribution in each channel in a module of PMD for pp collisions at  $\sqrt{s} = 0.9$  TeV.

of clusters associated with different photons falling on PMD in a high-multiplicity environment such as in Pb-Pb collisions. This method is called refine clustering.

### 7.3.4 Photon-hadron discrimination

The performance of PMD have been studied by exposing the detector modules to the pion and electron beam (ranging from 1 to 6 GeV) at the CERN-PS. It has been observed that the charged hadrons mostly hits on an average 1.1 cells depositing

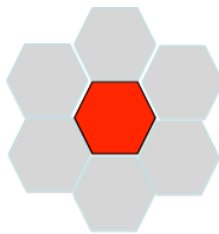


Figure 7.5: (Color online) An isolated cell in PMD. The red region indicates the cell having non-zero energy deposition, the grey region having no energy deposition.

a minimum energy, whereas the electrons affect a large number of cells depending

on their energy. The distribution of energy deposition of pions called the minimum ionizing particles (called MIPs) can be described by a Landau distribution [12]. The Fig. 7.5 pictorially shows isolated cell in PMD, where a cell having non-zero energy deposited surrounded by cells having no energy deposited. The isolated cell are assumed to be formed by MIPs. The Fig 7.6 shows the ADC distribution of such isolated cells in pp collisions at  $\sqrt{s} = 0.9$  TeV, which forms a Landau distribution with a Most Probable Value (MPV) of 71 ADC. Since the electrons deposits a large amount of energy and hits more than one cell, we take this advantage of different response of the detector towards hadrons and electro-magnetic particles (photons and electrons) to discriminate them.

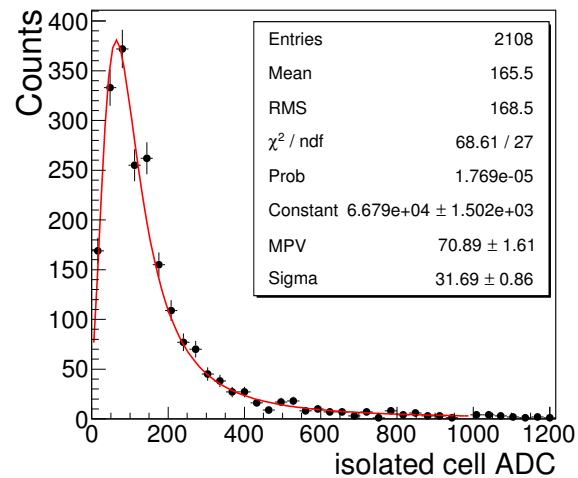


Figure 7.6: (Color online) Isolated cell ADC distribution in PMD for pp collisions at  $\sqrt{s} = 0.9$  TeV.

So one can discriminate photon and hadrons by applying a threshold on the cluster ADC and number of cells ( $N_{cell}$ ). The number of clusters which pass the discrimination threshold are termed as  $\gamma$ -like clusters ( $N_{\gamma-like}$ ). The number of identified photons in the  $N_{\gamma-like}$  sample are called  $N_{\gamma-detected}$ . We define two quantities:

$$Efficiency = \frac{N_{\gamma-detected}}{N_{\gamma-incident}} \quad (7.1)$$

and

$$Purity = \frac{N_{\gamma-detected}}{N_{\gamma-like}} \quad (7.2)$$

where  $N_{\gamma-incident}$  is the number of photon incident on the PMD. The values of

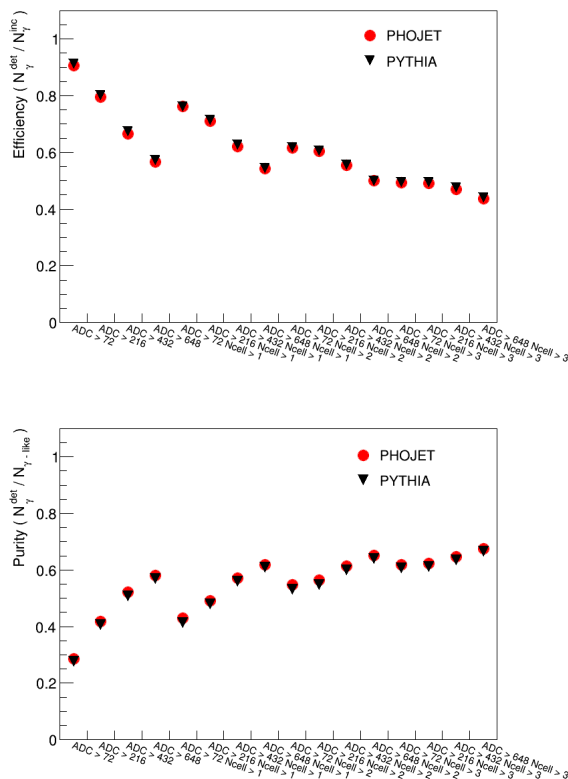


Figure 7.7: (Color online) Efficiency (top panel) and purity (bottom panel) of photons in PMD as a function of photon-hadron discrimination thresholds for pp collisions at  $\sqrt{s} = 0.9$  TeV.

efficiency and purity are obtained using event generators PYTHIA and PHOJET are shown in Fig. 7.7. We observe that the efficiency decreases and purity increases with increasing (tighter cut) the photon-hadron discrimination thresholds. In the present analysis, we have chosen the following thresholds for the photon-hadron discrimination to ensure high purity photon samples with reasonable efficiency:

- ADC > 6 MPV and  $N_{cell} > 2$

- $ADC > 9$  MPV and  $N_{cell} > 2$ .

## 7.4 Event Selection

The data used in this analysis are from pp collisions at  $\sqrt{s} = 0.9$  TeV collected with a magnetic field of 0.5 T and at low luminosities ( $\mathcal{L} \sim 10^{26} \text{ cm}^2 \text{ s}^{-1}$ ). For the analysis of inelastic (INEL) events, a logical OR between the signals from the SPD and VZERO

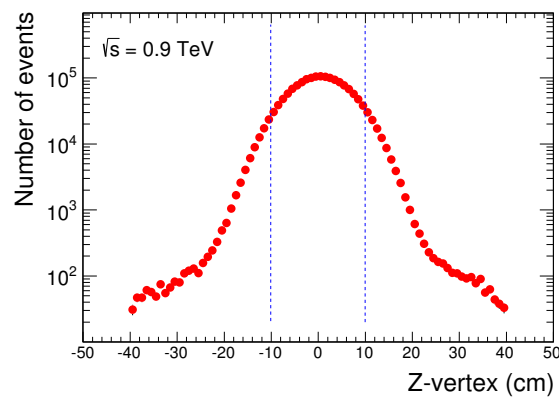


Figure 7.8: (Color online) Z-vertex distribution in cm for pp collisions at  $\sqrt{s} = 0.9$  TeV. The dotted lines indicate the Z-vertex used in this analysis.

(V0) detectors ( $MB_{OR}$ ) are required, while for the non single diffractive (NSD) events, we have selected the event by requiring a coincidence between the two sides of the VZERO detectors ( $VZERO_{AND}$ ) [2]. Additionally, to ensure the uniformity of the detector acceptance, the data sample is restricted to events having vertices with Z positions within  $\pm 10$  cm from the nominal interaction point. The Fig. 7.8 shows the distribution of the position of the Z-vertex at  $\sqrt{s} = 0.9$  TeV. The blue dotted line indicates the region of selected events for the present analysis.

### 7.4.1 Corrections for trigger and vertex reconstruction efficiency

Since the multiplicity of the produced particles is small, the data is need to be corrected for the event loss due to trigger selection and vertex selection efficiencies. Trigger and vertex reconstruction efficiency have been calculated using the simulated data where the monte carlo event generators are tuned to match the diffraction cross-sections measured by LHC experiments [16].

Trigger reconstruction ( $C_{trg}$ ) and vertex reconstruction efficiency ( $C_{vtx}$ ) is defined as :

$$C_{trg} = \frac{\frac{1}{N_{All}} \frac{dN_{\gamma}}{d\eta}(All)}{\frac{1}{N_{Trigg}} \frac{dN_{\gamma}}{d\eta}(Trigg)} ;$$

$$C_{vtx} = \frac{\frac{1}{N_{Trigg}} \frac{dN_{\gamma}}{d\eta}(Trigg)}{\frac{1}{N_{TriggVtx}} \frac{dN_{\gamma}}{d\eta}(TriggVtx)} ;$$

where,

- $\frac{1}{N_{All}} \frac{dN_{\gamma}}{d\eta}(All)$  for all events,
- $\frac{1}{N_{Trigg}} \frac{dN_{\gamma}}{d\eta}(Trigg)$  for all events which satisfy the trigger criteria,
- $\frac{1}{N_{TriggVtx}} \frac{dN_{\gamma}}{d\eta}(TriggVtx)$  for triggered events having a reconstructed vertex,

The measured photon pseudo-rapidity density ( $\frac{dN_{\gamma}}{d\eta}$ ) is corrected using the above corrections:

$$\frac{1}{N} \frac{dN_{\gamma}}{d\eta}(Measured) \times C_{trg} \times C_{vtx};$$

The values of the trigger and vertex reconstructed efficiencies are obtained from monte carlo simulations and reported in the table 7.1 below:

$\sqrt{s}(TeV)$	MB(OR) Trigger efficiency	Vertex reconstruction efficiency
0.9	0.905	0.914

Table 7.1: Trigger and vertex reconstruction efficiency

## 7.5 Material budget study

### 7.5.1 Material distribution in front of the PMD

PMD is located in the forward rapidity at a distance of 3.67 meter from the interaction point towards the side opposite to the Muon detector of ALICE. In GEANT3 simulation the material between the PMD and the interaction point, the frames of the Time Projection Chamber (TPC), services of the Inner Tracking System (ITS), Forward Multiplicity Detector (FMD), VZERO (V0) detector and the beam pipe, are implemented to the best of our knowledge. Since the particles coming from the interaction point has to traverse through these detector materials, they are affected by the upstream materials and hence may split into two or more secondary particles. So the contamination of the charged particles in the photon sample may change due to the presence of material and this can introduce a large uncertainty in photon counting as well on position resolution of the photons. We carry out a detailed analysis in simulation to understand the effect of upstream material in measuring the photons. The Fig. 7.9 and Fig. 7.10 shows an AliRoot simulation plot of the detector and services in front of PMD. First we estimate the material in terms of radiation length in front of PMD. Fig. 7.11 shows the material budget plots in terms of radiation lengths in  $\eta - \phi$  bins for each of the systems in front of the PMD and finally with all of the material in front of the PMD as implemented in Aliroot (version v5-03-Rev-28).

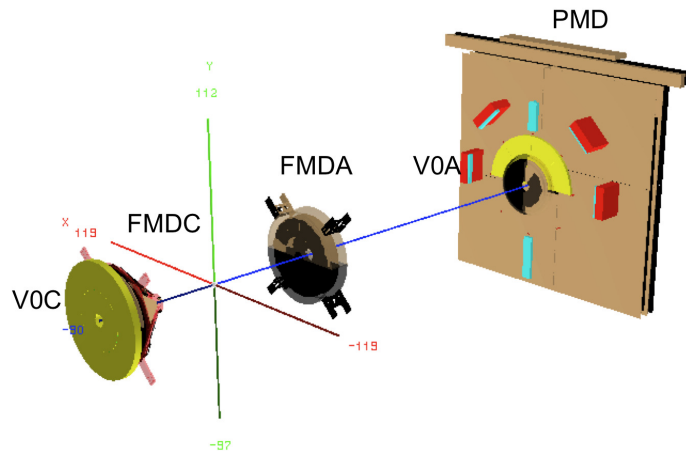


Figure 7.9: (Color online) An Aliroot simulation plot of the FMD and V0 services in front of the PMD.

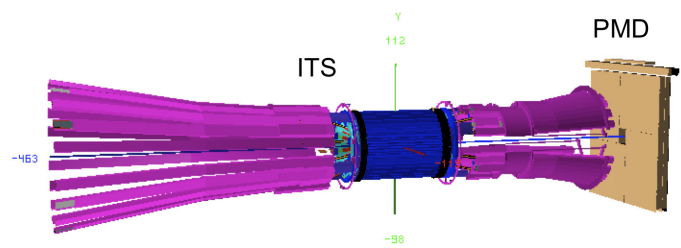


Figure 7.10: (Color online) An Aliroot simulation plot of ITS and its services in front of the PMD.

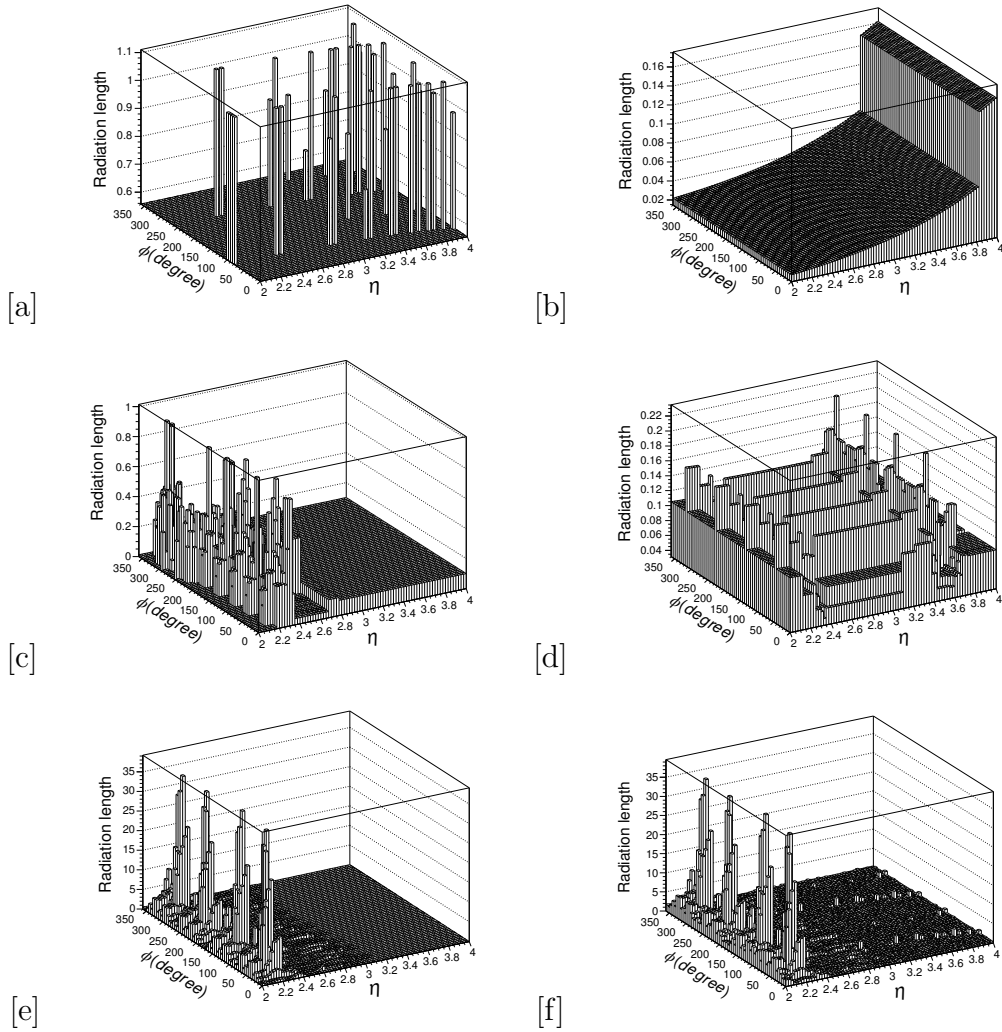


Figure 7.11:  $\eta - \phi$  lego plot showing the amount material (in radiation length) in front of the PMD for six cases: (a) PMD itself, (b) only the beam pipe, (c) only VZERO, (d) only FMD, (e) only ITS, and (f) all detectors and services as implemented in Aliroot in front of PMD.

## 7.5.2 Effect of upstream material: Deflection of the original photon track

The photon tracks from the vertex  $(\eta_{orig}, \phi_{orig})$  can undergo scattering and conversion due to the upstream material, which results in a deflection of the original track. This deflection effect of the photon tracks can be studied in terms of  $\eta - \eta_{orig}$  and  $\phi - \phi_{orig}$ , where  $\eta, \phi$  are the pseudo-rapidity and azimuthal angle of the deflected tracks. The Fig. 7.12 shows the distribution of  $\eta - \eta_{orig}$  and  $\phi - \phi_{orig}$  of photons in two different cases, (1) keeping only PMD in the simulation and (2) keeping all detectors including PMD in the simulation with varying photon-hadron discrimination thresholds. We observe a deviation of the tracks in case of PMD with all detector with respect to the PMD only case. These results are obtained without use of any photon-hadron discrimination threshold. This deviation depict the effect of upstream material. We observe a small bump at large  $\eta - \eta_{orig}$  ( $\sim -3.5$ ) in the top panel of Fig. 7.12. These photons are most likely falling on the PMD after getting scattered from the beam pipe. It is observed that (Fig. 7.12) with the application of photon-hadron discrimination threshold the deviation from the original track is reduced to a large extent. Next we will try to quantify the amount of background due to the upstream material. We followed the procedure below:

First we take the PMD only simulation case (shown by dotted lines in Fig. 7.12) and compute the root mean square (RMS) value of the  $\eta - \eta_{orig}$  case. Then we calculate the fraction of area of the  $\eta - \eta_{orig}$  distribution for all detector simulation case (denoted by the solid curve), outside a window expressed in terms of RMS of the PMD only case. This will give an estimate of the background in the photon sample due to the effect of the upstream material. The Fig. 7.13 shows the fraction of area outside the PMD only window (or, background ) in term of RMS value of the PMD only case. As expected, the fraction of area of the solid curve outside the window of the dotted curve decreases with increasing RMS values. We observe that the effect of background is significantly reduced from 16% to a level less than 4% with the application of a photon-hadron discrimination threshold ( $ADC > 6$  MPV,  $N_{cell} > 2$

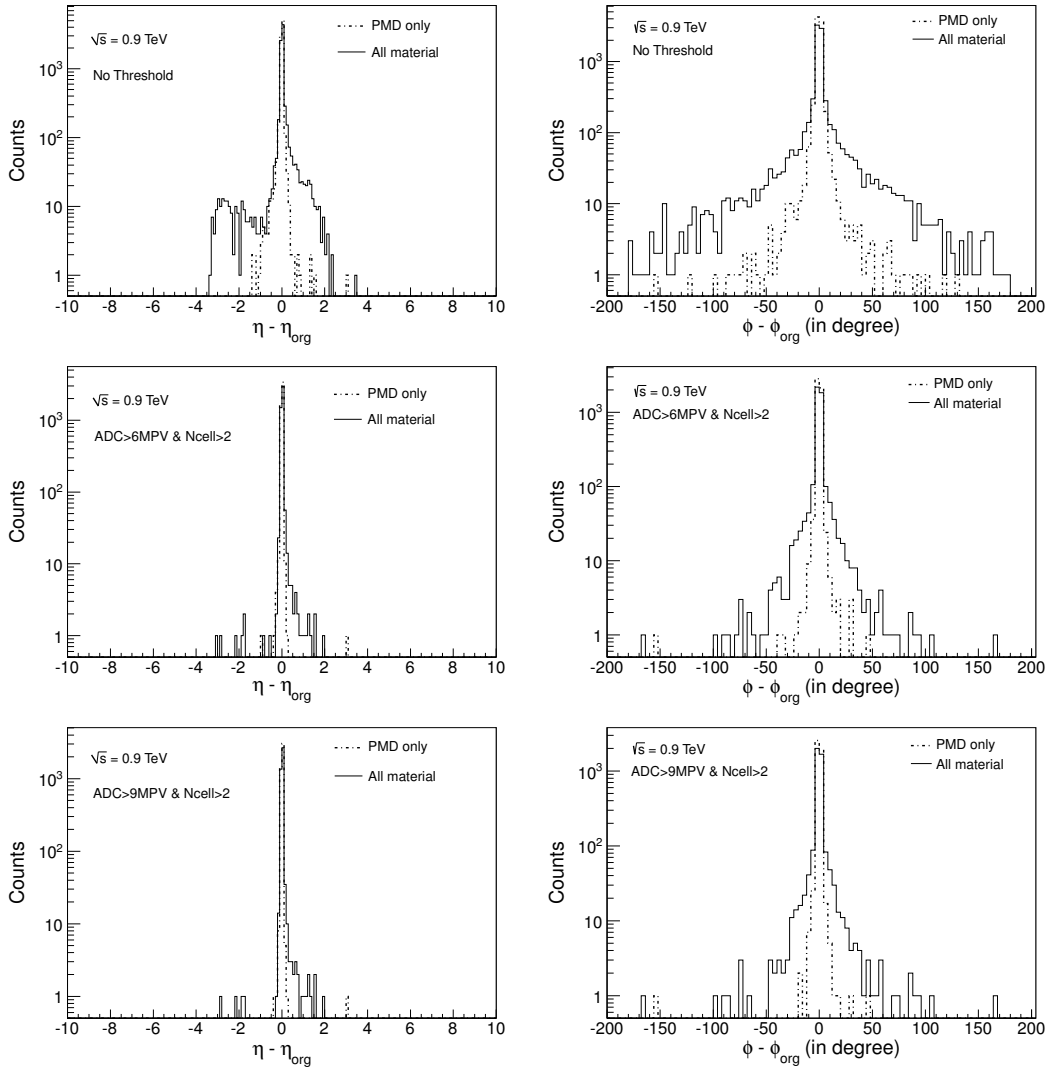


Figure 7.12: Deflection of photon tracks in pp collisions at  $\sqrt{s} = 0.9$  TeV. Upper panel: the case with no discrimination threshold; the middle and lower panel: with two different discrimination thresholds. Solid line is for the case of PMD with all detectors and dotted line is for the case only PMD in the simulation.

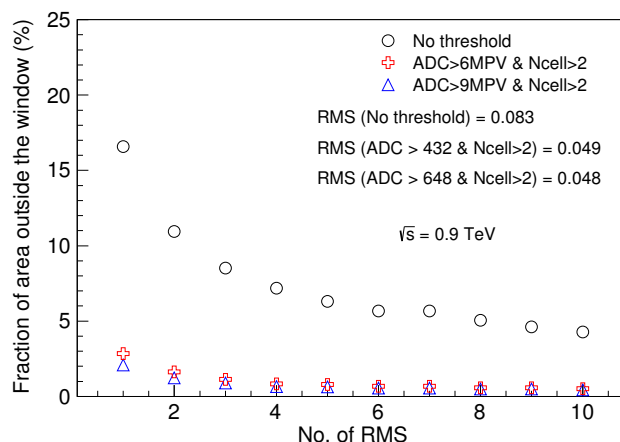


Figure 7.13: (Color online) Fraction of area of the solid curve outside the window of the dotted curve for no threshold (open circles), and two different thresholds (open plus and open triangles) for pp collisions at  $\sqrt{s} = 0.9$  TeV

and  $\text{ADC} > 9$  MPV,  $N_{cell} > 2$ ).

### 7.5.3 Study of split clusters

Usually, one incoming photon track produces one cluster in the preshower plane of PMD. Then that cluster is tagged by the track number corresponding to the incident photon. It was found that, in some cases more than one cluster has the same track number. One of the cluster has to represent the true cluster corresponding to the original photon track, the others are its split clusters. In such cases the cluster with highest ADC value are identified as the main cluster, while the remaining are called split clusters. The split clusters have low ADC values. The split cluster may arise from the conversion of photons in the lead converter of PMD and also from the upstream materials in front of PMD. We have studied the percentage of split clusters using simulations. It is the ratio of the number of photon split clusters assigned by the association algorithm [14] to the total number of photon clusters in an event. The Fig. 7.14 shows the percentage split clusters as a function of  $\eta$  with and without photon-hadron discrimination thresholds. It is observed that after

application of photon-hadron discrimination thresholds, the fraction of split clusters are significantly reduced from a level of 50% to below 10%. This is of the similar level of as seen with our test beam data using a prototype detector of PMD [14].

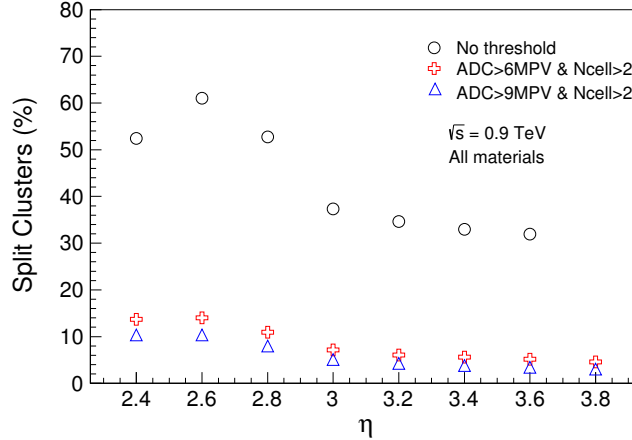


Figure 7.14: (Color online) Number of split clusters in % plotted versus  $\eta$  for no threshold (open circles) and two different threshold settings for pp collisions at  $\sqrt{s} = 0.9$  TeV.

### 7.5.4 Study of occupancy

Occupancy is defined as the ratio of the number of cells hit in an  $\eta$  window to the total number of cells available in that  $\eta$  window. The cell occupancies in the preshower plane from real data and simulations are plotted in Fig. 7.15 as a function of pseudo-rapidity, with a bin size of  $\delta\eta = 0.2$  units. The overall occupancy is between 0.1% to 0.5% for pp collisions at 0.9 TeV. The occupancy from PHOJET [9] generator underestimates that of experimental data. Then in simulation overall material budget in ALICE is increased (density of all the material) by 10% and the resulting occupancy is presented in the Fig. 7.15. The occupancy from the data and PHOJET + 10% additional material are comparable. We have used the simulation of PHOJET + 10% increased material density to obtain the systematic uncertainty of material budget on the photon multiplicity and pseudo-rapidity distributions.

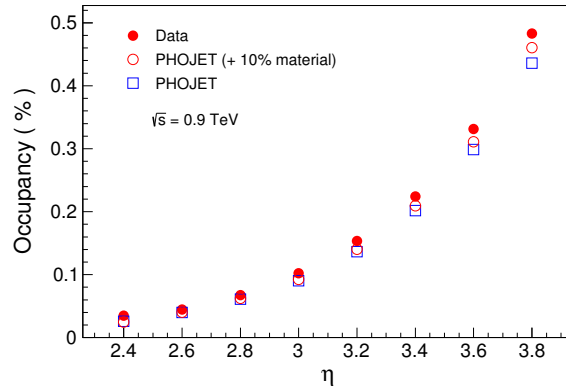


Figure 7.15: (Color online) Occupancy as a function of pseudo-rapidity for pp collisions at  $\sqrt{s} = 0.9$  TeV. The results are compared with PHOJET and PHOJET with 10% additional material simulations.

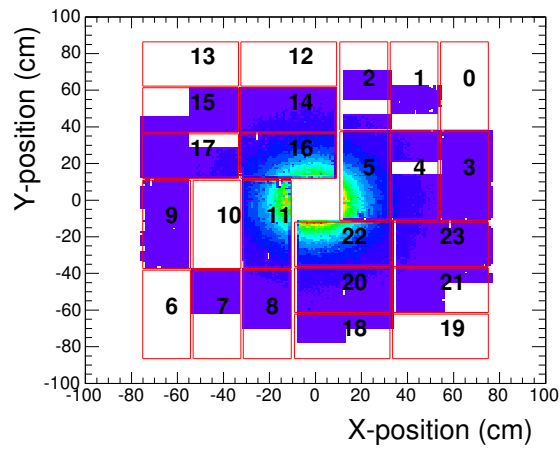


Figure 7.16: (Color online) The XY scatter plot of hits on the preshower plane of PMD for pp collisions at  $\sqrt{s} = 0.9$  TeV.

## 7.6 Acceptance of PMD

During the real data taking all the modules of PMD were not in operation. The Fig. 7.16 shows the XY scatter plot in the preshower plane of PMD. The geometric acceptance of PMD have been implemented in the OCDB so that the simulation used for acceptance correction are exactly similar to that of real data. The acceptance of PMD as a function of  $\eta$  is shown in Fig. 7.17.

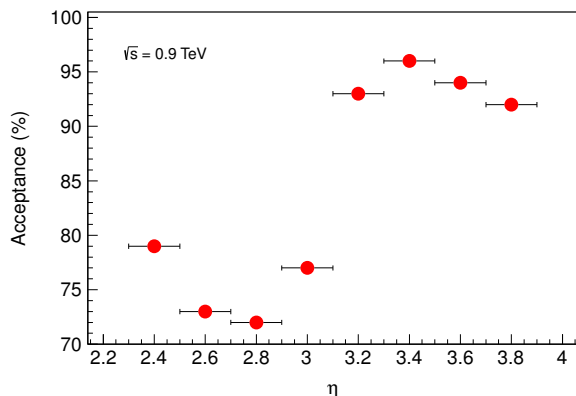


Figure 7.17: (Color online) Acceptance of PMD versus  $\eta$  for pp collisions at  $\sqrt{s} = 0.9$  TeV.

## 7.7 Analysis details

The basic flow chart of the analysis is shown in Fig. 7.18 and the procedure of correcting the measured photon multiplicity will be described in subsections below.

## 7.8 Uncorrected photon multiplicity ( $N_{\gamma-like}$ )

The uncorrected photon multiplicity distributions obtained after the photon-hadron discrimination threshold ( $ADC > 6$  MPV,  $N_{cell} > 2$  and  $ADC > 9$  MPV,  $N_{cell} > 2$ ), i.e.,  $N_{\gamma-like}$  distributions are shown in Fig. 7.19. This distribution need to be corrected for the detector acceptance and efficiency. We have employed a technique of unfolding

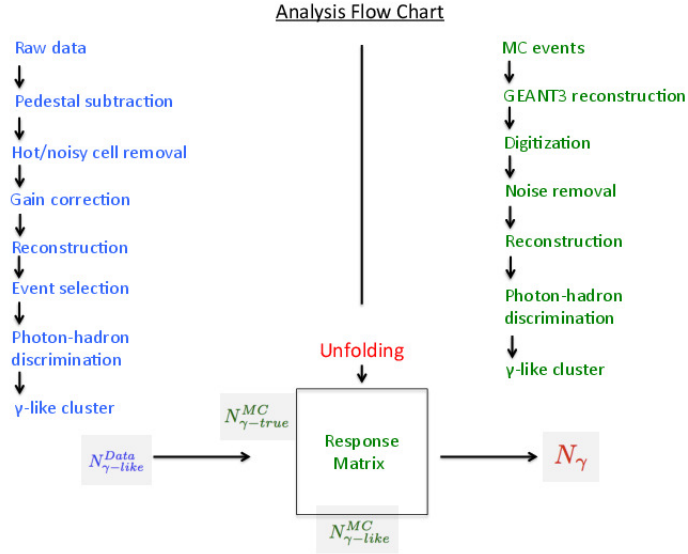


Figure 7.18: (Color online) Analysis flow chart for obtaining photon multiplicity distribution using data from PMD.

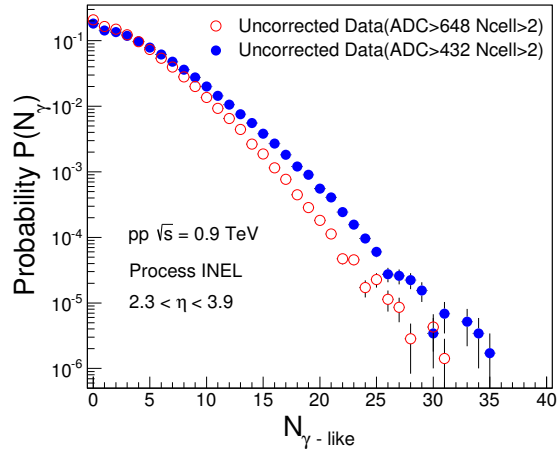


Figure 7.19: (Color online)  $N_{\gamma\text{-like}}$  distributions for two different photon hadron discrimination thresholds for pp collisions at  $\sqrt{s} = 0.9$  TeV.

for this correction. The method of unfolding [17, 18, 19] is discussed in section 7.9 below.

## 7.9 Method of unfolding

If  $\hat{f}$  is the true distribution which is modified because of the detector effects, described by the response function  $A$ , the measured distribution  $\hat{g}$  can be written as,

$$\hat{g} = A\hat{f}. \quad (7.3)$$

Since  $\hat{g}$  is measured distribution, the true distribution can be obtained by matrix inversion:

$$\hat{f} = A^{-1}\hat{g}. \quad (7.4)$$

This is called unfolding. The matrix inversion can cause a large oscillation in the final unfolded distribution, hence a regularization method is employed to suppress the statistical oscillation. In the present analysis we have used two different methods of unfolding, namely  $\chi^2$  minimization [17, 18, 19] and Bayesian method [20]. A brief description of both the methods are given in the following section.

### 7.9.1 $\chi^2$ minimization method

In this method we define the  $\chi^2$  as,

$$\hat{\chi}^2(f) = (g - Af)'C_{1/e_i^2}(g - Af) = \sum_i \left( \frac{g_i - \sum_j A_{ij}f_j}{e_i} \right)^2, \quad (7.5)$$

where

- $f_i$  is the guessed (or true) distribution,
- $g_i$  is the measured distribution,
- $e_i$  is the error in the measured distribution  $g_i$ ,

- $C_{1/e_i^2}$  is the covariant matrix whose diagonal elements are  $1/e_i^2$ ,
- and  $A_{ij}$  is the response matrix,
- the  $\prime$  in the equation denotes the transpose of the matrix.

When the  $\chi^2$  is minimum the guessed distribution multiplied by the response matrix gives the measured distribution and the guessed distribution becomes the true distribution. Now to minimize the oscillation in the final solution, a regularization term  $P$  with a weight factor  $\beta$  is added:

$$\chi^2(f) = \hat{\chi}^2(f) + \beta P(f), \quad (7.6)$$

The regularization parameters  $P$  and  $\beta$  are optimized using simulated data. If the  $\beta$  value is too small, it could cause a violent oscillation in the final solution. On the other hand, if the  $\beta$  value is too large, it could bias the measurement to the choice of regularization used. One need to optimize the  $\beta$  values in order to have a physical solution. Here in the analysis, we have the measured distribution  $N_{\gamma-like}$  from real data, which is affected by detector finite resolution and acceptance. Next we construct a detector response matrix ( $A_{ij}$ ) (shown in Fig. 7.20), which is a two dimensional histogram with the  $N_{\gamma-true}$  on the X-axis and  $N_{\gamma-like}$  on the Y-axis, from the PHOJET monte carlo simulation. The response matrix gives the conditional probability that a collision with a multiplicity  $N_{\gamma-true}$  is measured as an event with multiplicity  $N_{\gamma-like}$ . This matrix characterises the properties of the detector and does not depend on the choice of the event generator used apart from the second order effects like particle composition and spectra. For this reason we have tested the unfolding method using two different event generators, PYTHIA and PHOJET. Now to suppress the oscillation in the final distribution, the following regularization functions have been applied:

$$P(f) = \sum_i \left(\frac{f'_i}{f_i}\right)^2 = \sum_i \left(\frac{f_{i-1} - f_i}{f_i}\right)^2 \quad (7.7)$$

$$P(f) = \sum_i \left(\frac{f''_i}{f_i}\right)^2 = \sum_i \left(\frac{f_{i-1} - 2f_i + f_{i+1}}{f_i}\right)^2 \quad (7.8)$$

$$P(\ln f) = \sum_i \left(\frac{f_i''}{f_i}\right)^2 = \sum_i \left(\frac{\ln f_{i-1} - 2\ln f_i + \ln f_{i+1}}{\ln f_i}\right)^2 \quad (7.9)$$

The equations 7.7, 7.8 and 7.9 minimizes the oscillation with respect to a constant function (pol0), a linear function (pol1) and a logarithmic (log) function respectively. We have tested our results in simulations with above regularization schemes and by varying weight factor.

## 7.9.2 Bayesian method

An alternative approach of unfolding is based on Bayes' theorem [20]. According to this theorem, if A and B are two events, then the conditional probabilities of A with B given and B with A given, are related by the relation

$$P(A|B) = \frac{P(B|A)P(A)}{P(B)} \quad (7.10)$$

where  $P(A)$  and  $P(B)$  are the probabilities for the event A and B respectively.  $P(A|B)$  denotes the probability of event A under the condition of event B is true.  $P(B|A)$  denotes the probability of event B under the condition of event A is true.

In our notation,

$$\bar{A}_{ij} = \frac{A_{ji}f_i}{\sum_k A_{ik}f_k} \quad (7.11)$$

where  $f_K$  is a prior distribution of the true distribution. After obtaining  $\bar{A}_{ij}$ , the unfolded distribution ( $f$ ) can be obtained as

$$f_i = \sum_j \bar{A}_{ij}g_j \quad (7.12)$$

The resultant  $f$  of an iteration is used as the new priori distribution for the next iteration. This method is used as a systematic check on the unfolding method. The difference in results using  $\chi^2$  minimization and Bayesian methods are added in the systematic uncertainty.

### 7.9.3 Optimization of unfolding

In this section we will discuss the optimization of the unfolding parameters using the AliRoot simulations. We have generated two statistically independent simulations using a PHOJET monte carlo generator. The response matrix (Fig. 7.20) is constructed from one of the sets. Another set of data is used for testing the unfolding method with various schemes. In Fig. 7.21 the blue circles denote the  $N_{\gamma\text{-true}}$  distribution and black lines the  $N_{\gamma\text{-like}}$  distribution. Now we apply the response matrix on the  $N_{\gamma\text{-like}}$  distribution through the  $\chi^2$  minimization method. The minimization is done using the TMinuit program in the ROOT framework [15]. The choice of weight factor is very important in  $\chi^2$  minimization method. In this method the value of  $\chi^2$  is de-

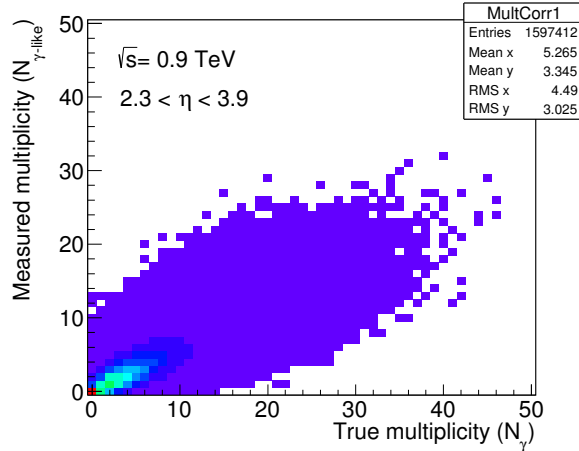


Figure 7.20: (Color online) Response matrix for pp collisions at  $\sqrt{s} = 0.9$  TeV using PHOJET event generator. The x-axis is the true photon multiplicity and the y-axis is the measured photon multiplicity within  $2.3 < \eta < 3.9$ .

pendent on the  $\beta$  value. Lower values of  $\beta$  would give lower  $\chi^2$  but the final solution will be driven by statistical oscillation, called under-regularization. If the  $\beta$  value is too high then the final unfolded solution is biased to the regularization function used, called over-regularization. In the Fig. 7.21 the solid red symbols are the unfolded distribution using logarithmic regularization function with various  $\beta$  values. It can be observed that a low  $\beta$  value can generate oscillations in the unfolded solution,

whereas high  $\beta$  bias the distribution towards the regularization used. The  $\beta$  value is thus optimized for each regularization. Here the unfolding is done with two different  $\beta$  values, one for the two lowest multiplicity (0 and 1) bins and the other for rest of multiplicity bin. The optimized regularization parameters with  $\beta$  values are given in Table 7.2 below:

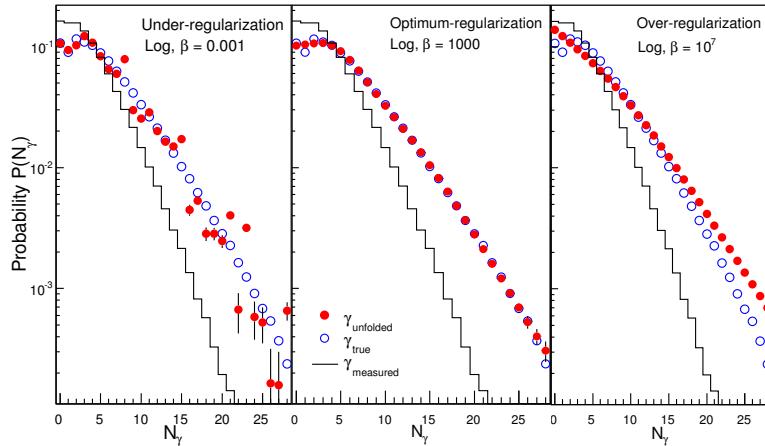


Figure 7.21: (Color online) Test of unfolding using a PHOJET simulation with different  $\beta$  values for pp collisions  $\sqrt{s} = 0.9$  TeV.

Regularization	$\beta (N_\gamma < 2)$	$\beta (N_\gamma > 2)$
Pol0	0.01	10
Pol1	0.001	1
Log	1	1000

Table 7.2: Regularization parameters at  $\sqrt{s} = 0.9$  TeV.

For the default measurement in data we have used the logarithmic (Log) regularization with  $\beta = 1$  for  $N_\gamma < 2$  and  $\beta = 1000$  for  $N_\gamma > 2$ . The Fig. 7.22 shows the test of unfolding using PHOJET simulation with these parameters. In the upper panel of Fig. 7.22, the blue circle denotes the true multiplicity distribution, black line the

measured multiplicity and the solid red symbols the unfolded multiplicity distribution. The ratio of the unfolded to the true distribution is shown in the bottom panel of Fig. 7.22. As one can see from Fig. 7.22 that the unfolding can reproduce the true distribution within a 10% limit. The fluctuation at higher values of  $N_\gamma$  is because of the very low statistics of the response matrix at high  $N_\gamma$ . The other regularizations (pol0 and pol1) are used for systematic study (Fig. 7.36 in Appendix).

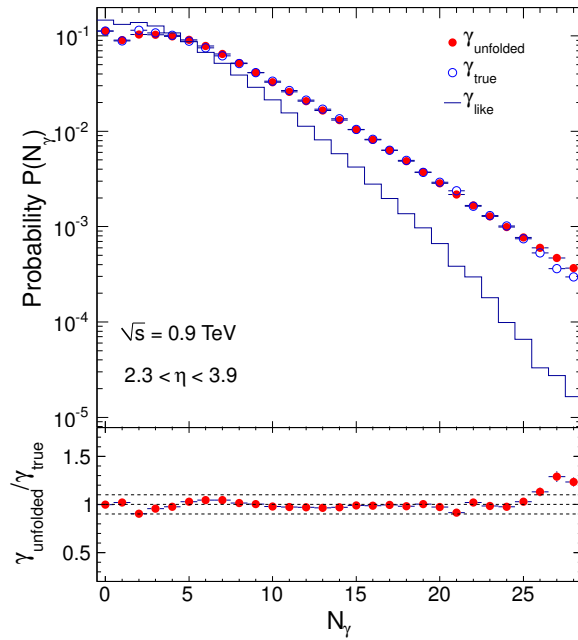


Figure 7.22: (Color online) Test of unfolding method in simulated data using PHOJET event generator: True multiplicity distributions, the  $\gamma$ -like distributions and the unfolded distributions for pp collisions at  $\sqrt{s} = 0.9$  TeV. The lower panel shows the ratio of unfolded to true distribution.

## 7.10 Results

### 7.10.1 Corrected Photon multiplicity

The unfolding is applied on the  $N_{\gamma-like}$  cluster as described above and the corrected photon multiplicity is obtained. The Fig. 7.33 shows the unfolded multiplicity distribution using two different photon-hadron discrimination thresholds ( $ADC > 6$  MPV,  $N_{cell} > 2$  and  $ADC > 9$  MPV,  $N_{cell} > 2$ ). The results of two different thresholds are comparable to each other. The difference between the two distributions are added to the systematic uncertainties on the photon multiplicity.

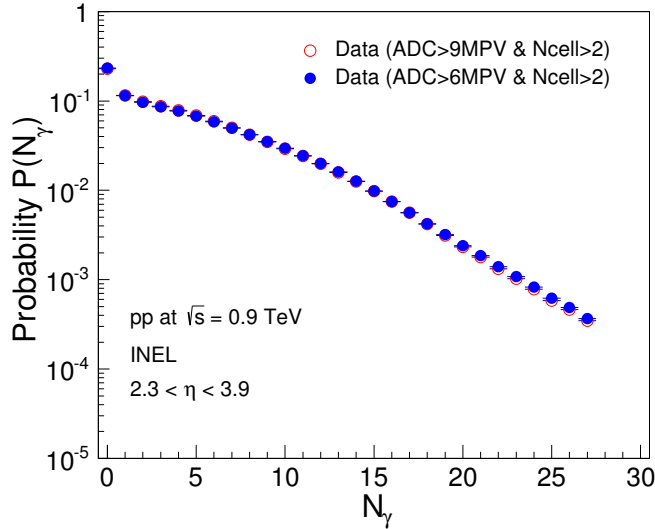


Figure 7.23: (Color online) Unfolded multiplicity distributions using two different discrimination thresholds for pp collisions at  $\sqrt{s} = 0.9$  TeV.

### 7.10.2 Comparison with models

The corrected photon multiplicity distributions are compared to the results from models PYTHIA-Perugia 0 [21], PYTHIA-Perugia 2011 [22], PYTHIA ATLAS-CSC [23] and PHOJET [9] in Fig. 7.24. The bars on the data denote the statistical uncertainties and the shaded band denote the systematic uncertainties. The models are shown

by different lines of different colors. The bottom panel of Fig. 7.24 shows the ratio between the data and the models. It is observed that the PHOJET results are close to the data, whereas the PYTHIA tunes underpredict the data at high multiplicities. The PYTHIA tunes have been developed by different groups through extensive

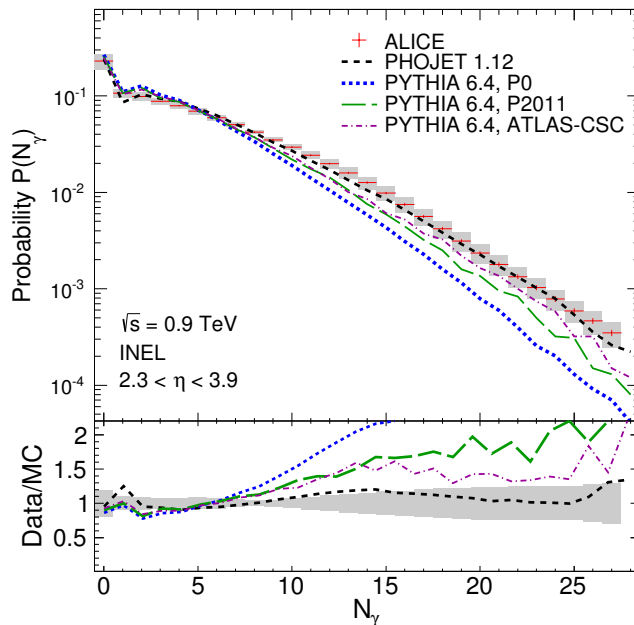


Figure 7.24: (Color online) Multiplicity distribution of photons for pp collisions at 0.9 TeV within  $2.3 < \eta < 3.9$ . The red crosses are data points with statistical errors and the shaded regions represent the systematic errors. The black solid dotted are the expectations from PHOJET, the blue dotted lines are from PYTHIA Perugia 0, the green dashed lines are from PYTHIA Perugia 2011 and the dot-dashed magenta line from PYTHIA ATLAS-CSC. The bottom panel shows the ratio between data and MC.

comparison of monte carlo distributions with the underlying events and minimum bias data measured in Tevatron and LHC. PYTHIA - Perugia 0 and Perugia 2011 tunes uses new multiple scattering model provided by PYTHIA 6.4 and transverse momentum ordered showering. The Perugia are not tuned for diffractive processes and thus the model results may not be valid for a few bins at low multiplicity. The final state radiation and hadronization processes in Perugia tunes are tuned to a fitted

LEP data. The ATLAS-CSC tune is developed by the ATLAS collaboration. In this case, the PYTHIA parameters are tuned to the multiplicity distributions in full phase space and pseudo-rapidity distributions of NSD events from the 200 GeV to 1.8 TeV data. The PHOJET is a two component model where the soft processes are governed by a Dual Parton Model and the hard processes by a perturbative QCD similar to PYTHIA.

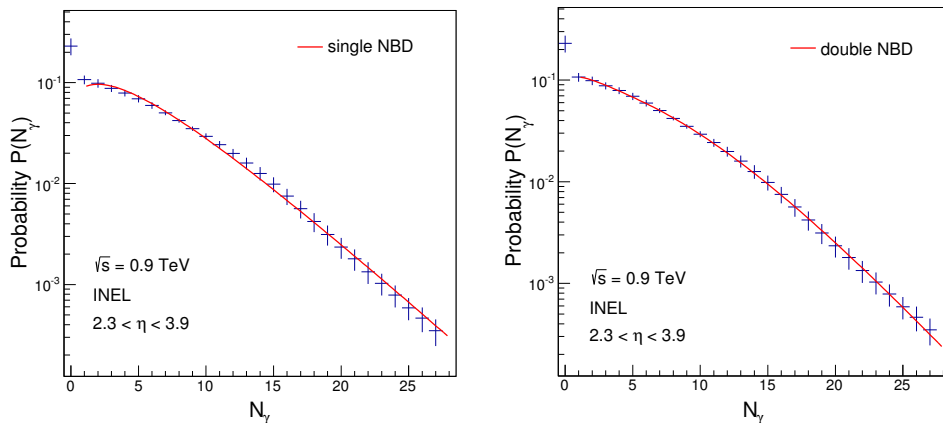


Figure 7.25: (Color online) Photon multiplicity distributions are fitted with both single NBD (top panel) and double NBD (bottom panel) function for pp collisions at  $\sqrt{s} = 0.9$  TeV.

## 7.11 Negative binomial distributions (NBD) Fitting

The multiplicity distributions have been traditionally fitted with a negative binomial distributions (NBD) to extract the informations regarding the particle production mechanism. The functional form of single NBD is given by

$$P_{NBD}(m, k; n) = \frac{\Gamma(n+k)}{\Gamma(n+1)\Gamma(k)} \frac{(m/k)^n}{(m/k+1)^{n+k}} \quad (7.13)$$

where  $m = \langle n \rangle$  and  $k = \langle n^2 \rangle - \langle n \rangle^2$ , related to dispersion of multiplicity ( $n$ ). If  $k \rightarrow \infty$  the distribution becomes Poissonian and if  $k = 1$  the distribution becomes geometric. The left panel of Fig 7.25 shows the multiplicity distribution of photons fitted to a single NBD function. The parameters are given in Table 7.3. Further the multiplicity distribution is fitted with a double NBD distributions (right panel of Fig 7.25 ). It is mathematically defined below:

$$P_{double\ NBD}(W, m_1, k_1, m_2, k_2; n) = WP_{NBD}^1(m_1, k_1; n) + (1 - W)P_{NBD}^2(m_2, k_2; n) \quad (7.14)$$

where  $W$  is a weight factor, which indicates the contribution from soft processes. The fit parameters of double-NBD functions are given in Table 7.4.

$\sqrt{s}$ in TeV	k	m	$\chi^2/ndf$
0.9	$1.841 \pm 0.104$	$5.328 \pm 0.134$	13.76 / 26

Table 7.3: Fit parameters for single NBD.

$\sqrt{s}$ in TeV	k (k1, k2)	m (m1, m2)	W	$\chi^2/ndf$
0.9	$3.15 \pm 1.91$	$6.93 \pm 2.62$	$0.57 \pm 0.34$	1.74 / 23
	$1.28 \pm 1.66$	$1.84 \pm 2.90$		

Table 7.4: Fit parameters for double NBD.

## 7.12 KNO scaling

It was suggested by Z. Koba, H. B. Nielsen and P. Olesen that the multiplicity distribution in high energy collisions would follow a scaling behavior known as KNO scaling [24] by their names. According to this scaling, if the particle multiplicity is plotted in terms of KNO variables ( $z = N_\gamma / \langle N_\gamma \rangle$ ) [24, 25], they should follow

a universal scaling. The top panel in Fig. 7.26 shows the photon multiplicity at forward rapidities ( $2.3 < \eta < 3.9$ ) measured at  $\sqrt{s} = 0.9, 2.76$  and  $7$  TeV in terms of KNO variable. The bottom panel show the ratios of the distribution at  $\sqrt{s} = 2.76, 7$  TeV to that at  $0.9$  TeV. The ratio is close to unity up to  $z = 3$  and it tends to deviate from unity for  $z > 3$ . This implies that the KNO scaling is broken at high multiplicities at forward rapidity, similar to what has been observed for charged particles at mid-rapidity [2].

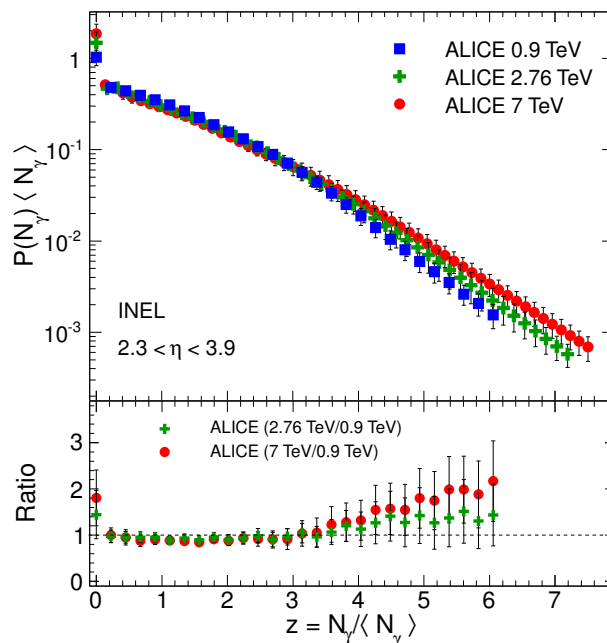


Figure 7.26: (Color online) Top panel: photon multiplicity distribution in terms of KNO variable within  $2.3 < \eta < 3.9$  for pp collisions at  $\sqrt{s} = 0.9, 2.76$  and  $7$  TeV. Bottom panel: ratio of multiplicity distribution at  $2.76$  and  $7$  TeV to that in  $0.9$  TeV.

### 7.13 Energy dependence of photon multiplicity

To understand the nature of particle production, we have studied the energy dependence of photon multiplicity (Fig. 7.27) within the forward rapidity region of  $2.3 < \eta < 3.9$ . The UA5 experiment [26] provides the data at center of energies of  $200,$

546 and 900 GeV. We observe an increase of average photon multiplicity with the increase in beam energy. Now to understand the dependence on beam energy, we have fitted the data to a logarithmic and a power law function as shown in Fig. 7.27. It is observed that the beam energy dependence of average photon multiplicity within  $2.3 < \eta < 3.9$  can be described by a logarithmic as well as by a power law function. The parameters of both the fit functions are given in the table 7.5. We need data at higher energies to conclude the nature of beam energy dependence of photon multiplicity.

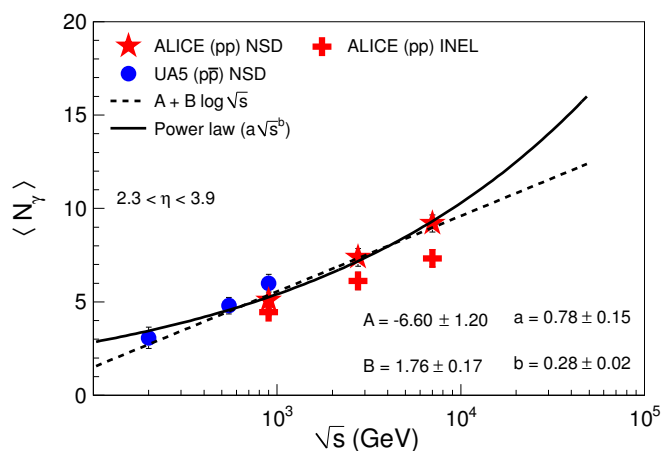


Figure 7.27: (Color online) Energy dependence of the average photon multiplicity in pp ( $p\bar{p}$ ) collisions. The blue circles are UA5 data and the red stars are PMD data within  $2.3 < \eta < 3.9$ .

	Logarithmic fit		Power law fit
A	$-6.60 \pm 1.2$	a	$0.78 \pm 0.15$
B	$1.76 \pm 0.17$	b	$0.28 \pm 0.02$

Table 7.5: The parameters of the fit functions of Fig 7.27

## 7.14 Pseudo-rapidity distributions of photons

To obtain the corrected photon pseudo-rapidity distribution we have divided the whole  $\eta$  range ( $2.3 < \eta < 3.9$ ) in eight  $\delta\eta$  rings of width 0.2 and the unfolding method is applied for each  $\delta\eta$  ring. We have constructed response matrix for each  $\delta\eta$  ring. We applied the response matrix through the  $\chi^2$  minimization method on the measured  $dN_{\gamma\text{-like}}/d\eta$  distribution. The Fig. 7.28 shows the example of testing the unfolding method using simulation. In Fig. 7.28, the solid black squares denote the measured  $dN_{\gamma\text{-like}}/d\eta$ . After the application of the unfolding on the measured distribution, the unfolded distribution ( $\gamma_{unfolding}$ ) can reproduce the true distribution ( $\gamma_{true}$ ). Here we have used pol0 regularization with  $\beta = 1$ . The same parameters will be applied on the data to unfold and get the corrected  $dN/d\eta$  distribution.

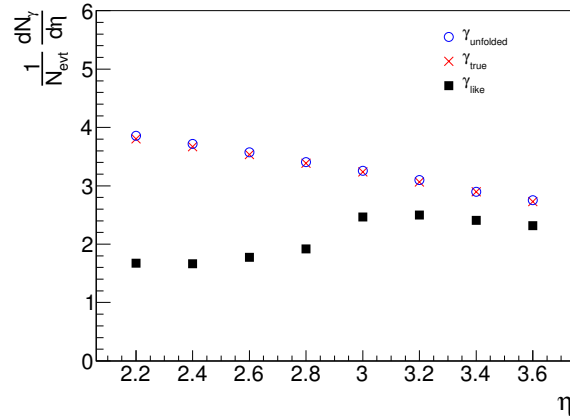


Figure 7.28: (Color online) Test of unfolding method in simulated data using PHOJET event generator: True pseudo-rapidity distributions, the  $\gamma$ -like distributions and the unfolded distributions for pp collisions at 0.9 TeV.

The Fig. 7.29 shows the pseudo-rapidity distribution of photons for pp collisions at  $\sqrt{s} = 0.9$  TeV. The statistical uncertainties are within the marker size and the systematic uncertainties are shown by the shaded bands. The data is compared to the models PYTHIA - Perugia 0, PYTHIA - Perugia 2011, PYTHIA ATLAS-CSC and PHOJET shown by different colored lines in Fig. 7.33. It is observed that the

models PHOJET, PYTHIA - Perugia 2011 and PYTHIA ATLAS-CSC more or less consistent with the data. But PYTHIA - Perugia 0 under predicts the data.

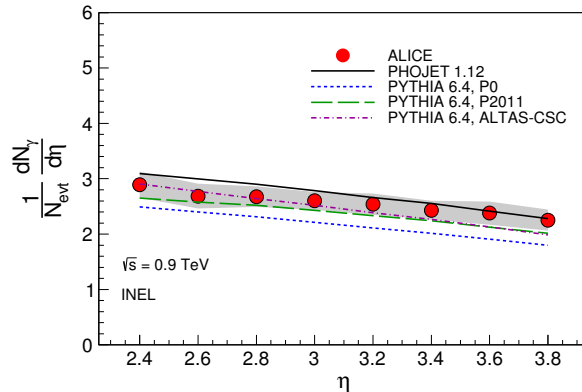


Figure 7.29: (Color online) Pseudo-rapidity distribution of photons for pp collisions at  $\sqrt{s} = 0.9$  TeV. Statistical errors are smaller than the size of the symbols and systematic errors are represented by the shaded regions. The black dotted lines are the expectation from PHOJET, the blue dotted lines are from PYTHIA Perugia 0 and the green dashed lines are from PYTHIA Perugia 2011 and the magenta dot-dashed line from PYTHIA ATLAS-CSC.

## 7.15 Comparison between photon and charged particle production

Since most of the photons are produced from  $\pi^0$  decays, the number of photons should be similar to that of charged particles. The pseudo-rapidity distribution for photons and charged particles is compared using the two different event generators PHOJET and PYTHIA (Fig. 7.30). It is observed that in both the models the pseudo-rapidity density of photons and charged particle are comparable within the  $\eta$  coverage of PMD. Next we compare the pseudo-rapidity distribution of photons to that measured in UA5 experiment [26] and to the charged particles measured in ALICE [1] at mid-rapidity. The results are presented in left panel of Fig 7.31. It is observed that our

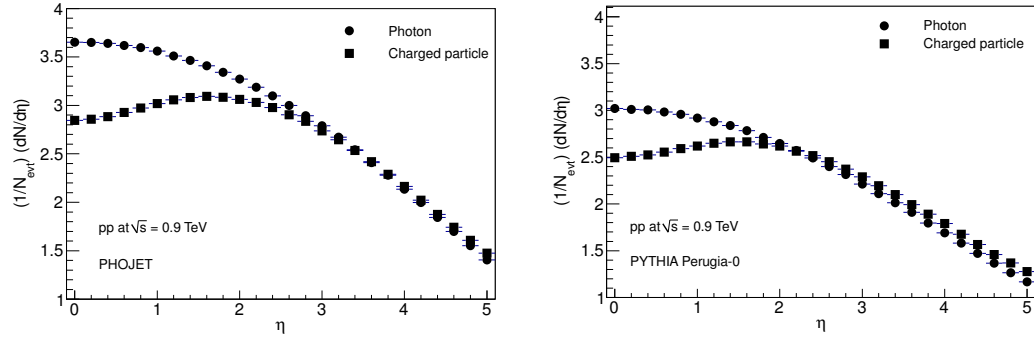


Figure 7.30: Pseudo-rapidity distributions of photons and charged particles at  $\sqrt{s} = 0.9$  GeV in monte carlo. The circles represent photons and the squares represent charged particles. Left panel : PHOJET right panel: PYTHIA

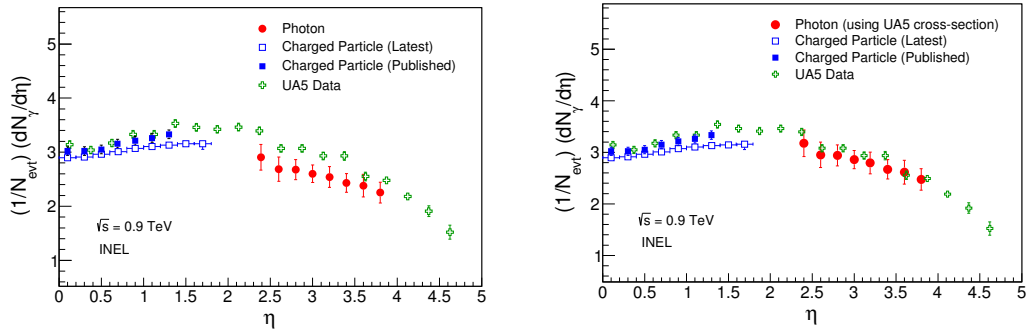


Figure 7.31: (Color online) Left panel: Pseudo-rapidity distribution of photons and charged particles for pp collisions at  $\sqrt{s} = 0.9$  TeV. The blue squares and green open crosses represent ALICE and UA5 data for charged particles, respectively. Open blue squares represent the latest charged particle results. The solid red circles represent the ALICE data for photons. Right panel : The photon results (solid red points) are calculated using the UA5 cross-section.

photon measurement under predicts the measurement at UA5 experiment. It is to be mentioned that the definition of INEL events (INEL = NSD + 1-arm-SD) [27] in UA5 experiment is different than ours. For this reason, the UA5 cross-section <sup>4</sup> has been used to re-calculate the pseudo-rapidity distribution of photons and compared with UA5 results as shown in the right panel of Fig 7.31. It is observed that the photon production is similar to the UA5 charged particle production within our  $\eta$  coverage after considering the same cross section.

## 7.16 Limiting fragmentation behavior

For very high energy collisions observed in lab frame (target at rest) some of the outgoing particles approach limiting distributions [28]. These distributions represent the broken fragments of the target. In the lab frame, the incoming particle is a Lorentz contracted system which passes through the target. Due to the excitation, the target may break up into fragments. In order to have a limiting distribution, one has to assume that the total hadronic cross section is approximately constant. If this occurred, then the excitation and break up of a hadron would be independent of the center of mass energy and the distribution in the fragmentation region would approach a limiting curve [29]. If we plot number of produced particles (photons or hadrons) as a function of  $\eta - y_{beam}$  ( $y_{beam}$  is the beam rapidity), then this number should be independent of beam energy at forward rapidities. This is known as limiting fragmentation. In this section we will discuss the limiting fragmentation behavior of photons within  $2.3 < \eta < 3.9$  in pp collisions at LHC energies. The Fig. 7.32 presents the  $dN_\gamma/d\eta$  distribution of photons at  $\sqrt{s} = 0.9$  TeV along with the measurements at  $\sqrt{s} = 2.76$  and 7 TeV [30], where the  $\eta$  in x-axis is shifted by the corresponding beam rapidities ( $y_{beam}$ ). The values of  $y_{beam}$  are 6.86, 7.98 and 8.97 for  $\sqrt{s} = 0.9, 2.76$  and 7 TeV respectively. Due to the limited acceptance of the detector, it is difficult to make any conclusion on the behavior of limiting fragmentation. Fu-

---

<sup>4</sup>We have used the same inelastic cross-section measured by UA5 experiment  $\sigma_{INEL} = 50.3 \pm 0.4 \pm 1.0$  mb [26, 27] in the monte carlo, used for correcting the trigger efficiency.

ture measurements at forward rapidity will help in better understanding the limiting fragmentation behavior.

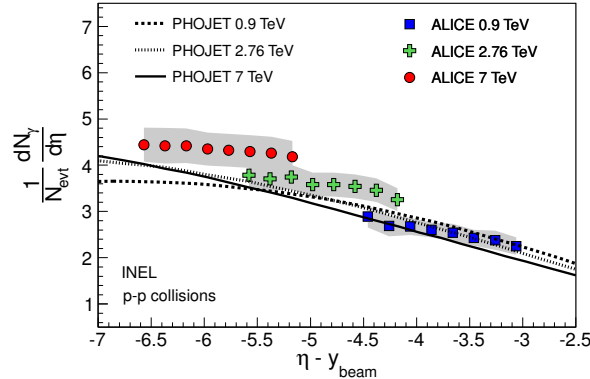


Figure 7.32: (Color online) Limiting fragmentation for pp collisions at 0.9, 2.76 and 7 TeV. The solid points represent the data and the lines represent the expectations from the PHOJET event generator.

### 7.16.1 Systematic Uncertainties

This section describes the sources of systematic uncertainties on the measurement of photon multiplicity and pseudo-rapidity at  $\sqrt{s} = 0.9$  TeV. The following are the sources of systematic uncertainties:

- Upstream Material
- Photon-hadron of discrimination thresholds

To study the effect of photon-hadron discrimination, we have created two different set of response of matrices with the following thresholds:

- (a) Cluster  $\text{ADC} > 432$  (6 times the MPV value of MIP) and  $N_{cell} > 2$
- (b) Cluster  $\text{ADC} > 648$  (9 times the MPV value of MIP) and  $N_{cell} > 2$

The differences between the extracted photon multiplicities are assigned as systematic errors.

- Unfolding using different event generators

The detector response matrix should not depend on the choice of the event generators, but there are second order effects due to the particle composition and spectra are different in different event generators. To study the sensitivity on event generators, we have constructed two different set of response matrices using the event generator PYTHIA and PHOJET. Then we apply it on the data to get the unfolded distribution. The difference in the unfolded distribution from two different response matrices gives the systematic uncertainty on the multiplicity and pseudo-rapidity due to the choice of event generators in the construction of response matrix.

- Unfolding using different methods:  $\chi^2$  minimization versus Bayesian methods

We have unfolded the data using the  $\chi^2$  minimization method of unfolding. To test correctness of the unfolding method, a different method of unfolding (Bayesian) is applied to the data and compared. The results are compatible with each other. The difference in results using two different unfolding methods are added in the systematic uncertainty of the photon multiplicity and pseudo-rapidity distribution.

- Different regularization schemes for unfolding

As discussed in the section 1.9 that we need to regularize the unfolded distribution to suppress the statistical oscillation originating from the matrix inversion employed in the unfolding method. To test the sensitiveness to the choices of regularization we have used the polynomial 0, polynomial 1 and logarithmic regularizations with appropriate  $\beta$  factors. The difference between them is added in the systematic uncertainty of the photon multiplicity and pseudo-rapidity distributions.

The multiplicity and pseudo-rapidity distributions with the above variations are shown in Fig. 7.33 and Fig. 7.34.

The final systematic uncertainties are calculated taking the difference from the mean of each sources and adding them in quadrature.

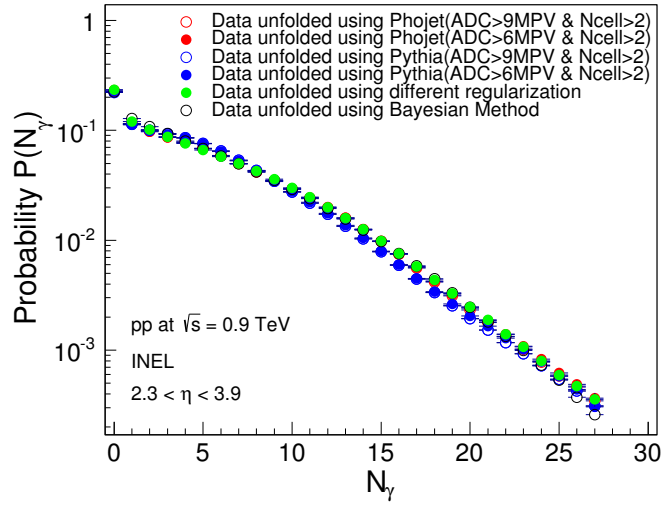


Figure 7.33: (Color online) Different sources of systematic errors: unfolded multiplicity distributions using two different discrimination thresholds, different event generators and different methods of unfolding for pp collisions at  $\sqrt{s} = 0.9$  TeV.

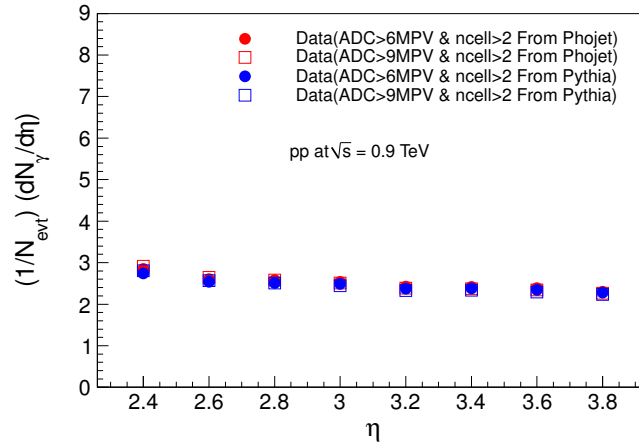


Figure 7.34: (Color online) Different sources of systematic errors: pseudo-rapidity distributions using two different discrimination thresholds and different event generators for pp collisions at  $\sqrt{s} = 0.9$  TeV.

## 7.16.2 Estimation of systematic errors due to upstream materials in front of PMD

To estimate the systematic error due to upstream material in front of the PMD we have used PHOJET simulation with default material as a response matrix and with material density increased by 10% (called PHOJET+10% in the text). We have taken the response matrix as that of the normal material. Then we unfold the measured multiplicity from normal PHOJET and PHOJET + 10% increased materials. The

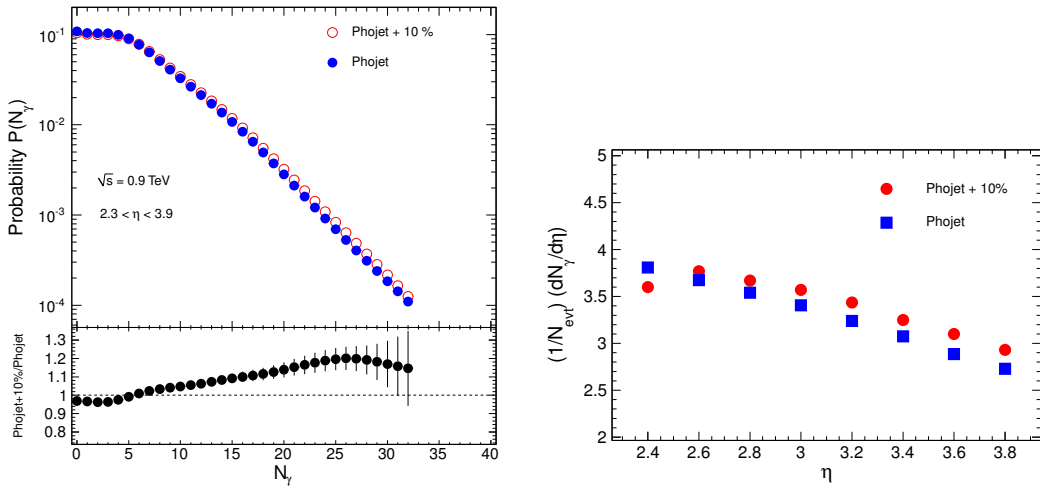


Figure 7.35: (Color online) The left panel shows the unfolded multiplicity distribution of photons from PHOJET and PHOJET + 10% for pp collisions at  $\sqrt{s} = 0.9$  GeV, lower half of the left panel shows the ratio of these distributions. In right panel unfolded pseudo-rapidity distribution is shown for both the cases.

unfolded distributions from normal PHOJET and PHOJET + 10% increased materials are shown in the left panel of Fig. 7.35. The difference with respect to the normal case is added as the systematic uncertainty in the photon multiplicity. The right panel shows the pseudo-rapidity distributions for both the cases. The difference between the two cases (PHOJET and PHOJET + 10% increased materials) is quoted as the systematic error due to material budget in the pseudo-rapidity distributions. The systematic uncertainties contributing to the photon multiplicity and pseudo-rapidity

distribution are reported in Table 7.6 and 7.7 respectively.

Source	0.9 TeV (1 -10)
Effect of upstream material	3 - 5 %
Discrimination Thresholds (MIP and ncell cuts)	0.36 - 0.9 %
Method of Unfolding (Event generators)	1.12 - 7.47 %
Method of Unfolding ( $\chi^2$ and Bayesian)	0.3 - 7.75 %
Different regularizations functions	2.04 - 2.8 %
Total	3.8 - 12.2 %

Table 7.6: The magnitude of the sources of systematic errors in multiplicity distribution for pp collisions at  $\sqrt{s} = 0.9$  TeV. The values are quoted here for 1-10 multiplicity for all the energies.

Source	0.9 TeV
Effect of upstream material	7 %
Discrimination Thresholds (MIP and cell cuts)	2%
Method of Unfolding (Event generators)	1 - 3%
Method of Unfolding ( $\chi^2$ and Bayesian)	negligible
Different regularizations functions	negligible
Total	7 - 7.9 %

Table 7.7: The magnitude of the sources of systematic errors and their contributions to the pseudo-rapidity distributions for pp collisions at  $\sqrt{s} = 0.9$  TeV.

## 7.17 Summary

In summary, we have presented the results of inclusive photon production at  $\sqrt{s} = 0.9$  TeV using the Photon Multiplicity Detector at forward rapidity in ALICE. We

have employed the unfolding method to correct the detector acceptance and efficiency. We have optimised the unfolding parameters in simulations which is applied to the data. We have studied in detail the material budget in front of PMD and shown that the photon-hadron discrimination threshold reduces the contamination to a large extent. Finally we have obtained the photon multiplicity and pseudo-rapidity distribution within the coverage of  $2.3 < \eta < 3.9$ . The results are compared to various models. We have observed that the multiplicity distribution from the PHOJET model is comparable to the data. The multiplicity distribution is well described by a single as well as a double NBD function. The multiplicity distribution deviates from KNO scaling at forward rapidity for  $z > 3$ . The pseudo-rapidity distribution of the models are close to the data. The beam energy dependence of average photons follows a logarithmic as well as a power law. Due to the limited acceptance of the detector we can not make any conclusion regarding the limiting fragmentation behavior of photons. The experimental data in future high energies will provide more insight.

## 7.18 Appendix

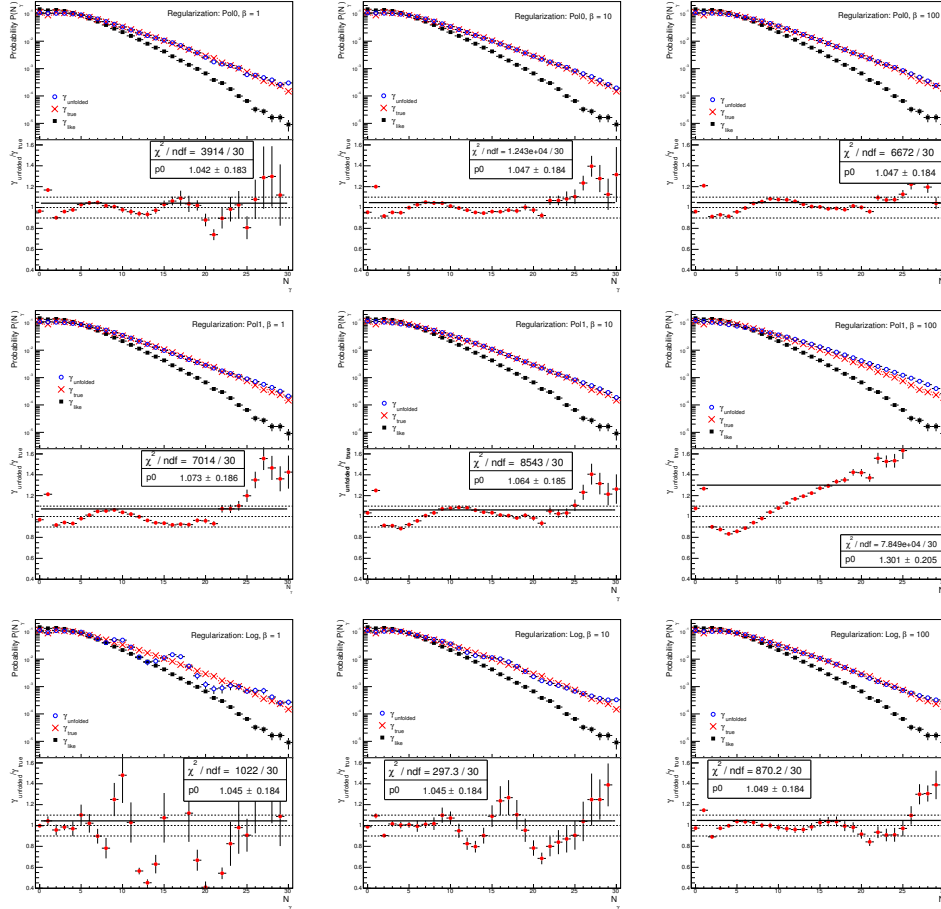


Figure 7.36: (Color online) Test of unfolding method in simulated data: True multiplicity distributions, the  $\gamma$ -like distributions and the unfolded distributions for pp collisions at 0.9 TeV. The lower panels in the figures show the ratios of unfolded to true distributions.

$N_\gamma$	Probability $P(N_\gamma)$	statistical uncertainties	systematic uncertainties
0	0.22471	0.00116	0.04769
1	0.11539	0.00117	0.01054
2	0.09810	0.00099	0.00935
3	0.08741	0.00106	0.00689
4	0.07848	0.00108	0.00595
5	0.06890	0.00102	0.00562
6	0.05918	0.00096	0.00436
7	0.04997	0.00089	0.00280
8	0.04176	0.00080	0.00181
9	0.03485	0.00071	0.00169
10	0.02923	0.00064	0.00194
11	0.02413	0.00055	0.00215
12	0.01974	0.00049	0.00221
13	0.01586	0.00042	0.00210
14	0.01255	0.00035	0.00190
15	0.00980	0.00030	0.00164
16	0.00746	0.00025	0.00136
17	0.00560	0.00020	0.00111
18	0.00418	0.00016	0.00089
19	0.00312	0.00013	0.00070
20	0.00233	0.00011	0.00054
21	0.00178	9.10293e-05	0.00042
22	0.00133	7.44729e-05	0.00032
23	0.00102	6.31726e-05	0.00025
24	0.00078	5.23063e-05	0.00019
25	0.00058	4.07377e-05	0.00014
26	0.00046	3.25818e-05	0.00013
27	0.00035	2.52425e-05	0.00010
28	0.00028	2.30647e-05	9.70920e-05
29	0.00021	2.2168e-05	8.06312e-05

Table 7.8: Photon multiplicity for pp collisions at  $\sqrt{s} = 0.9$  TeV.

$\eta$	$dN_\gamma/d\eta$	systematic uncertainties
2.4	2.890	0.2357
2.6	2.686	0.2253
2.8	2.677	0.1855
3.0	2.601	0.1604
3.2	2.541	0.1914
3.4	2.431	0.1722
3.6	2.380	0.2090
3.8	2.252	0.1908

Table 7.9: Photon pseudo-rapidity density for pp collisions at  $\sqrt{s} = 0.9$  TeV.

# Bibliography

- [1] K. Aamodt *et al.* (ALICE Collaboration), Eur. Phys. J C 65, 111 (2010).
- [2] K. Aamodt *et al.* (ALICE Collaboration), Eur. Phys. J C 68, 89-108 (2010).
- [3] V. Khachatryan *et al.* (CMS Collaboration), Phys. Rev. Lett. 105, 022002 (2010).
- [4] G. Aad *et al.* (ATLAS Collaboration), Phys. Lett. B 688, 21 (2010).
- [5] ALICE Technical Design Report of PMD, CERN /LHCC 2003nn ALICE TDR nn (August 2003).
- [6] J. Adams *et al.* (STAR Collaboration), Phys. Rev. Lett. 95, 062301 (2005).
- [7] B. B. Back *et al.* (PHOBOS Collaboration), Phys. Rev. Lett. 91, 052303 (2003).
- [8] M.G. Albrow *et al.* (Tev4LHC QCD Working Group), D6T (109) tune, arXiv:hep-ph/0610012 (2006).
- [9] R. Engel, J. Ranft, S. Roesler, Phys. Rev. D 52, 1459 (1995).
- [10] R. Brun *et al.*, GEANT3 User Guide (CERN Data Handling Division) DD/EE/841.
- [11] Test Results for the Photon Multiplicity Detector of ALICE experiment, (<https://aliceinfo.cern.ch/Notes/node/22>).
- [12] Techniques for Nuclear and Particle Physics Experiments, W. R. Leo, Springer-Verlag.

- [13] S. C. Phatak, Clustering Algorithm For PMD Data (<http://www.iopb.res.in/phatak/cluster/clusters.html>).
- [14] A. K. Dash, PhD thesis, (<http://www.hbni.ac.in/phdthesis/11phdthesis.htm>).
- [15] R. Brun and F. Rademaker, "ROOT: An object oriented data analysis framework", Nucl. Instr. Meth. A 389, 81 (1997) ([www.root.cern.ch](http://www.root.cern.ch)).
- [16] K. Aamodt *et al.* (ALICE Collaboration), Eur. Phys. J C 73, 2456 (2013).
- [17] V. Blobel, arXiv:hep-ex/0208022v1 (2002).
- [18] V. Blobel, Unfolding for HEP experiments-Introduction to inverse problems DESY Computing Seminar 23.rd June (2008).
- [19] J. F. Grosse-Oetringhaus, PhD thesis, University of Munster, Germany, (2009).
- [20] G. D. Agostini, Nucl. Instr. Meth. A 362, 487-498 (1995).
- [21] P. Z. Skands, Multi-Parton Interaction Workshop, Perugia, Italy, 28-31 Oct. 2008, Perugia-0 (320) tune, arXiv:0905.3418[hep-ph] (2009).
- [22] P. Z. Skands, Phys. Rev. D 82, 074018 (2010).
- [23] A. Moraes, ATLAS Note ATL-COM-PYS-2009-119, (2009).
- [24] Z. Koba, H.B. Nielsen, P. Olesen, Nucl. Phys. B 40, 317 (1972).
- [25] W. D. Walker, Phys. Rev. D 69, 034007 (2004).
- [26] G. J. Alner *et al.* (UA5 Collaboration), Z. Phys. C 33, 1 (1986).
- [27] M. G. Poghosyan, arXiv:1005.1806.
- [28] J. Benecke, T.T. Chou, C.N. Yang and E. Yen, Phys. Rev. 188, 2159 (1969).
- [29] F. Gelis, A. M. Stasto and R. Venugopalan, Eur. Phys. J C 48, 489 (2006).
- [30] S. De, PhD thesis, Home Bhabha National Institute, (2014).

- [31] S. K. Prasad, PhD thesis, Calcutta University, (2010).
- [32] M. M. Mondal, PhD thesis, Calcutta University, (2010).
- [33] C. Nygaard, PhD thesis, University of Copenhagen, (2011).
- [34] H. H. Dalsgaard, PhD thesis, University of Copenhagen, (2012).

# Chapter 8

## Energy dependence of anti-proton to proton ratio in pp collisions

### 8.1 Introduction

Protons ( $p$ ) and anti-protons ( $\bar{p}$ ) are the most abundantly produced baryons in high energy collisions. These have been measured at various center of mass energies ( $\sqrt{s}$ ) in hadron-hadron [1, 2] and nucleus-nucleus collisions [3] as a function of rapidity ( $y$ ) and transverse momentum ( $p_T$ ). Rapidity dependence of baryon production is expected to provide information on baryon transport and stopping [4] and the  $p_T$  dependence of the yields is expected to help in understanding the baryon production mechanism [2]. The  $\bar{p}/p$  ratio within the assumption of a thermal model is used to obtain the baryon chemical potential in heavy-ion collisions [5, 6]. Recently it has been argued based on QCD that there are constraints on allowing quarks to trace the baryon number [7], although they carry a baryon number of  $1/3$  based on quark model classification. It is argued that the trace of the baryon number could be associated with non-perturbative configurations of gluon fields rather than to valence quarks. All these make the study of the energy dependence of  $\bar{p}/p$  ratio important in high energy collisions, where

the role of the gluonic contributions to particle production is expected to increase with  $\sqrt{s}$ . In this thesis, we have compiled [8] experimentally measured  $\bar{p}/p$  ratio from 23 GeV to 7 TeV and compared with the models PYTHIA [9], PHOJET [10] and HIJING/B- $\bar{B}$  [11]. The baryon production mechanism are not similar in these models and are described in the section below.

## 8.2 Baryon production mechanism in models

In the string picture the process of baryon production is not unique. Mesons in such a picture can be viewed with a short string between a quark and anti-quark endpoints. However for the baryons consisting of three quarks it is difficult to visualize in a simple way. Baryon production in string picture is implemented in the PYTHIA model [9]. The simplest mechanism of baryon production in such a picture is through a diquark model. Any quark of a given flavor is assumed to be represented either by a quark or an antiquark in a color triplet state. Then the baryon and antibaryon are produced as nearest neighbors along the string. Such a model has to deal with the relative probability to pick a diquark over a quark. The extra suppression associated with a diquark containing a strange quark purely from phase space considerations and when a baryon is formed by joining a diquark and a quark, it has to be a symmetric three-quark state. Another equivalent mechanism is that in which diquarks as such are never produced, but baryons appear due to the successive production of several quark-antiquark pairs. Such a mechanism is referred to as the *popcorn* mechanism. These pairs exist by means of the color fluctuations in the field [13]. An advanced version of the popcorn mechanism is described in Ref. [14]. While the simpler popcorn mechanism admits at most one intermediate meson formation, the advanced version, on the other hand, allows for the possibility of many such mesons.

Another model of particle production which is widely used for comparison to data is the PHOJET [10]. The PHOJET, is a two component model that combines the ideas of the Dual Parton Model (DPM) [15] (soft processes) with perturbative QCD (hard processes). The mechanism of Pomeron exchange is at the heart of the DPM.

According to the DPM, the leading contribution to multiparticle production in high-energy hadron-hadron collisions arises from the exchange of a single Pomeron between the colliding hadrons. Secondary Pomeron exchanges account for the remaining activity in the event. Each exchanged Pomeron gives rise to two color-neutral chains stretching between quarks and diquarks, for baryons, or quarks and anti-quarks for mesons. The basic difference between PYTHIA and PHOJET lies in their approach towards an event formation. The starting point of particle production in PYTHIA is through the description of possible hard interactions in  $e^+ + e^-$ ,  $p+p(\bar{p})$  or  $e+p$  colliders and then combines several ideas for the soft hadronic interactions, whereas in PHOJET model it initializes the event generation by describing the soft component of hadron-hadron, photon-hadron or photon-photon interactions at high energies. The hard component is introduced later and calculated by perturbative QCD at the partonic level.

A novel mechanism of baryon transport motivated by the Regge theory [16] and differing from the diquark breaking model has been implemented in the form of an event generator, the HIJING/B- $\bar{B}$  [11]. The mechanism is motivated from the non-perturbative gluon field configuration called the the baryon junction. The baryon junction is found to be originating from the basic concepts of QCD and is a vertex where the color flux lines flowing from the three valence quarks are connected. The junction is expected to play a dynamical role through the Regge exchange of junction states in high energy collisions. The junction exchange could provide a natural mechanism for the transport of baryon number into the central rapidity region. Further details can be found in Ref. [7, 11]

### 8.3 Results

We have compared the energy dependence of the experimentally measured  $\bar{p}/p$  ratio at midrapidity in  $p+p$  collisions for various  $\sqrt{s}$  to the above discussed models. The data for the  $\sqrt{s} = 23, 31, 45$  and  $53$  GeV are from the ISR experiments [1]. The  $\bar{p}/p$  ratio at  $\sqrt{s} = 62.4$  GeV is from the PHENIX experiment at RHIC [12] and  $\sqrt{s} =$

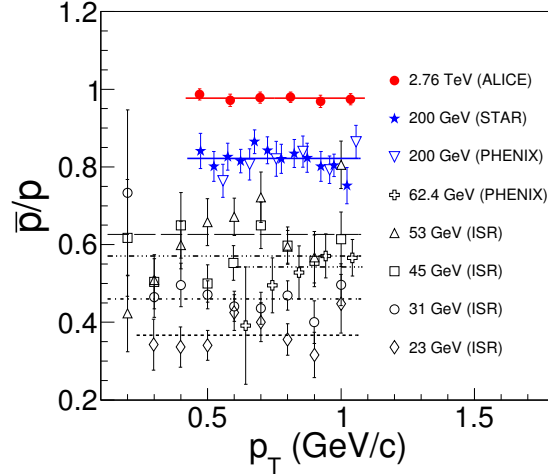


Figure 8.1: (Color online)  $\bar{p}/p$  ratio at midrapidity as a function of  $p_T$  for  $p+p$  collisions. The solid lines corresponds to new data from ALICE at LHC [2]. The  $\bar{p}/p$  ratio for  $\sqrt{s} = 200$  GeV is from the STAR experiment at RHIC [6]. The data for  $\sqrt{s} < 200$  GeV are from the ISR [1]. The dashed lines are straight line fits to the  $p_T$  dependence of the  $\bar{p}/p$  ratios at various  $\sqrt{s}$ , assuming the ratios do not depend on  $p_T$  for the measured range.

200 GeV from the STAR experiment at RHIC [6] and that at the highest energies of 900 GeV, 2.76 and 7 TeV are from ALICE at LHC [2]. Fig. 8.1 shows the  $\bar{p}/p$  ratio at midrapidity for various  $\sqrt{s}$  in  $p+p$  collisions as a function of  $p_T$ . All data points are only shown for the  $p_T < 1$  GeV/c. We observe that the ratios are constant as a function of  $p_T$  for each  $\sqrt{s}$  and the value of the  $\bar{p}/p$  ratio increases with  $\sqrt{s}$ . The solid lines show the recent measurements by the ALICE experiment at LHC [2].

Then, we have compared the experimental  $\bar{p}/p$  measurements to the expectation from PYTHIA (Ver. 6.4), PHOJET (Ver. 1.12) and HIJING/B- $\bar{B}$  (Ver. 1.34) models all with default settings.. Fig. 8.2 shows the increase of the  $p_T$  integrated  $\bar{p}/p$  ratio at midrapidity with increase in  $\sqrt{s}$  for  $p+p$  collisions. The  $\bar{p}/p$  ratio for  $\sqrt{s} = 63$  GeV shows an abnormally high value, although shown in the figure, we would not consider it for physics discussions. It is expected that RHIC data collected in the year 2005 at  $\sqrt{s} = 63$  GeV will help in resolving the abnormality in the  $\bar{p}/p$  ratio. All models studied show that the  $\bar{p}/p$  ratio increases with  $\sqrt{s}$  and approaches unity for

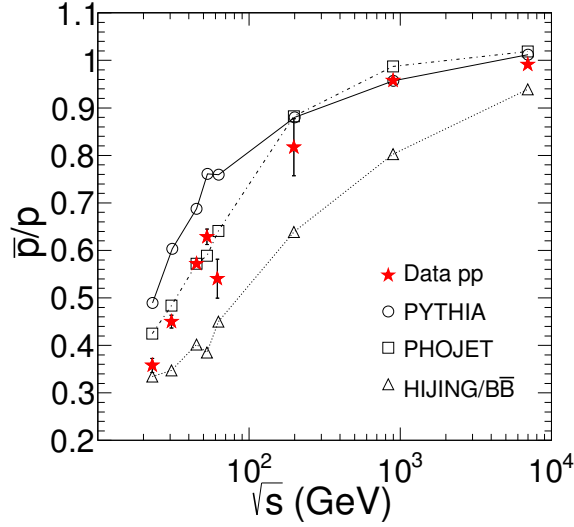


Figure 8.2: (Color online)  $\bar{p}/p$  ratio at midrapidity as a function of  $\sqrt{s}$  for  $p+p$  collisions. The experimental data are compared to model calculations from PYTHIA [9], PHOJET [10] and HIJING/B- $\bar{B}$  [11] with default settings.

higher energies (LHC). Infact, the PYTHIA and PHOJET models give very similar values at the LHC energies, while HIJING/B- $\bar{B}$  under predicts the  $\bar{p}/p$  ratio. The major difference occurs for  $\sqrt{s} < 200$  GeV, PYTHIA model gives higher values and HIJING/B- $\bar{B}$  continues to give lower values of  $\bar{p}/p$  ratio. Only the PHOJET model with default settings gives a reasonable description of the  $\sqrt{s}$  dependence of the measured  $\bar{p}/p$  ratio for  $p+p$  collisions.

The PYTHIA model has some variations in the baryon production mechanism. In Fig. 8.3 we compare the experimental  $\bar{p}/p$  ratio to such variations as implemented in the model. The parameter that we varied is known as MSTJ(12), it can take up values from 0 to 5, with the value of 2 as the default setting (one used in Fig 8.2). We did not consider MSTJ(12) = 0, as it corresponds to no baryon-antibaryon pair production. The condition MSTJ(12) = 1 refers to the mechanism where baryon production is through diquark-antidiquark pair production with the diquark being treated as a unit. While MSTJ(12) = 2 has the additional possibility for diquark to be split according to the popcorn scheme. The mechanism of baryon production for

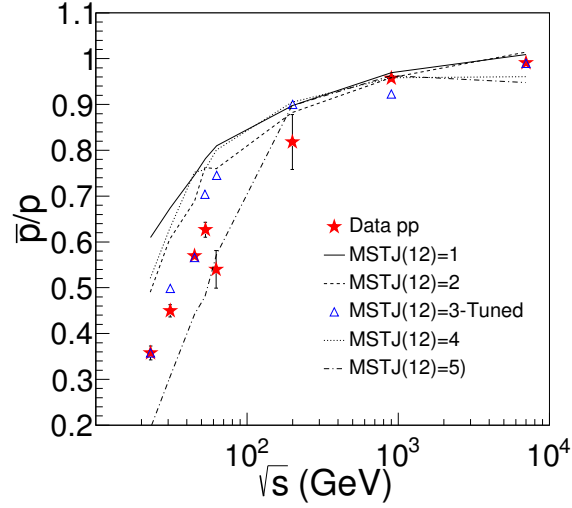


Figure 8.3: (Color online)  $\bar{p}/p$  ratio at midrapidity as a function of  $\sqrt{s}$  for  $p+p$  collisions compared to various implementation of the baryon production schemes in PYTHIA. See text for more details.

the case  $\text{MSTJ}(12) = 3$  is same as that for  $\text{MSTJ}(12) = 2$ , but has an additional condition that the production of first rank baryons may be suppressed. For this case, we additionally changed the value of the parameter which governs the suppression of diquark-antidiquark pair production in the color field, compared with quark-antiquark production. The value we put in for this parameter is 0.05 compared to the default value of 0.1. This is referred to as  $\text{MSTJ}(12)=3\text{-Tuned}$  in the Fig. 8.3. The condition  $\text{MSTJ}(12) = 4$  again revolves around  $\text{MSTJ}(12) = 2$  with an extra condition that the diquark vertices are suppressed. The last scheme implemented corresponds to  $\text{MSTJ}(12)= 5$  is similar to  $\text{MSTJ}(12) = 2$ , but with an advanced version of the popcorn model. Fig. 8.3 shows that for the lower beam energies the model results with the condition  $\text{MSTJ}(12)=3\text{-Tuned}$  has a reasonable agreement with the experimental data. For higher  $\sqrt{s}$  all the above conditions give similar values of  $\bar{p}/p$  ratio.

Different baryon production mechanisms could lead to an asymmetry in the production of protons and anti-protons. This asymmetry can be measured by construct-

ing the following ratio,

$$\frac{N_p - N_{\bar{p}}}{N_p + N_{\bar{p}}}, \quad (8.1)$$

where  $N_p$  and  $N_{\bar{p}}$  are the number of protons and anti-protons. As pair production would lead to same number of protons and anti-protons, the asymmetry will have a value of zero. Any non-zero value indicates the fraction of protons in midrapidity due to effects such as stopping. Fig. 8.4 shows the asymmetry ratio for protons and anti-protons as measured in  $p+p$  collisions for various  $\sqrt{s}$  ranging from 23 GeV to 7 TeV. The asymmetry is found to decrease with increase in  $\sqrt{s}$ , indicating the decreasing contributions of protons due to stopping at midrapidity. The ratio changes from about 46% at  $\sqrt{s} = 23$  GeV to 0.5% at the top LHC energy of 7 TeV. This range in  $\sqrt{s}$  corresponds to a range in  $y_{\text{beam}}$  of 3 to 9 units, respectively. This information is useful to study double baryon production in  $p+p$  collisions [7] and baryon number flow over long rapidity interval [17]. The solid line in Fig. 8.4 is a fit ( $\chi^2/ndf = 3/4$ ) to the experimental data with the function  $Ae^{-B \log \sqrt{s}}$ , with the parameters  $A = 6.7 \pm 0.9$  and  $B = 0.85 \pm 0.04$ .

In Fig. 8.5 we compare the beam energy dependence of the experimentally measured midrapidity  $\bar{p}/p$  ratio in  $p+p$  collisions to the available  $\bar{p}/p$  ratios at midrapidity in nucleus-nucleus (A+A) collisions. The A+A collision data are taken from the experiments at AGS [18], SPS [19] and RHIC [3]. For both the systems the  $\bar{p}/p$  rapidly rises with beam energy and approaches unity. For the  $p+p$  collisions the  $\bar{p}/p$  ratio has a value of  $0.991 \pm 0.005(\text{stat.}) \pm 0.014(\text{syst.})$  at 7 TeV, while for heavy-ion collisions the  $\bar{p}/p$  ratio has a value of  $0.77 \pm 0.14$  at 200 GeV. Looking at the region in beam energy where there is overlap between  $p+p$  and A+A collisions, the relative proton contributions at midrapidity for A+A collisions is more than for  $p+p$  collisions. The values of the ratio seem to become equal around 200 GeV. Also shown in the figure are fits to the experimental  $\bar{p}/p$  ratio in the  $p+p$  collisions to a function of the form  $[1 + C \exp[(\alpha_J - \alpha_P)y_{\text{beam}}]]^{-1}$ . The dashed line corresponds to  $\alpha_J - \alpha_P = (1.2 - 0.5) = -0.7$ , values as expected from a Regge model where the baryon pair production at very high energy is governed by Pomeron exchange and baryon transport by string-junction exchange [7, 20]. The  $\alpha_J$  and  $\alpha_P$  parameters corresponds to the junction

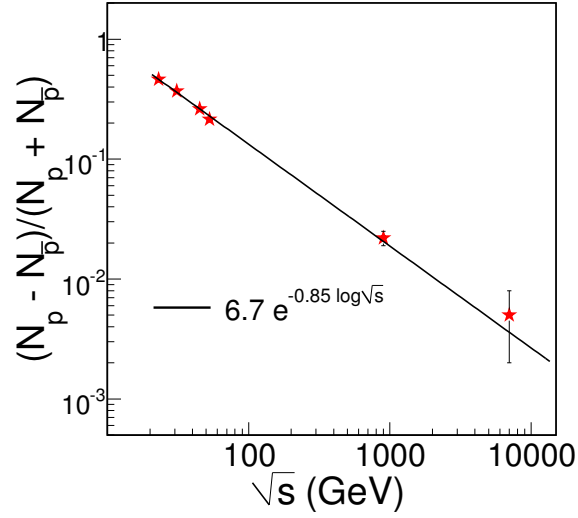


Figure 8.4: (Color online) Asymmetry for proton and anti-proton production at midrapidity for  $p+p$  collisions as a function of  $\sqrt{s}$ . The solid line is a fit to the data, with the functional form shown.

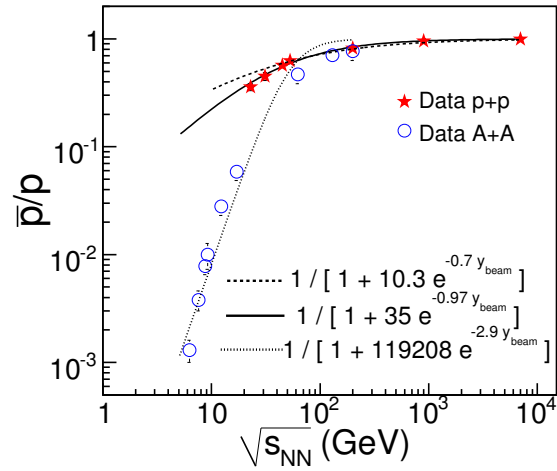


Figure 8.5: (Color online) Comparison of beam energy of  $\bar{p}/p$  ratio at midrapidity for  $p+p$  and nucleus-nucleus (A+A) collisions. The solid, dash and dotted lines are fits to the  $p+p$  and A+A data inspired by the model based on baryon string junction picture [7, 20].

intercept and the Pomeron intercept in the models. The  $\chi^2/ndf$  for the fit is 66/6. The best fit ( $\chi^2/ndf = 4/5$ ) is however obtained for  $\alpha_J - \alpha_P = -0.97 \pm 0.05$  (solid line), with about a factor of 3 increase in the value of parameter  $C$  compared to the results presented in dashed lines. The value of  $C$  for the case is  $10.3 \pm 0.4$  and that for the second case (solid line) is  $35 \pm 7$ . The Regge model inspired fit to the heavy-ion data (dotted line), yields a poor  $\chi^2/ndf = 33/7$ , with fit parameters  $C = 119208 \pm 49600$  and  $\alpha_J - \alpha_P = -2.9 \pm 0.2$ . The fit misses the the higher energy data points where such a model is more reliable. Constraining the fit to the energy range of 23 to 200 GeV gives  $C = 205 \pm 580$  and  $\alpha_J - \alpha_P = -1.2 \pm 0.6$  with  $\chi^2/ndf = 0.6/1$ .

## 8.4 Summary

In summary, we have presented a compilation of the available data for  $\bar{p}/p$  ratio at midrapidity for  $p+p$  collisions as a function of  $\sqrt{s}$ . We have also compared these ratios to the beam energy dependence from heavy-ion collisions and found that below  $\sqrt{s_{NN}} = 200$  GeV, the proton contribution at midrapidity in A+A collisions is significantly more compared to those in  $p+p$  collisions. The  $\bar{p}/p$  ratio is constant as a function of  $p_T$  for all the beam energies for  $p_T < 1$  GeV/ $c$ . This experimental observation already puts a constrain on mechanism of baryon production such as those implemented in HIJING/B- $\bar{B}$ . We also compared the  $\bar{p}/p$  ratio vs.  $\sqrt{s}$  to results from various models with different baryon production mechanisms, such as PYTHIA, PHOJET and HIJING/B- $\bar{B}$  with default settings. It is observed that PHOJET gives the best description of the data for all  $\sqrt{s}$ , PYTHIA gives higher values of the  $\bar{p}/p$  ratio for  $\sqrt{s} < 200$  GeV and HIJING/B- $\bar{B}$  under predicts the ratio for all beam energies. A detailed investigation of various mechanisms of baryon production as implemented in PYTHIA shows that the baryon production through diquark-antidiquark pair production with the diquark being treated as a unit and the additional possibilities (arrived by tuning various parameters) of diquark splitting according to the popcorn scheme and the production of first rank baryons suppressed gives a reasonable description for the  $\bar{p}/p$  ratio for  $\sqrt{s} < 200$  GeV. The asymmetry, a measure of proton stopping at the

midrapidity in  $p+p$  collisions are presented. The fraction of protons stopped around midrapidity varies from 46% at  $\sqrt{s} = 23$  GeV to 0.05% for  $\sqrt{s} = 7$  TeV. This energy range corresponds to a range in  $y_{\text{beam}}$  from 3 to 9 units, respectively. The data has also been compared to baryon string junction motivated phenomenological function whose parameters can constrain the Regge-model inspired descriptions of baryon asymmetry in  $p+p$  collisions.

# Bibliography

- [1] B. Alper *et al.*, (British-Scandinavian Collaboration) Nucl. Phys. B 100, 237 (1975).
- [2] K. Aamodt *et al.*, (ALICE Collaboration) arXiv:1006.5432.
- [3] B. I. Abelev *et al.*, (STAR Collaboration) Phys. Rev. C 81, 024911 (2010) and the references therein.
- [4] I. G. Bearden *et al.*, (BRAHMS Collaboration) Phys. Rev. Lett. 93, 102301 (2004).
- [5] J. Cleymans and K. Redlich, Phys. Rev. C 60, 054908 (1999); A. Andronic, P. Braun-Munzinger and J. Stachel, Nucl. Phys. A 772, 167 (2006).
- [6] B. I. Abelev *et al.*, (STAR Collaboration) Phys. Rev. C 79, 034909 (2009).
- [7] D. Kharzeev, Phys. Lett. B 378, 238 (1996) and the reference therein.
- [8] S. Singha, P. K. Netrakanti, L. Kumar and B. Mohanty, Phys. Rev. C 82, 044902 (2010).
- [9] T. Sjostrand, *et al.*, Computer Physics Commun. 135, 238 (2001); T. Sjostrand and M. van Zijl, Phys. Rev. D 36, 2019 (1987); T. Sjostrand and P. Skands, Eur. Phys. J. C 39, 129 (2005); T. Sjostrand and P. Skands, JHEP 0605, 026 (2006).

- [10] R. Engel, Z. Phys. C 66, 203 (1995); R. Engel, J. Ranft and S. Roesler, Phys. Rev. D 52, 1459 (1995).
- [11] S. E. Vance, M. Gyulassy, and X. N. Wang, Phys. Lett. B 443, 45 (1998).
- [12] A. Adare et. al, (PHENIX Collaboration) Phys. Rev. C 83, 064903 (2011)
- [13] B. Andersson, G. Gustafson and T. Sjostrand, Physica Scripta 32, 574 (1985).
- [14] P. Eden and G. Gustafson, Z. Phys. C 75, 41 (1997); P. Eden, hep-ph/9610246.
- [15] A. Capella *et al.*, Phys. Lett. 81B(1), 68 (1979); A. Capella and J. T. T. Van, Phys. Lett. 93B(1,2), 146 (1980); A. Capella and J. T. T. Van, Z. Phys. C 10, 249 (1981); A. Capella *et al.* Phys. Rep. 236(4,5), 225 (1994).
- [16] G.C. Rossi, G. Veneziano, Nucl. Phys. B 123, 507 (1977); Phys. Rep. 63, 153 (1980).
- [17] Boris Kopeliovich and Bogdan Povh, Phys. Lett. B 446, 321 (1999).
- [18] J. Barrette *et al.*, (E877 Collaboration) Phys. Rev. C 62, 024901 (2000); L. Ahle *et al.*, (E802 Collaboration) Phys. Rev. C **60**, 064901 (1999).
- [19] C. Alt *et al.*, NA49 Collaboration Phys. Rev. C 73, 044910 (2006); T. Anticic *et al.*, Phys. Rev. C 69, 024902 (2004).
- [20] A.B. Kaidalov, L.A. Ponomarev and K.A. TerMartirosyan, Sov. J. Nucl. Phys., 44, 468 (1986).

# Chapter 9

## Summary

In this thesis we have investigated identified particle production in Pb-Pb and pp collisions at the LHC energies. Specifically we have studied the production of  $K^{*0}$  resonance in these collisions. The  $K^{*0}$  is identified by reconstructing the invariant mass through its hadronic decay channel ( $K^{*0} \rightarrow \pi^- K^+$  and  $\overline{K}^{*0} \rightarrow \pi^+ K^-$ ). For this analysis we have used the data from the Inner Tracking System (ITS), Time Projection Chamber (TPC) and Time Of Flight (TOF) detector in ALICE. Also we have studied the production of inclusive photons in pp collisions identified by using the Photon Multiplicity Detector (PMD) at forward rapidity in ALICE. We have carried out phenomenological model studies to understand the baryon production mechanism in pp collisions.

The first part of the thesis presents the study of  $K^{*0}$  resonance production for Pb-Pb collisions at  $\sqrt{s_{NN}} = 2.76$  TeV and for pp collisions at  $\sqrt{s} = 2.76$  TeV. We have obtained the mass and invariant mass distribution width of  $K^{*0}$  as a function of transverse momentum ( $p_T$ ) in various collision centrality classes in Pb-Pb and in

minimum bias pp collisions. The mass and invariant mass distribution width are found to be consistent with the standard PDG value. The measurement does not show any evidence of mass shift and/or invariant mass distribution width broadening in heavy ion collisions relative to pp collisions. We have obtained the transverse momentum ( $p_T$ ) spectra of  $K^{*0}$  in various collision centralities in Pb-Pb and minimum bias pp collisions. The  $p_T$  spectra of  $K^{*0}$  is fitted with Boltzmann Gibbs Blast-Wave function for Pb-Pb collisions and Tsallis Levy function for pp collisions. The  $p_T$  integrated invariant yield ( $dN/dy$ ) and mean transverse momentum ( $\langle p_T \rangle$ ) are extracted from data in the measured region and using the fits for the extrapolation region. The  $dN/dy$  and  $\langle p_T \rangle$  are compared with the measurements at lower energies from the STAR experiment at RHIC. The  $K^{*0} \langle p_T \rangle$  is found to be about 20% higher than that at RHIC, which is consistent with the increase in the radial flow at higher energies. Further the  $\langle p_T \rangle$  of  $K^{*0}$  is compared with that of identified hadrons ( $\pi$ ,  $K$  and  $p$ ) measured for Pb-Pb collisions at  $\sqrt{s_{NN}} = 2.76$  TeV in ALICE. The  $K^{*0} \langle p_T \rangle$  is found to be comparable with that of protons (having mass close to  $K^{*0}$ ). This may be related to the hydrodynamic like behavior (that lighter particle moves faster than the heavier one) of the system formed in heavy ion collisions. The  $\langle p_T \rangle$  is studied as a function of mass of hadrons in pp collisions and it is found to increase with increase in mass. The  $\langle p_T \rangle$  of  $K^{*0}$  is found to follow the same trend like all the other hadrons in pp collisions. Such increase of  $\langle p_T \rangle$  as a function of mass can be understood through the effect of color reconnection in multiple parton interactions in pp collisions. We have obtained the  $K^{*0}/K^-$  ratio as a function of centrality in Pb-Pb and in minimum bias pp collisions. The smaller value of  $K^{*0}/K^-$  in Pb-Pb relative to pp collisions indicates the dominance of hadronic re-scattering over re-generation in heavy ion collisions. We have compared the  $K^{*0}/K^-$  and  $\phi/K^-$  ratio as a function of centrality. Due

to small lifetime ( $\sim 4$  fm/c), the  $K^{*0}$  is more probable to decay inside the medium formed in heavy ion collisions. Whereas the  $\phi$  meson has a lifetime about 10 times more than that of  $K^{*0}$  and the former is expected to decay outside the medium. We observed that the  $K^{*0}/K^-$  ratio decreases from peripheral to central collisions but  $\phi/K^-$  ratio is almost independent of collision centrality. This observation shows that the production of  $K^{*0}$  is affected due to the presence of more hadronic interaction in central collisions relative to peripheral collisions. From HBT studies it has been observed that the radii of the system formed in heavy ion collisions increases linearly with  $(dN_{ch}/d\eta)^{1/3}$ . So the variable  $(dN_{ch}/d\eta)^{1/3}$  can be used to study the system size dependence. The  $K^{*0}/K^-$  ratio is studied as a function of  $(dN_{ch}/d\eta)^{1/3}$  and compared with the results from RHIC. It is found that  $K^{*0}/K^-$  ratio decreases with increase in  $(dN_{ch}/d\eta)^{1/3}$ , which is equivalent to previously discussed centrality dependence. The  $K^{*0}/K^-$  as a function of  $(dN_{ch}/d\eta)^{1/3}$  appears to follow similar trend for both RHIC and LHC energies and for different collision systems.

It has been observed that the combined fit to the spectra of  $\pi^\pm$ ,  $K^\pm$  and  $p(\bar{p})$ , measured for Pb-Pb collisions at  $\sqrt{s_{NN}} = 2.76$  TeV, is well described by a Blast-Wave model. So the spectral shape of  $K^{*0}$  in Pb-Pb collisions is compared with the expectation from such Blast-Wave model. The predicted spectra from Blast-Wave model is normalized to the expected  $K^{*0}$  yield from thermal model which does not include the effect of hadronic re-scattering. The suppression of  $K^{*0}$  yield at low  $p_T$  with respect to the Blast-Wave prediction is observed for central collisions. Whereas the  $\phi$  meson does not show such suppression with respect to Blast-Wave model. This loss of  $K^{*0}$  yield can be attributed to the effect of re-scattering.

The nuclear modification factor ( $R_{CP}$  and  $R_{AA}$ ) for  $K^{*0}$  has been obtained using the present results in Pb-Pb and pp collisions. The  $R_{CP}$  of  $K^{*0}$  is compared with

that of  $\Lambda$ ,  $K_S^0$  and  $\phi$  measured in Pb-Pb collisions at  $\sqrt{s_{NN}} = 2.76$  TeV. The  $R_{CP}$  of  $K^{*0}$  is found to follow that of  $K_S^0$  meson in the intermediate  $p_T$  ( $2 < p_T < 5$  GeV/c). Such a picture supports the quark coalescence to be dominant mechanism for hadron formation. The  $R_{AA}$  of  $K^{*0}$  is found to be smaller than unity for central collision and a significant centrality dependence in  $R_{AA}$  is observed. The  $R_{AA}$  of  $K^{*0}$  is compared with the charged hadrons measured in Pb-Pb collisions at  $\sqrt{s_{NN}} = 2.76$  TeV. A large suppression of  $K^{*0}$   $R_{AA}$  relative to the charged hadrons at low  $p_T$  is observed for central collisions and this may be attributed to the effect of hadronic re-scattering.

Further to support the fact that the re-scattering effect is dominant over the re-generation in the hadronic phase of the matter formed in heavy ion collisions, we have carried out the study of  $K^{*0}$  production using A Multi-Phase Transport (AMPT) model. In the AMPT model one can vary the termination time of hadronic cascade. Larger the hadronic cascade time, more is the re-scattering among the decay daughters ( $\pi K$ ) of the  $K^{*0}$  meson. We observed that reconstructed  $K^{*0}$  signal is lost with the increase in hadronic cascade time. There is a clear decrease in  $dN/dy$  and increase in  $\langle p_T \rangle$  of  $K^{*0}$  with increase in hadronic cascade time. This can be attributed to the effect of re-scattering due to which we can not reconstruct the low  $p_T$   $K^{*0}$  meson and the signals are lost. We observed that the  $K^{*0}/K^-$  ratio is affected by re-scattering. So under certain assumptions one can estimate the lower limit of the time difference between the chemical and kinetic freeze out ( $\Delta t = t_{kinetic} - t_{chemical}$ ) using this  $K^{*0}/K^-$  ratio. We have estimated the  $\Delta t$  using the measurements at the RHIC and LHC energies and it is found to be increasing with increase in beam energy and system size. The lower limit of the hadronic phase lifetime at the LHC is about 4.6 fm/c for central collisions.

We have studied the  $v_2$  of  $K^{*0}$  in Pb-Pb collisions at  $\sqrt{s_{NN}} = 2.76$  TeV. The results are compared with the measurement at lower energy at RHIC. The deviation of  $K^{*0}$   $v_2$  in ALICE at low  $p_T$  may be due to the effect of increasing re-scattering at higher energies.

We have also presented the correlation of  $K^{*0}$  resonance with respect to a leading hadron in pp collisions at  $\sqrt{s} = 7$  TeV. The mass and invariant mass distribution width is found to be consistent with the standard PDG values as a function of the leading particle azimuthal angle. A nice correlation in the  $K^{*0}$  yield is observed with respect to the leading particle azimuthal angle. This analysis may act as a baseline for future analysis in Pb-Pb collisions.

In the second part of this thesis, we have studied the inclusive photon production at forward pseudo-rapidity ( $2.3 < \eta < 3.9$ ) in pp collisions at  $\sqrt{s} = 0.9$  TeV using the data from the Photon Multiplicity Detector (PMD) in ALICE. We have employed an unfolding method to correct the efficiency and acceptance of the detector. We have carried out detailed simulation study to optimize the unfolding parameters before applying it to the real data. A detailed study of the material present in front of the PMD has been done. It is shown that with the optimized photon-hadron discrimination threshold, the effect of upstream material is significantly reduced. The photon multiplicity distribution is obtained for  $\sqrt{s} = 0.9$  TeV and compared with various models: PYTHIA Perugia 0, PYTHIA Perugia 2011, PYTHIA ATLAS CSC and PHOJET. Among the models, the PHOJET is closer to the data. The multiplicity distribution is fitted to a double NBD function to estimate the contribution of soft and semi-hard processes in photon production at forward rapidity. The energy dependence of average photon multiplicity ( $\langle N_\gamma \rangle$ ) is studied along with the measurement at  $\sqrt{s} = 2.76$  and 7 TeV in ALICE. The  $\langle N_\gamma \rangle$  is found to follow both

power law and logarithmic dependence as a function of beam energy. Future data at higher energies can differentiate between this energy dependent behavior. The multiplicity distribution are also studied in terms of KNO variable. The KNO scaling is observed to be violated at higher multiplicities. The  $dN/d\eta$  of photons is obtained as a function of pseudo-rapidity and compared with various models: PYTHIA Perugia 0, PYTHIA Perugia 2011, PYTHIA ATLAS CSC and PHOJET. It is found that except PYTHIA-Perugia 0 all the models are consistent with the data. The limiting fragmentation behavior of photons have been attempted using the measured  $dN/d\eta$  distribution. However, no physics conclusion can be made due to the limited acceptance of the current PMD in ALICE.

Finally we have compiled the available data for  $\bar{p}/p$  ratio at mid-rapidity for pp collisions as a function of  $\sqrt{s}$ . We have compared these ratios to the beam energy dependence from heavy-ion collisions and found that below  $\sqrt{s_{\text{NN}}} = 200$  GeV, the proton contribution at mid-rapidity in A+A collisions is significantly more compared to those in pp collisions. The  $\bar{p}/p$  ratio is constant as a function of  $p_T$  for all the beam energies for  $p_T < 1$  GeV/c. This observation already puts a constraint on mechanism of baryon production such as those implemented in HIJING/B- $\bar{B}$ . We also compared the  $\bar{p}/p$  ratio vs.  $\sqrt{s}$  to results from various models with different baryon production mechanisms, such as PYTHIA, PHOJET and HIJING/B- $\bar{B}$  with default settings. We have observed that PHOJET gives the best description of the data for all  $\sqrt{s}$ , while PYTHIA gives higher values of the  $\bar{p}/p$  ratio for  $\sqrt{s} < 200$  GeV and HIJING/B- $\bar{B}$  under predicts the ratio for all beam energies. We have done a detailed investigation of various mechanisms of baryon production as implemented in PYTHIA. Our study shows that the baryon production through diquark-antidiquark pair production with the diquark being treated as a unit and the additional possibilities (arrived by tuning

various parameters) of diquark splitting according to the popcorn scheme and the production of first rank baryons suppressed gives a reasonable description for the  $\bar{p}/p$  ratio for  $\sqrt{s} < 200$  GeV. We have studied the asymmetry ratio, a measure of proton stopping at the mid-rapidity in  $pp$  collisions. We have observed that the fraction of protons stopped around mid-rapidity varies from 46% at  $\sqrt{s} = 23$  GeV to 0.05% for  $\sqrt{s} = 7$  TeV. This energy range corresponds to a range in  $y_{\text{beam}}$  from 3 to 9 units, respectively. The data has also been compared to baryon string junction motivated phenomenological function whose parameters can constrain the Regge-model inspired descriptions of baryon asymmetry in pp collisions.

This thesis thus demonstrated the importance of re-scattering on resonance production in high energy heavy-ion collisions through the measurements involving the  $K^{*0}$  meson. It presented the first measurements of inclusive photon production at LHC in forward rapidity. Finally we have attempted to understand baryon production in high energy pp collisions by confronting the large body of data on  $\bar{p}/p$  ratio to various model calculations.